Activity of M dwarfs in the CARMENES sample

Dissertation
zur Erlangung des mathematisch-naturwissenschaftlichen Doktorgrades
“Doctor rerum naturalium”
der Georg-August-Universität Göttingen

im Promotionsprogramm PROPHYS
der Georg-August University School of Science (GAUSS)

vorgelegt von
Patrick Schöfer
aus Northeim

Göttingen, 2021

Betreuungsausschuss

Prof. Dr. Ansgar Reiners, Institut für Astrophysik, Georg-August-Universität Göttingen

Prof. Dr. Stefan Dreizler, Institut für Astrophysik, Georg-August-Universität Göttingen

Dr. Sandra Jeffers, Institut für Astrophysik, Georg-August-Universität Göttingen,
bis 15. November 2020

Mitglieder der Prüfungskommission

Referent: Prof. Dr. Ansgar Reiners
Institut für Astrophysik, Georg-August-Universität Göttingen

Korreferent: Prof. Dr. Stefan Dreizler
Institut für Astrophysik, Georg-August-Universität Göttingen

Weitere Mitglieder der Prüfungskommission:

Prof. Dr. David J. E. Marsh
Institut für Astrophysik, Georg-August-Universität Göttingen

Prof. Dr. Hardi Peter
Abteilung Sonne und Heliosphäre, Max-Planck-Institut für Sonnensystemforschung

Prof. Dr. Ariane Frey
II. Physikalisches Institut, Georg-August-Universität Göttingen

Prof. Dr. Andreas Tilgner
Institut für Geophysik, Georg-August-Universität Göttingen

Tag der mündlichen Prüfung: 18. Februar 2021

Die Pferde der Hoffnung galoppieren,
doch die Esel der Erfahrung schreiten langsam.

— russisches Sprichwort

The horses of hope gallop,
but the asses of experience go slowly.

— Russian proverb

Abstract

The Calar Alto high-Resolution search for M dwarfs with Exo-earths with Near-infrared and optical Echelle Spectrographs (CARMENES) has been searching and finding planets for five years by looking for periodic Doppler-shift variations down to $1\,\mathrm{m\,s^{-1}}$. One challenge in detecting planetary signals with this precision is that activity phenomena on the star can mimic Doppler signals in the same order of magnitude. While stellar activity imposes this challenge for finding planets, the spectra obtained in the survey also provide a treasury of data for studying stellar activity itself. In this thesis, I aim to quantify the stellar activity of 337 M dwarfs in the CARMENES sample by measuring the strength of chromospheric emission lines and photospheric absorption bands, to identify correlations, and to investigate the temporal variability of the activity indicators. I used a spectral subtraction technique to measure pseudo-equivalent widths of the He I D_3, Hα, He I λ10833 Å, and Paβ lines, the Na I D doublet, and the Ca II infrared triplet. For three TiO, two CaH, and two VO absorption bands and the FeH Wing-Ford band, I calculated indices as the flux ratio of two spectral regions on either side of the band heads. Using generalised Lomb-Scargle periodograms, I searched for periodicities in the measured indicators. I analysed four out of eighteen stars that show a periodic modulation with the rotation period in more than two indicators in more detail.

I find that He I D_3 and Hα show a very similar spectral-type dependence and are strongly correlated. For Na I D and the Ca II infrared triplet, the correlation with Hα is weaker, as the subtraction method cannot adjust for the very different shapes of these lines. No strong correlations with the other indicators are found for He I λ10833 Å and Paβ. The photospheric bands are strongly correlated with each other and show activity effects of different intensities. I outline a new indicator to quantify these effects. All results are in good agreement with previously published results. He I D_3 and Hα show smaller relative variations at higher activity levels, whereas the relative variations of other indicators show no clear correlations. One TiO band, one CaH band, one line of the Ca II infrared triplet, and Hα undergo periodic modulations with the rotation period most commonly. The more detailed analysis of four stars shows the peculiarities in the signals of each star and reveals changing signals over time.

Contents

List of Figures

List of Tables

1. Introduction

This chapter gives an overview of the physical background for this thesis: While Sect. 1.1 introduces spectroscopy as the concept for collecting the information analysed in this thesis from the stars, Sects. 1.2 and 1.3 outline how stars are classified and how their planets are discovered. This aims to explain the terms *M dwarf* and *CARMENES* used in the title of this thesis. Stellar *activity* is explained in Sect. 1.4 with a description of the observed phenomena, their physical interpretation, and their relevance in the context of M dwarfs and exoplanets. The remaining chapters of this thesis are outlined in Sect. 1.4.4.

1.1. Spectroscopy

The spectrum of a light source is given by the flux as a function of the wavelength λ or the frequency ν. As an example, I consider a body with a constant temperature T that completely absorbs any incoming radiation. Such a body is called a *black body* and emits light with a continuous spectrum that is described by *Planck's law*. The spectral radiance per unit wavelength depends on T and is given by

$$B_\lambda(\lambda, T) = \frac{2hc^2}{\lambda^5} \frac{1}{\exp(\frac{hc}{\lambda k_B T}) - 1}, \tag{1.1}$$

where h is the Planck constant, c is the speed of light, and k_B is the Boltzmann constant. At any given wavelength λ, B_λ is higher for a black body with a higher temperature. However, the wavelength $\lambda_{\max}$ where B_λ is maximum increases with decreasing temperature as given by *Wien's displacement law*:

$$\lambda_{\max} T = 2.897771955 \cdot 10^{-3}\,\mathrm{m\,K} \tag{1.2}$$

The total emitted energy per unit time of a body is called its luminosity. For a black body with radius R and temperature T, the luminosity L follows from integration of Planck's law over all wavelengths and the body's surface, and is given by the *Stefan-Boltzmann law*:

$$L = 4\pi R^2 \sigma T^4, \tag{1.3}$$

where σ is the Stefan-Boltzmann constant. This relation can also be used to define an *effective temperature* T_{eff} of a body that is not a perfect black body.

1.1.1. Spectral lines

With its emitted light, each star sends out its fingerprint. The radiation generated in the core passes through the stellar atmosphere that can contain a variety of atoms and molecules in various states. Photons with an energy that corresponds to the difference between two energy levels of a molecular entity can be absorbed. The entity is then in an excited state and loses the energy either in a collision or by re-emitting a photon in a random direction. An observer now sees an *absorption line* in the spectrum, as there is less flux at the wavelength corresponding to the absorbed photon's energy. Similarly, molecular entities can be excited by other mechanisms and then emit additional photons with a specific energy. The observer now sees an *emission line* in the spectrum. As the wavelengths of absorption or emission lines can be compared with theoretical calculations or experimental results, the spectral lines allow to identify atoms or molecules that are present in the star's atmosphere. Because of their rotational and vibrational energy levels, molecules can absorb photons with similar energies, leading to a forest of lines rather than a single absorption line. This is called an *absorption band*.

Several effects cause a spectral line to appear broader than an infinitesimally narrow line. From the limited lifetime of an excited state follows an uncertainty in the energy according to Heisenberg's uncertainty principle. This *natural broadening* can be further increased by a higher pressure that leads to more collisions and thus faster collisional de-excitation and shorter effective lifetimes of the excited state. Additionally, the molecular entities in the stellar atmosphere move with different velocities according to a Maxwell distribution related to the temperature. Therefore, some entities move towards and other entities move away from the observer, causing different Doppler shifts resulting in *thermal broadening*. Similarly, the entities can move with different velocities with respect to the observer as the star rotates, causing *rotational broadening*. Further broadening can be caused by electrical or magnetic fields, e.g. via the *Zeeman effect*. While all these broadening mechanisms take place in the stellar atmosphere and affect the real line shapes, the instrument used to observe the spectrum will also affect the observed line shapes.

1.1.2. Spectrographs

Before a stellar spectrum can be analysed, the wavelength dependence of the light emitted by the star has to be measured. Most commonly, this is done by dispersing the light with a prism, a grating, or a grism, although Fourier transform spectrocopy with interferometers emerged as an alternative in the second half of the twentieth century (Loewenstein 1966). Prisms were used for the first spectral observations of the Sun and the brightest stars by Isaac Newton in the late seventeenth century and for the discovery of absorption lines by William Hyde Wollaston and Joseph von Fraunhofer in the early nineteenth century, whereas gratings were first used by Thomas Young in 1801 for solar observations, but were not useful for stellar observations before the development of the blazed grating in

the early twentieth century (Hearnshaw 2009, 2014). After Jacquinot (1954) had demonstrated the superiority of blazed gratings, prisms widely disappeared from astrophysical spectroscopy, but returned in combination with gratings in form of the grism (Bowen & Vaughan 1973).

The smallest wavelength difference $\Delta\lambda$ that can be resolved by a spectrograph varies with the wavelength range. Therefore, the resolution of a spectrograph is usually quantified by the *resolving power* R. For a grating with N illuminated grooves, the resolving power in the mth spectral order is given by

$$R = \frac{\Delta\lambda}{\lambda} = mN. \tag{1.4}$$

Using the grating equation

$$m\lambda = \frac{W}{N}(\sin\alpha + \sin\beta), \tag{1.5}$$

where W is the spacing of the grooves, α the angle of incidence and β the angle of diffraction, N can be eliminated as pointed out by Harrison (1949). For a blazed grating with blaze angle θ_B, the angles of incidence and diffraction are given by $\alpha = \theta_\mathrm{B} + \theta$ and $\beta = \theta_\mathrm{B} - \theta$. In quasi-Littrow mode, the diffracted light travels back along the path of the incident light, so $\theta \approx 0$. The resolving power is then given by

$$R = \frac{2W\sin\theta_\mathrm{B}}{\lambda}. \tag{1.6}$$

Therefore, high-resolution spectrographs use gratings with high blaze angles such as the reflective *echelle gratings*. Modern echelle spectrographs usually follow the design of the ELODIE spectrograph (Baranne et al. 1996) that has a blaze angle of $\theta_\mathrm{B} = 76°$. In an echelle spectrograph, the light diffracted by an echelle grating is cross-dispersed to separate the spectral orders. This leads to a two-dimensional spectrum such as Fig. 1.1.

To calibrate the wavelength corresponding to a position in the two-dimensional spectrum, spectral lines with known wavelengths have to be observed. On its way to the observer, parts of the stellar light are absorbed by molecules in the Earth's atmosphere causing *telluric* absorption lines in the spectrum. Particularly in the near-infrared range, strong telluric absorption bands can cover significant parts of a spectral order, as can be seen in Fig. 1.1. The wavelengths of telluric lines are known from models and can thus be used to calibrate the spectrum (e.g. Griffin & Griffin 1973; Seifahrt et al. 2010). Similarly, the stellar light can be passed through an absorption gas cell that superimposes absorption lines with known wavelengths before entering the spectrograph (e.g. Campbell & Walker 1979; Marcy & Butler 1992). Alternatively, the spectrum of a light source with known emission lines can be observed, either before and after the stellar spectrum or in parallel. A common light source used for wavelength calibration of echelle spectrographs are hollow cathode lamps (e.g. Kerber et al. 2007; Sarmiento et al. 2018). Because the observable spectral lines are inherent to the molecular entities that absorb or emit the light, these techniques may provide too few or too sparsely distributed lines in parts of the covered wavelength range. In contrast, Fabry-Pérot interferometers (e.g. Wildi et al. 2010; Bauer

Figure 1.1.: CARMENES spectrum of Luyten's star on 25 February 2016 at 21:07:51 UT with Fabry-Pérot etalon spectrum for radial-velocity drift correction. The upper third is from the near-infrared channel (9600 – 17100 Å), the two bottom thirds are from the visible-light channel (5200 – 9600 Å) of the spectrograph.

et al. 2015) and laser frequency combs (e.g. Murphy et al. 2007; Metcalf et al. 2019) provide a grid of evenly spaced lines in wavelength and frequency space, respectively, and can thus significantly increase the precision of the wavelength calibration.

1.2. Star classification

Already in ancient times, stars were classified by their apparent brightness. With a revised definition, the ancient system of magnitudes is still in use today. Another difference between stars that is apparent to the naked eye in some cases is their colour. The apparent colour depends on the wavelength of maximum flux, which according to Eq. 1.2 depends on the effective temperature. A classification by colour is therefore the same as a classification by temperature.

1.2.1. Spectral types

Another approach that turns out to be equivalent to a classification by colour or temperature is a classification by spectral features. According to Eq. 1.1, there are relatively few photons of short wavelengths and high energies in cool stars, and thus they cannot be absorbed. However, while photons of all wavelengths and energies are more common in hot stars, the atoms can be in higher energy states or ionised and molecules can be broken up. In thermal equilibrium, molecular entities of the same species occupy different energy states and atoms appear in different ionisation states according to temperature-dependent ratios. Therefore, presence and strength of spectral lines are indicative for the temperature of the star.

First classifications based on the strength of hydrogen lines were done by Angelo Secchi and Williamina Fleming in the late nineteenth century (Giridhar 2010). Fleming used the classes A to N with decreasing strength of hydrogen lines. Cannon & Pickering (1901) discarded some classes and reordered the remaining classes to the sequence of spectral types O, A, B, F, G, K, and M, with intermediate types such as “A 5 F”. With further modifications by Morgan et al. (1943) and Johnson & Morgan (1953), and the addition of the spectral types L, T, and Y (Kirkpatrick et al. 1999; Burgasser et al. 2006), this system is still used today. As it was earlier believed that the hot stars are young and the cool stars are old, spectral types are traditionally called *early* (towards O) and *late* (towards Y).

1.2.2. Luminosity classes

Scatter plots of the classification by apparent brightness and the classification by colour, temperature, or spectral type, are called colour-magnitude diagrams. Using the absolute

magnitude or the luminosity L as defined in Sect. 1.1 instead of the apparent brightness yields the *Hertzsprung-Russell diagram* (HRD) that was originally described by Hertzsprung (1911) and Russell (1913) and was crucial to understand how stars evolve. A schematic view of a HRD is shown in Fig. 1.2.

Most stars appear on a line extending from hot and bright to cool and faint. This line is called the *main sequence*. However, there are groups of outliers above and below the main sequence. For a fixed temperature, the luminosity can, according to Eq. 1.3, only change if the radius changes. Therefore, the stars above the main sequence must have larger radii than main-sequence stars with the same temperature and are called *giants*. In contrast, the main-sequence stars are also called *dwarfs*. While a star spends most of its life as a dwarf, it does not move much on the main sequence. Giants are in a later state of stellar evolution. Based on the different regions in the HRD, the spectral type definition by Johnson & Morgan (1953) also includes *luminosity classes* denoted by Roman numbers. Main-sequence stars or dwarfs are luminosity class V. As only dwarfs are analysed in this thesis, I generally leave out the luminosity class when specifying spectral types and give the full spectral type with luminosity class only in Table A.1.

1.2.3. M dwarfs

Combining the classifications from two previous sections, stars with spectral type M and luminosity class V are called *M dwarfs*, sometimes abbreviated as dM. In the original classification by Cannon & Pickering (1901), M was the latest spectral type and defined by the clear presence of titanium oxide absorption bands in the spectrum. While this classification was based on visible-light spectra, Kirkpatrick et al. (1991) defined standard stars for spectral subtypes between K5 and M9 using TiO and VO absorption bands in near-infrared spectra. Pecaut & Mamajek (2013) created a table of the typical effective temperature from $T_{\rm eff}$ measurements and estimates of the most common standard stars for each spectral subtype. I list their effective temperatures for M dwarf subtypes in Table 1.1. For M7.5 and M8.5, I give the average effective temperatures of M7.0 and M8.0, and of M8.0 and M9.0, respectively. Using these effective temperatures and Eq. 1.2, the wavelength of maximum flux for M dwarfs is between around 7500 Å for M0.0 and 12100 Å for M9.5. As illustrated in Fig. 1.3, M dwarfs thus emit most of their light at near-infrared wavelengths.

M dwarfs cover a wide range of fundamental stellar parameters (in the following, the subscript $\odot$ refers to solar units): Masses range from $0.6\,M_\odot$ for M0 down to $0.075\,M_\odot$ for M9 (Reid & Hawley 2005), which is the minimum mass required to sustain hydrogen burning in the core (Chabrier & Baraffe 2000). Because of their low mass, M dwarfs of various ages can be observed, as even the first formed M dwarfs have not yet evolved beyond the main sequence with lifetimes up to 10^{13} years (Laughlin et al. 1997). Typical

[1] https://www.eso.org/public/images/eso0728c/

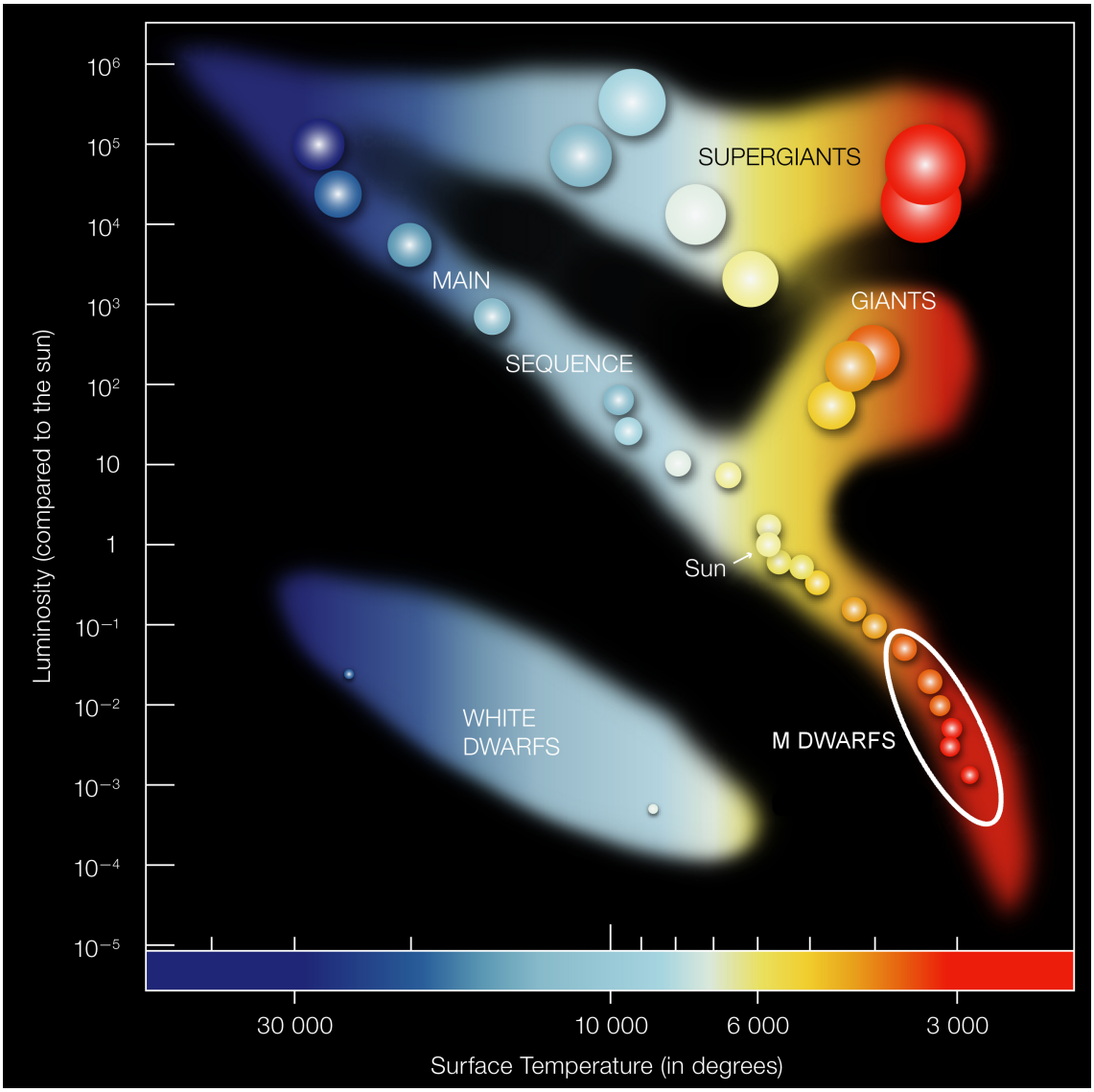

Figure 1.2.: Schematic view of a Hertzsprung-Russell diagram. Image credit: adapted from ESO[1], used under CC-BY 4.0

Table 1.1.: Effective temperatures corresponding to spectral subtypes as compiled by Pecaut & Mamajek (2013).

Spectral type	T_{eff} [K]	Spectral type	T_{eff} [K]
M0.0	3850	M5.0	3050
M0.5	3800	M5.5	3000
M1.0	3680	M6.0	2800
M1.5	3600	M6.5	2700
M2.0	3550	M7.0	2650
M2.5	3450	M7.5	2610
M3.0	3400	M8.0	2570
M3.5	3250	M8.5	2510
M4.0	3200	M9.0	2450
M4.5	3100	M9.5	2400

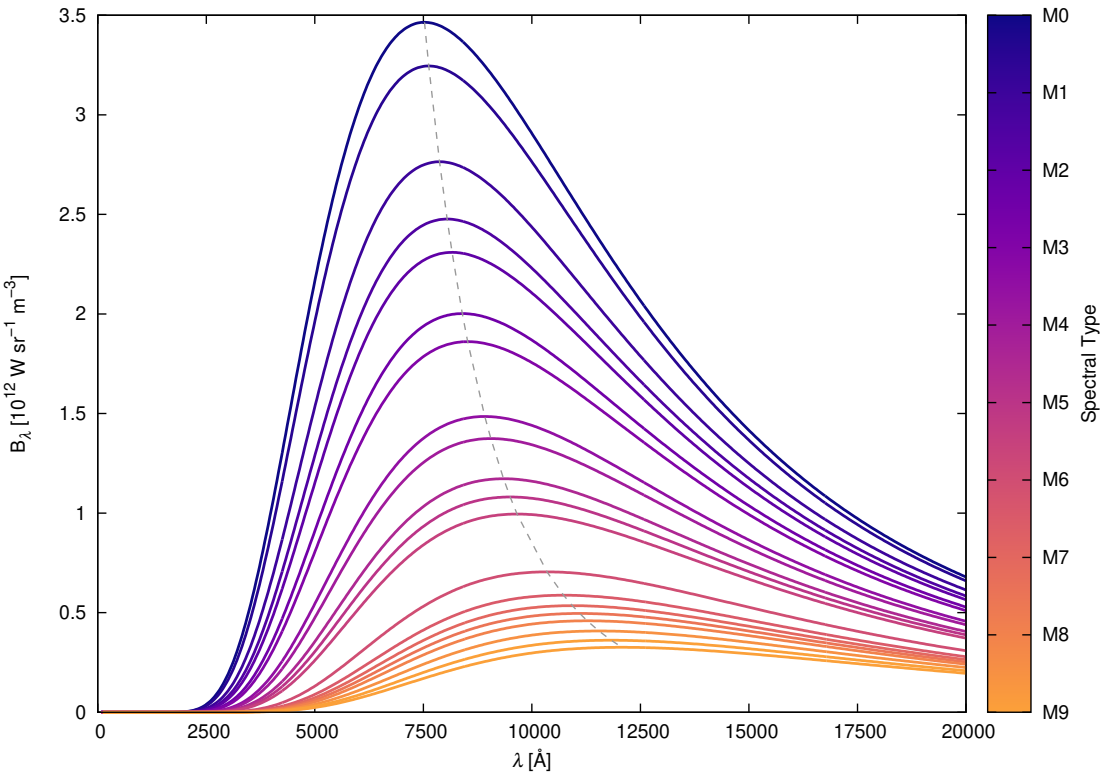

Figure 1.3.: Spectral radiance per unit wavelength of black bodies with effective temperatures corresponding to different M subtypes as listed in Table 1.1 according to Eq. 1.1. The dashed grey line connects the maxima of the curves at the wavelengths given by Eq. 1.2.

radii between 0.08 $R_\odot$ for M9 and 0.62 $R_\odot$ for M0 correspond to typical luminosities between $1.5 \cdot 10^{-4}\,L_\odot$ for M9 and $7.2 \cdot 10^{-2}\,L_\odot$ for M0 (Reid & Hawley 2005). Therefore, M dwarfs are very faint stars, and even Proxima Centauri, at a distance of 1.301 pc (Gaia Collaboration et al. 2018) the closest stellar neighbour of the Sun and an M dwarf with spectral type M5.5 (Boyajian et al. 2012), is invisible to the naked eye from Earth, as are all other M dwarfs. Still, with 283 M dwarfs among 378 known stars within 10 pc (Henry et al. 2018, RECONS[2]), they are the most common type of stars in the solar neighbourhood and planets occur more frequently at later spectral types (Mulders et al. 2015; Gaidos et al. 2016; Hardegree-Ullman et al. 2019), making this class of stars an interesting field of research.

1.2.4. Structure and atmospheres of main-sequence stars

Low-mass stars at the red end of the main sequence are not simply scaled-down versions of hotter and more massive main-sequence stars, but differ in the way energy is produced in their cores and transported outwards. While the energy source of all main-sequence stars is the fusion of hydrogen into helium, the dominant process in hot early-type dwarfs is the CNO cycle, whereas the proton-proton chain dominates in Sun-like and later-type dwarfs (e.g. Adelberger et al. 2011). The dominant energy transfer mechanisms are convection and radiation. Convection is most efficient in regions with a steep temperature gradient, whereas radiation does not require a temperature gradient, but works best if the opacity is low. In stars with masses above 1.5 $M_\odot$ or spectral type A and earlier, the extreme temperature dependence of the CNO cycle constrains the energy production to a relatively small inner core. This leads to a steep temperature gradient above the inner core, and thus a convection zone in the inner part, while radiation is dominant in the outer part, where the temperature gradient is shallower. For Sun-like stars with masses below 1.5 $M_\odot$, the energy production via proton-proton chain is more distributed and does not lead to a sufficient temperature gradient for efficient convection. Therefore, the inner part is radiative. However, in the outer part, the temperature is sufficiently low for the recombination of hydrogen atoms. This results in a higher opacity, and convection becomes more efficient than radiation in this part. The transition layer between the inner radiation and the outer convection zones is called tachocline. With decreasing mass and temperature, the outer convection zone becomes deeper until the inner radiation zone vanishes completely at around 0.3 $M_\odot$ or spectral type M4 (Chabrier & Baraffe 1997; Stassun et al. 2011). Later M dwarfs are thus fully convective. The different internal structures of stars along the main sequence are summarised in Fig. 1.4.

While the stellar interior contributes most to the stellar mass, it is optically thick and can thus not be observed directly. Photons can only escape from the more transparent outer layers, collectively referred to as the stellar atmosphere. It is this region where spectral lines are formed as described in Sect. 1.1.1. As can be seen in the cross-section of the Sun

[2] http://www.recons.org, census of objects nearer than 10 pc as of 12 April 2018

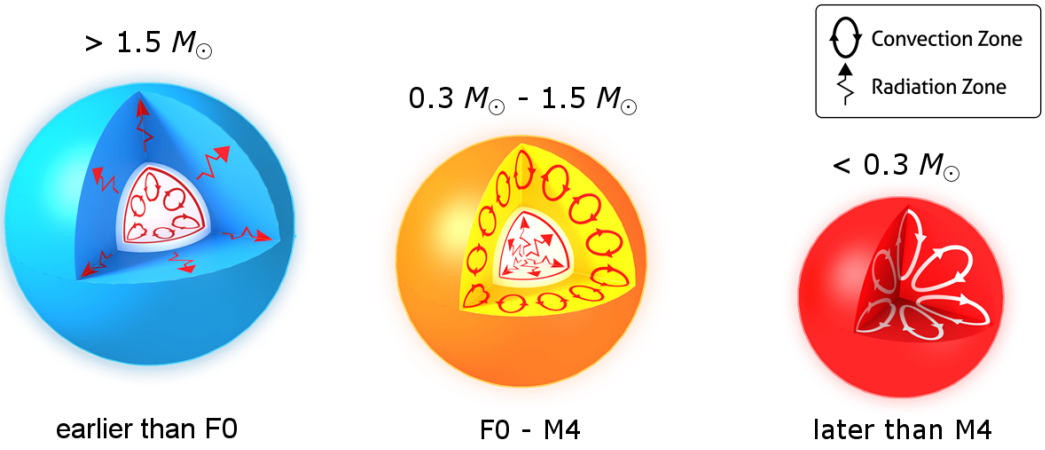

Figure 1.4.: Energy transfer mechanisms in the interiors of stars with different masses and spectral types. Massive early-type stars have a convective core and an outer radiation zone, whereas Sun-like stars have a radiative core and an outer convection zone. Low-mass late M dwarfs are fully convective. Image credit: adapted from Sun.org - www.sun.org[3], used under CC-BY-SA 3.0, modifications released under CC-BY-SA 4.0

in Fig. 1.5, three layers of stellar atmospheres are distinguished. Most of the light that finally reaches the observer originates from the lowest atmospheric layer, the *photosphere*. This layer therefore determines the observed effective temperature and spectral type of a star, while the upper atmospheric layers are less dense and usually outshined. Lockyer (1868) introduced the term *chromosphere* for the layer above the photosphere that appears red during a solar eclipse. Unlike in the photosphere, the temperature does not decrease with increasing height and decreasing pressure in the chromosphere (e.g. Fontenla et al. 2016). In the narrow transition region between chromosphere and corona, the temperature increases drastically (e.g. Mariska 1986). The *corona*, named after its appearance during solar eclipses, is the outermost and also hottest and least dense atmospheric layer. It can extend to several stellar radii as defined by the photosphere (e.g. Benz et al. 1998; Pestalozzi et al. 2000; Shopov et al. 2008). While a photosphere can be defined for every main-sequence star, chromospheres and coronae are ubiquitous among Sun-like and later-type stars, but not observed for spectral types earlier than late A (e.g. Simon et al. 2002). As these early-type stars do not have an outer convection zone in their interiors, this suggests that an outer convection zone is required for the formation of the hot outer atmospheric layers. I will describe observations and the heating of chromospheres and coronae in the context of stellar activity in Sect. 1.4.

[3] http://www.sun.org/images/heat-transfer-in-stars

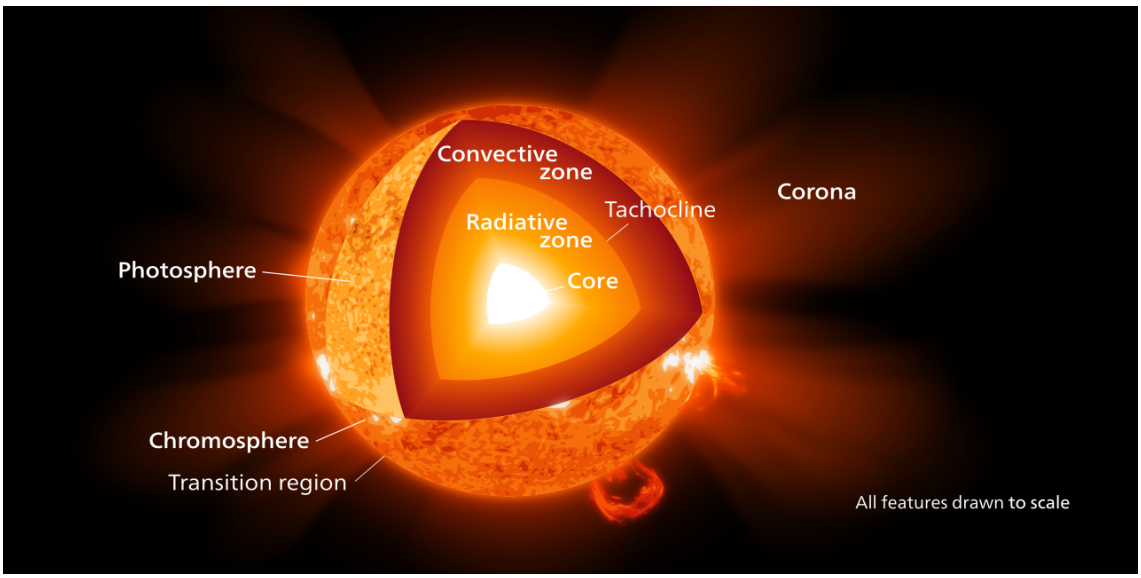

Figure 1.5.: Cross-section of the Sun with marked interior and atmospheric layers. Image credit: adapted from Kelvinsong via Wikimedia Commons[4], used under CC-BY-SA 3.0, modifications released under CC-BY-SA 4.0

1.3. Exoplanets

One of the first recorded methods to detect planets around other stars was already proposed in the nineteenth century by Niven (1874), but it took more than a century until the first successes. While the first confirmed exoplanet orbiting a pulsar was discovered by Wolszczan & Frail (1992), three years later, Mayor & Queloz (1995) discovered the first exoplanet around a main-sequence star and were awarded the Nobel prize for this discovery in 2019. Several methods to detect exoplanets have been used successfully since then:

- *Transit method*: A transiting planet blocks out a small fraction of the stellar light as it passes in front of the star, causing periodic dips in the light curve.
- *Radial-velocity method*: As the star moves around the common centre of mass of the system, a periodic modulation in its radial velocity is observed.
- *Direct imaging*: An image of the planet itself is obtained.
- *Microlensing*: Star and planet act as gravitational lenses on the light of a background source. The observed effect is different than the effect of a star alone.
- *Timing variations*: The star emits a periodic signal (e.g. a pulsar, an eclipsing binary, a pulsating star, or a transiting planet). While the star moves around the centre of mass of the system, its light has to travel a variable distance to the observer, and the periodic signal is observed earlier or later than expected.

[4] https://commons.wikimedia.org/wiki/File:Sun_poster.svg

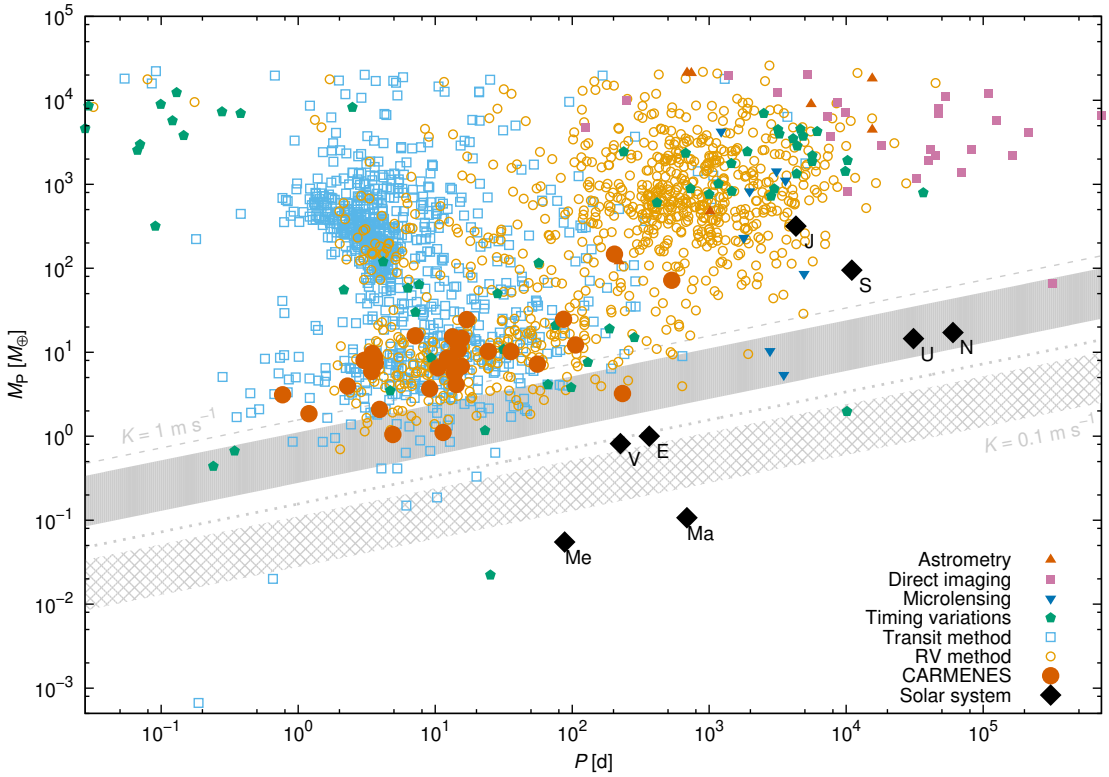

Figure 1.6.: Mass-period diagram of confirmed exoplanets using data from The Extrasolar Planets Encyclopaedia[5] as of 15 October 2020. Only planets with known orbital period P and mass M_P or minimum mass $M_P \sin i$ are shown. Masses are given in Earth masses $M_\oplus$. Different symbols correspond to different detection methods, the solar system planets are shown for comparison as black diamonds with their first letters. Exoplanets discovered by CARMENES are highlighted by red circles. The dashed grey line and the grey area mark the detection limits of the radial-velocity method with a semi-amplitude $K = 1\,\mathrm{m\,s^{-1}}$ for a solar-mass star and the M dwarf mass range, respectively, whereas the dotted grey line and the hatched area show the same but for $K = 0.1\,\mathrm{m\,s^{-1}}$.

- *Astrometry*: As the star moves around the common centre of mass of the system, periodic changes of its position are measured.

While the radial-velocity method is described in the following section, I refer to Perryman (2018) for more details on the other detection methods. As can be seen in the mass-period diagram in Fig. 1.6, the astrometric and direct imaging methods are most sensitive for massive planets with orbital periods of several years because these planets show the largest angular separations from their host stars and have the highest impact on the common centre of mass of the system. Microlensing also works best for long-period planets, but can detect lower-mass planets. The radial-velocity, timing variations, and transit methods cover a larger parameter space. With the exception of Jupiter, the solar system planets are located in sparsely populated regions of the diagram. Finding a solar system analogue would require observations with improved sensitivity over longer times.

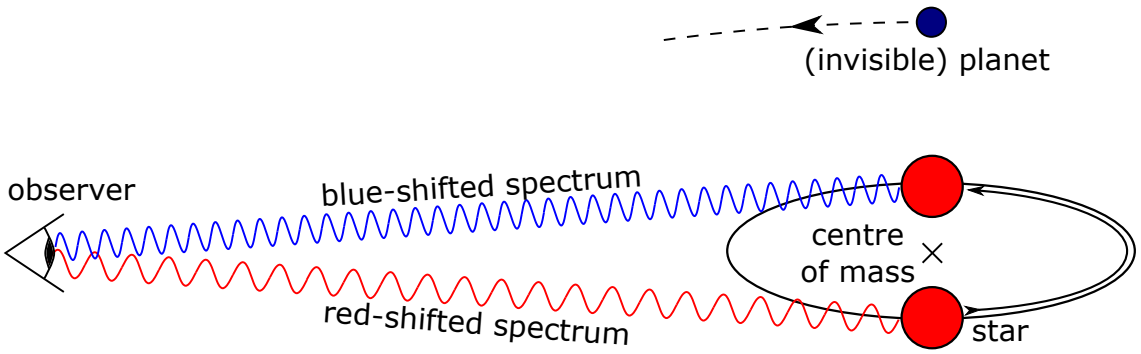

Figure 1.7.: Illustration of the idea behind the radial-velocity method: A planet and its host star orbit their common centre of mass. While the star moves away from the observer, its spectrum is red-shifted, whereas it is blue-shifted while the star moves towards the observer.

1.3.1. Radial-velocity method

A star that is orbited by a planet performs a motion around their common centre of mass. If the orbital plane is not perpendicular to the line of sight, the radial component of the velocity of the star with respect to the observer undergoes a periodic modulation. As illustrated in Fig. 1.7, the radial velocity (RV) and its variations can be measured from the *Doppler shift* of spectral lines:

$$\frac{\mathrm{RV}}{c} = \frac{\lambda - \lambda_0}{\lambda_0}, \tag{1.7}$$

where c is the speed of light, λ the observed wavelength and λ_0 the rest wavelength of the spectral line. If the star moves towards the observer, the RV is negative and $\lambda < \lambda_0$, so the spectrum appears blue-shifted. On the other hand, if the star moves away from the observer, the RV is positive and $\lambda > \lambda_0$, so the spectrum appears red-shifted. For a planet with mass M_P that orbits a star with mass $M_\star$ in a period P on an orbit with numerical eccentricity e, the semi-amplitude K of the RV modulation is given by

$$K = \left(\frac{2\pi G}{P}\right)^{\frac{1}{3}} \frac{M_\mathrm{P} \sin i}{(M_\mathrm{P} + M_\star)^{\frac{2}{3}}} \frac{1}{\sqrt{1-e^2}}, \tag{1.8}$$

where G is Newton's constant and i is the inclination angle between the orbital plane and a plane perpendicular to the line of sight. This angle is generally unknown, so only a minimum mass for the planet can be derived from the RV modulation, unless the planet can also be detected with the transit, direct imaging, or astrometric methods.

For an outside observer viewing the solar system edge-on, Eq. 1.8 yields a semi-amplitude $K \approx 0.09\,\mathrm{m\,s^{-1}}$ for the Sun caused by the Earth. This is comparable to the precision of the ESPRESSO spectrograph (Pepe et al. 2021) and below the detection thresholds of other current instruments, so Earth-like planets around Sun-like stars could not yet be found with the RV method. For a fixed planet mass, K is larger for shorter orbital

[5] http://exoplanet.eu

periods P and smaller stellar masses $M_\star$. This makes M dwarfs suitable targets for the search for Earth-like planets in the liquid water habitable zone. Because of their low temperatures and luminosities, the habitable zone is located closer to the star for M dwarfs than for Sun-like stars (e.g. Kasting et al. 1993; Kopparapu et al. 2013). This translates into orbital periods in the order of days to weeks and thus, combined with the low masses, to RV semi-amplitudes of $K \gtrsim 1\,\mathrm{m\,s^{-1}}$ (Endl et al. 2003). While high-resolution Echelle spectrographs such as HARPS (Mayor et al. 2003), HIRES (Vogt et al. 1994), and UVES (Dekker et al. 2000) reached the necessary precision for detecting RV modulations in that order of magnitude around twenty years ago, more recent instruments such as CRIRES+ (Dorn et al. 2014), HPF (Mahadevan et al. 2014), IRD (Kotani et al. 2014), NIRPS (Wildi et al. 2017), and SPIRou (Donati et al. 2018) aim to reach the same precision at near-infrared wavelengths, where M dwarfs emit more light than at visible-light wavelengths. However, with the exception of spectral subtypes later than M7, the far-red spectral range between 7000 Å and 9000 Å allows for a higher RV precision than the near-infrared range covered by these spectrographs because it contains more spectral lines that can be used for measuring the Doppler shift (Artigau et al. 2018; Reiners et al. 2018b; Reiners & Zechmeister 2020).

1.3.2. CARMENES

The *Calar Alto high-Resolution search for M dwarfs with Exo-earths with Near-infrared and optical Echelle Spectrographs* (CARMENES, Quirrenbach et al. 2018) has been surveying a sample of more than 350 stars using the RV method since January 2016. With a beam splitter separating the light at 9600 Å into the visible-light (VIS) and near-infrared (NIR) channels, CARMENES covers the wavelength range from 5200 Å to 17100 Å with the exception of several inter-order gaps at wavelengths $\lambda > 11400$ Å, as shown in Fig. 1.8. While the VIS channel spectrograph operates at room temperature, the NIR channel spectrograph is cooled to 140 K to avoid thermal contamination of the spectra. Both spectrograph channels provide high-resolution Echelle spectra with a resolving power of $R = 94\,600$ in the VIS and $R = 80\,400$ in the NIR channel. Each channel is fed by two fibers, one carrying the stellar light and the other used for simultaneously monitoring either sky emission close to the star or RV drifts using Fabry-Pérot etalons (Schäfer et al. 2018). Bauer et al. (2020) demonstrated that the VIS channel has a median RV precision of $1.2\,\mathrm{m\,s^{-1}}$, whereas the NIR channel reaches a median RV precision of $3.7\,\mathrm{m\,s^{-1}}$ using only the orders that contain most RV information and are least contaminated by telluric absorption bands.

CARMENES is mounted at the 3.5 m telescope of the Calar Alto Observatory in southern Spain. Both the size and the location of the telescope impose limits on which stars can reasonably be observed. In general, only stars that are well observable from the geographical latitude of Calar Alto (37°N) are considered, so most stars in the CARMENES sample have a declination $\delta > -23°$. To minimise the required exposure time for each spectrum, the brightest suitable stars should be observed. A pre-selection of 2190 late-type stars (as

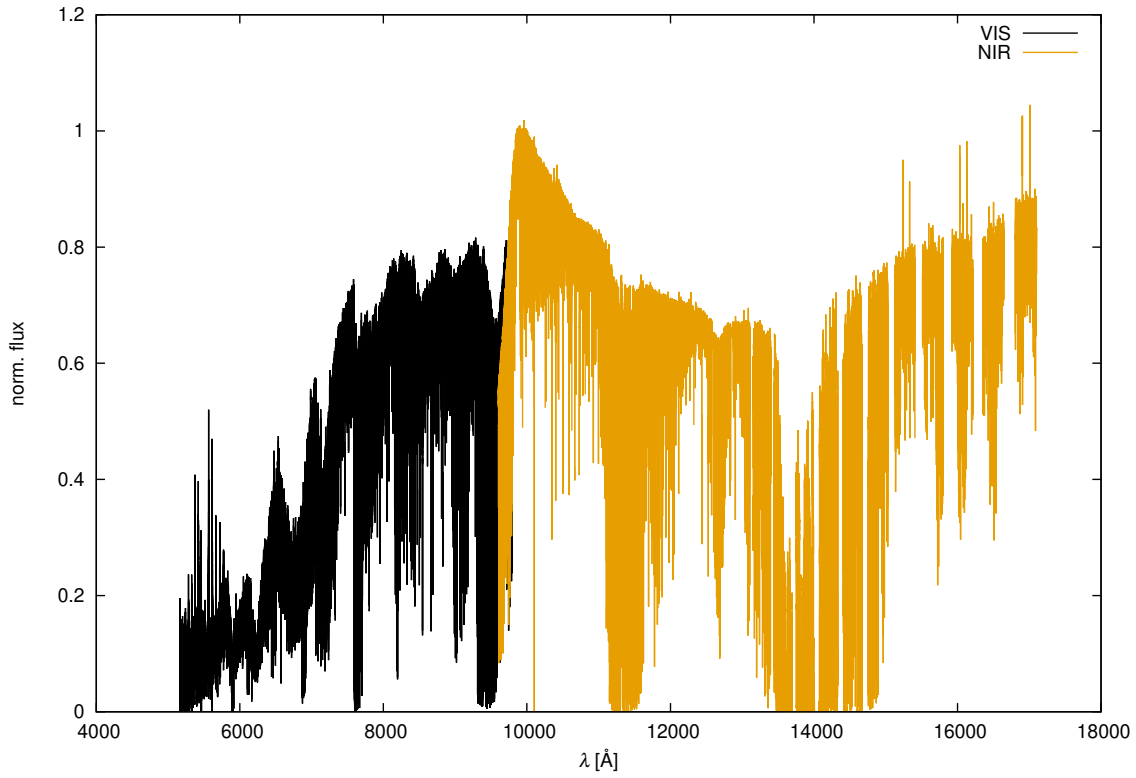

Figure 1.8.: One-dimensional spectrum extracted from the CARMENES spectrum of Luyten's star on 25 February 2016 at 21:07:51 UT shown in Fig. 1.1. The VIS channel spectrum is shown in black, the NIR channel spectrum is shown in orange. Inter-order gaps occur in the NIR channel at wavelengths $\lambda > 11400$ Å.

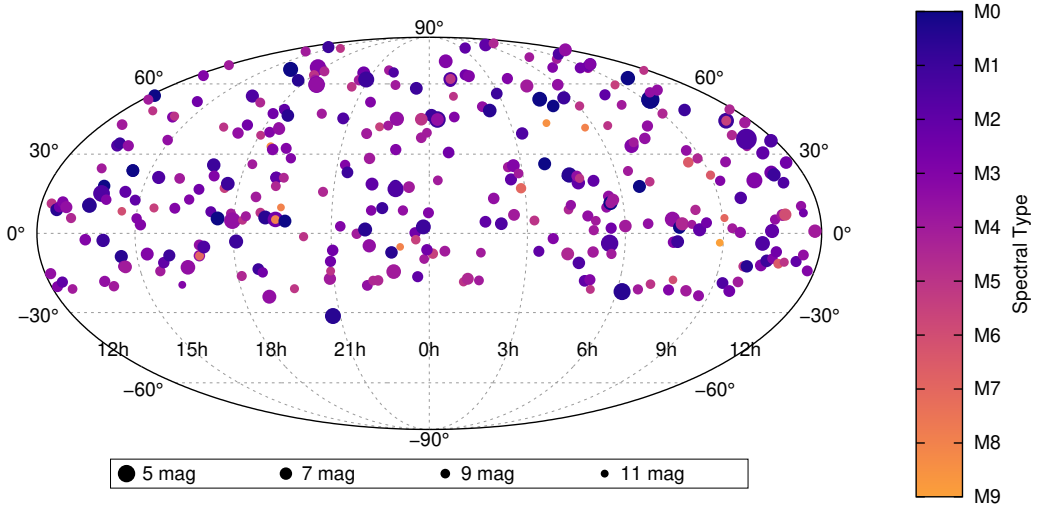

Figure 1.9.: Distribution of the 337 CARMENES sample stars analysed in this thesis on the sky. Colours correspond to spectral subtypes, circle size reflects the J-band magnitude.

of 13 November 2019) with a spectral-type dependent J-band magnitude threshold between 8.5 mag for M0 and 11.5 mag for M6 and later was collected in the *CARMEN(ES) Cool dwarf Information and daTa Archive* (Carmencita, Caballero et al. 2016). From this input catalogue, more than 300 stars were selected for the CARMENES survey, mostly with a J-band magnitude brighter than 7 mag for M0 and 11.5 mag for M9, and discarding stars with a known physical or optical companion within 5″ (Reiners et al. 2018b). As M dwarfs of the same spectral type have similar luminosities, the brightness threshold effectively translates into a distance limit. While the distribution of the 337 CARMENES sample stars analysed in this thesis on the sky that is shown in Fig. 1.9 is close to uniform, the sample contains very few stars with a spectral type later than M5.

As of 15 October 2020, CARMENES has discovered 24 planets around M dwarfs including the first discovery based only on CARMENES data (HD 147379 b, Reiners et al. 2018a), a planet around the closest single star to Sun (Barnard's Star b, Ribas et al. 2018), two Earth-like planets around Teegarden's star (Zechmeister et al. 2019), a three-planet system with a transiting Earth-like planet (GJ 357 b, Luque et al. 2019b), and a giant planet that further contrains planet formation theories (GJ 3512 b, Morales et al. 2019). Another eight planets were found around earlier-type stars (Luque et al. 2019a; Palle et al. 2019; Hidalgo et al. 2020). In addition to finding planets, CARMENES has been used to derive stellar parameters (e.g. Passegger et al. 2018; Schweitzer et al. 2019), and to study exoplanet atmospheres (e.g. Allart et al. 2018; Nortmann et al. 2018; Alonso-Floriano et al. 2019; Yan et al. 2019) and stellar activity (e.g. Tal-Or et al. 2018; Fuhrmeister et al. 2018; Hintz et al. 2019; Schöfer et al. 2019).

1.4. Stellar activity

Stellar activity is an umbrella term for a plethora of variability phenomena in the stellar atmosphere that evolve on time scales from minutes to years, much shorter than the time scales of stellar evolution. Because these phenomena can be observed with detailed spatial resolution only for the Sun, the mostly disc-integrated observations of other stars are generally interpreted against the background of the solar phenomena. I therefore combine both the solar and the stellar perspective in the following overview of activity phenomena.

1.4.1. Observed phenomena

The first observed stellar activity phenomenon was the presence of dark *spots* on the Sun. As the largest sunspots can be visible without optical magnification if the light is sufficiently dimmed, the oldest recorded observations date back more than two millennia (e.g. Yau & Stephenson 1988; Vaquero 2007). While first direct images of spots on other stars were obtained using interferometry in more recent years (Parks et al. 2015; Roettenbacher

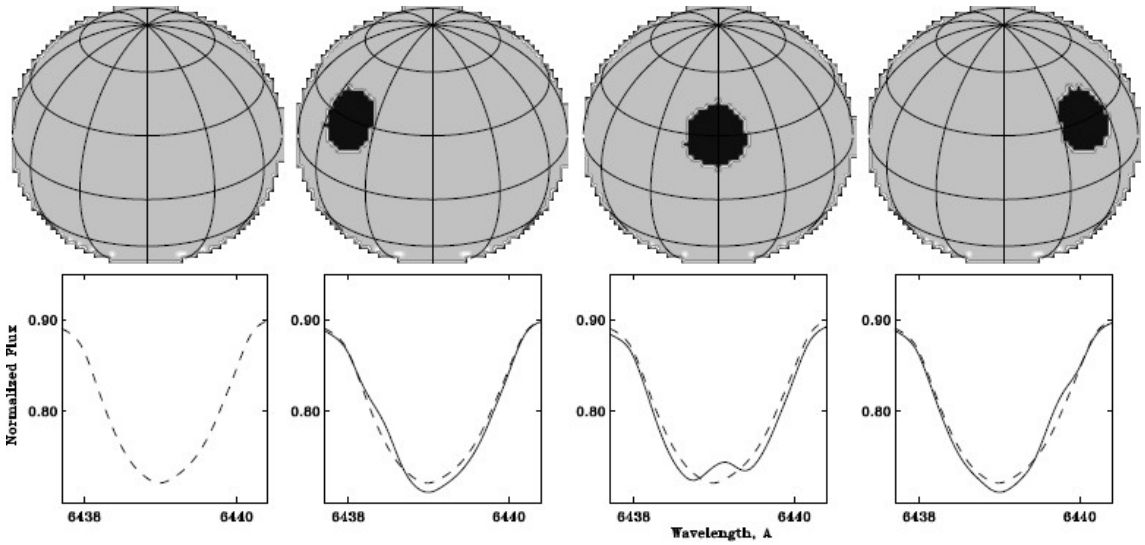

Figure 1.10.: A starspot on a fast rotating star moves across the hemisphere faced towards the observer as the star rotates, disturbing the observed flux at different Doppler shifts corresponding to the radial velocity of the spot with respect to the observer. This leads to a changing distortion in the observed spectral line profile (solid line) from the spectrum of the same star with no spots (dashed line). Image credit: Berdyugina (2005), used under CC-BY 4.0

et al. 2016), evidence for the existence of starspots was found before in photometric and spectroscopic data. As the star rotates, asymmetric spot distributions can lead to varying spot coverages of the hemisphere faced towards the observer and thus disc-integrated brightness variations. Kron (1947) proposed spots as an explanation for asymmetries and depth variations of the minima in the light curve of an eclipsing binary. Chugainov (1966) reported a periodic brightness variation for BY Dra, a star that did not show this behaviour in previous observations and was not known to be a binary system by then. While it was found to be a spectroscopic binary later, the orbital period did not match the photometric period and the observations were best explained as the star having spots and rotating with the photometric period (Bopp & Evans 1973). Light curves of planet transits provide another photometric way to study starspots, as the planet blocks less light while it passes a spot (e.g. Silva 2003; Silva-Valio et al. 2010; Tregloan-Reed & Unda-Sanzana 2019).

Starspots appear darker than the surrounding photosphere because they are cooler by hundreds of Kelvin for M dwarfs and up to 2000 K for Sun-like stars (Berdyugina 2005). As described in Sect. 1.2.1, presence and strength of spectral lines are temperature-dependent, so the spectrum of a cooler spot is different from the spectrum of the surroundings. Vogt (1979) first reported the presence of molecular absorption bands characteristic for M dwarfs in the spectrum of a spotted earlier-type star, and Huenemoerder et al. (1989) found a correlation between the strength of a TiO absorption band and the brightness of another earlier-type star. Neff et al. (1995) developed a method to derive the spot temperature and the fraction of the stellar disc covered by spots from molecular absorption bands, whereas Catalano et al. (2002) derived the same parameters from a set

of atomic lines. Depending on its location on the stellar surface, a spot moves towards or away from the observer at different velocities as the star rotates. For fast rotating stars with sufficient rotational line broadening, this causes measurable a measurable distortion in the spectral line profiles at the position corresponding to the velocity of the spot as illustrated in Fig. 1.10. The Doppler Imaging technique by Vogt & Penrod (1983) uses these distortions to create stellar surface maps and has been successfully used for various types of stars including M dwarfs (e.g. Barnes et al. 2002, 2015). Doppler Imaging maps revealed that many stars, unlike the Sun, have spots at high latitudes or even at the poles (e.g. Strassmeier et al. 1991; Kuerster et al. 1994; Jeffers et al. 2002), and that otherwise similar stars can have significantly different spot distributions (Barnes et al. 2017).

A complicating factor for indirect observations of starspots is that they are not constant, but can emerge and decay on time scales similar to the stellar rotation period. For the Sun, the lifetime of both individual and groups of spots is roughly proportional to their area (e.g. Petrovay & van Driel-Gesztelyi 1997; Henwood et al. 2010). For other stars, individual spots in a group may not be resolved, but the observed spot lifetimes also increase with their area (e.g Hall & Henry 1994; Namekata et al. 2019). As spots decay and new spots emerge, the total number of spots and fraction of the stellar surface covered by them vary. Schwabe (1844) and Wolf (1852) found a cycle of around 11 years in the number of sunspots, although Spörer (1887) and Maunder (1922) found evidence for an extended period with few sunspots in the second half of the seventeenth century. Long-term brightness variations reveal similar cycles for other stars (e.g. Strassmeier et al. 1997; Suárez Mascareño et al. 2016). Carrington (1858) first reported that sunspots appear predominantly at certain latitudes that change over the course of the cycle. Because the Sun does not rotate like a rigid body, but slower at higher latitudes than at the equator (*differential rotation*, e.g. Stix 1989), this has the consequence that a rotation period derived from disc-integrated solar brightness measurements also changes over the cycle. Evidence for changing active latitudes and differential rotation was also found in other stars (e.g. Donati & Collier Cameron 1997; Reiners & Schmitt 2003), with weaker shears at lower effective temperatures (e.g. Barnes et al. 2005; Reinhold et al. 2013). As shown by Basri & Shah (2020), the impact of limited spot lifetimes on the light curve is larger than the impact of differential rotation, and both factors can lead to light curves with one dip per rotation period at some times, but two dips at other times. This behaviour is commonly observed in photometric surveys (e.g. Basri & Nguyen 2018). For further information on starspots in general, I refer to the reviews by Berdyugina (2005) and Strassmeier (2009).

Contrary to intuition, the Sun appears brighter at the maximum of the sunspot cycle than at the minimum (e.g. Willson & Hudson 1991). This is caused by smaller hot and thus bright *faculae*, which appear both in the vicinity of the cool, dark spots and in a network across the photosphere (e.g. Fröhlich 2002; Walton et al. 2003). While the solar luminosity over the course of a cycle is dominated by the facular contribution, spots can dominate the brightness variations of other stars. Radick et al. (1998) found that the brightness of more active stars decreases towards the maxima of their activity cycles and is hence spot-dominated, whereas the brightness of less active stars, including the Sun, increases with increasing activity and is hence faculae-dominated. This pattern does not hold true for

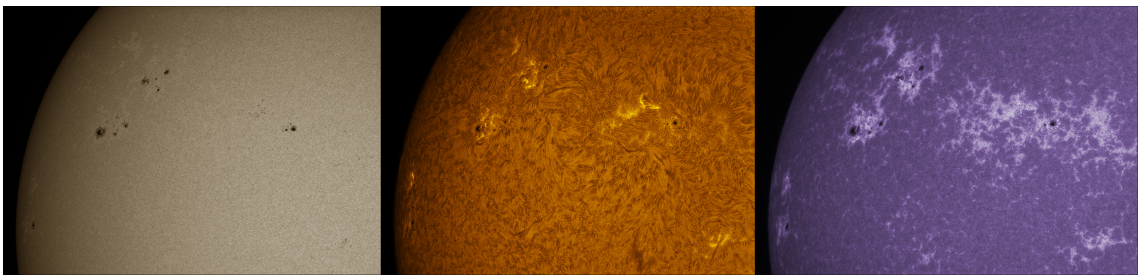

Figure 1.11.: Sector of the solar disc with sunspots, faculae, and plages in visible light (*left*) and narrowband Hα (*centre*) and Ca K (*right*) filters on 6 June 2015. Image credit: Pedro Ré[6]

brightness variations on the rotational time scale. As shown by Shapiro et al. (2016), the rotational solar brightness variability is spot-dominated, but would be faculae-dominated if observed from lower inclination angles. Based on the rotational modulation in the light curves of the M8 dwarf TRAPPIST-1, Morris et al. (2018) suggested the existence of bright spots that are larger and hotter than expected for faculae. Therefore, faculae may not be the only hot and bright stellar surface features.

Hale (1908) found Zeeman splitting of spectral lines from sunspots and thus related sunspots to *magnetic fields*. Magnetic fields also appear in the network of faculae outside of sunspots (e.g. Chapman & Sheeley 1968). Preston (1971) first derived mean surface magnetic fields of other stars from Zeeman splitting. More advanced methods allow to quantify both the magnetic field strength and the fraction of the stellar disc covered by magnetic fields from Zeeman-broadened spectral lines (e.g. Robinson 1980; Saar 1988; Valenti & Johns-Krull 2001; Shulyak et al. 2017). As found by Berdyugina & Solanki (2002), the dominant molecular absorption bands in M dwarf spectra are magnetically sensitive and therefore useful to measure the magnetic fields of M dwarfs or spots on earlier-type stars. By combining the Doppler Imaging technique with polarimetry, Zeeman Doppler Imaging reveals information on the geometry of the magnetic fields (Semel 1989; Donati et al. 1989). A series of papers by Donati et al. (2008), Morin et al. (2008), and Morin et al. (2010) presented Zeeman Doppler images for a sample of early-, mid-, and late-type M dwarfs, revealing that early M dwarfs have large-scale magnetic fields with strong toroidal and non-axisymmetric poloidal components similar to those observed on Sun-like stars, whereas on fully convective late M dwarfs, also fields with an axisymmetric poloidal components are found. In the case of the Sun, the polarity of the magnetic field flips with each 11-year sunspot cycle, resulting in a 22-year magnetic cycle (Weiss 1990). Boro Saikia et al. (2016) found evidence for a similar cycle in Zeeman Doppler images of a late K dwarf. The methods and results of stellar magnetic field measurements were reviewed by Reiners (2012) and Linsky & Schöller (2015).

While the photosphere is the dominant layer of the stellar atmosphere in the visible-light spectral range, activity phenomena can also be observed in the outer layers. Young (1872) first observed the Ca II H and K Fraunhofer lines (hereafter Ca H&K) to be in emission in

[6] https://re.apaaweb.com/sun_h_alpha_2015-06.html

spectra of the solar chromosphere obtained at the limb of the solar disc and in spectra of regions close to sunspots. Narrowband observations of the Sun in Ca H or K filters reveal that bright chromospheric *plage* regions mirror the bright photospheric network (e.g. Hall 2008), as can be seen in Fig. 1.11. In disc-integrated solar spectra, the intensity of the Ca H&K lines varies with the same 11-year cycle as the number of sunspots (Livingston et al. 2007). After Eberhard & Schwarzschild (1913) found emissive cores in the Ca H&K lines of Arcturus and other stars, these lines became a widely used proxy for stellar chromospheric activity, with surveys such as the Mount Wilson Observatory HK Project (e.g. Wilson 1968, 1978; Vaughan et al. 1978; Duncan et al. 1991; Baliunas et al. 1995; Boro Saikia et al. 2018) collecting data of thousands of stars over multiple decades. Similar to starspots causing brightness modulations with the rotation period, asymmetrically distributed plage regions can lead to measurable modulations of the Ca H&K intensity (e.g. Vaughan et al. 1981; Donahue et al. 1996; Suárez Mascareño et al. 2015). Baliunas et al. (1995) found that some stars also have a chromospheric activity cycle similar to the Sun, whereas other stars show high average activity levels with no cyclic variation or low average activity levels with little variation.

For M dwarfs, the Ca H&K lines are difficult to observe because they are located at the blue edge of the visible-light range, where M dwarfs emit little flux. A more conveniently located and thus frequently used chromospheric activity indicator for M dwarfs is the hydrogen Balmer-α line (Hα; e.g. Stauffer & Hartmann 1986; West et al. 2004; Jeffers et al. 2018). It is this spectral feature that causes the solar chromosphere to appear as a thin red line at the solar limb during a total eclipse and led to the name *chromosphere* for that atmospheric layer. As M dwarfs show Hα either in emission or in absorption, those with Hα in emission are also called dMe stars (Joy 1947) or active M dwarfs (e.g. Young et al. 1989). However, even M dwarfs with Hα in absorption can be active in the sense of showing emission in Ca H&K (e.g. Joy & Abt 1974). To avoid this ambiguity, I will use the terms *Hα active* and *Hα inactive* for M dwarfs with and without significant emission in Hα, respectively, throughout this thesis. Chromospheric models by Cram & Mullan (1979) and Cram & Giampapa (1987) showed that while the core emission in Ca H&K increases monotonically with increasing chromospheric temperature and density, Hα first appears as an increasingly deep absorption line, then starts to show emission in the line wings and a shallower core, and finally becomes an increasingly strong emission line with a central reversal. Houdebine (2012) found observational evidence for a non-linear correlation between the strengths of the Hα and Ca K lines in sets of M1 dwarfs and, less clear, M4 dwarfs. Therefore, Hα is no conclusive activity indicator at low chromospheric activity levels, i.e. for Hα inactive M dwarfs.

A number of further spectral features has been explored as chromospheric activity indicators. Among these features is the Na I D doublet (hereafter Na D, e.g. Andretta et al. 1997; Díaz et al. 2007; Gomes da Silva et al. 2011), which is located in the bluest part of the spectral range covered by CARMENES. A nearby helium line, often called He I D_3 (hereafter He D_3), usually appears in emission when emissive line cores in Na D are observed (Houdebine et al. 2009) and is correlated with Hα (Gizis et al. 2002). In the far-red spectral range, the K I λ7700 Å and Na I λ8200 Å doublets were found to become stronger

absorption lines with increasing Hα emission for late-type members of the Praesepe cluster by Kafka & Honeycutt (2006), whereas Robertson et al. (2016) found the opposite for Proxima Centauri. The Ca II infrared triplet (hereafter Ca IRT) lines correspond to transitions between the same upper energy state of the Calcium ion as Ca H&K and a different lower energy state (e.g. Linsky & Avrett 1970). As a consequence, the Ca IRT lines indicate the chromospheric activity level in a similar way to Ca H&K, as was observed both in spectra of different regions on the solar disc (e.g. Shine & Linsky 1972) and in stellar surveys (e.g. Linsky et al. 1979; Busà et al. 2007; Martínez-Arnáiz et al. 2011; Martin et al. 2017). Models by Andretta et al. (1997) and Short & Doyle (1997) suggested that the lines of the hydrogen Paschen (Pa) series at near-infrared wavelengths are sensitive to the chromospheric conditions in active M dwarfs. Short & Doyle (1998) and Houdebine et al. (2009) found examples of Paβ and Paϵ appearing as absorption lines. Another chromospheric line in the near-infrared range is the He I λ10833 Å (hereafter He 10833) line (e.g. Vaughan & Zirin 1968; Zirin 1982; Sanz-Forcada & Dupree 2008; Fuhrmeister et al. 2019a). The spectral regions around the chromospheric lines analysed in this thesis are shown in Fig. 2.2. A more complete list of chromospheric activity indicators including the blue and ultraviolet (UV) spectral range not accessible with CARMENES, and a discussion of their formation mechanisms can be found in a review by Linsky (2017). While all chromospheric activity indicators suggest that chromospheres are hotter and less dense than the underlying photospheres, each indicator is most sensitive in a different temperature and density range and can thus be attributed to a certain region within the chromosphere (e.g. Vernazza et al. 1981; Mauas 2000). Different indicators can therefore track different active regions, as is illustrated by the different appearances of the Sun in Hα and Ca K in Fig. 1.11.

Occasionally, the spectral lines sensitive to chromospheric activity can be observed in significantly enhanced emission. An example of such a *flare* in Hα is shown in Fig. 1.12: The Hα emission line in the spectrum of the active M3.5 dwarf EV Lac appeared very strong on 1 September 2016 before going back to its quiescent strength in the next days. While the first stellar flare was observed in chromospheric hydrogen and helium lines in the blue part of the visible-light range (Joy & Humason 1949), flares affect all chromospheric activity indicators and the continuum flux across the spectrum (e.g. Liebert et al. 1999; Fuhrmeister et al. 2008; Schmidt et al. 2012). The enhanced continuum flux can also be detected photometrically, not only at visible-light wavelengths (e.g. Kunkel 1970; Hawley & Pettersen 1991; Schmidt et al. 2019), but from X-rays to radio emission (e.g. Haisch et al. 1981; Osten et al. 2005; Smith et al. 2005). Flares have been reported for various types of stars (e.g. Pettersen 1989; Linsky 2000) and are increasingly common in later-type dwarfs (e.g. Davenport 2016; Yang et al. 2017). Observations of solar flares date back to Carrington (1859) and Hodgson (1859, incidentally, 157 years to the day prior to the EV Lac flare in Fig. 1.12), and revealed that they are localised events and occur preferably in regions with complex magnetic fields (e.g. Benz 2017). As these regions are associated with sunspots, the flaring rate of the Sun is strongly correlated with the 11-year sunspot cycle (Hathaway 2015). Similarly, more flares are observed from Hα active M dwarfs than from Hα inactive M dwarfs (e.g. Kowalski et al. 2009). Gershberg (1972) and

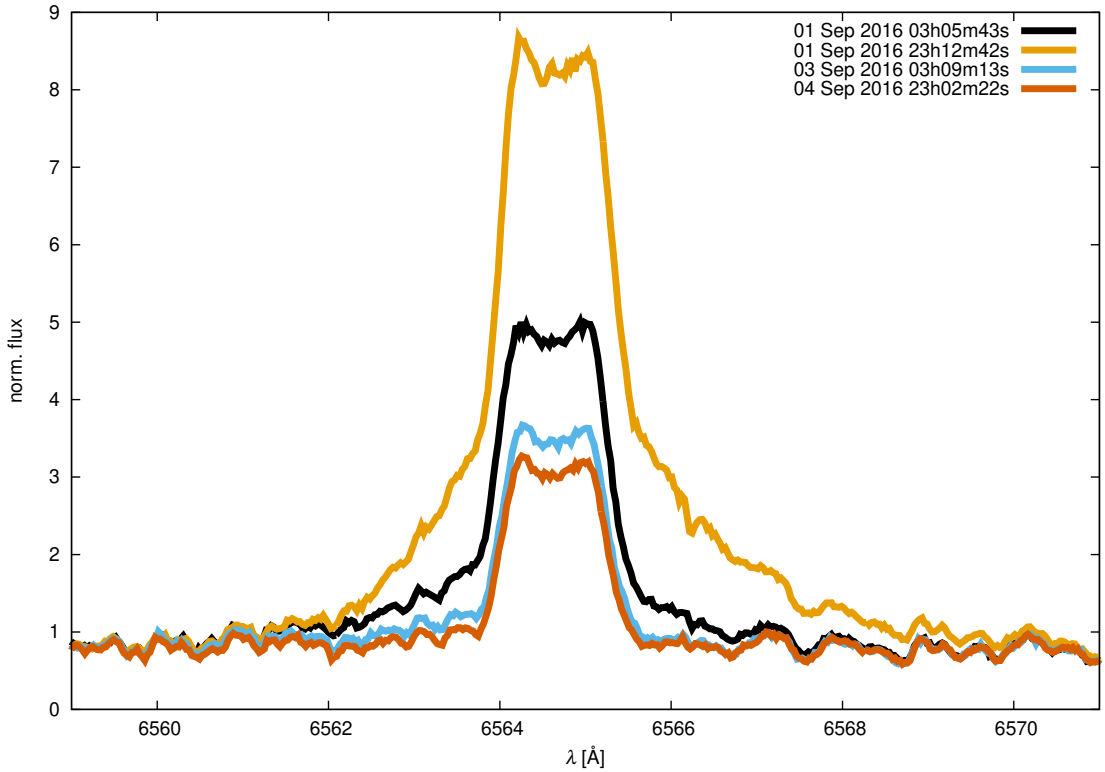

Figure 1.12.: Hα line in spectra of EV Lac. The emission increases significantly during flares on 1 September 2016 (black, orange) in comparison to the quiescent strength in the following days (blue, red).

Lacy et al. (1976) first found that stronger flares occur less frequently following a power law in a sample of M dwarfs. Similar power-law relations with different exponents were found for other stars, including the Sun (e.g. Schrijver et al. 2012). Stronger flares decay slower (e.g. Pettersen 1989), with the strongest flares being detectable for several hours (Kowalski et al. 2010). As can also be seen in Fig. 1.12, the enhancement of emission lines during a flare is not necessarily symmetric around the line cores. Line asymmetries are especially prominent in Hα (Fuhrmeister et al. 2018) and can be attributed to a Doppler shift caused by the emitting material rising in the chromosphere at the onset of the flare (blue asymmetry) or moving down again during the decay (red asymmetry; Ichimoto & Kurokawa 1984; Cho et al. 2016; Johnson et al. 2021). Flares were discussed in detail in the reviews by Haisch et al. (1991) and Benz & Güdel (2010).

Above the chromosphere lies the corona. As the solar corona becomes visible during total eclipses, it has been observed for millennia, and in the late nineteenth century, Jules Janssen noticed that the shape of the solar corona varies with the sunspot cycle (Littmann et al. 2008). The detection of highly ionised and forbidden metal lines in solar corona spectra lead to the assumption that the corona consists of hot, low-density plasma (Edlén 1943). As a consequence, stellar coronae are best observed at extreme UV and X-ray wavelengths, while the photosphere outshines the corona at longer wavelengths such as

the visible-light and near-infrared range covered by CARMENES. Because X-rays are absorbed by the Earth's atmosphere, the first detections of X-rays from the Sun (Burnight 1949) and another star (Capella, Catura et al. 1975) were obtained during rocket flights. X-ray space observatories such as ROSAT, Chandra, and XMM-Newton revealed that X-ray emission similar to the solar corona is common among Sun-like and later-type stars, as outlined in the reviews by Güdel (2004) and Güdel & Nazé (2009). A second window into stellar coronae is provided by nonthermal radio emission, as detailed in a review by Güdel (2002). Güdel & Benz (1993) found a very strong correlation between X-ray and radio emission for a variety of active stars, which also holds true for solar flares (Benz & Güdel 1994). Similar correlations were found between coronal X-ray emission and chromospheric activity indicators (e.g. Ayres et al. 1981; Schrijver 1987).

In addition to electromagnetic radiation, the high temperature and the resulting high kinetic energy allow plasma particles to escape the corona. Parker (1958) first presented a model of a continuous solar *wind* of escaping coronal plasma motivated by the suggestion of Biermann (1951) that a plasma stream can explain the observed shapes of comet tails. While the solar wind was first directly observed with the Luna spacecrafts (Gringauz et al. 1962), the clearest evidence for stellar winds of Sun-like and and later-type stars is provided indirectly by absorption in the UV hydrogen Lyman-α line as reviewed by Wood (2004). Wood et al. (2005) found that more active stars have stronger stellar winds, but this relation breaks down for the most active stars. A short-term but more violent coronal plasma release phenomenon are *coronal mass ejections* (CMEs). From the Sun, CMEs have been observed for 50 years since the first report by Tousey (1973) and occur often, but not always, together with flares (e.g. Kahler 1992; Yashiro et al. 2005). As with flares, the occurrence rate of solar CMEs strongly follows the 11-year sunspot cycle (e.g. Webb & Howard 1994; Lamy et al. 2019). Webb & Howard (2012) and Chen (2017) reviewed observations and theoretical models of solar CMEs. On other stars, CMEs may be detected indirectly through X-ray absorption by the ejected material at the onset of large flares (e.g. Favata & Schmitt 1999; Moschou et al. 2017) or strong blue asymmetries of emission lines (e.g. Houdebine et al. 1990; Guenther & Emerson 1997; Bond et al. 2001; Vida et al. 2016). Moschou et al. (2019) compiled a list of all stellar CME candidates that contains only 15 stars. However, blue asymmetries that correspond to material velocities below the escape velocity of the stars are observed more commonly and may still be signatures of CMEs because the Doppler shift measures only the line-of-sight component of the velocity (e.g. Leitzinger et al. 2011; Vida et al. 2019; Muheki et al. 2020). An alternative way to detect CMEs is provided by low-frequency radio bursts that are often generated by solar CMEs (e.g. Gopalswamy et al. 2009). For M dwarfs, however, efforts to observe the same type of radio bursts have remained unsuccessful so far (e.g. Crosley & Osten 2018; Villadsen & Hallinan 2019) and models arrive at different conclusions whether they can be generated (Mullan & Paudel 2019; Alvarado-Gómez et al. 2020).

1.4.2. Origin of stellar activity

The local activity phenomena described in the previous section often occur together, not only in the same atmospheric layer, but also across different layers. Global activity indicators for different atmospheric layers also show correlations. Therefore, it is plausible that all stellar activity phenomena can be traced back to one or more common sources. A first hint towards a possible source are the magnetic fields measured in solar spots and faculae. Stronger magnetic fields are measured on stars with stronger chromospheric and coronal emission (e.g. Pevtsov et al. 2003; Reiners et al. 2009; Reiners & Basri 2010; Vidotto et al. 2014; Marsden et al. 2014). Because a direct heat flow from the cooler photosphere to the hotter outer atmospheric layers is ruled out by the second law of thermodynamics, other heating mechanisms are required to explain the hot temperatures in the chromosphere and corona that lead to the observed emission. First ideas suggested energy transport through acoustic waves (Biermann 1946; Schwarzschild 1948; Schatzman 1949) or magnetohydrodynamic waves (Alfvén 1947). In complementary theories, magnetic fields are dissipated to heat (e.g. Heyvaerts 1990). Parker (1988) proposed that the corona is heated by magnetic reconnections similar to flares, but on smaller scales (*nanoflares*). On the Sun, smaller flares are less often accompanied by CMEs than larger flares, supporting the theory that the energy released in nanoflares contributes to heating the corona (Yashiro et al. 2006). Schrijver (1987) found that the chromospheric emission has a basal component that is not correlated with coronal emission and decreases towards later spectral types, and suggested that this component is caused by acoustic wave heating. However, Judge et al. (2003) found evidence that weak magnetic fields cause the basal chromospheric heating, whereas Jefferies et al. (2006) proposed a combined magnetoacoustic heating mechanism. I refer to the reviews by Narain & Ulmschneider (1990, 1996) for details on the various proposed heating mechanisms in outer stellar atmospheres.

Narain & Ulmschneider (1996) conclude that magnetic mechanisms dominate the heating of chromospheres and coronae. This leads to the question of how the required magnetic fields are generated. As shown for a sample of M dwarfs in the left panel of Fig. 1.13, stars with short rotation periods are in general more active in terms of Hα emission than slow-rotating stars, with a saturation at the shortest rotation periods. This rotation-activity relation was found for various samples of Sun-like and later-type stars not only using chromospheric Hα emission as activity indicator (e.g. Soderblom et al. 1993; Delfosse et al. 1998; Reiners et al. 2012; Newton et al. 2017; Jeffers et al. 2018), but also using Ca H&K emission (e.g. Catalano & Marilli 1983; Noyes et al. 1984; Astudillo-Defru et al. 2017), or coronal X-ray or radio emission (e.g. Pallavicini et al. 1981; Stewart et al. 1988; Pizzolato et al. 2003; Wright et al. 2011; McLean et al. 2012). While some of the referenced studies considered the Rossby number $\mathrm{Ro} = P_{\mathrm{rot}}/\tau$ with the convective overturn time τ instead of the rotation period P_{rot}, the scatter around the relation can be minimised with a formulation using only P_{rot} (Reiners et al. 2014). An interpretation of the relation between rotation and activity is that the kinetic energy of the rotating and convecting plasma in the stellar interior is converted to magnetic energy by *dynamo* processes. In most widely-accepted models, the solar dynamo is driven by the alternation between a poloidal and

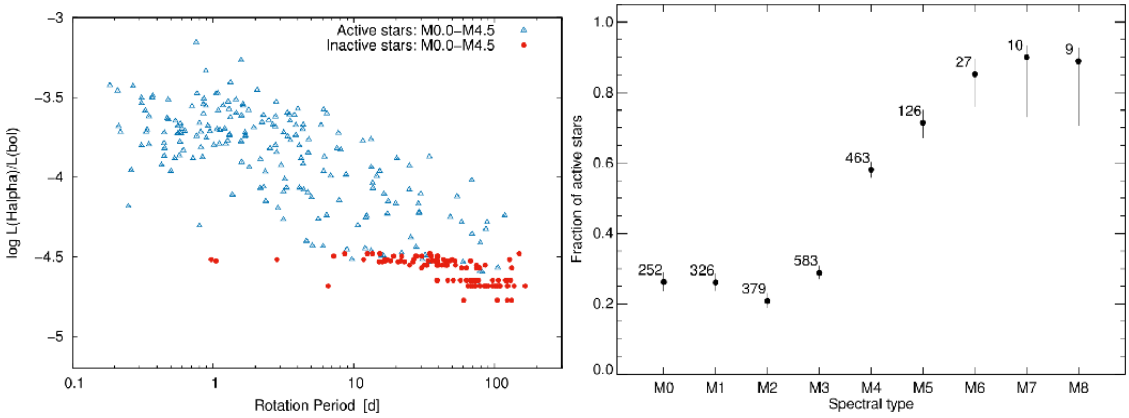

Figure 1.13.: *Left:* Normalised Hα luminosity as a function of the rotation period for stars in Carmencita. *Right:* Fraction of Hα active stars per spectral subtype. Numbers reflect the total number of stars of each subtype. Image credit: Jeffers et al. (2018), reproduced with permission, © ESO

a toroidal magnetic field over the course of the solar cycle. As demonstrated by Parker (1955), the shear from differential rotation generates the toroidal field component from the poloidal component (Ω effect), and the poloidal component can be regenerated from the toroidal field by cyclonic convection (α effect). In an alternative suggestion by Babcock (1961) and Leighton (1964, 1969), active regions drive the regeneration of the poloidal field instead of convection. Detailed discussions of solar dynamo models can be found in the reviews by Ossendrijver (2003) and Charbonneau (2020).

Models commonly place the solar dynamo in the tachocline between the radiative core and the convection zone. While later-type dwarfs down to early M dwarfs have a similar internal structure and thus can host a Sun-like dynamo, M dwarfs of spectral subtypes later than M4 are fully convective and thus have no tachocline, as described in Sect. 1.2.4. However, the fraction of active stars increases at these spectral subtypes (e.g. West et al. 2004, 2015; Reiners et al. 2012; Jeffers et al. 2018), as shown in the right panel of Fig. 1.13, indicating the existence of a dynamo process within the convection zone. Durney et al. (1993) found that turbulent small-scale magnetic fields can be generated in the convection zone and suggested that fully convective stars thus have only small-scale turbulent dynamos. However, more recent models showed that fully convective stars can also generate large-scale magnetic fields (Chabrier & Küker 2006; Dobler et al. 2006; Browning 2008). While the exact dynamo mechanisms at work remain unclear, Spruit (2011) suggested that Sun-like dynamos operate in the convection zone and not in the tachocline. Therefore, the fully convective stars may also have Sun-like dynamos. This is supported by the fact that the same rotation-activity relation is observed for both early and late M dwarfs (Wright & Drake 2016; Wright et al. 2018).

Wilson (1963) found that stars in young clusters show stronger emission in Ca H&K than old field stars of similar spectral types, thereby relating stellar activity and age. This relation was first quantified by Skumanich (1972), who found that both Ca H&K emission

and rotational velocity decay with the inverse square root of the age. A power-law decay with age is also observed for coronal X-ray and chromospheric UV emission, with a steeper decay at shorter wavelengths (e.g. Ribas et al. 2005; Stelzer et al. 2013). The declining activity is a consequence of the star spinning down because the stellar wind leads to a loss not only in mass, but also in angular momentum (e.g. Weber & Davis 1967).

In binary systems, both tidal effects (e.g. Schrijver & Zwaan 1991) and interaction of the stellar magnetic fields (e.g. Siarkowski et al. 1996) can affect the activity of each companion. Cuntz et al. (2000) suggested that close-by giant planets may strengthen the activity of their host stars in the same ways. Shkolnik et al. (2005) found two stars that showed periodic modulations of the Ca H&K lines with the orbital periods of their planets instead of their rotation periods. However, this result could not be confirmed in later observations (Shkolnik et al. 2008). Additional observational hints at star-planet interactions were reviewed by Poppenhaeger (2019).

1.4.3. Implications for exoplanet surveys

The effects of stellar activity are an important factor for the detectability of exoplanets. In the context of RV surveys, stellar activity can introduce RV jitter in the same order of magnitude as the periodic modulation caused by an Earth-like exoplanet, and may therefore lead to false or controversial planet detections (e.g. Dumusque et al. 2012; Hatzes 2013; Anglada-Escudé et al. 2014, 2016; Robertson et al. 2015). On short time scales from minutes to days, one source of RV jitter is a blueshift caused by rising material in convection cells covering a larger fraction of the stellar surface than sinking material on the edges of the convection cells (e.g. Beckers & Nelson 1978; Dravins 1982). While the impact of variations of this convective blueshift on RV measurements can be mitigated by using multiple observations per night (Dumusque et al. 2011), stellar activity increases these variations on longer time scales, as convection is suppressed by magnetic fields (e.g. Lagrange et al. 2010; Meunier et al. 2010; Jeffers et al. 2014; Bauer et al. 2018). In addition, line profile distortions introduced by active regions as shown in Fig. 1.10 can affect the RV measurements (e.g. Saar & Donahue 1997; Queloz et al. 2001). Depending on the distribution and the lifetime of the active regions, this can lead to RV modulations with periods similar to the rotation period or its integer fractions (e.g. Desort et al. 2007; Hatzes 2013). On long time scales of several years, a magnetic cycle can induce an additional RV modulation (e.g. Lindegren & Dravins 2003; Lovis et al. 2011; Delisle et al. 2018). While statistical methods (e.g. Tuomi et al. 2013; Haywood et al. 2014) or excluding activity-sensitive lines from the RV measurement (Dumusque 2018) can help to mitigate activity effects on the measured RV, monitoring activity indicators remains important to improve these methods and avoid false detections.

Furthermore, stellar activity has to be considered in assessing the habitability of exoplanets. Not only may close-by planets affect the activity of their host stars as discussed in

the last paragraph of the previous section, but an active star can also significantly influence the atmospheres of its planets. Stellar winds and CMEs can lead to a significant atmospheric mass loss, particularly if the planet lacks a shielding magnetic field (e.g. Wood 2006; Khodachenko et al. 2007; Zendejas et al. 2010; Cohen et al. 2014; Kay et al. 2016). Comparing the time scales of stellar evolution, atmosphere erosion by stellar winds, and life evolution, Lingam & Loeb (2017a) found that early-type M dwarfs with masses around 0.55 $M_\odot$ may host the planets with the largest biological diversity. Strong X-ray and extreme UV radiation from the corona heats the atmosphere and thus contributes to the erosion of the atmosphere (e.g. Vidal-Madjar et al. 2003; Lammer et al. 2003; Sanz-Forcada et al. 2011), but the remaining atmosphere after the evaporation of excess hydrogen and helium may be more life-friendly (e.g. Luger et al. 2015; Owen & Mohanty 2016). Chromospheric UV emission can change the atmospheric composition by dissociating molecules such as carbon dioxide, ozone, and water (e.g. Barnes & Heller 2013; Tian et al. 2014; Luger & Barnes 2015). As shown by Segura et al. (2010), the increased short-wavelength radiation during typical M dwarf flares is effectively shielded by an ozone layer and may therefore not affect the habitability of a planet, unless the planet is hit by accompanying CMEs. The strongest flares may drive mass extiction events (Lingam & Loeb 2017b), but the additional UV radiation may also enable the synthesis of biochemical compounds required for life (Toupance et al. 1977). Overall, less active stars with masses from the early-type M dwarf range up to solar mass stars may provide a more life-friendly environment on planets in their liquid water habitable zone than more active very late-type stars, and are therefore more promising targets for follow-up studies on planetary atmospheres and signs of extraterrestrial life. However, the minimum and maximum levels of stellar activity necessary to create and sustain life-friendly atmospheres are unclear.

1.4.4. Outline

This thesis uses M dwarf spectra obtained with CARMENES to derive indicators of their activity and investigates the correlations and temporal variation of these indicators. Because CARMENES covers the visible-light and near-infrared range, the spectra contain mainly information about the photospheres and several spectral features formed in the chromospheres of the studied stars, while their coronae are beyond the scope of this thesis.

I explain the data and the methods I used to derive activity indicators in Chapter 2. Chapters 3 and 4 present and analyse the obtained chromospheric and photospheric indicators, respectively, whereas Chapter 5 focuses on the modulation of the indicators with stellar rotation. Each of these chapters includes a discussion of the presented results. Chapter 6 concludes the thesis with a summary of the results and suggestions for further work.

2. Data and methods

This chapter introduces the input data and the methods I used to derive the two sets of spectral indicators that are presented and analysed in this thesis. I describe the used set of CARMENES spectra in Sect. 2.1, and explain how I measured the strengths of atomic lines with a component generated in the chromosphere using a spectral subtraction technique in Sect. 2.2, and of molecular absorption bands formed in the photosphere in Sect. 2.3.

2.1. CARMENES spectra

The CARMENES survey started in January 2016 and is still ongoing as of December 2020. For this thesis, only spectra recorded until 8 November 2019 were considered. Until that date, 354 stars were observed in total 16 684 times with the VIS channel and 16 142 times with the NIR channel during Guaranteed Time Observations. Of these 354 stars, I excluded nine double-lined spectroscopic binaries discovered by Baroch et al. (2018) from my analysis because the activity indicators of the two binary components cannot be measured separately using my methods. However, combined indicators of both components might not include the full activity signal if measured in the same spectral range as used for single stars. I also excluded five K dwarfs, as they are a separate group of objects. A further three stars were observed only once or twice. Therefore, the temporal variation of their activity indicators could not be analysed. I list the remaining 337 stars in Appendix A. Not all spectra of these stars yielded successful measurements. In total, 15 868 VIS spectra and 15 351 NIR spectra could be successfully analysed for this thesis. As the histogram in Fig. 2.1 shows, these spectra are very unevenly distributed among the target stars. While less than 10 VIS spectra could be analysed for 56 stars and less than 10 NIR spectra could be analysed for 62 stars, there are 10 stars with more than 200 analysed spectra from each channel. For both channels, the median is 23 spectra per star. The colour-coding by spectral subtype reveals that earlier-type M dwarfs constitute a larger fraction of the heavily observed stars than of the stars with fewer observations.

All spectra were reduced by Dr. Mathias Zechmeister (Institut für Astrophysik Göttingen) and Dr. Florian Bauer (Instituto de Astrofísica de Andalucía, Granada, Spain) using CARACAL v2.20. The CARACAL pipeline is based on the IDL REDUCE package (Piskunov & Valenti 2002) and implements standard data reduction steps, the flat-relative

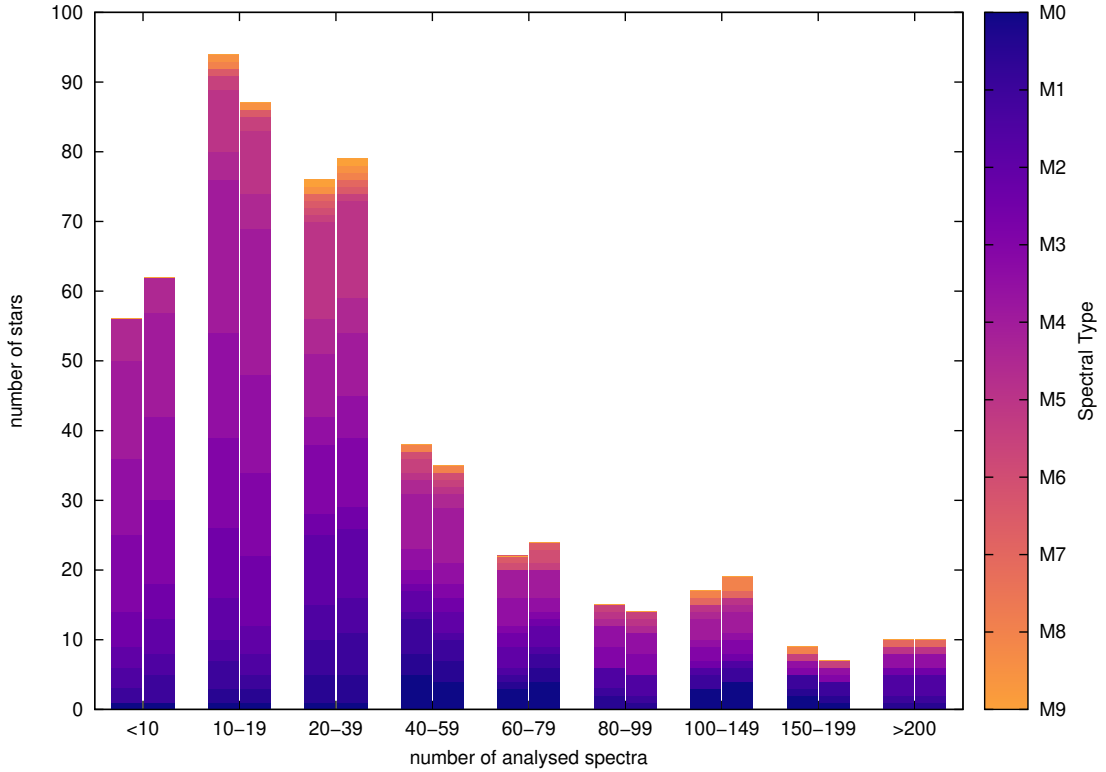

Figure 2.1.: Number of stars with a given number of analysed spectra, colour-coded by spectral subtype. For each bin, the left bar corresponds to the VIS channel and the right bar corresponds to the NIR channel.

optimal extraction (FOX, Zechmeister et al. 2014), and a wavelength calibration using Fabry-Pérot etalons (Bauer et al. 2015).

In addition to the reduced spectra from individual observations, I also used co-added template spectra created by Dr. Mathias Zechmeister from all individual spectra of each star for each spectrograph channel using SERVAL (Zechmeister et al. 2018). These template spectra have two advantages over the individual spectra: The signal-to-noise ratio (SNR) is higher and telluric lines are mitigated because the co-adding procedure excludes data points outlying by more than 5σ. The telluric lines are strong outliers, because different barycentric velocities cause them to appear at different positions in the stellar spectrum at different observation times. I therefore used the co-added template spectra to measure the typical value of each of my spectral indicators for each star instead of averaging the values derived from the individual spectra. As spectra recorded during strong flaring events can also cause strong outliers that are excluded by the co-adding procedure, the values derived from the template spectra may be more representative of the usual activity level of the star than the average of individual spectra. However, I still used the individual spectra for investigating the temporal variations of the spectral indicators.

2.2. Strengths of chromospheric lines

As Ca H&K are not covered by CARMENES, Hα is the most established chromospheric activity indicator that can be measured in the scope of this thesis. Of the other spectral lines with a chromospheric component mentioned in Sect. 1.4.1, I consider the He D_3 line, the Na D doublet, and the Ca IRT in the spectral range of the VIS channel, and the He 10833 and Paβ lines in the NIR channel. The regions around these lines in selected spectra are shown in Fig. 2.2. I discard the K I λ7700 Å and Na I λ8200 Å doublets because they are heavily contaminated by telluric lines, and the higher order lines of the Paschen series because they are weaker than Paβ. The Paα line at 18756.4 Å is outside of the spectral coverage.

A common measure of the strength of a spectral line is the *equivalent width* (EW). It is defined as the width of a hypothetical rectangular complete absorption feature that covers the same area as the spectral line in a spectrum normalised to the surrounding continuum. This allows to compare the strength of spectral lines with different shapes. Emission lines can be described as negative absorption lines and therefore have negative EWs. In M dwarf spectra, a true continuum is hard to find. Therefore, the spectrum is usually normalised to a *pseudo-continuum* (PC), and the EW measured with respect to the PC is called a *pseudo-equivalent width* (pEW). In this thesis, I measure the pseudo-equivalent width after subtracting the spectrum of an inactive reference star, similar to the spectral subtraction technique used by Young et al. (1989) and Montes et al. (1995). Inspired by the R'_{HK} index of the Ca H&K lines (Noyes et al. 1984), where the prime denotes the subtraction of the photospheric components, I refer to the pseudo-equivalent width measured after the spectral subtraction as pEW′.

The steps for measuring the pEW′ are as follows: First, an artificial rotational broadening was applied to the co-added template spectrum of the reference star, if the investigated star has a measured projected rotational velocity according to Carmencita as listed in Table A.1. Next, the investigated spectrum was transformed to the same wavelength grid as the reference star spectrum. The Doppler shift between the spectra was determined from a Gaussian fit to the highest peak of the cross-correlation function of the spectral order containing the considered spectral line. Both the reference star spectrum and the investigated spectrum were then normalised to the mean flux in the respective PC ranges $\lambda_{\mathrm{l/r}} \pm \Delta\lambda_{\mathrm{PC}}$ as listed in Table 2.1. The PC was then defined as a linear interpolation between the PC ranges in the normalised reference star spectrum:

$$\mathrm{PC}(\lambda) = \mathrm{PC_l} + \frac{\mathrm{PC_r} - \mathrm{PC_l}}{\lambda_\mathrm{r} - \lambda_\mathrm{l}} (\lambda - \lambda_\mathrm{l}) \,, \tag{2.1}$$

where $\mathrm{PC_{l/r}}$ are the 90th percentile of the flux in the PC ranges $\lambda_{\mathrm{l/r}} \pm \Delta\lambda_{\mathrm{PC}}$ in the reference star spectrum. The choice of the 90th percentiles ensures that the PC is close to an upper envelope of the spectrum in the PC ranges.

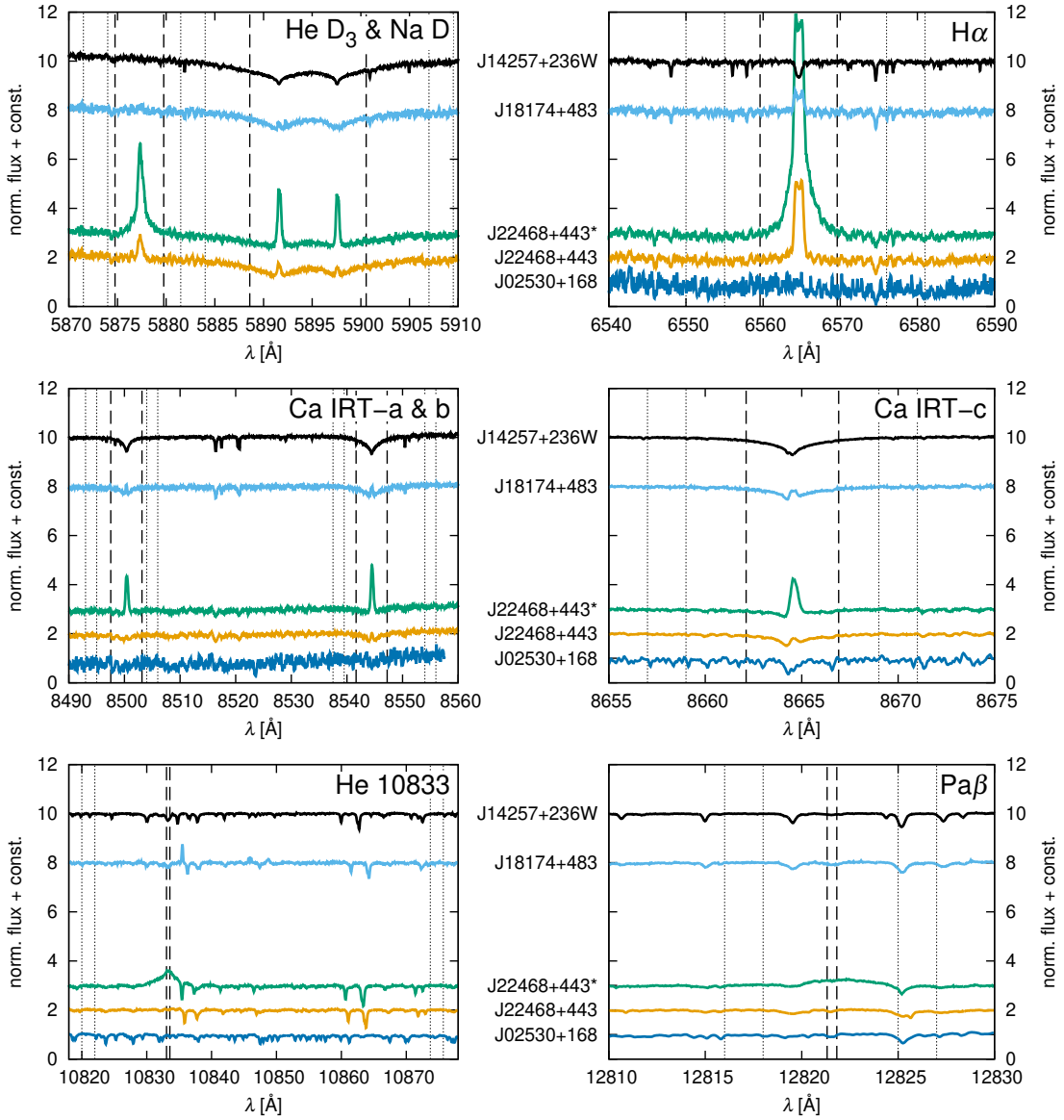

Figure 2.2.: Selected spectra in regions around the eight considered chromospheric lines: J14257+236W (M0.0, black), J18174+483 (M2.0, light blue), J22468+443 (M3.5) in flaring (green) and quiescent (orange) state, J02530+168 (M7.0, dark blue). J02530+168 is not shown in the region around He D_3 and Na D because of low SNR. Dashed vertical lines encompass the line windows, dotted vertical lines the pseudo-continuum ranges as defined in Table 2.1.

Table 2.1.: Line windows and pseudo-continuum ranges for pEW′ measurements of selected lines with chromospheric components. All wavelengths are given in vacuum.

Line	λ_0 [Å]	$\Delta\lambda$ [Å]	λ_l [Å]	λ_r [Å]	$\Delta\lambda_\mathrm{PC}$ [Å]
He D_3	5877.25	2.50	5872.75	5882.75	1.25
Na D	5894.57	5.98	5882.75	5908.25	1.25
Hα	6564.60	5.00	6552.50	6578.50	2.50
Ca IRT-a	8500.35	2.80	8494.00	8505.00	1.00
Ca IRT-b	8544.44	2.80	8538.50	8555.00	1.00
Ca IRT-c	8664.52	2.40	8658.00	8670.00	1.00
He 10833	10833.31	0.25	10821.0	10874.7	1.00
Paβ	12821.57	0.25	12817.0	12826.0	1.00

The pEW′ was then calculated as

$$\mathrm{pEW}' = -\int_{\lambda_0-\Delta\lambda}^{\lambda_0+\Delta\lambda} \left(\frac{S(\lambda)}{\mathrm{PC}(\lambda)} - \frac{T(\lambda)}{\mathrm{PC}(\lambda)}\right) \mathrm{d}\lambda \tag{2.2}$$

using the trapezoidal rule to approximate the integral, where $S(\lambda)$ is the normalised investigated spectrum and $T(\lambda)$ is the normalised reference star spectrum. The line windows $\lambda_0 \pm \Delta\lambda$ are listed in Table 2.1. The pEW′ is defined to be negative in the case of excess emission to be consistent with the traditional definition of the EW. Using the inverse root mean square (*rms*) of the PC ranges in the residual spectrum $R(\lambda) = S(\lambda) - T(\lambda)$ as an approximation for the SNR, the uncertainty of the pEW′ was estimated following Vollmann & Eversberg (2006) as

$$\epsilon_{\mathrm{pEW}'} = \sqrt{1 + \frac{\mathrm{PC}(\lambda_0)}{\langle R\rangle + 1}} \cdot rms \cdot (2\Delta\lambda - \mathrm{pEW}'), \tag{2.3}$$

where $\langle R\rangle$ is the mean of $R(\lambda)$ in the line window $\lambda_0 \pm \Delta\lambda$.

In contrast to a pEW measurement without spectral subtraction, the pEW′ measurement is less affected by photospheric absorption components of spectral features such as Na D or Ca IRT as long as these components are sufficiently similar in the considered spectrum and the reference star spectrum. Similarly, the spectral subtraction mitigates the impact of any absorption band lines close to the considered spectral line from the line window. This allows the choice of sufficiently broad line windows to measure most of the chromospheric emission even during flaring events, which can lead to very broad emission lines as seen in Fig. 1.12. Without the spectral subtraction, a broad line window can introduce a spectral-type dependent bias, as the strength of included absorption band lines can depend on the temperature. Alternatively, a variable line window chosen based on the width of the line in each spectrum separately could mitigate this effect, but this would lose the advantage that the pEW method requires little information on the line shape.

Both the He 10833 and the Paβ line are weak in comparison to nearby telluric lines that appear in the line windows for absolute observed RVs between 14 km s^{-1} and 125 km s^{-1} for He 10833, and between 10 km s^{-1} and 43 km s^{-1} for Paβ. I exclude any spectra with telluric contamination based on the absolute observed RV from further analysis for these lines.

For Hα as the most commonly used activity indicator for M dwarfs, I defined an activity threshold of $\mathrm{pEW}'_{\mathrm{H}\alpha} = -0.3$ Å. Stars with a stronger excess emission are Hα active, whereas stars with a weaker excess emission or with excess absorption are Hα inactive. Previous studies defined different activity thresholds for the pEW of Hα without spectral subtraction, e.g. -1 Å (Newton et al. 2017) or -0.5 Å (Jeffers et al. 2018). However, I will show that a lower threshold for the excess emission is justified in Sect. 3.3.

2.2.1. Grouping of stars and selection of reference stars

By definition, the pEW′ of all lines is 0 Å for reference stars. To obtain meaningful results for as many stars as possible, the stars thus have to be grouped into as few groups as possible. As the strength of the absorption lines that the spectral subtraction aims to remove depends mainly on the temperature, I grouped the stars by their spectral subtypes given in Carmencita as listed in Table A.1. However, all stars with spectral subtype M6.0 or later were merged into one group because the sample of very late-type stars is sparse and inactive stars that could be used as reference stars are elusive. This introduces a bias in the results for very late-type stars, as the surrounding lines in the reference star spectrum may be stronger or weaker than in the investigated spectrum. Alternatively, the stars could be grouped by effective temperature. However, while the effective temperature was determined by Schweitzer et al. (2019) for most of the 337 sample stars, this would not solve the problem with the coolest, very late-type stars, and a reasonable binning would lead to groups that are similar to the spectral subtype groups.

Ideally, the reference star should be the most inactive star in each group, so the spectral subtraction does not remove any sign of activity. However, there are multiple ways to define the most inactive stars. Given the correlation between chromospheric activity and stellar rotation described in Sect. 1.4.2, I generally selected for each subtype the star with the longest rotation period as given in Carmencita and tabulated in Table A.1. For spectral subtype M1.5, J16254+543 was chosen as the reference star instead of J03181+382 ($P_{\mathrm{rot}} = [77.2 \pm 3.0]$ d) based on a longer reported rotation period of (100 ± 5) d that was revised later. The rotation periods of J23381–162 ($P_{\mathrm{rot}} = 61.66$ d) and J09360–216 ($P_{\mathrm{rot}} = [74.3 \pm 1.7]$ d) were not included in Carmencita when the reference stars were selected, so J06103+821 and J17198+417 were chosen instead. For M5.5 and M6.0, the only stars with Hα not in emission were selected. The selected reference stars and their rotation periods P_{rot} are listed in Table 2.2.

For each sample star, the reference star of the same spectral subtype should show the most similar spectrum in the temperature-dependent PC ranges. Therefore, I calculated

Table 2.2.: Reference stars with the longest rotation periods and with the smallest MNI variations for each spectral subtype. Both sets of reference stars contain the same star for spectral subtypes M5.5 and M6.0. The same reference star is used for all spectral subtypes later than M6.0.

	longest $P_{\rm rot}$		smallest MNI variation	
Spectral type	Reference star	$P_{\rm rot}$ [d]	Reference star	$P_{\rm rot}$ [d]
M0.0	J14257+236W	111 ± 12	J09144+526	...
M0.5	J18580+059	35.2 ± 0.3	J22503–070	...
M1.0	J18051–030	127.8 ± 3.2	J13209+342	...
M1.5	J16254+543	76.79 ± 0.13	J17052–050	50.2 ± 1.3
M2.0	J06103+821	44.6 ± 1.0	J22115+184	36.3 ± 0.2
M2.5	J17198+417	71.5 ± 2.6	J19169+051N	46.0 ± 0.2
M3.0	J15194–077	132.5 ± 6.3	J18419+318	...
M3.5	J17578+046	148.6 ± 0.1	J14310–122	...
M4.0	J11477+008	163 ± 3	J21466–001	...
M4.5	J19216+208	133 ± 9	J19098+176	80.1 ± 3.2
M5.0	J03133+047	126.2	J18027+375	123.8
M5.5	J00067–075	...	J00067–075	...
M6.0	J07403–174	...	J07403–174	...

the *rms* of the PC ranges in the residual spectra after subtracting each of the reference star spectra from the co-added template spectra for all sample stars as a sanity check. In Fig. 2.3, I show the resulting *rms* of the PC ranges around the Hα line for all M3.0 stars as a function of the spectral subtype of the reference star. The *rms* is minimised by using the M3.0 reference star for 37 of 43 M3.0 stars in the sample, whereas it is minimised by using the M3.5 reference star for 5 stars and by using the M2.5 reference star for only one star. As shown by the histograms for all considered lines in Fig. 2.4, it generally holds true for all lines and all spectral subtype that the *rms* is minimised by using a reference star of a similar spectral type. The deviations are larger for He D_3, Na D, He 10833 and Paβ than for Hα and the Ca IRT lines. This can be explained by the lower SNR at the short wavelengths of He D_3 and Na D, particularly at later spectral subtypes, and the comparatively flat PC regions for He 10833 and Paβ. For spectral types later than M6.0, the *rms* is always minimised by an earlier-type reference star, because there are no later-type reference stars. Similarly, for M0.0 stars, the *rms* is always minimised by the reference star of the same or a later spectral subtype.

As the rotation period is known for only 169 of the 337 sample stars, this selection of reference stars may be biased. It is possible that the remaining stars are even less active and show less brightness variation, so the rotation period could not be measured from photometric data. To investigate the impact of the reference stars, I selected a second set of reference stars based on the molecular-normalised index (MNI) of the Hα line defined and calculated by Erik Johnson (Institut für Astrophysik Göttingen). The MNI is calculated by dividing the mean flux in the line window by the mean flux in two PC regions on either side of the line window and dividing again by the mean flux in two

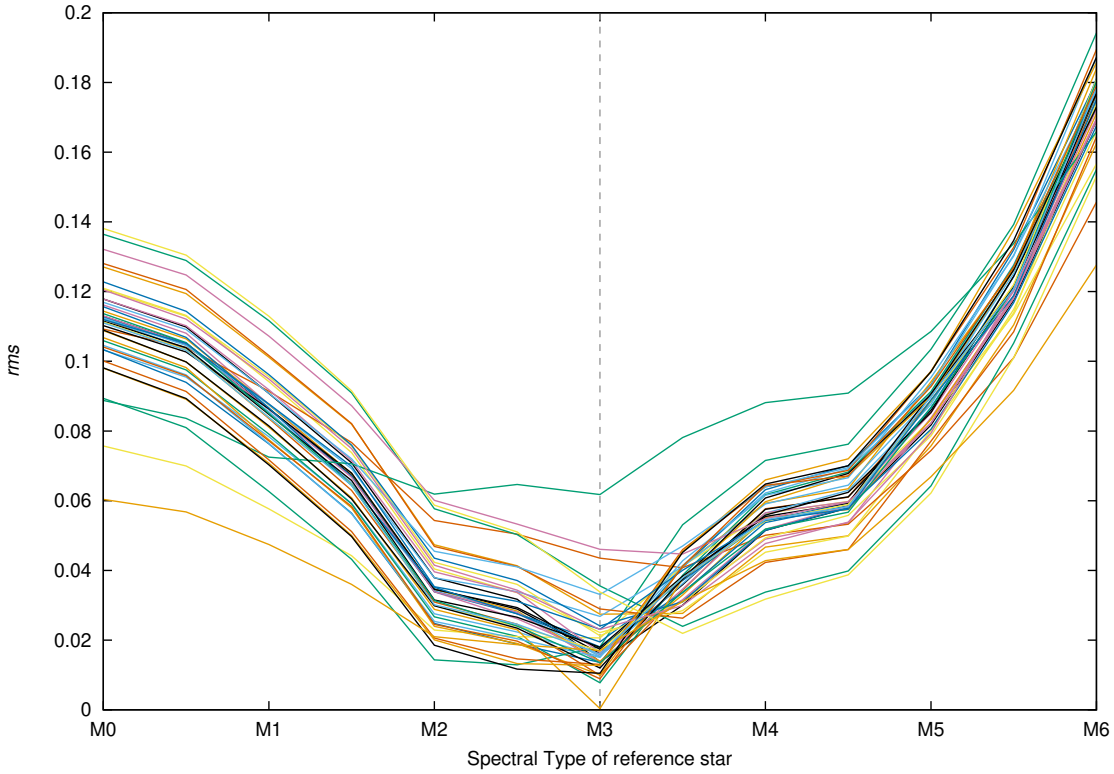

Figure 2.3.: *rms* of PC ranges in residual spectra around the Hα line after subtraction of different reference star spectra for all M3.0 stars in the sample as a function of the spectral subtype of the reference star. To improve the visibility of the minima, the measurements for each star are connected with a curve.

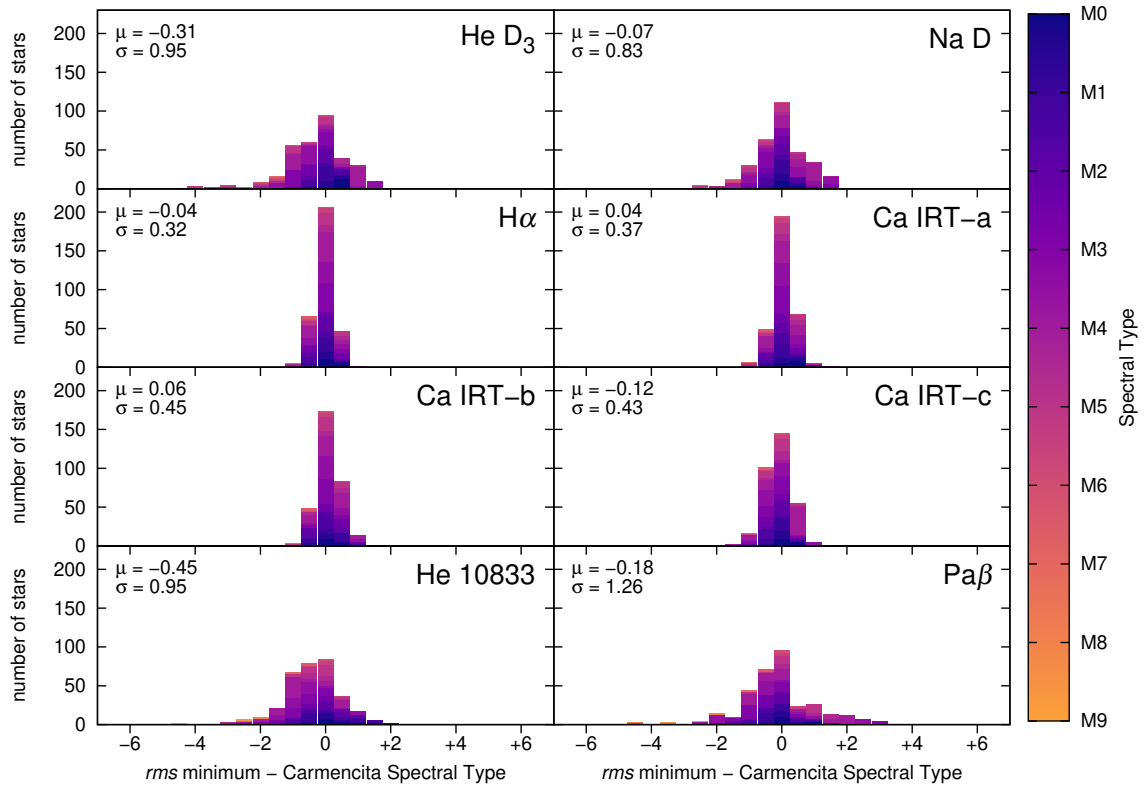

Figure 2.4.: Histogram of deviations between spectral subtype of the reference star that minimises the *rms* of the PC ranges in the residual spectra and spectral subtype according to Carmencita.

further PC regions, and is less variable for less active stars. Therefore, the stars with the smallest MNI variation are selected as a second set of reference stars and also listed in Table 2.2. Their rotation periods are listed for comparison, but are unknown for eight of the thirteen stars. For three of the five stars with a known rotation period, the period is less than two thirds of the rotation period of the reference star with the longest period of that subtype.

2.2.2. Normalised Hα luminosity

If two pEW′ values of the same line in different stars were derived using different reference stars, a direct comparison is difficult because the PC changes with the effective temperature similar to Eq. 1.1. This is similar to the changes in the black-body radiation that were described in Sect. 1.1. To remove this temperature dependence, I converted the $\mathrm{pEW}'_{\mathrm{H}\alpha}$ values to the normalised Hα luminosity $L_{\mathrm{H}\alpha}/L_{\mathrm{bol}}$ using the ratio χ between the PC flux around Hα and the bolometric flux as described by Walkowicz et al. (2004):

$$\frac{L_{\mathrm{H}\alpha}}{L_{\mathrm{bol}}} = -\frac{\mathrm{pEW}'_{\mathrm{H}\alpha}}{1\,\text{Å}} \cdot \chi(T_{\mathrm{eff}}), \tag{2.4}$$

where I used a quintic function derived from PHOENIX model spectra by Reiners & Basri (2008) for the flux ratio $\chi(T_{\rm eff})$, and $T_{\rm eff}$ based on the spectral subtype of the reference star as given by Pecaut & Mamajek (2013) and tabulated in Table 1.1. Because the normalised Hα luminosity is usually given on a logarithmic scale, I only calculated it for Hα active stars, as $\log(L_{\rm H\alpha}/L_{\rm bol})$ goes to minus infinity as $\mathrm{pEW}'_{\rm H\alpha}$ approaches 0 Å.

2.3. Indices of photospheric bands

As discussed in Sect. 1.2.3, molecular absorption bands formed in the photosphere are dominant features in M dwarf spectra. An absorption band can extend over several Echelle orders, complicating the definition of a pseudo-continuum for the pEW′ method described in the previous section. Moreover, a wide absorption band likely blends with other spectral features, thus also complicating the choice of an integration window for measuring the strength of the absorption band only. Therefore, I quantified the absorption band strength by an index that is calculated as the flux ratio of two small spectral ranges on either side of the band head:

$$\mathrm{index} = \frac{\langle S \rangle_{\rm num.}}{\langle S \rangle_{\rm den.}}, \tag{2.5}$$

where $\langle S \rangle$ is the mean flux in the numerator or denominator range. To mitigate the impact of ill data points from cosmic rays or detector artefacts, the top and bottom 10 percent of the data points in each range are not considered for the mean.

The uncertainty of the index is given by

$$\epsilon_{\rm index} = \mathrm{index} \sqrt{\left(\frac{\epsilon_{\rm num.}}{\langle S \rangle_{\rm num.}}\right)^2 + \left(\frac{\epsilon_{\rm den.}}{\langle S \rangle_{\rm den.}}\right)^2} \tag{2.6}$$

from propagating the errors of each mean flux. According to Zechmeister et al. (2018), these can be estimated from the data error ϵ_i of each spectral bin as

$$\epsilon_{\langle S \rangle} = \frac{1}{N} \sqrt{\sum \epsilon_i^2}. \tag{2.7}$$

Similar indices have been defined and used for deriving spectral types (e.g. Reid et al. 1995; Martín et al. 1999) and metallicities (e.g. Woolf & Wallerstein 2006; Lépine et al. 2007) before, but with broader or farther apart numerator and denominator ranges tailored to low-resolution spectra. To measure the strength of each band head as accurately as possible in high-resolution spectra, I defined new indices using narrower spectral ranges as given in Table 2.3. I considered the strongest band head of the TiO γ, δ, and ϵ systems according to Valenti et al. (1998); their strength is measured by the TiO 7050, TiO 8860, and TiO 8430 indices, respectively. While the strongest band heads of the TiO α, β, and γ' systems are also covered by the VIS channel, they are located at shorter wavelengths than the Hα line and hence in a spectral range with a poor SNR for the later-type stars.

Table 2.3.: Numerator and denominator ranges for photospheric absorption band indices. All wavelengths are given in vacuum.

Index	Numerator [Å]	Denominator [Å]
CaH 2*	6817.0–6819.0	6813.0–6815.0
CaH 3*	6974.0–6977.0	7047.0–7050.0
TiO 7050	7056.0–7060.0	7046.0–7050.0
VO 7436	7435.9–7436.9	7434.3–7435.3
VO 7942	7941.7–7943.7	7936.0–7938.0
TiO 8430	8436.0–8440.0	8430.5–8434.5
TiO 8860	8862.5–8864.5	8859.0–8861.0
FeH WFB	9898.0–9907.0	9887.0–9896.0

Therefore, I consider neither these systems nor the TiO ϕ system, which is covered by the NIR channel but located in a range with strong telluric contamination. The VO band heads listed by Tinney & Reid (1998) are more diffuse and many of them are located within TiO bands. I defined the VO 7436 and VO 7942 indices to measure the strengths of two VO band heads not blended with TiO bands. In addition to the TiO and VO indices, I defined high-resolution counterparts of the CaH 2 and CaH 3 indices from Reid et al. (1995) and measured the strength of the FeH Wing-Ford band (first detected by Wing & Ford 1969) with the FeH WFB index, which is the only index derived from NIR spectra. All considered bands are visualised for selected stars in Fig. 2.5.

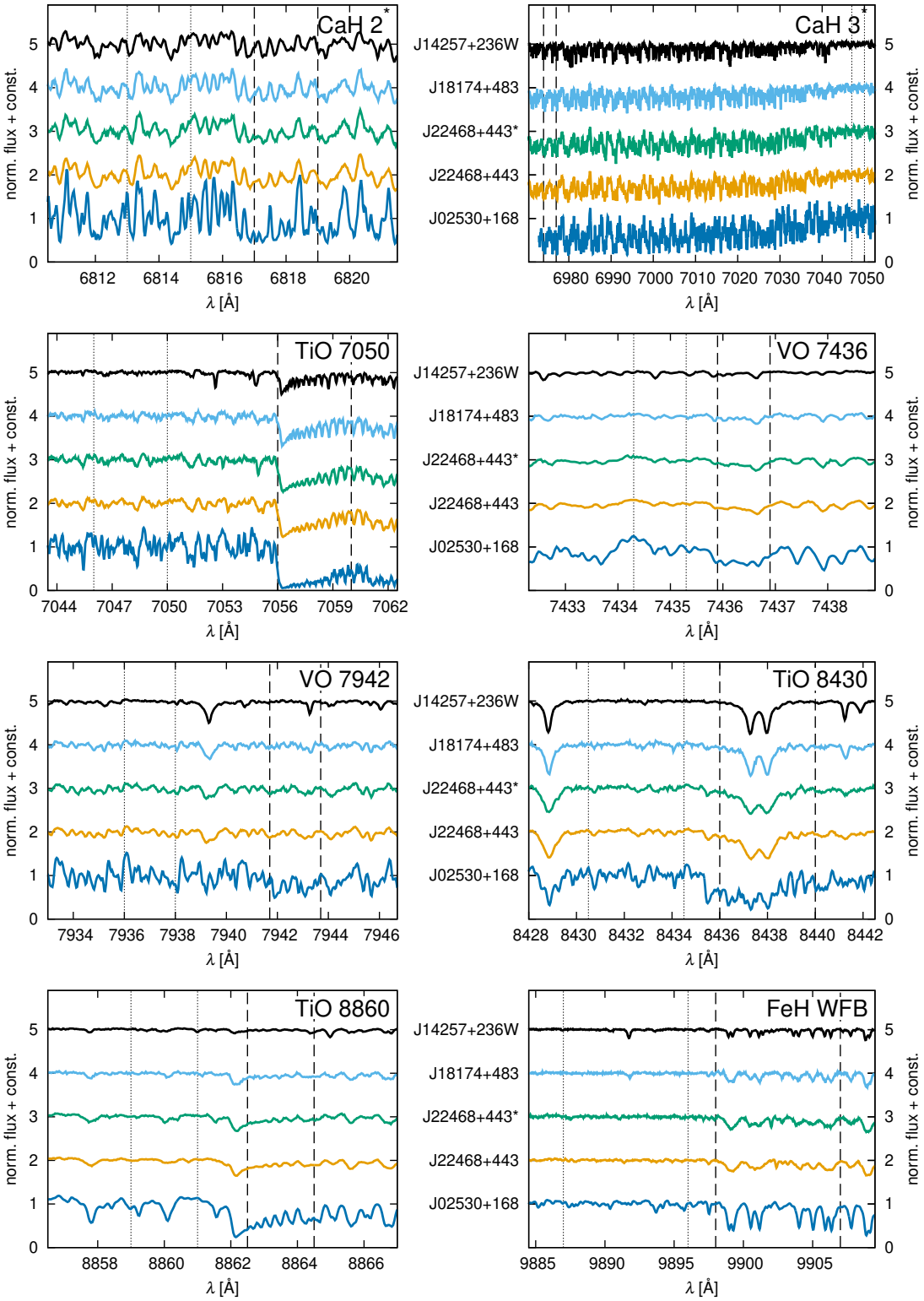

Figure 2.5.: Same spectra as in Fig. 2.2 in regions around the eight considered photospheric bands: Dashed vertical lines encompass the numerator ranges, dotted vertical lines the denominator ranges as defined in Table 2.3.

3. Chromospheric indicators

This chapter aims to quantify the chromospheric activity in the CARMENES sample of the M dwarfs. As described in Sect. 1.2.4, the chromosphere is the atmospheric layer above the photosphere. Several spectral lines that are sensitive to the hotter temperatures in comparison to the photosphere can be used as indicators for chromospheric activity as explained in Sect. 1.4.1.

I present and analyse the chromospheric activity indicators derived with the spectral subtraction method described in Sect. 2.2. As a starting point, I show the pEW′ values derived from each star's co-added template spectrum in Sect. 3.1. I then explore the correlations between the pEW′ of different lines in Sect. 3.2, before quantifying the variations among individual observations of each star in Sect. 3.3. These three sections mostly follow the analysis presented in Schöfer et al. (2019), but include also observations after July 2018 and all spectra have been reprocessed using the latest co-added template spectra of the reference stars. In Sect. 3.4, I demonstrate how the choice of the reference stars affects the results. Finally, I provide a comparison with previous results and a discussion of the findings in Sect. 3.5.

3.1. Sample overview

For all eight considered spectral lines, Fig. 3.1 shows the pEW′ values derived from the co-added template spectra grouped by spectral subtype using the reference stars with the longest rotation periods per spectral subtype. The $\mathrm{pEW}'_{\mathrm{H}\alpha}$ values are also tabulated in Table A.1. As defined in Sect. 2.2, negative pEW′ values mean excess emission and positive pEW′ values mean excess absorption with respect to the reference star for the same spectral subtype, which by definition has pEW′ = 0 Å for all lines. Stars with Hα excess emission stronger than the activity threshold of −0.3 Å are marked as Hα active.

All Hα inactive stars show only minor deviations from $\mathrm{pEW}'_{\mathrm{He\ D_3}} = 0$ Å. In contrast, most Hα active stars show stronger excess emission in He D_3 than any Hα inactive star. The maximum observed excess emission per spectral subtype tends to increase with the spectral subtype up to a maximum at M5.5. Na D behaves in a similar way to He D_3, but with a less clear separation between Hα active and Hα inactive stars at early and mid subtypes and excess absorption in two very late Hα active stars. In addition, there is a larger spread for Hα inactive stars; in particular, all other Hα inactive M1.5 stars show significant Na D excess emission with respect to the reference star for this subtype.

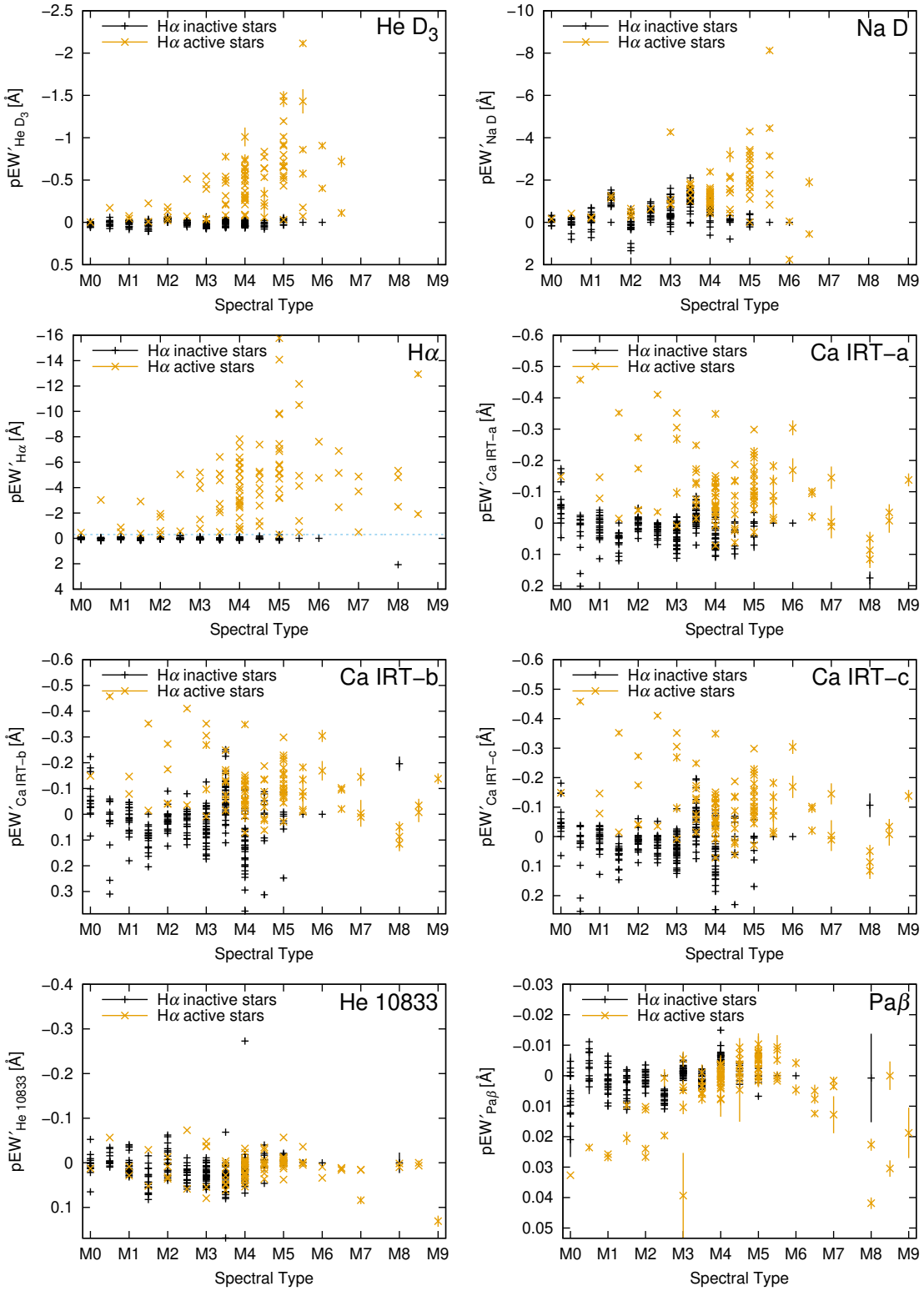

Figure 3.1.: pEW′ of spectral lines with a chromospheric component as a function of spectral type for Hα inactive stars (black pluses) and Hα active stars (orange crosses). The dashed blue line in the Hα panel marks the activity threshold at $\mathrm{pEW}'_{\mathrm{H}\alpha} = -0.3$ Å.

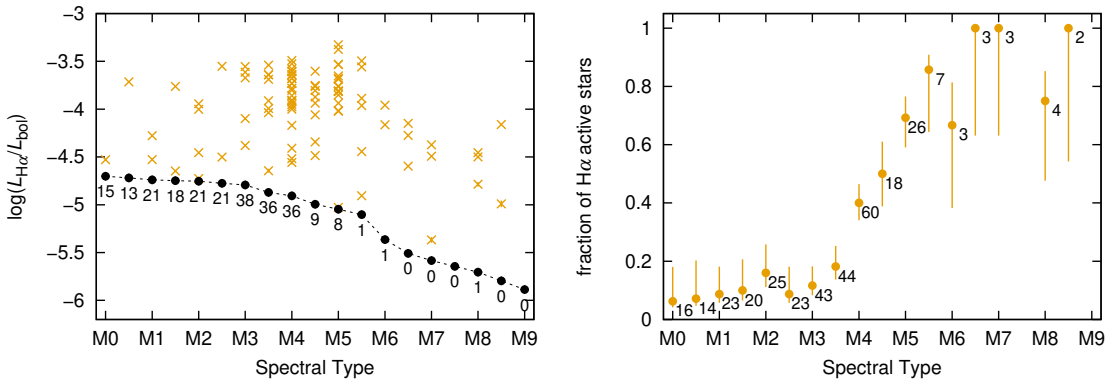

Figure 3.2.: *Left panel:* normalised Hα luminosity of Hα active stars as a function of spectral type. The black circles correspond to the activity threshold and the numbers are the number of Hα inactive stars for each spectral subtype. *Right panel:* fraction of Hα active stars as a function of spectral type with error bars from binomial statistics. The numbers indicate the total number of sample stars for each spectral subtype.

Unlike He D_3 and Na D, Hα could be measured also for nine very late-type stars between M7.0 and M8.5. Among these stars, only J19255+096 is classified as Hα inactive with the strongest Hα excess absorption of all sample stars. The overall distribution of the measured $\mathrm{pEW}'_{\mathrm{H}\alpha}$ values among spectral subtypes is similar to He D_3, but with the global maximum observed excess emission at M5.0 instead of M5.5. This difference can be explained with the different flux ratios of the pseudo-continua. The normalised Hα luminosity $L_{\mathrm{H}\alpha}/L_{\mathrm{bol}}$ was calculated as described in Sect. 2.2.2 and is shown as a function of spectral type for all Hα active stars in the left panel of Fig. 3.2 and tabulated in Table A.1. In general, later-type stars have a lower normalised Hα luminosity than earlier-type stars with a comparable $\mathrm{pEW}'_{\mathrm{H}\alpha}$. The M5.0 star with the most negative $\mathrm{pEW}'_{\mathrm{H}\alpha}$, J05084–210, also has the highest normalised Hα luminosity of all sample stars at $\log(L_{\mathrm{H}\alpha}/L_{\mathrm{bol}}) = -3.33$. The right panel of Fig. 3.2 shows the fraction of Hα active stars for each spectral subtype. While below 20% of the stars are Hα inactive for each spectral subtype up to M3.5, the fraction increases rapidly for subtypes M4.0 to M5.5 up to more than 80%. Almost all very late-type stars with subtype M6.0 or later are classified as Hα active, but the sample is too sparse to rule out that the fraction decreases again. Overall, 95 of 334 sample stars with a measured $\mathrm{pEW}'_{\mathrm{H}\alpha}$ are classified as Hα active.

The other spectral lines shown in Fig. 3.1 are located at longer wavelengths than Hα, so the pEW′ for the only M9.0 and the latest-type star in the sample, J08536–034, could be measured. Although $\mathrm{pEW}'_{\mathrm{H}\alpha}$ could not be measured for this star, as the order containing the Hα line is not included in the co-added template spectrum, it is marked as an Hα active star based on visual inspection of the Hα line in individual spectra. All three Ca IRT lines show a similar distribution of the measured pEW′ as a function of spectral subtype. Most Hα active stars show excess emission, with earlier-type stars showing a stronger maximum excess emission as later-type stars. Again, this difference to the previously described indicators can be explained with the different pseudo-continuum flux ratios.

Table 3.1.: Correlation table of pEW′ values of spectral lines with a chromospheric component using Spearman's rank coefficient r_S. Strong correlations with $r_S > 0.60$ are highlighted in boldface.

	Hα	He D_3	Na D	Ca IRT-a	Ca IRT-b	Ca IRT-c	He 10833
He D_3	**0.68**	...					
Na D	0.23	0.26	...				
Ca IRT-a	**0.73**	**0.66**	0.22	...			
Ca IRT-b	**0.63**	0.41	0.15	**0.77**	...		
Ca IRT-c	0.41	0.22	0.03	**0.61**	**0.91**	...	
He 10833	0.23	0.15	−0.33	0.22	0.12	0.06	...
Paβ	−0.18	−0.08	0.13	−0.13	−0.26	−0.28	0.34

Similar to Na D, the Hα inactive stars show a larger spread in the Ca IRT lines than in He D_3 or Hα. While most Hα inactive stars show excess emission with respect to the reference star for spectral subtypes M0.0 and M3.5, excess absorption is more common in Hα inactive stars for M1.0 and M4.0.

For the two lines in the range of the NIR channel, He 10833 and Paβ, the spectral-type dependence of the measured pEW′ values is significantly different than for the other lines. In He 10833, the Hα active stars are not separated from the Hα inactive stars. In Paβ, most Hα active stars show excess absorption at early to mid types and at very late types, whereas the $\mathrm{pEW}'_{\mathrm{Pa}\beta}$ values of Hα active stars at mid to late types are similar to the values of Hα inactive stars.

3.2. Correlations

As seen in the previous section, there are similarities in the distributions of the measured pEW′ values of different spectral lines. This suggests that these indicators are not independent of each other. To investigate the correlations, I show scatter plots of $\mathrm{pEW}'_{\mathrm{H}\alpha}$ paired with all other indicators in Fig. 3.3, and of $\mathrm{pEW}'_{\mathrm{He\ D_3}}$ versus $\mathrm{pEW}'_{\mathrm{He\ 10833}}$ and of all combinations of the Ca IRT lines in Fig. 3.4. As a more quantitative approach, I also calculated the correlation coefficients between all pairs of indicators. Because the distributions of most indicators are heavy-tailed with the Hα inactive stars clustered around 0 Å and a long tail of Hα active stars, I use Spearman's rank coefficient r_S rather than Pearson's correlation coefficient. The resulting correlation table is given in Table 3.1. In addition, a correlation table for only the Hα active stars is given in Table 3.2.

The first scatter plot in the left column of Fig. 3.3 shows a strong correlation between Hα and He D_3. The correlation coefficient is $r_S = 0.68$ and increases to $r_S = 0.95$ if the Hα inactive stars are excluded. This is the strongest correlation measured for any pair of chromospheric indicators. No different slopes for different spectral subtypes are

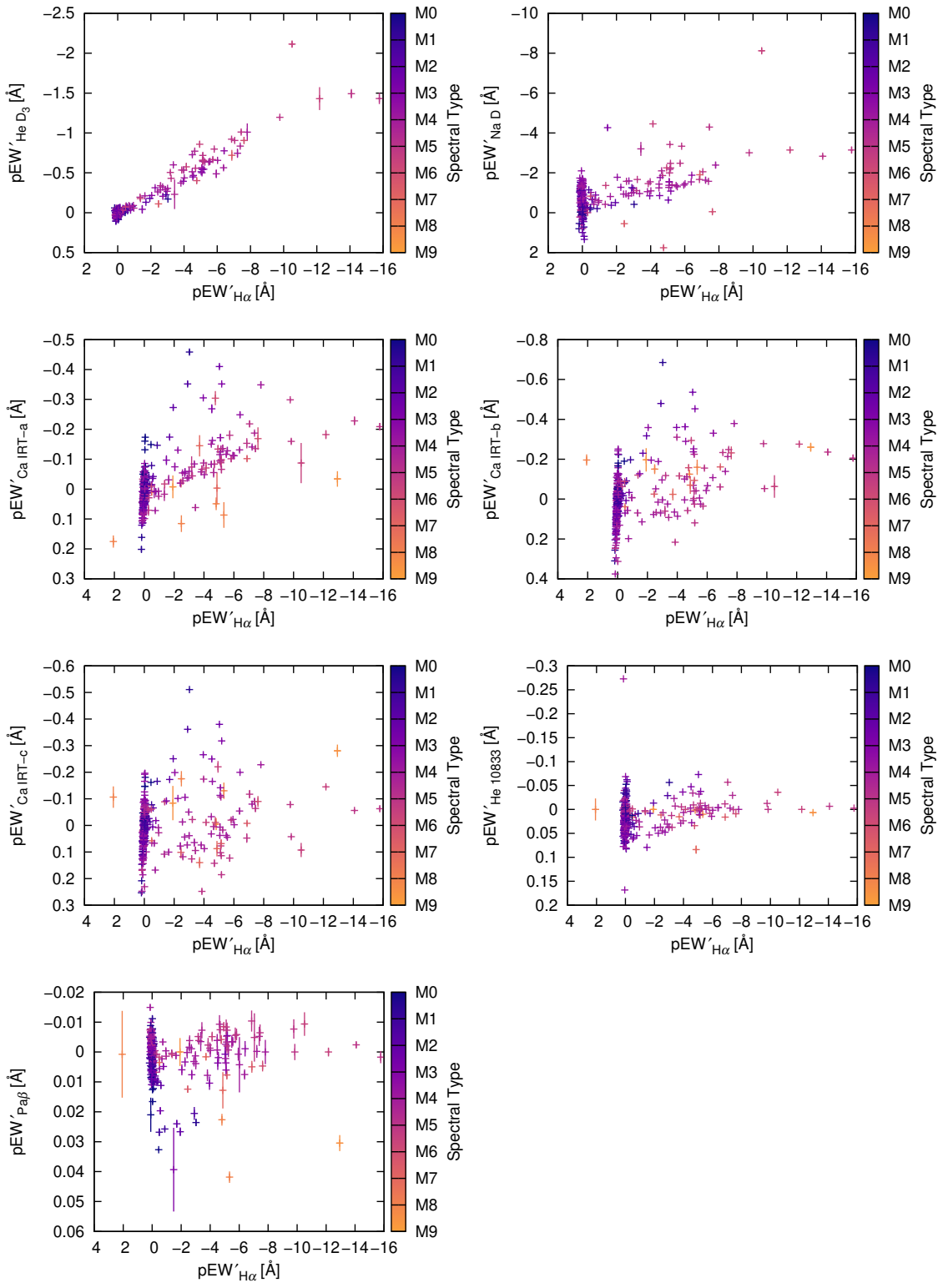

Figure 3.3.: Scatter plots of $pEW'_{H\alpha}$ versus pEW′ of other spectral lines with a chromospheric component. Colours correspond to spectral subtypes.

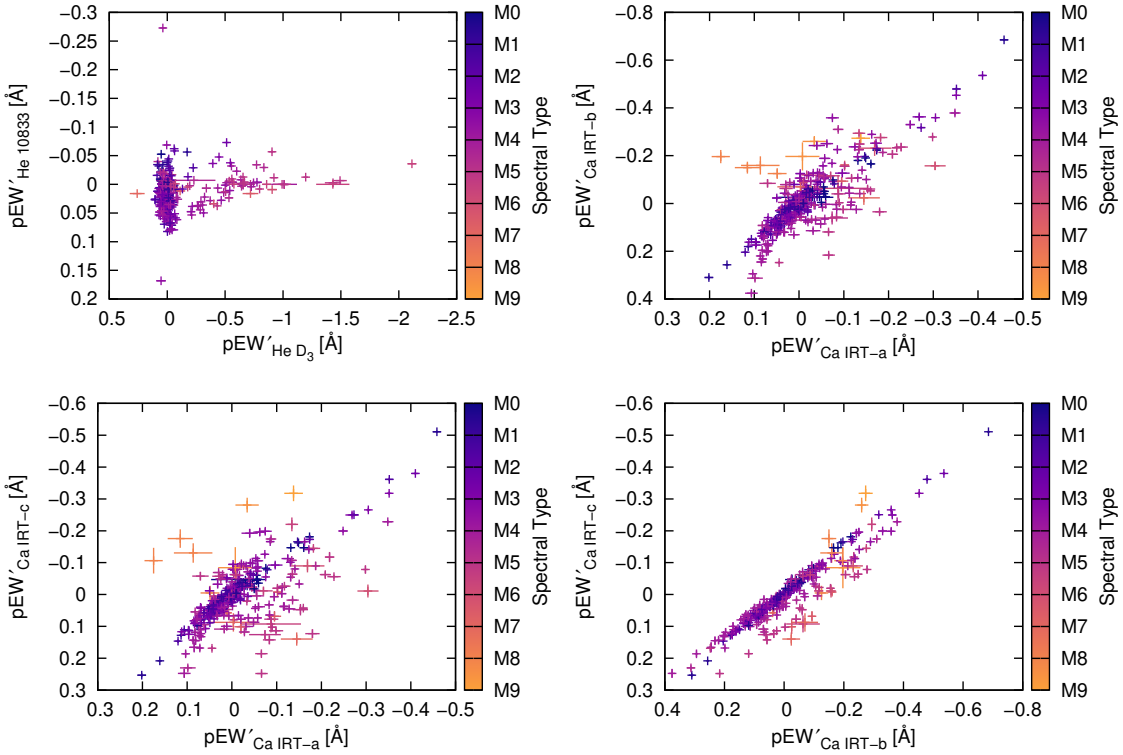

Figure 3.4.: Scatter plots of $pEW'_{He\ D_3}$ versus $pEW'_{He\ 10833}$ and of $pEW'_{Ca\ IRT-a}$, $pEW'_{Ca\ IRT-b}$, and $pEW'_{Ca\ IRT-c}$ versus each other. Colours correspond to spectral subtypes.

visible, but most Hα active stars are of similar, mid-to-late subtypes, while the earlier-type Hα active stars span only a small range of $pEW'_{H\alpha}$ values and $pEW'_{He\ D_3}$ could not be measured for the latest subtypes.

In the scatter plot of Hα versus Na D, the Hα inactive stars form an elongated point cloud, as $pEW'_{H\alpha} \approx 0$ Å for all of them, but $pEW'_{Na\ D}$ takes values between -2.10 Å and 1.34 Å. This is consistent with the spread of the Hα inactive stars in Na D described the previous section. By excluding the cloud of Hα inactive stars, the correlation coefficient increases from a weak $r_S = 0.23$ to a strong $r_S = 0.68$.

Similar to Hα versus Na D, the scatter plots of Hα versus the Ca IRT lines show the Hα inactive stars as an elongated point cloud. However, this cloud is slightly tilted and appears to increase the correlation coefficients because the majority of the sample stars is Hα inactive. For the Hα active stars only, the correlations coefficients are significantly weaker. Unlike in the previously described scatter plots, the slope of the Hα active stars appears steeper for earlier spectral subtypes. This is expected because the pseudo-continuum flux is temperature-dependent similar to Eq. 1.1.

The scatter plots of Hα versus He 10833 and Paβ in Fig. 3.3, and of He D_3 versus He 10833 in Fig. 3.4 show no strong correlations between these indicators. Excess absorption in He 10833 and Paβ is less common in stars with stronger excess emission in

Table 3.2.: Same as Table 3.1, but for only the Hα active stars.

	Hα	He D_3	Na D	Ca IRT-a	Ca IRT-b	Ca IRT-c	He 10833
He D_3	**0.95**	...					
Na D	**0.68**	**0.72**	...				
Ca IRT-a	0.56	0.58	0.26	...			
Ca IRT-b	0.32	0.26	0.17	**0.62**	...		
Ca IRT-c	0.08	0.01	−0.02	0.47	**0.91**	...	
He 10833	0.53	0.57	0.30	0.52	0.26	0.14	...
Paβ	0.41	**0.64**	0.55	0.11	−0.21	−0.36	0.43

Hα and He D_3, leading to moderate correlation coefficients for the Hα active stars only. However, the strong excess absorption in He 10833 and Paβ is only seen for earlier spectral subtypes and there is no correlation visible for mid-to-late type stars only.

In the remaining scatter plots in Fig. 3.4, strong correlations between the Ca IRT lines are visible. However, the correlation coefficients decrease if the Hα inactive stars are excluded. Therefore, the strong correlation is likely caused by a correlation of the deviations in the line profiles of the photospheric components. The very late-type stars appear as outliers because the M6.0 reference star is used for the subtraction, but the pseudo-continua around the three Ca IRT lines behave differently at later types.

3.3. Temporal variability

While the previous sections explored the typical pEW′ values of each star as derived from the co-added template spectra, I now investigate how the pEW′ values from individual spectra vary for each star. Occasional strong flares can cause drastic short-term variations that lead to a heavy-tailed non-normal distribution of a star's pEW′ values. Unlike the variance or standard deviation, a difference between percentiles does not assume a normal distribution. Therefore, I defined the absolute variation of each indicators as the difference between the 20th and 80th percentiles calculated using the quantile estimator by Harrell & Davis (1982). This estimator does not assume a specific distribution and also provides the errors of the percentiles. The error of the absolute variation is the root sum of squares of the percentile errors. Division of the absolute variation by the pEW′ from the co-added template spectrum yields the relative variation. For each chromospheric indicator, this relative variation of each Hα active star is shown as a function of the normalised Hα luminosity in Fig. 3.5. Hα active stars can have pEW′ values close to 0 Å in the other indicators, leading to very large relative variations with large error bars. For reasons of clarity, I excluded four stars with a relative He D_3 variation larger than 3, and three stars, four stars, five stars, and six stars with relative Na D, Ca IRT-a, Ca IRT-b, and Ca IRT-c variations larger than 5 from Fig. 3.5. The relative He 10833 and Paβ variations are not shown. Although measurements from spectra with telluric contamination are excluded as

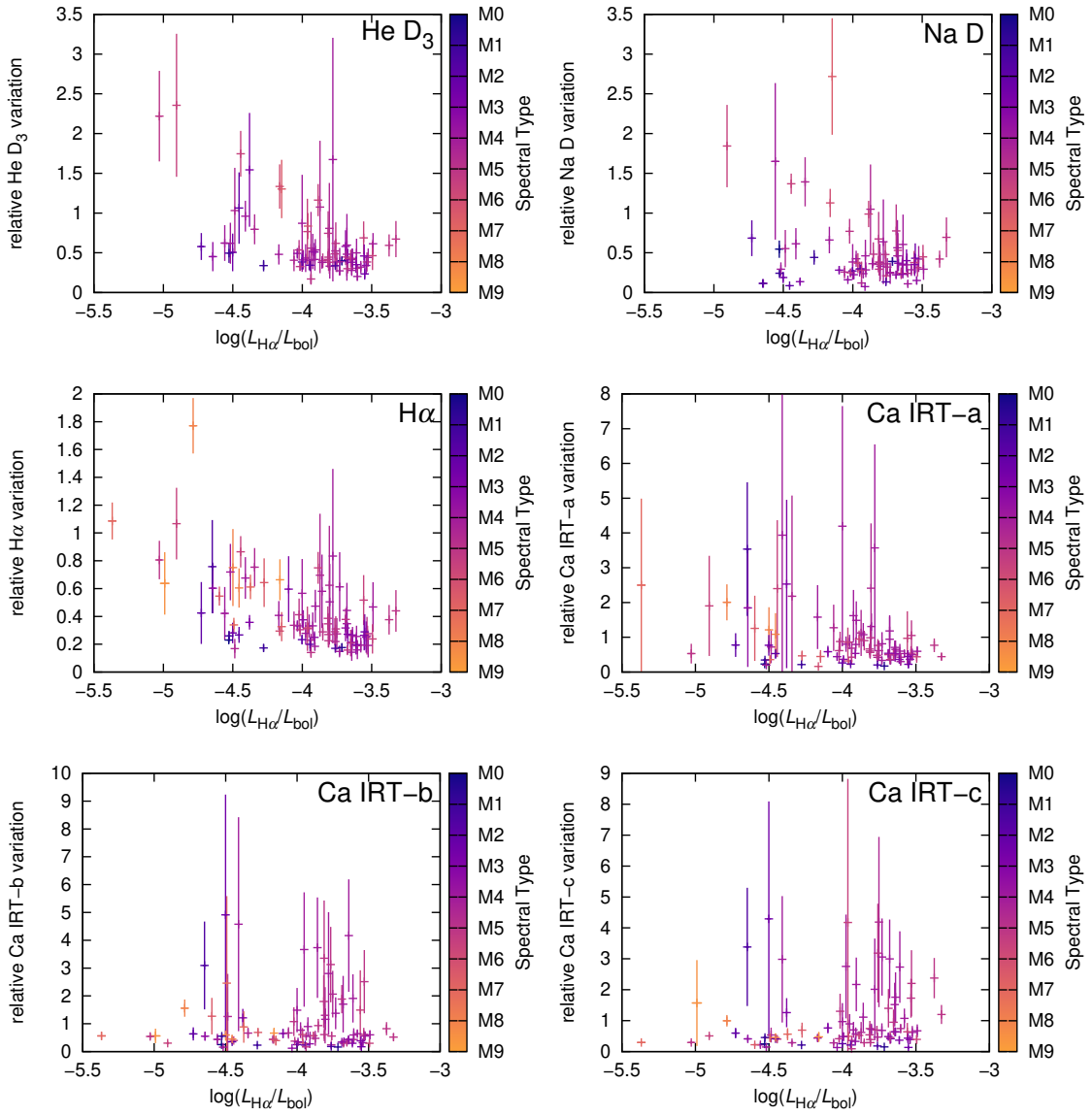

Figure 3.5.: Relative pEW′ variations of Hα active stars as functions of normalised Hα luminosity. Colours correspond to spectral subtypes.

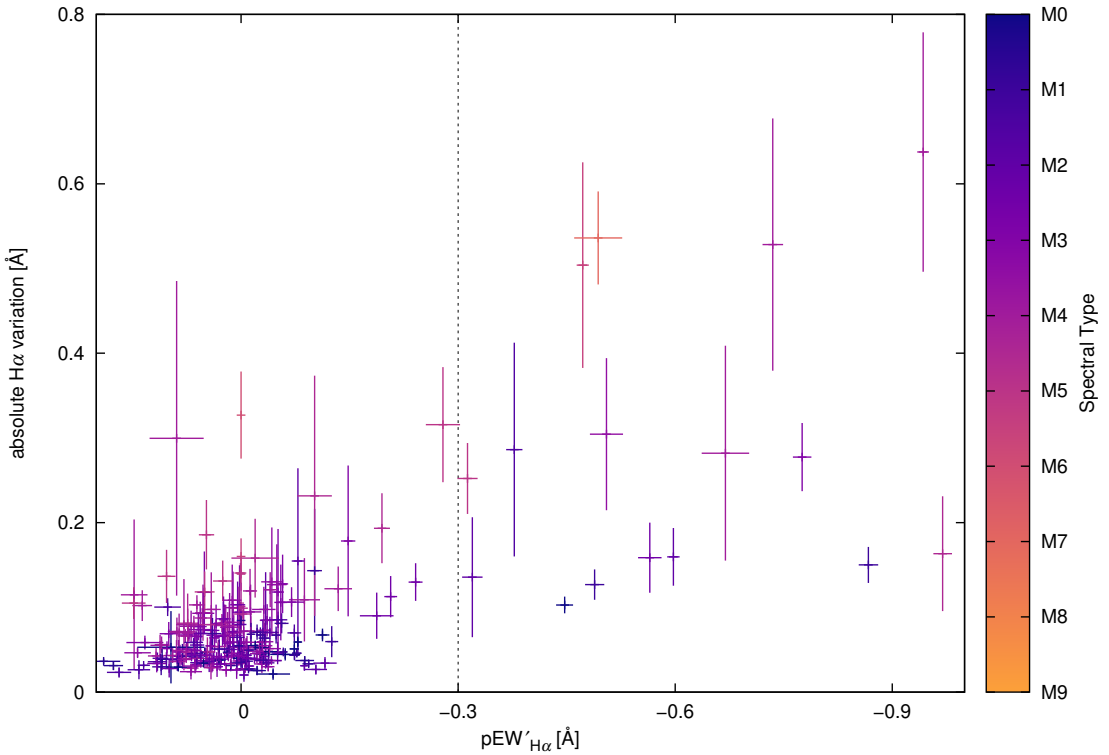

Figure 3.6.: Absolute Hα variation as a function of $\mathrm{pEW}'_{\mathrm{H}\alpha}$ for Hα inactive and low-active stars. The dashed black line marks the activity threshold at $\mathrm{pEW}'_{\mathrm{H}\alpha} = -0.3$ Å. Colours correspond to spectral subtypes.

described in Sect. 2.2, even more stars show large variations and error bars in these two indicators. I again calculated Spearman's rank coefficient r_S to quantify the correlations between the relative variations and the normalised Hα luminosity. The stars excluded from Fig. 3.5 are included in the calculation of the correlation coefficients.

With a moderate correlation coefficient of $r_S = -0.50$, the relative He D_3 variation shows the strongest anti-correlation with the normalised Hα luminosity. At $r_S = -0.48$, the relative Hα variation is also moderately anti-correlated with the normalised Hα luminosity, and includes very late-type stars for which He D_3 could not be measured. The relative Na D and Ca IRT-a variations are weakly anti-correlated with the normalised Hα luminosity with $r_S = -0.15$ and $r_S = -0.34$, whereas the relative Ca IRT-b, Ca IRT-c, He 10833, and Paβ variations show no correlation or weak positive correlations with $r_S = 0.02$, $r_S = 0.20$, $r_S = 0.32$, and $r_S = 0.22$.

For the Hα inactive stars, I show the absolute Hα variation as a function of $\mathrm{pEW}'_{\mathrm{H}\alpha}$ in Fig. 3.6. Not shown is J19255+096 with $\mathrm{pEW}'_{\mathrm{H}\alpha} = (2.07 \pm 0.08)$ Å and an absolute Hα variation of (3.2 ± 0.5) Å. The Hα inactive stars are concentrated around 0 Å in $\mathrm{pEW}'_{\mathrm{H}\alpha}$ and have a median absolute Hα variation of 0.053 Å. In general, the absolute variations are larger for later spectral subtypes because a lower SNR leads to higher statistical fluc-

tuations. The Hα active stars with an excess emission barely above the activity threshold at $\mathrm{pEW}'_{\mathrm{H}\alpha} = -0.3$ Å show generally larger absolute variations than Hα inactive stars of the same spectral subtype. This reaffirms the choice of an activity threshold close to the boundary of the cloud of Hα inactive stars.

3.4. Impact of reference stars

All results presented in the previous sections were derived using the stars with the longest rotation period for each spectral subtype as reference stars for the spectral subtraction. As outlined in Sect. 2.2.1, I also measured all pEW′ values using the stars with the smallest variation of the Hα MNI for each subtype as reference stars. For each pEW′ measurement, I calculated the difference $\Delta_{\mathrm{rot}}^{\mathrm{MNI}}$ between the result using the stars with the smallest Hα MNI variation and the result using the stars with the longest rotation period as reference stars. The differences $\Delta_{\mathrm{rot}}^{\mathrm{MNI}}$ from the co-added template spectra for all chromospheric indicators are shown in Fig. 3.7 as a function of the pEW′ measured using the reference stars with the longest rotation period. Error bars are derived from the uncertainties of both pEW′ measurements via propagation of uncertainty. Spectral subtypes later than M5.0 are not shown because both sets of reference stars include the same stars for the latest spectral subtypes, and hence there are no differences.

A different reference star can introduce a constant offset and a linear trend for all stars of the same spectral subtype. Both effects are seen for some subtypes in some indicators: While constant offsets are most clearly seen for Na D and the Ca IRT lines, which all have a strong photospheric component, and for He 10833, the most obvious linear trend is seen for the M4.0 stars in Hα, where $\Delta_{\mathrm{rot}}^{\mathrm{MNI}}$ decreases from −0.09 Å for the Hα inactive stars at $\mathrm{pEW}'_{\mathrm{H}\alpha} \approx 0$ Å to −0.15 Å for the star with the strongest excess emission at $\mathrm{pEW}'_{\mathrm{H}\alpha} = -7.81 \pm 0.06$ Å. However, most linear trends are insignificant compared to the measurement uncertainties. In general, for He D_3 and Hα, the differences are on the order of the spread of the Hα inactive stars, but become insignificant with increasing excess emission. On the other hand, the differences in the other indicators are significant also for Hα active stars, but they are dominated by only a constant offset.

I also calculated the pEW′ variations of each star as defined in the previous section using the pEW′ measurements derived with both sets of reference stars. In Fig. 3.8, the absolute variations derived from the pEW′ measurements using the reference stars with the smallest Hα MNI variations are shown as a function of the absolute variations derived from the pEW′ measurements using the reference stars with the longest rotation periods. As the variation is the difference between two pEW′ measurements of the same star, any constant offset introduced by the choice of the reference star is eliminated. Therefore, the absolute variations derived with both sets of reference stars are in good agreement with each other.

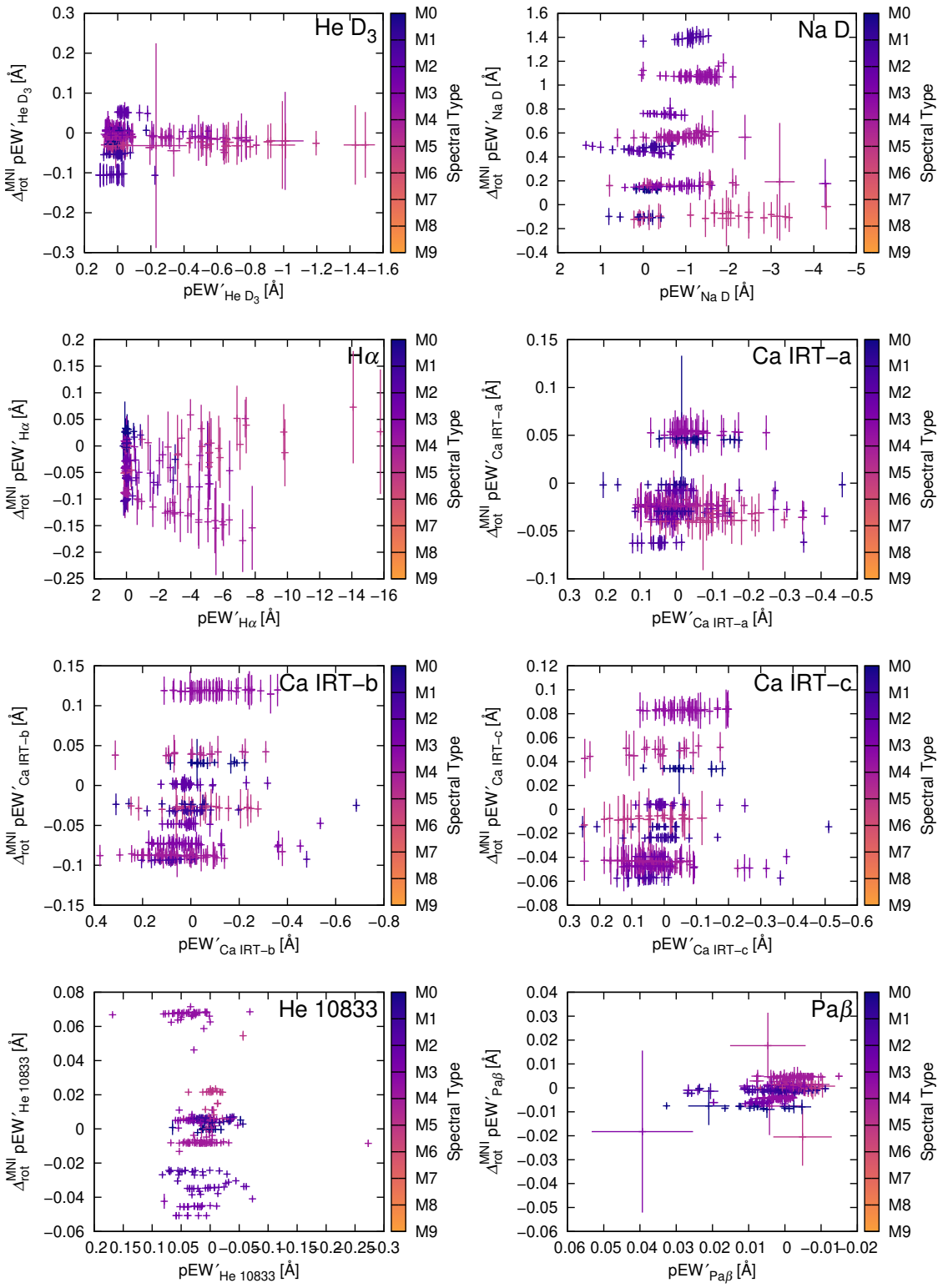

Figure 3.7.: Differences between pEW′ values calculated with different sets of reference stars as a function of pEW′ values from the previous sections. Colours correspond to spectral subtypes.

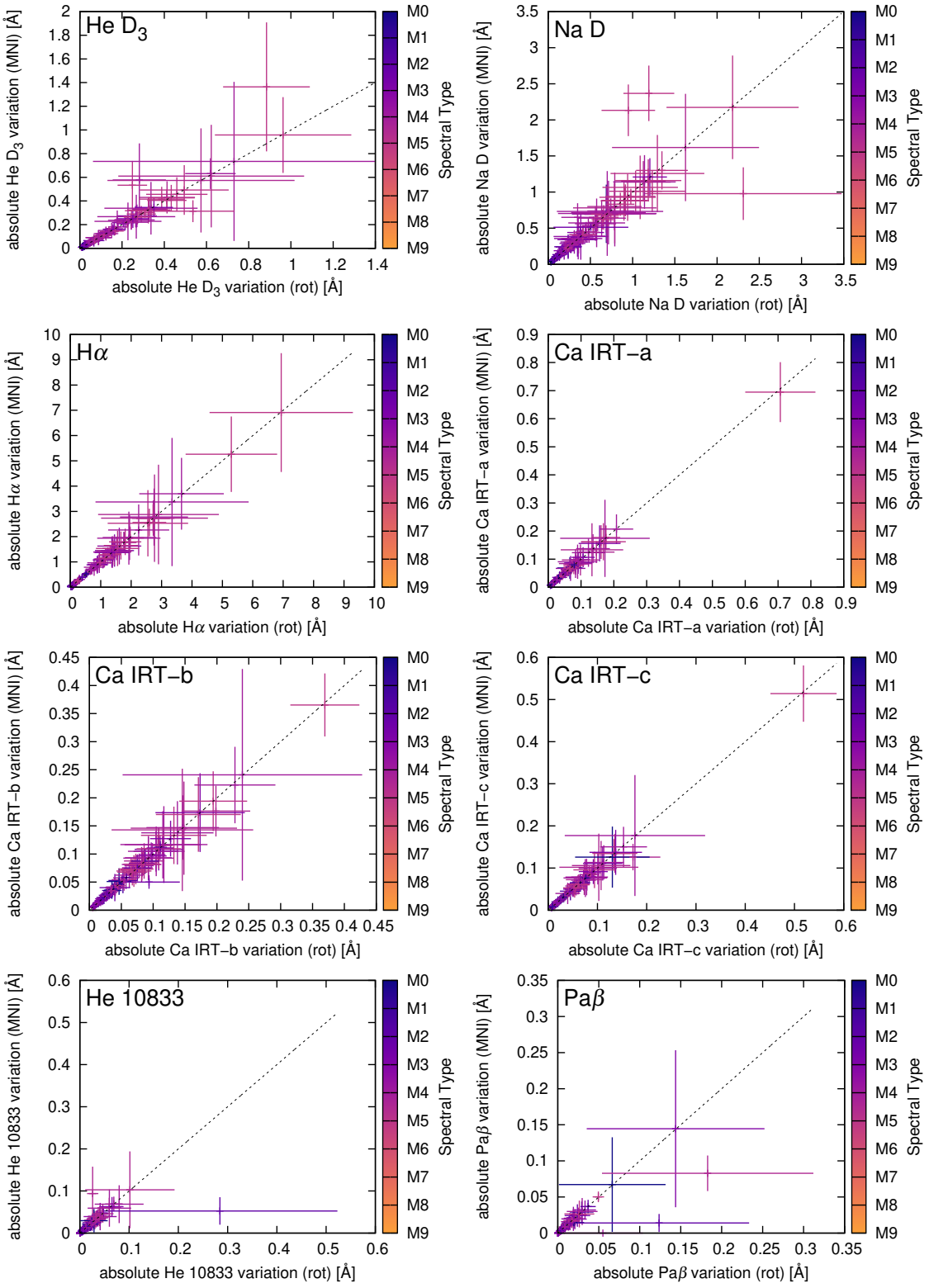

Figure 3.8.: Scatter plots of pEW′ variations calculated with different sets of reference stars. Dashed black lines mark the one-to-one relation. Colours correspond to spectral subtypes.

3.5. Discussion

In Fig. 3.9, I compare the pEW′ values presented in this thesis with the earlier results from Schöfer et al. (2019) that do not include observations after July 2018. While the results generally agree with each other for all chromospheric lines, a few outliers from the one-to-one relation are visible. The outliers are mostly later-type stars, so a larger statistical fluctuation because of a lower SNR is expected, particularly for He D_3 and Na D. In Hα, the two most significant outliers are J10584–107 and J19255+096. The former star is also the only significant outlier in the Ca IRT lines. In this case, the co-added template spectrum used in the earlier work included a mislabelled spectrum of a nearby K dwarf and therefore showed erroneously strong absorption. The latter star already appeared as an outlier previously as it is the only star later than M6.0 that was classified as Hα active. Although the number of observations increased significantly from 36 to 111, the co-added template spectrum is very noisy around Hα. At spectral type M8.0, the flux is insufficient in this wavelength region for a robust measurement. In He 10833, a group of outliers with large error bars in the earlier results is visible. The co-added template spectra of these stars were bad because of a bad background subtraction for some observations, but were fixed after July 2018. In Paβ, most outliers also have large error bars and are still consistent with the one-to-one relation.

A comparison of the $\mathrm{pEW}'_{\mathrm{H}\alpha}$ values with $\mathrm{pEW}_{\mathrm{H}\alpha}$ values compiled by Jeffers et al. (2018) and derived without the spectral subtraction is shown in Fig. 3.10. Despite the different methods, the results generally agree with each other. There are more stars below the one-to-one relation than above, so the subtraction method leads to more negative values. This is expected, as the spectral subtraction removes photospheric absorption lines in the line window.

I now compare the normalised Hα luminosity to independent activity indicators. While the catalogue of Ca H&K measurements by Boro Saikia et al. (2018) contains R'_{HK} values for 28 sample stars, only one of these stars (J18075–159) is Hα active. With $\log R'_{\mathrm{HK}} = -4.345$, it shows a higher normalised chromospheric Ca H&K flux than the 27 Hα inactive stars with $-5.434 < \log R'_{\mathrm{HK}} < -4.420$. The top left panel of Fig. 3.11 shows the projected rotational velocities $v \sin i$ as tabulated in Table A.1 as a function of $\log(L_{\mathrm{H}\alpha}/L_{\mathrm{bol}})$. As expected from the correlation between chromospheric activity and rotation, the stars with a higher normalised Hα luminosity are the fastest rotators. For very late-type stars, the normalised Hα luminosity is lower than for earlier-type stars with the same $v \sin i$. It is possible that $\log(L_{\mathrm{H}\alpha}/L_{\mathrm{bol}})$ is systematically lower for very late spectral subtypes, because less absorption in the Hα line window is removed by the spectral subtraction, as the reference star is of an earlier spectral subtype. In the top right panel of Fig. 3.11, the rotation periods P_{rot} are shown as a function of $\log(L_{\mathrm{H}\alpha}/L_{\mathrm{bol}})$. The result is similar to the result from Jeffers et al. (2018) shown in Fig. 1.13 and also to the previous panel, although the inclination angle of the stellar rotation axis is removed as a factor. Stars with a higher normalised Hα luminosity have shorter rotation periods and are thus faster rotators. Shulyak et al. (2019) measured magnetic fields of 29 Hα active sample stars.

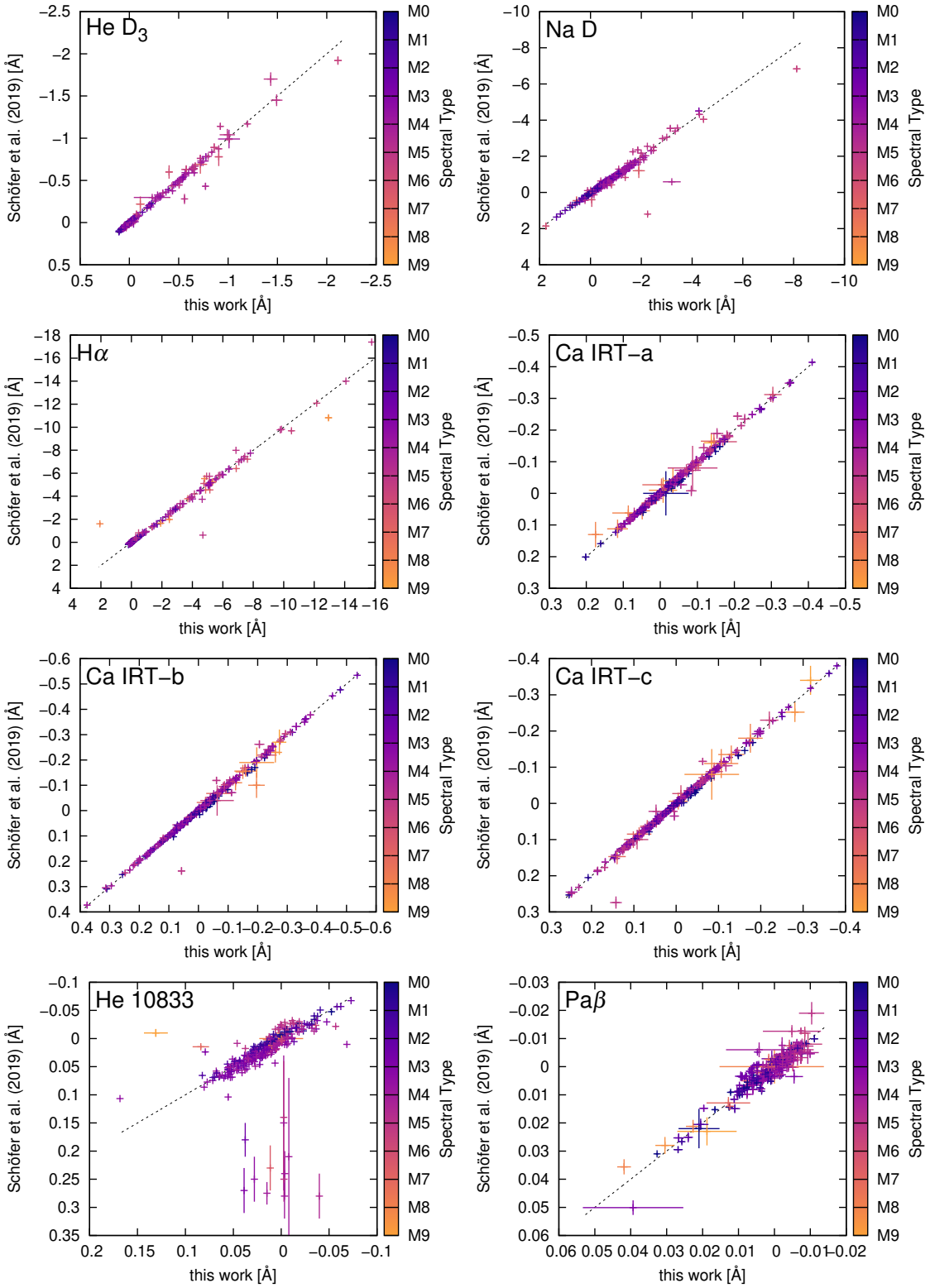

Figure 3.9.: Comparison of pEW′ values derived in this thesis and in Schöfer et al. (2019). Dashed black lines mark the one-to-one relation. Colours correspond to spectral subtypes.

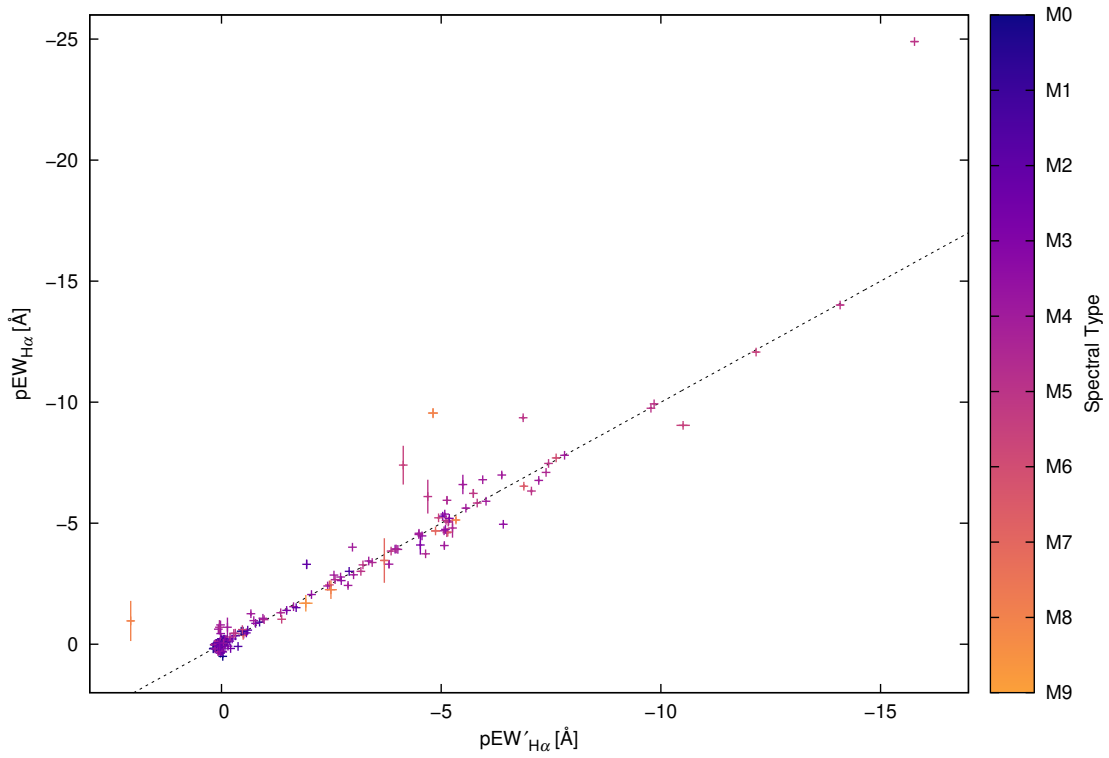

Figure 3.10.: Comparison of pEW′ values with pEW values reported by Jeffers et al. (2018). The dashed black line marks the one-to-one relation. Colours correspond to spectral subtypes.

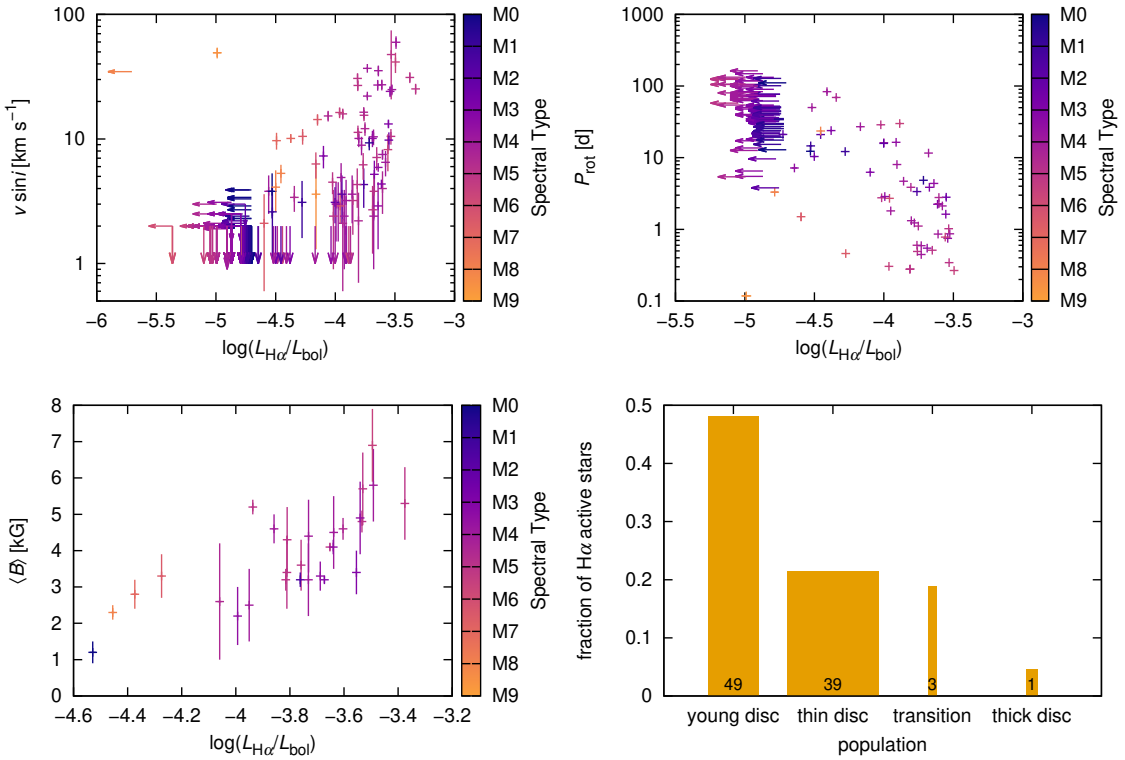

Figure 3.11.: *Top left:* projected rotational velocity $v \sin i$ as given in Table A.1 as a function of normalised Hα luminosity. Arrows denote lower limits, colours correspond to spectral subtypes. *Top right:* rotation period P_{rot} as given in Table A.1 as a function of normalised Hα luminosity. Arrows denote lower limits, colours correspond to spectral subtypes. *Bottom left:* total magnetic field strength $\langle B \rangle$ derived by Shulyak et al. (2019) as a function of normalised Hα luminosity. Colours correspond to spectral subtypes. *Bottom right:* fraction of Hα active stars in stellar populations as given by Cortés-Contreras et al. (in prep.). Box width is proportional to the number of stars in each population, so the area of each bar corresponds to the specified number of Hα active stars in that population.

As shown in the bottom left panel of Fig. 3.11, the normalised Hα luminosity is strongly correlated with the total magnetic field strength $\langle B \rangle$, consistent with the assumption that the chromospheric emission is driven by magnetic heating. The bottom right panel of Fig. 3.11 shows the fraction of Hα active stars for the different kinematic stellar populations identified by Cortés-Contreras et al. (in prep.). While 48% of the stars in the young disc population are Hα active, the fraction decreases to 21% for the remaining thin disc population, 3 of 16 stars in transition region between the thin and the thick disc, and only 1 of 22 stars in the thick disc population. As these populations are a rough indicator of the age of the stars, the decreasing fraction of Hα active stars is consistent with the correlation of chromospheric activity and age.

With an overall tally of 95 Hα active stars, one star less has been classified as Hα active than in Schöfer et al. (2019), although 6 new stars were included in the sample. In addition

to the already discussed very late-type star J19255+096, $pEW'_{H\alpha}$ could not be measured in the co-added template spectrum of the previously Hα active star J06318+414 because the spectral order containing Hα was excluded from the spectrum, and the $pEW'_{H\alpha}$ of J06594+193 changed from (-0.428 ± 0.026) Å to (-0.279 ± 0.024) Å below the activity threshold. On the other hand, the $pEW'_{H\alpha}$ of J03217–066 changed from (-0.274 ± 0.022) Å to (-0.320 ± 0.015) Å above the activity threshold, and the early-type Hα active star J20451–313 was added. Therefore, the classification of Hα active stars is relatively stable. The distribution of the Hα active stars among spectral subtypes is similar to the distribution found in previous studies of nearby M dwarfs (e.g. Reiners et al. 2012; West et al. 2015; Jeffers et al. 2018) that was discussed in Sect. 1.4.2, and a drastic increase in the fraction of Hα active stars occurs between spectral subtypes M3.5 and M4.0, where stars no longer have a radiative core and become fully convective, as described in Sect. 1.2.4.

The correlations presented in Sect. 3.2 are as expected from the distribution of the pEW′ values among the spectral subtypes described in Sect. 3.1. $pEW'_{H\alpha}$ and $pEW'_{He\ D_3}$ show the most similar distribution and this translates into a very strong correlation. A linear correlation between Hα and He D_3 was previously reported by Gizis et al. (2002) and suggests that these lines are formed in the same region of the chromosphere. In Na D and the Ca IRT lines, the Hα inactive stars of each spectral subtype are spread around the respective reference stars. As the spectral subtypes are a coarse classification that groups stars with a range of different effective temperatures, metallicities, and surface gravity together, the differences in these parameters cause different line shapes of the photospheric component (e.g. Mallik 1997; Schlieder et al. 2012), and the subtraction of a reference star spectrum can only remove photospheric lines with the same shape. While the correlation between Na D and Hα is stronger for the Hα active stars only, the correlations between the Ca IRT lines and Hα become weaker when the Hα inactive stars are excluded. This is likely an effect of the different pseudo-continuum flux ratios for different spectral subtypes. He 10833 and Paβ show distributions per spectral type that are very different from Hα and are therefore weaker correlated with Hα. The narrow line windows for these two lines increase the chance that not the full excess absorption or emission is measured, as either the true line may be broader or an imprecise Doppler shift correction may lead to the line not being centred in the line window. However, Fuhrmeister et al. (2019a) measured the pEW of the He 10833 line by fitting a Voigt profile and found a similar spectral type distribution, but with an additional spectral-type dependent trend that is removed by the spectral subtraction in the pEW′ measurements. A broader line window would cause even more measurements from individual spectra to be contaminated by the nearby telluric lines. CARMENES spectra with telluric absorption lines removed are available (Nagel et al. submitted), but there is also an airglow line close to He 10833 that is not removed in those spectra.

In He D_3 and Hα, the relative variations decrease with increasing activity as measured by the normalised Hα luminosity. Bell et al. (2012) found the same behaviour for Hα. If a star has many active regions on its surface, then the contribution of a single active region that appears or disappears to the global activity level is negligible. Therefore, it

is plausible that the relative variation is anti-correlated with the activity level. In Na D and the Ca IRT line, the anti-correlation is not clearly seen. While the bias introduced by the spectral subtraction is removed in the calculation of the absolute variation, it is re-introduced by the division to obtain the relative variation. The relative variations of He 10833 and Paβ are not useful, as the measured pEW′ values can be very close to 0 Å also for Hα active stars and a division by a value close to zero yields very large results.

As shown in Sect. 3.4, a different choice of the reference star introduces mostly a constant offset. For the lines with a photospheric absorption component, this offset can be significant. However, there is no easy way to remove the offset. A more fine-grained grouping of the stars leads to a larger number of groups and the pEW′ values from different groups cannot be directly compared. An alternative approach is the subtraction of a synthetic model spectrum instead of a reference star spectrum. However, while high-resolution PHOENIX models are available for a large parameter space (Husser et al. 2013), the line lists for the photospheric absorption bands may not be sufficiently accurate to reproduce the absorption lines that should be removed by the spectral subtraction. In addition, results derived using different model spectra would also need to be normalised before they can be compared with each other.

4. Photospheric indicators

The photosphere is the lowest layer of a stellar atmosphere, but dominates the light that reaches the observer, as described in Sect. 1.2.4. Strong absorption bands by titanium oxide and other molecules in the photosphere are the characteristic feature in M dwarf spectra.

In this chapter, I present and analyse the indices described in Sect. 2.3 that measure the strength of these absorption band in the M dwarfs of the CARMENES sample, starting with the spectral-type dependence as an overview in Sect. 4.1. While TiO 7050, TiO 8430, VO 7436, and VO 7942 were also presented in Schöfer et al. (2019), CaH 2*, CaH 3*, TiO 8860, and FeH WFB are new indices, and I include additional observations after July 2018 in this thesis. In Sect. 4.2, I explore correlations both among the band indices and with chromospheric activity as measured by the normalised Hα luminosity. This leads to the definition of a new activity indicator. Sect. 4.3 quantitatively investigates the temporal variations of the band indices. In Sect. 4.4, I compare the results with previous results and discuss them.

4.1. Sample overview

The photospheric absorption band indices derived from the co-added template spectra for each star are shown in Fig. 4.1 as a function of spectral type. Hα active stars are colour-coded by their normalised Hα luminosity, whereas Hα inactive stars and the M9.0 star with no valid normalised Hα luminosity measurement are shown in black.

All indices show a clear spectral-type dependence. While CaH 2*, CaH 3*, and TiO 7050 decrease linearly with the spectral type up to M6.0, the other indicators tend to decrease stronger with increasing spectral type. At very late types later than M6.0, the indices appear to be constant or increase again, but with only four or less stars per subtype, the sample is too sparse to detect if these are outliers. The CaH 3*, TiO 7050, TiO 8430, and FeH WFB index values of Hα active stars tend to be lower than the values of Hα inactive stars of the same spectral subtype. The opposite is true for CaH 2*, whereas VO 7436, VO 7942, and TiO 8860 show no clear trends for Hα active stars.

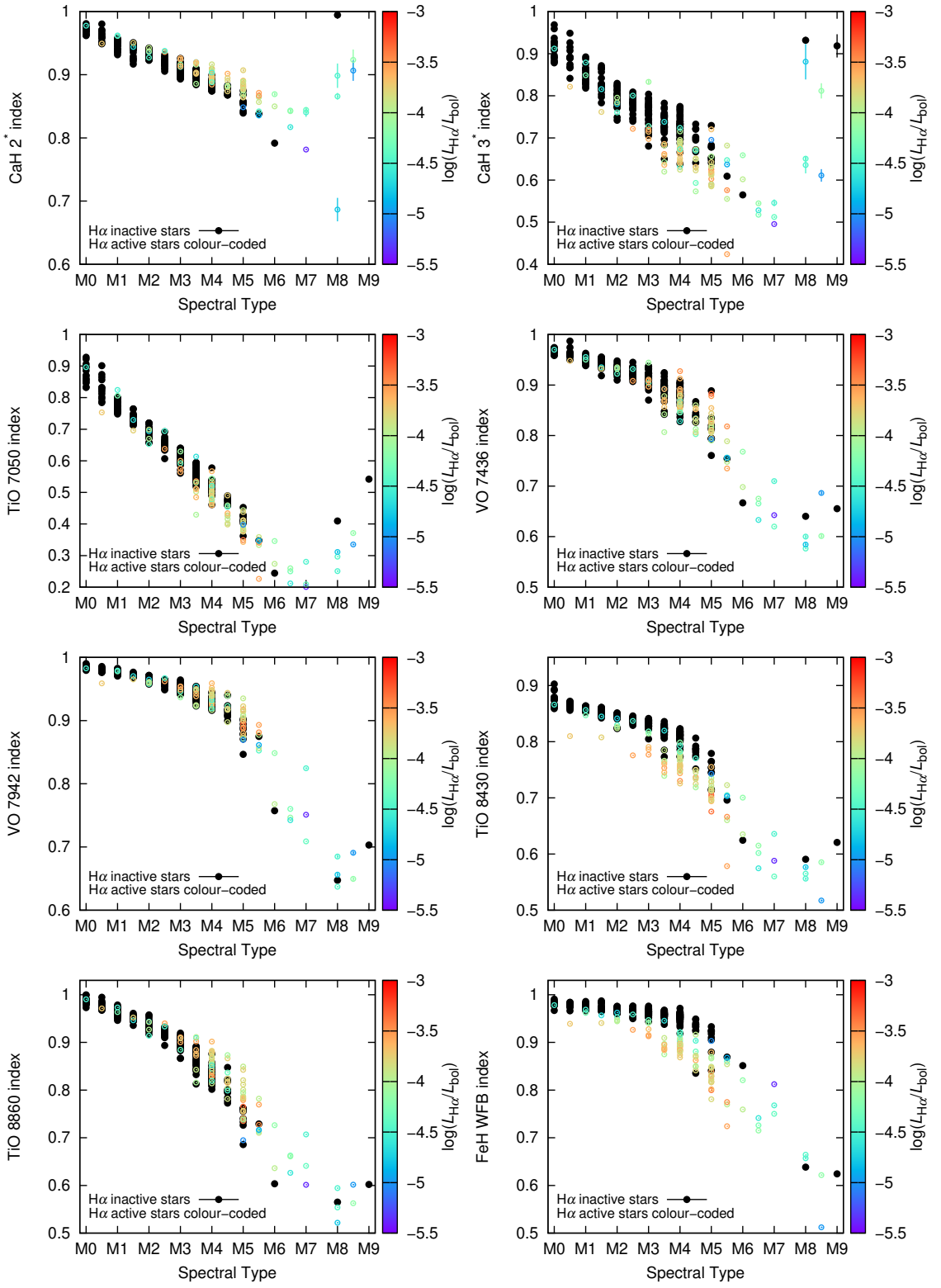

Figure 4.1.: Photospheric absorption band indices as a function of spectral type. Hα inactive stars are shown in black, Hα active stars are colour-coded by normalised Hα luminosity.

Table 4.1.: Correlation table of photospheric absorption band indices using Spearman's rank coefficient r_S. All correlations are strong with $r_S > 0.60$ and therefore highlighted in boldface.

	CaH 2*	CaH 3*	TiO 7050	VO 7436	VO 7942	TiO 8430	TiO 8860
CaH 3*	**0.81**	...					
TiO 7050	**0.92**	**0.89**	...				
VO 7436	**0.86**	**0.89**	**0.96**	...			
VO 7942	**0.93**	**0.81**	**0.97**	**0.92**	...		
TiO 8430	**0.84**	**0.90**	**0.96**	**0.95**	**0.92**	...	
TiO 8860	**0.94**	**0.81**	**0.97**	**0.92**	**0.99**	**0.91**	...
FeH WFB	**0.74**	**0.87**	**0.90**	**0.91**	**0.85**	**0.96**	**0.84**

4.2. Correlations

4.2.1. Correlations among band indices

The similar spectral-type dependence of all photospheric band indices suggests that the indices are strongly correlated with each other. Using the same colour-coding for Hα active and Hα inactive stars as in the previous section, Fig. 4.2 shows scatter plots of the TiO 7050 index versus all other indices, and Fig. 4.3 shows scatter plots of the two CaH band indices and of the two VO band indices. A correlation table with Spearman's rank coefficients r_S is given in Table 4.1.

All photospheric absorption band indices are strongly correlated with each other, with correlation coefficients ranging from $r_S = 0.74$ for CaH 2* versus FeH WFB to $r_S = 0.99$ for VO 7942 versus TiO 8860. The scatter plots of TiO 7050 versus CaH 2*, VO 7942, TiO 8430, TiO 8860, and FeH WFB in Fig. 4.2 all show the Hα inactive stars located on a narrow line, while the Hα active stars are located in general either above the line of Hα inactive stars (TiO 7050 versus CaH 2*, VO 7942, and TiO 8860) or below that line (TiO 7050 versus TiO 8430 and FeH WFB). This effect is more pronounced at lower index values that correspond to later spectral subtypes. In the scatter plots of TiO 7050 versus CaH 3* shown in Fig. 4.2 and CaH 2* versus CaH 3* shown in Fig. 4.3, the Hα inactive stars form a cloud rather than a line, and the Hα active stars are located at the bottom of that cloud. In contrast, the Hα inactive and Hα active stars are not separated in the scatter plots of TiO 7050 versus VO 7436 in Fig. 4.2 and VO 7436 versus VO 7942 in Fig. 4.3. As the monotonic decrease of the index values stops at different spectral subtypes for different indices, the very late-type stars indicate that there is a turnaround point in some of the scatter plots. However, as the sample is very sparse at very late spectral subtypes, these stars only have a minor impact on the correlation coefficients.

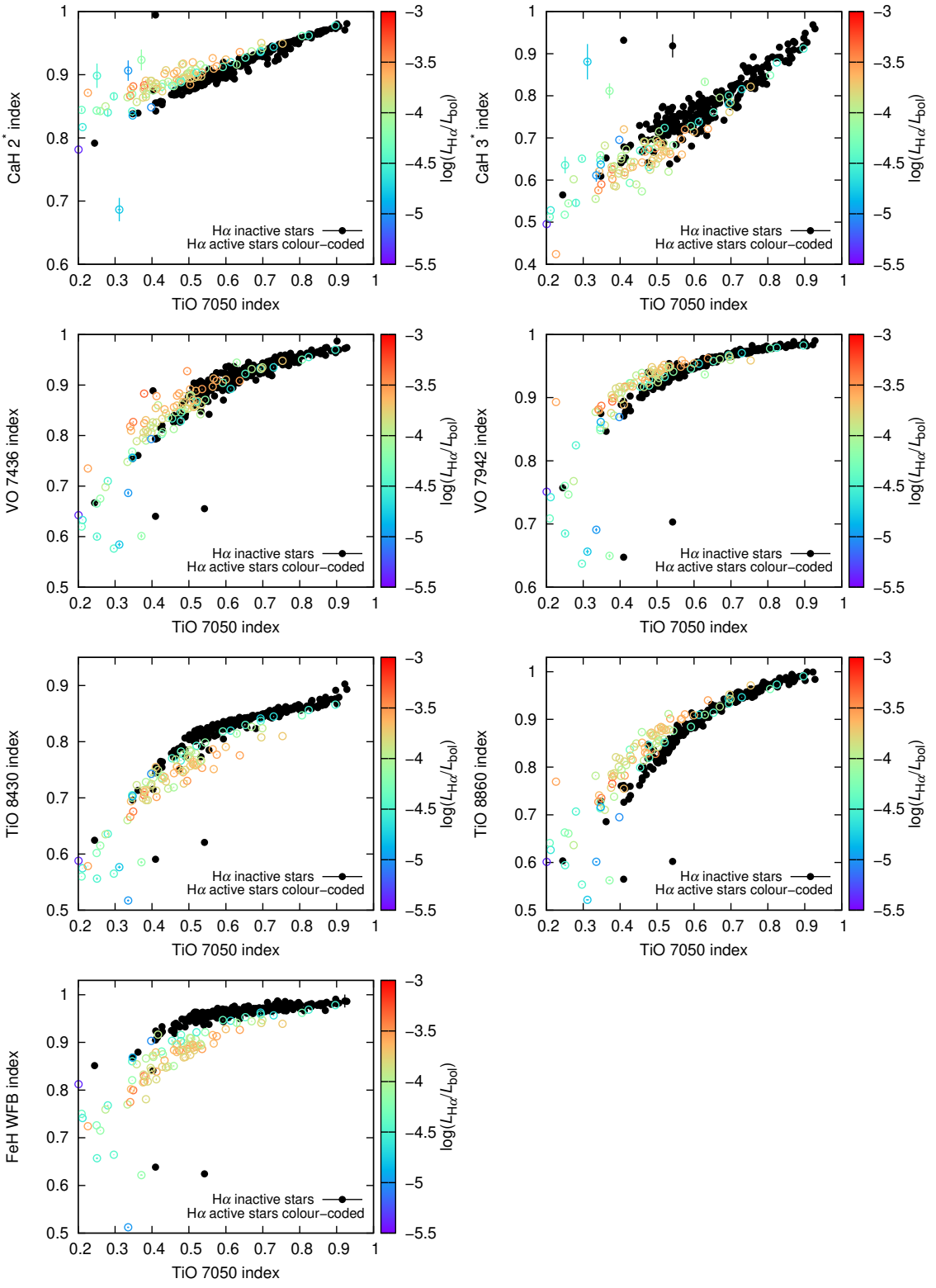

Figure 4.2.: Scatter plots of TiO 7050 versus other photospheric absorption band indices. Hα inactive stars are shown in black, Hα active stars are colour-coded by normalised Hα luminosity.

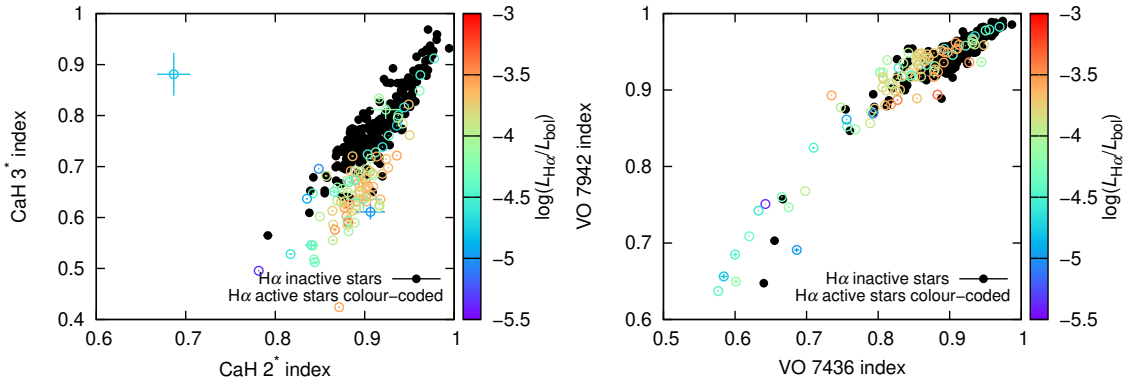

Figure 4.3.: Scatter plots of CaH 2* versus CaH 3* and of VO 7436 versus VO 7942. Hα inactive stars are shown in black, Hα active stars are colour-coded by normalised Hα luminosity.

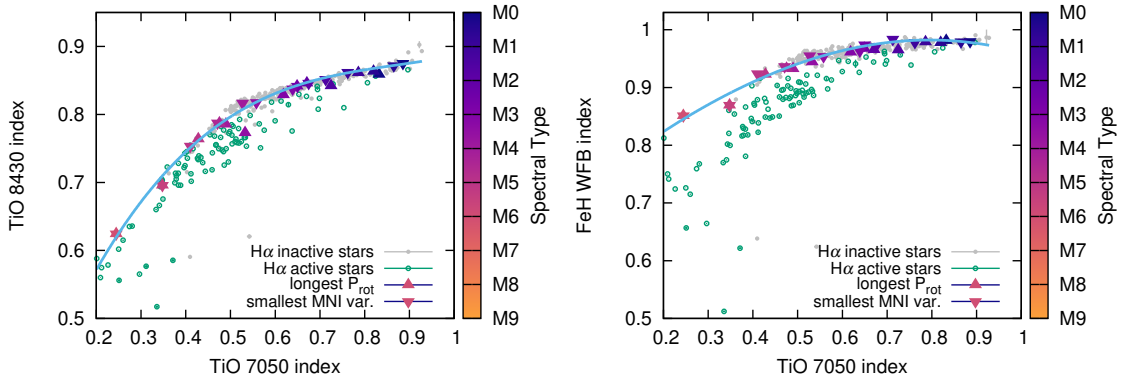

Figure 4.4.: Scatter plots of TiO 7050 versus TiO 8430 and of TiO 7050 versus FeH WFB. Hα inactive stars are shown in grey, Hα active stars in green. Two sets of reference stars are shown as triagles colour-coded by spectral subtype. Blue curves are polynomial fits to the reference stars with the smallest MNI variations.

4.2.2. Correlations with Hα

As described in the previous sections, the spectral-type dependences in Fig. 4.1 and the scatter plots in Figs. 4.2 and 4.3 revealed a difference between Hα inactive and Hα active stars. While the spread in the index values of the Hα inactive stars of each spectral subtype complicates the quantification of the activity effect as a function of spectral type, the scatter plots in general show a continuous, narrow line of Hα inactive stars. To avoid a selection bias from the definition of Hα active and Hα inactive, I define the *inactivity line* as a third-order polynomial fit to a set of reference stars classified as inactive by an independent measurement. The scatter plots of TiO 7050 versus TiO 8430 and of TiO 7050 versus FeH WFB are shown again in Fig. 4.4, but with the two sets of reference stars presented in Sect. 2.2.1 highlighted and colour-coded by their spectral subtype.

Because the M3.5 star with the longest known rotation period appears as an outlier in the scatter plot of TiO 7050 versus TiO 8430, I used the set of reference stars with the

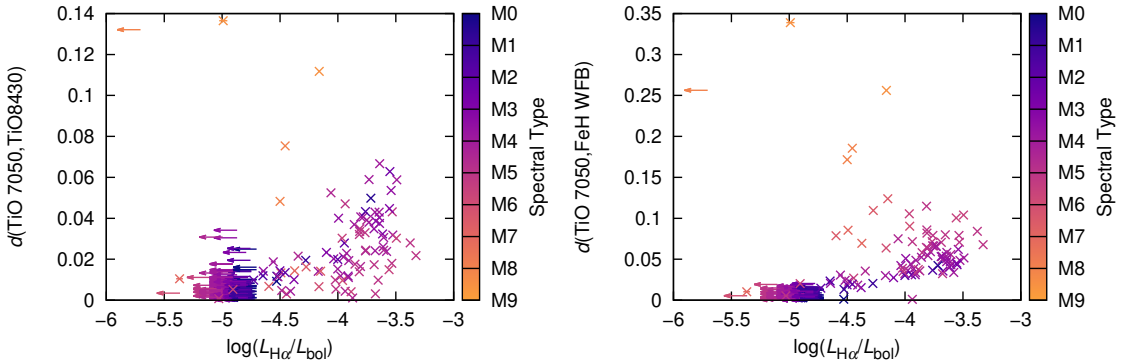

Figure 4.5.: d(TiO 7050, TiO 8430) and d(TiO 7050, FeH WFB) as functions of normalised Hα luminosity. Hα inactive stars are shown as arrows starting at the normalised Hα luminosity corresponding to the activity threshold. Colours correspond to spectral subtypes.

smallest MNI variations to fit the inactivity line. The resulting polynomials are also shown in Fig. 4.4 and are given as follows:

$$\text{TiO 8430} = g(\text{TiO 7050}) = 0.77 \cdot (\text{TiO 7050})^3 - 2.02 \cdot (\text{TiO 7050})^2 + 1.87 \cdot (\text{TiO 7050}) + 0.27$$

$$\text{FeH WFB} = h(\text{TiO 7050}) = -0.09 \cdot (\text{TiO 7050})^3 - 0.29 \cdot (\text{TiO 7050})^2 + 0.63 \cdot (\text{TiO 7050}) + 0.71$$

For each star, I then calculated the orthogonal distance d(TiO 7050, TiO 8430) from its position in the (TiO 7050, TiO 8430)-plane to the polynomial g, and the orthogonal distance d(TiO 7050, FeH WFB) from its position in the (TiO 7050, FeH WFB)-plane to the polynomial h. The resulting distances are shown as a function of the normalised Hα luminosity in Fig. 4.5.

In both the (TiO 7050, TiO 8430)- and the (TiO 7050, FeH WFB)-plane, larger distance values are more common for stars with higher normalised Hα luminosities, and the very late-type stars are outliers because the polynomials can not fit the turnaround point that occurs at very late spectral subtypes. While the d(TiO 7050, FeH WFB) values for most Hα active stars are larger than for Hα inactive stars, this is not true for d(TiO 7050, TiO 8430), as the polynomial g is close to the lower end of the line of Hα inactive stars in the mid-type range.

4.3. Temporal variability

In the same way as for the chromospheric indicators in Sect. 3.3, I calculated the absolute variations of the photospheric band indices from the individual spectra of each star and divided them by the index value derived from the co-added template spectrum to obtain the relative variation. The relative variations are shown as a function of the index value derived from the co-added template spectrum in Fig. 4.6.

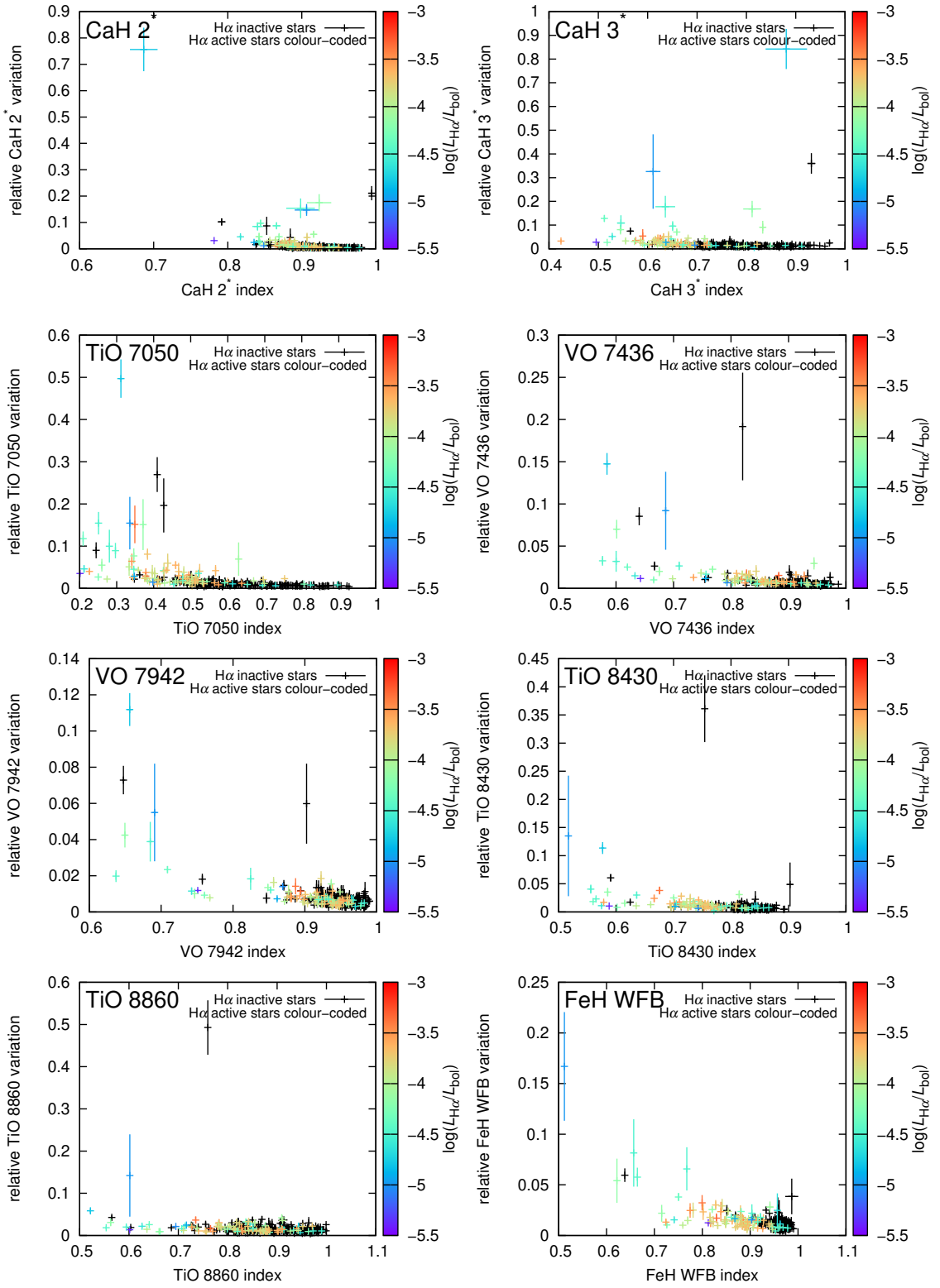

Figure 4.6.: Relative index variations as functions of index values. Hα inactive stars are shown in black, Hα active stars are colour-coded by normalised Hα luminosity.

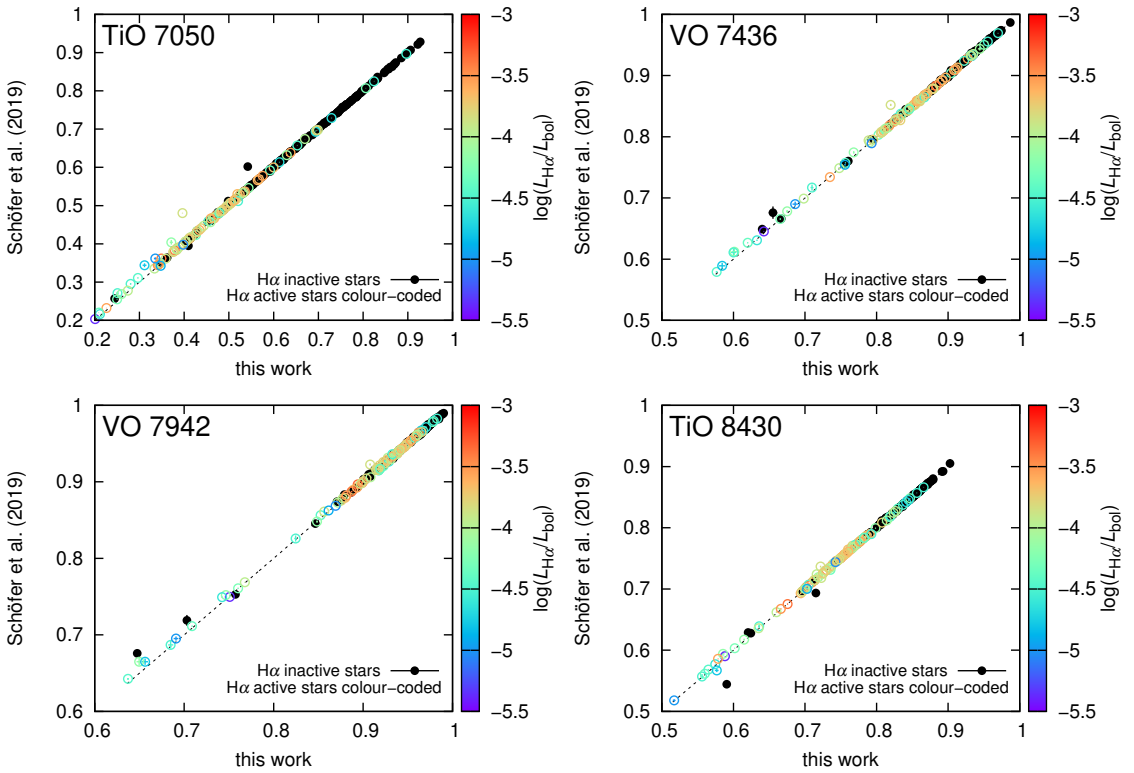

Figure 4.7.: Comparison of photospheric absorption band indices derived in this thesis and in Schöfer et al. (2019). Hα inactive stars are shown in black, Hα active stars are colour-coded by normalised Hα luminosity. Dashed black lines mark the one-to-one relation.

The relative variations generally decrease with increasing index value for all indices, outliers have large error bars. As the SNR is lower for stars with later spectral types and thus lower index values, the larger relative variations are likely caused by larger statistical fluctuations. There also appear to be larger relative variations for Hα active stars, but this is likely a selection effect, as the fraction of Hα active stars is higher at later spectral subtype and lower index values.

4.4. Discussion

For the four photospheric absorption band indices that were already presented in Schöfer et al. (2019), I compare the index values presented in this thesis with the earlier results in Fig. 4.7. The two significant outliers in TiO 7050 and VO 7436 are J10584–107 and J08536–034. While the former star also appeared as an outlier in the comparison of the chromospheric indicators, the latter star is the only M9.0 star in the sample and has a low SNR in this wavelength range. In VO 7942, two additional very late-type stars appear as outliers with J19255+096 and J04198+425, whereas in TiO 8430, J19255+096, and the two M5.0 stars J06318+414 and J10584–107 are the strongest outliers.

The CaH 2*, CaH 3*, and TiO 7050 indices measure the strengths of the same absorption band heads as the CaH 2, CaH 3, and TiO 2 indices defined by Reid et al. (1995). In Fig. 4.8, I compare my indices to the index values from low-resolution spectra reported by the Palomar/Michigan State University Survey (PMSU, Reid et al. 1995; Hawley et al. 1996) and by Alonso-Floriano et al. (2015, AF15). The CaH 2 index was only measured by the PMSU and uses the denominator range from 7042 Å to 7046 Å. This is at far longer wavelengths than the numerator range, whereas the denominator range of the CaH 2* index is close to the numerator range. Therefore, the CaH 2 index values are distinctly lower than the CaH 2* index values. Hα active stars generally have lower CaH 2 index values than Hα inactive stars with the same CaH 2* index value. The CaH 3 index uses a significantly larger numerator range than the CaH 3*, while the denominator ranges are similar. This results in similar index values. In general, the CaH 3 index values reported by PMSU are below and the CaH 3 index values reported by AF15 are above the one-to-one relation. The overlap between my sample and the PMSU and AF15 samples include mainly Hα inactive earlier-type and Hα active later-type stars, therefore, no distinct trends with increasing Hα activity can be seen. The strong outlier in the comparison with the CaH 3 index values from AF15 is the active M3.5 star J02002+130 that also appears as a strong outlier in the comparison of the TiO 7050 and TiO 2 index values. The TiO 2 index uses slightly narrower numerator and denominator ranges than the TiO 7050 index. For both PMSU and AF15, the TiO 2 index values are above the one-to-one relation with a constant offset.

In Fig. 4.9, I show again the scatter plots of TiO 7050 versus TiO 8430 and FeH WFB, but colour-coded by the effective temperatures $T_{\rm eff}$ and metallicities [Fe/H] derived by Schweitzer et al. (2019). The inactivity line polynomials defined in Sect. 4.2.2 are also shown again. As expected from theory and from the spectral-type dependence of the indices, $T_{\rm eff}$ decreases with decreasing indices until the turnaround point that is caused by the formation of dust that changes the contrast between the numerator and denominator ranges in very late M dwarfs (e.g. Tsuji et al. 1996; Allard et al. 2001). However, the metallicities show an unexpected behaviour, as the metal-rich stars appear below the inactivity line only for TiO 7050 > 0.7, whereas at lower index values, the stars below the inactivity line appear to be generally metal-poor. As most stars with large distances to the inactivity line are Hα active, and Hα active stars tend to be younger than Hα inactive stars as shown in the previous section, higher metallicities are expected. The inactivity line and the orthogonal distances from it as defined in Sect. 4.2.2 may therefore be helpful to better constrain metallicities. There is, however, room to improve the inactivity line fit. As the Hα active stars are located below the line of Hα inactive stars, it is plausible that the most inactive stars are located at the upper boundary of this line. Therefore, an upper envelope fit to this line might yield improved results. To improve the results for very late-type stars, the inactivity line would also need to follow the turnaround point. However, this is hard to fit, as the sample of very late-type stars is sparse and does not contain Hα inactive stars.

Orthogonal distances from an improved inactivity line may also help to understand the activity effects on the photospheric bands. Both PMSU and AF15 reported for their TiO 2 index a similar behaviour with activity as I described for the TiO 7050 index. Activity

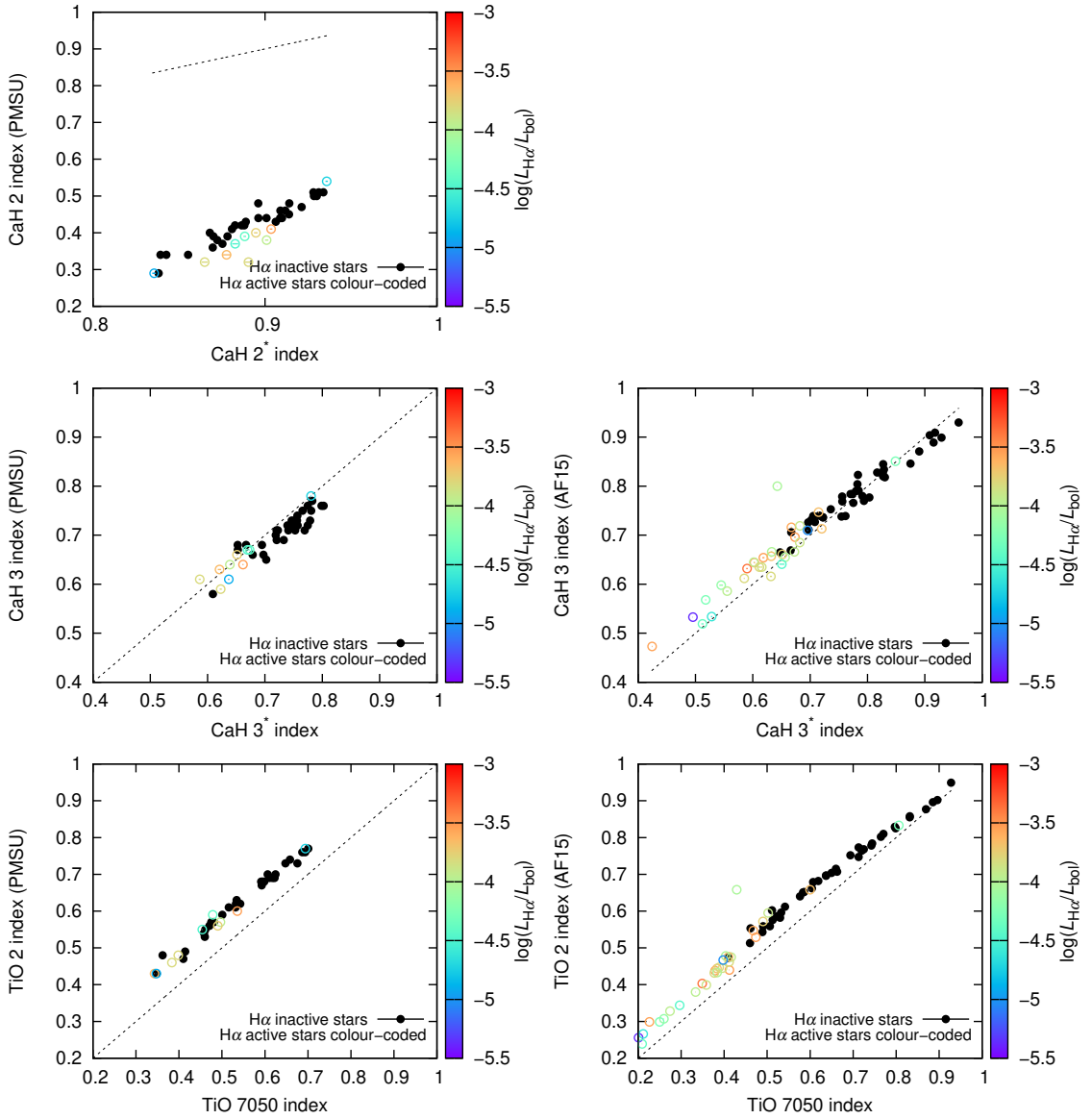

Figure 4.8.: Comparison of photospheric absorption band indices with indices from PMSU and AF15. Hα inactive stars are shown in black, Hα active stars are colour-coded by normalised Hα luminosity. Dashed black lines mark the one-to-one relation. The CaH 2* index is consistently higher than the CaH 2 index because of the different denominator range.

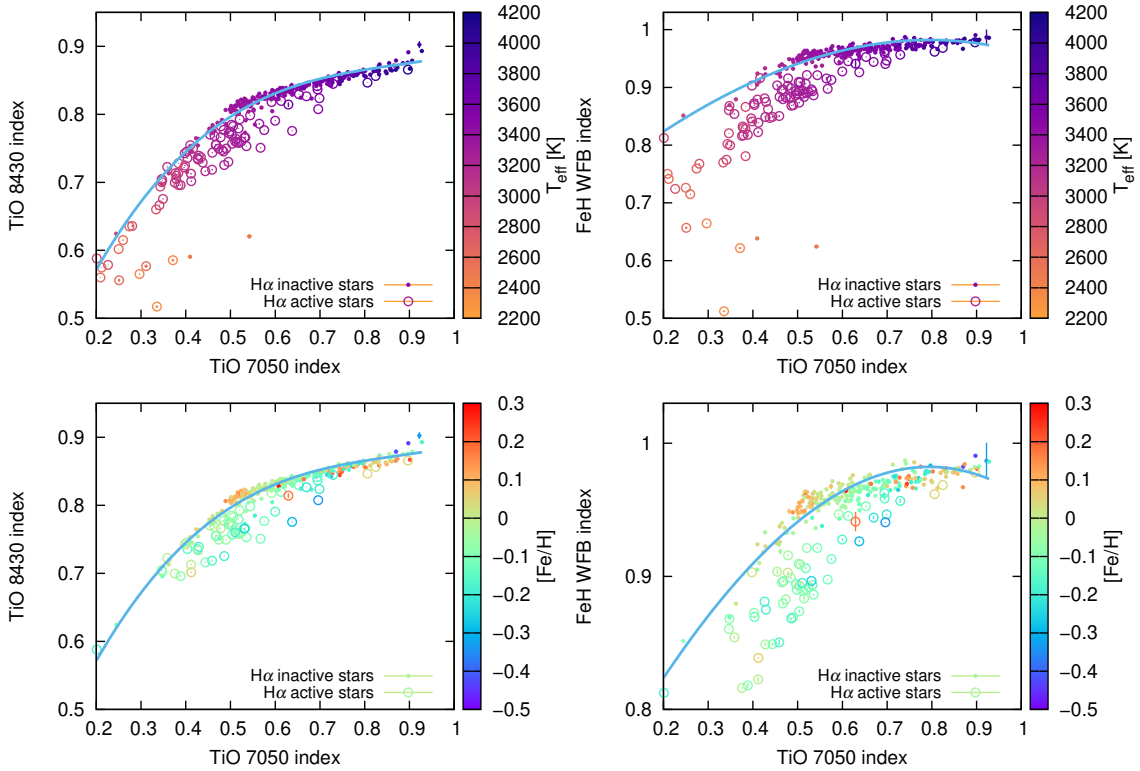

Figure 4.9.: Scatter plots of TiO 7050 versus TiO 8430 and of TiO 7050 versus FeH WFB, colour-coded by effective temperature and metallicity. Blue curves are the same polynomial fits to the reference stars with the smallest MNI variations as in Fig. 4.4

appears to affect different photospheric bands in different ways, so this did not affect the spectral types that were predominantly derived by PMSU and AF15 using a combination of multiple photospheric band indices. While the temperature dependence of TiO bands has also been used to measure starspot areas and temperatures (e.g. Neff et al. 1995; O'Neal et al. 1998), starspots should affect all photospheric bands. As shown in Schöfer et al. (2019), stellar rotation and magnetic fields may explain the observations.

The absolute or relative variations of the photospheric absorption band indices appear to be dominated by statistical fluctuations. However, the temporal variability of the indices still contains information about the stellar surface for some stars, as demonstrated in the next chapter.

5. Rotational variation of activity indicators

As described in Sect. 1.4.1, the rotation of a star can lead to periodic modulations of its light curve because over the course of one rotation, active regions appear and disappear on the hemisphere faced towards the observer. Similarly, the impact of active regions on the disc-integrated spectrum changes, leading to modulations of spectroscopic activity indicators.

This chapter further analyses the temporal variability of the activity indicators presented in Chapters 3 and 4 with a focus on periodicities. While Sect. 5.1 again extends the analysis presented in Schöfer et al. (2019) to include additional photospheric band indices and observations after July 2018, Sect. 5.2 summarises a more detailed analysis of four individual stars (Schöfer et al. submitted). I discuss the results presented in this chapter in Sect. 5.3.

5.1. Sample overview

Before searching for periodic changes in the activity indicators of each star, I excluded data points outlying by more than two standard deviations (2σ clipping). This removes poor spectra and strong flaring events that are not expected to occur periodically from the time series. In the cases of He 10833 and Paβ, measurements from spectra with telluric contamination were also excluded as described in Sect. 2.2. For each star and each indicator, I then calculated the generalised Lomb-Scargle (GLS) periodogram (Zechmeister & Kürster 2009) and identified the frequency with the highest GLS power as the *best-fit frequency*. After subtracting the best-fit frequency sine curve from each time series, I again calculated the GLS periodograms to obtain the second-best-fit frequencies and, after another iteration, the third-best-frequencies. The frequency space is restricted to frequencies between 0 and 1 d^{-1} because most stars were observed at most once per night, leading to a poor sampling of higher frequencies.

I now compare the obtained best-fit frequencies of the activity indicators with the rotation frequencies $1/P_{\mathrm{rot}}$ of the stars with a known rotation period P_{rot} as listed in Table A.1. Of these 169 stars, 21 have a rotation period shorter than 1 d and are therefore excluded from this comparison. The histogram in Fig. 5.1 shows the fraction of the 148 stars with

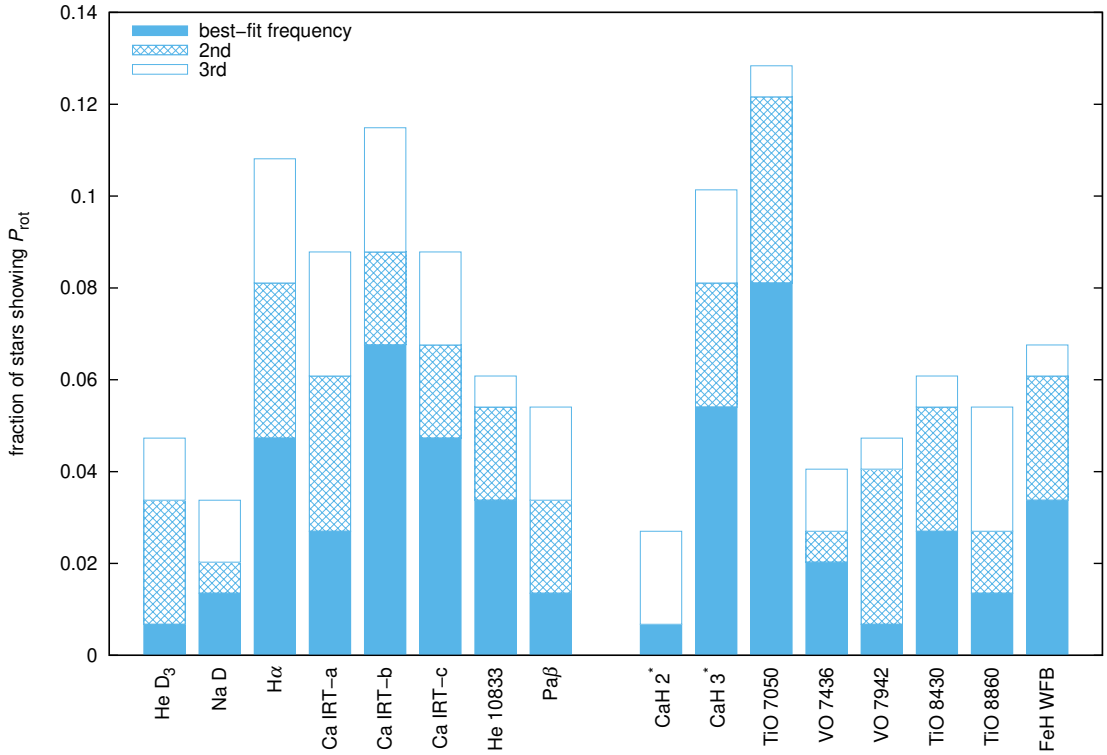

Figure 5.1.: Fraction of stars showing the rotation frequency as one of the three best-fit frequencies in each activity indicator

$P_{\rm rot} > 1$ d for that the best-fit frequencies for each indicator are within three times the error bar of the rotation frequency.

With 19 stars showing the rotation frequency as one of the three best-fit frequencies, TiO 7050 is the indicator that most commonly varies with the rotation period. Ca IRT-b, Hα, and CaH 3* are the only other indicators that show the rotation frequency as one of the three best-fit frequencies for more than 10% of the stars with $P_{\rm rot} > 1$ d. For every indicator, the rotation frequency appears among the three best-fit frequencies at least in four stars and as the single best-fit frequency in at least one star.

Overall, 69 stars show the rotation frequency as one of the three best-fit frequencies in at least one indicator. For only 18 of these stars, is this true in more than two indicators. The stricter criterion that the rotation frequency appears as the single best-fit frequency in more than two indicators is satisfied by only seven stars, of which I analyse four in detail in the next section.

Table 5.1.: Basic parameters and number of CARMENES observations of the four stars discussed in Sect. 5.2. References for the spectral types, $P_{\rm rot}$, and $v \sin i$ are given in Table A.1.

Karmn	Name	SpT	$P_{\rm rot}$ [d]	$v \sin i$ [km s^{-1}]	$\log(L_{\rm H\alpha}/L_{\rm bol})$	$N_{\rm obs}$
J01025+716	Ross 318	M3.0	51.5 ± 2.6	< 2	...	120
J07446+035	YZ CMi	M4.5	2.78 ± 0.01	4.0 ± 1.5	-3.60 ± 0.01	51
J18174+483	TYC 3529-1437-1	M2.0	15.8 ± 0.1	3.1 ± 1.0	-4.00 ± 0.01	71
J22468+443	EV Lac	M3.5	4.38 ± 0.03	5.9 ± 0.1	-3.64 ± 0.01	107

5.2. Four individual stars

For a more detailed analysis of the periodic modulations of the activity indicators, I selected four stars that not only showed the rotation frequency as the best-fit frequency in more than two indicators, but also were observed more than 40 times before January 2019. This additional requirement allows for a study of the stability of the signals seen in the GLS periodograms. The four stars and their basic parameters are listed in Table 5.1. While Ross 318 is an Hα inactive slow rotator, TYC 3529-1437-1 shows moderate Hα emission, but still rotates relatively slowly. In contrast, YZ CMi and EV Lac are very active fast rotators.

I calculated the GLS periodograms for these four stars not only of the activity indicators presented in this thesis, but also of the differential line width (dLW), the chromatic index (CRX), the radial velocity (RV), and the full-width at half-maximum (FWHM), contrast, and bisector inverse slope (BIS, Queloz et al. 2001) of the cross-correlation function (CCF) of the spectrum with a weighted binary mask. dLW and CRX were defined by Zechmeister et al. (2018) and calculated together with the RV by Dr. Mathias Zechmeister using SERVAL and a correction for an instrumental nightly zero-point RV-offset (Trifonov et al. 2018; Tal-Or et al. 2019). The CCF parameters were calculated by Marina Lafarga (Institut de Ciències de l'Espai, Barcelona, Spain) as described in Lafarga et al. (2020). All these additional indicators were calculated separately for the VIS and the NIR channel.

The GLS periodograms and the window functions for both spectrograph channels are shown in Fig. B.1 for Ross 318, Fig. B.2 for YZ CMi, Fig. B.3 for TYC 3529-1437-1, and Fig. B.4 for EV Lac. To quantify the significance of a signal at frequency f in the GLS periodogram, the probability $p(f)$ that a power higher than the GLS power at f could be caused purely by Gaussian noise can be calculated. Table 5.2 tabulates the logarithmic probabilities $p(1/P_{\rm rot})$ for the highest GLS power in the 3σ confidence interval around $1/P_{\rm rot}$ for all indicators of the four stars.

Ross 318 shows a significant signal at $1/P_{\rm rot}$ in all chromospheric indicators with the exceptions of He D_3 and Na D, in the CaH 3*, TiO 7050, VO 7436, and TiO 8860 indices, and in the additional indicators with the exceptions of the CCF contrast in both channels

Table 5.2.: log $p(1/P_{\mathrm{rot}})$ for all indicators of Ross 318, YZ CMi, TYC 3529-1437-1, and EV Lac. Logarithmic probabilities more negative than −2.87 indicate a significance higher than 3σ and are highlighted in boldface.

Indicator	Ross 318	YZ CMi	TYC 3529-1437-1	EV Lac
He D_3	−1.68	−2.28	−2.01	−1.51
Na D	−2.21	−1.10	**−3.51**	−2.68
Hα	**−7.14**	−2.29	**−5.12**	**−4.84**
Ca IRT-a	**−3.05**	−1.59	**−3.34**	**−3.29**
Ca IRT-b	**−6.52**	−1.63	**−4.54**	**−3.02**
Ca IRT-c	**−6.87**	−1.33	**−4.33**	−2.77
He 10833	**−5.91**	−1.45	−0.98	**−3.43**
Paβ	**−3.15**	−1.39	−0.75	−0.59
CaH 2*	−0.41	−1.72	−1.19	−0.88
CaH 3*	**−5.88**	**−9.04**	−1.17	**−4.94**
TiO 7050	**−11.91**	**−19.86**	−2.68	**−11.04**
VO 7436	**−3.01**	**−7.44**	−1.42	−2.47
VO 7942	−1.13	−1.50	−1.71	−1.72
TiO 8430	−1.60	**−13.35**	−1.49	**−5.10**
TiO 8860	**−5.37**	−2.66	−0.97	−0.56
FeH WFB	−1.01	**−6.55**	−1.15	−2.83
dLW VIS	**−6.11**	**−8.49**	−1.83	**−11.90**
dLW NIR	**−7.63**	−2.69	−2.24	**−9.11**
CRX VIS	**−3.38**	**−14.60**	−2.02	−2.59
CRX NIR	**−5.04**	**−11.57**	−2.06	−1.44
RV VIS	**−7.82**	**−18.72**	**−4.70**	**−4.61**
RV NIR	**−3.39**	**−14.03**	**−3.36**	−2.70
CCF FWHM VIS	**−5.38**	**−11.77**	−1.35	**−4.86**
CCF FWHM NIR	**−15.18**	**−9.18**	−2.19	**−4.16**
CCF contrast VIS	−2.57	**−12.22**	−1.77	**−7.54**
CCF contrast NIR	−1.62	**−3.77**	−1.60	**−6.36**
CCF BIS VIS	−1.46	**−19.23**	−1.11	**−3.51**
CCF BIS NIR	**−6.69**	**−6.32**	−1.62	−2.27

and CCF BIS VIS. However, in Ca IRT-a, Paβ, CaH 3*, VO 7436, TiO 8860, the dLW in both channels, and RV NIR, the periodogram peak at $1/P_{\rm rot}$ is not the highest. In contrast, YZ CMi shows a significant signal at $1/P_{\rm rot}$ in none of the chromospheric indicators, but in all other indicators with the exceptions of CaH 2*, VO 7942, TiO 8860, and dLW NIR. The signals are generally more significant than the signals seen for Ross 318, and correspond to the highest periodogram peaks in all cases but CCF contrast NIR.

In the case of TYC 3529-1437-1, only Na D, Hα, the Ca IRT lines, and the RV in both channels show a significant signal in $1/P_{\rm rot}$. While these signals are generally weaker than the signals seen for YZ CMi, they correspond to the highest periodogram peaks in all those indicators but RV VIS, where a higher peak appears at the first harmonic of the rotation frequency, $2/P_{\rm rot}$. Finally, EV Lac shows a significant signal at $1/P_{\rm rot}$ in Hα, Ca IRT-a, Ca IRT-b, He 10833, CaH 3*, TiO 7050, TiO 8430, the dLW in both channels, RV VIS, and all CCF parameters but CCF BIS NIR. While the highest periodogram peak is also located at $1/P_{\rm rot}$ in Hα, CaH 3*, TiO 7050, TiO 8430, the dLW in both channels, and CCF contrast VIS, the highest periodogram peak in RV VIS, CCF FWHM VIS, and CCF BIS VIS appears at $2/P_{\rm rot}$. The CRX in both channels and RV NIR also show a significant highest peak at $2/P_{\rm rot}$ despite not showing a significant signal at $1/P_{\rm rot}$. For the Ca IRT lines, the highest peak appears at $f = 1/P_{\rm rot} + 0.03\,{\rm d}^{-1}$. The window function suggests that this is a yearly alias of the rotation frequency.

For Hα and TiO 7050, which are the indicators showing the strongest signals among the chromospheric and photospheric indicators, respectively, and for RV VIS, which is the only indicator that shows a significant signal at $1/P_{\rm rot}$ for all four stars, I tested the stability of the signals over time. To do this, I calculated separate GLS periodograms for each possible subset of 21 consecutive data points. This is a compromise between creating a relevant amount of subsets and ensuring sufficient sampling in each subset. A graphical representation of the results are the *rolling periodograms* explained in Appendix B and shown in Fig. B.5 for Ross 318, in Fig. B.6 for YZ CMi, in Fig. B.7 for TYC 3529-1437-1, and in Fig. B.8 for EV Lac. To quantify the significance of the signals in the rolling periodograms, I calculated $\log p(1/P_{\rm rot})$ and $\log p(2/P_{\rm rot})$ for each subset. These logarithmic probabilities are shown as a function of the median Barycentric Julian Date (BJD) of the data subset in Fig. 5.2 for Ross 318, in Fig. 5.3 for YZ CMi, in Fig. 5.4 for TYC 3529-1437-1, and in Fig. 5.5 for EV Lac.

In the rolling periodograms for Ross 318, significant signals at $1/P_{\rm rot}$ are seen in RV VIS in the first half of the full time baseline, and in Hα and TiO 7050 in the second half. Barely significant signals at $2/P_{\rm rot}$ appear occasionally, but are generally weaker than signals at $1/P_{\rm rot}$ in the same data subsets of the same indicator. However, the long rotation period of 51.5 ± 2.6 d is not well sampled in most subsets, leading to weak signals in general. The rolling periodograms for YZ CMi reveal very stable signals at $1/P_{\rm rot}$ in TiO 7050 and RV VIS, and no significant signals at $1/P_{\rm rot}$ in Hα or at $2/P_{\rm rot}$ in any indicator. While the signal at the rotation frequency more significant in TiO 7050 in the first data subsets, it is more significant in RV VIS in the last data subsets. In addition, an insignificant signal at $1/P_{\rm rot}$ in Hα approaches the 3σ significance threshold in the last data subsets.

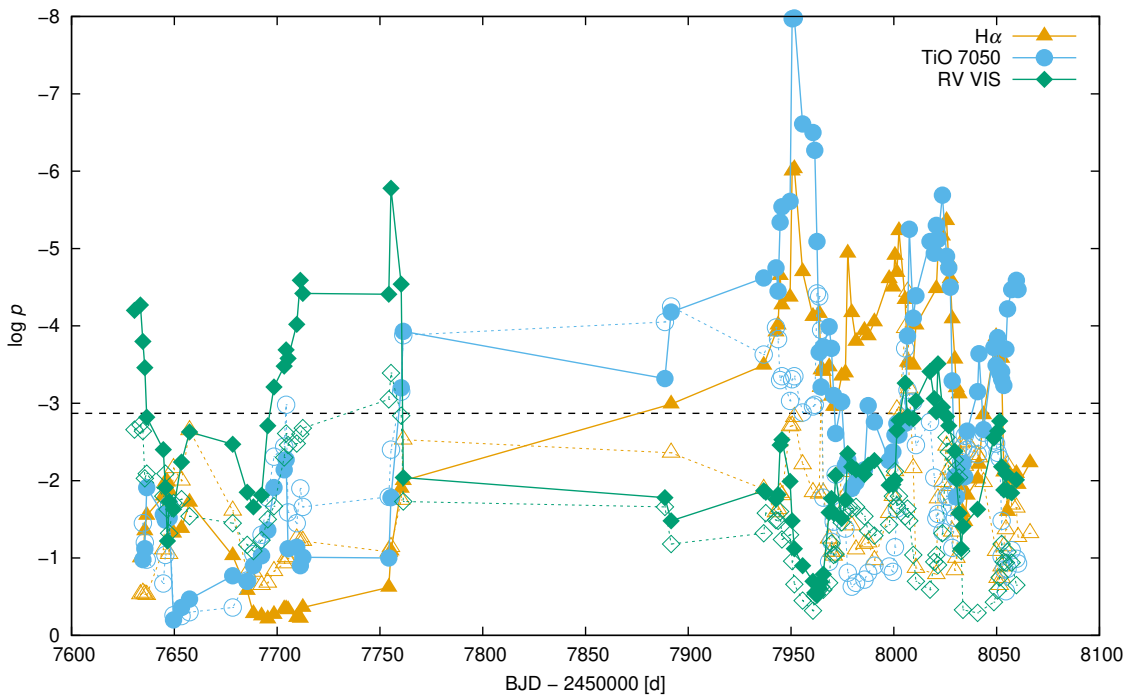

Figure 5.2.: $\log p(1/P_{\rm rot})$ (filled symbols connected with solid lines) and $\log p(2/P_{\rm rot})$ (empty symbols connected with dashed lines) from GLS periodograms of each subset of Hα (orange triangles), TiO 7050 (blue circles), and RV VIS (green diamonds) data points for Ross 318. The dashed black line marks the 3σ significance level.

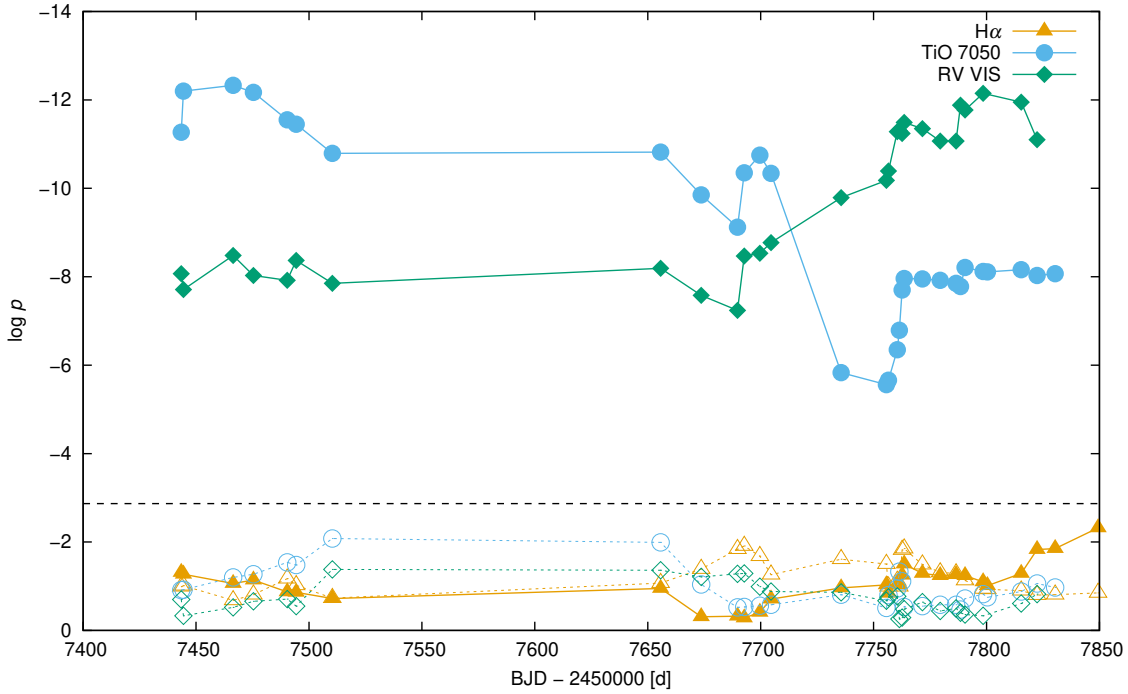

Figure 5.3.: Same as Fig. 5.2, but for YZ CMi.

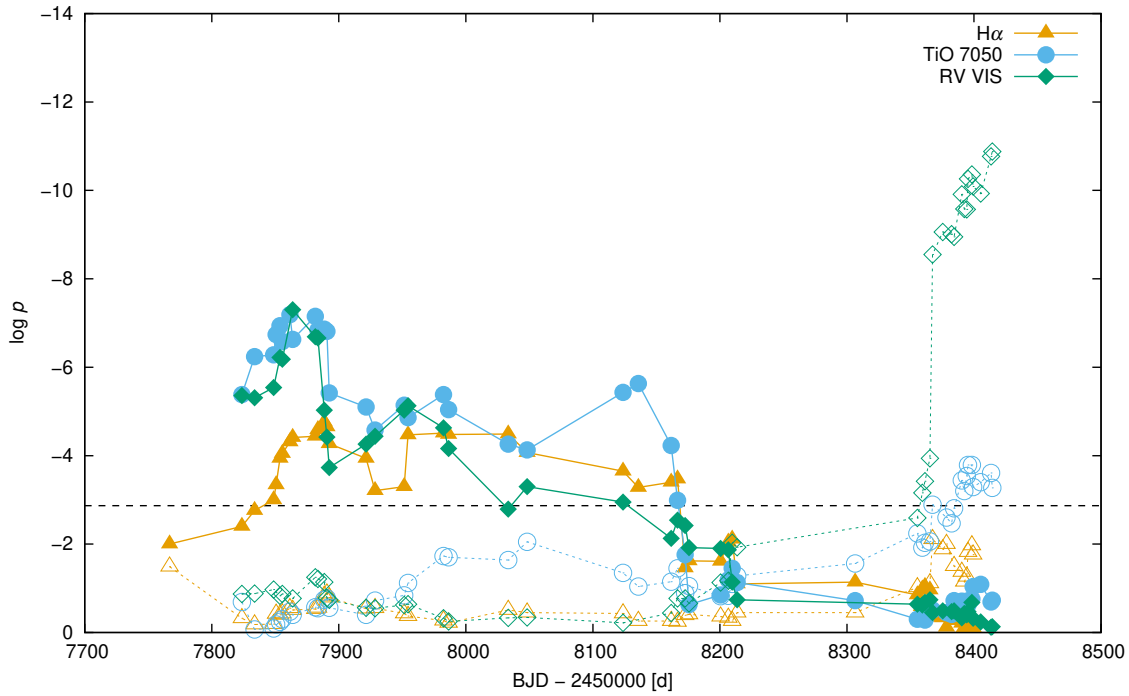

Figure 5.4.: Same as Fig. 5.2, but for TYC 3529-1437-1.

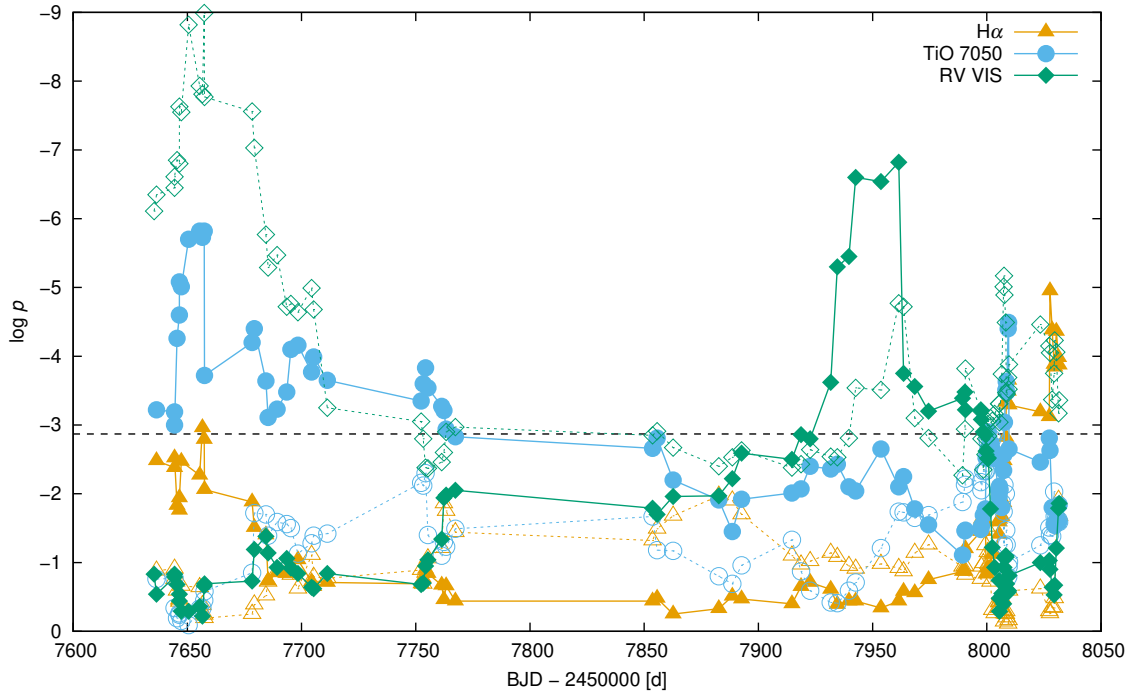

Figure 5.5.: Same as Fig. 5.2, but for EV Lac.

A more varied behaviour is seen for the other two stars. For TYC 3529-1437-1, the three indicators in general show a significant signal at $1/P_{\mathrm{rot}}$ and no signal at $2/P_{\mathrm{rot}}$ in the first part of the time baseline. However, the signals at $1/P_{\mathrm{rot}}$ disappear as the subsets include more and more data points from observations after July 2018. Instead, a very significant signal in RV VIS and a barely significant signal in TiO 7050 appear at $2/P_{\mathrm{rot}}$. While $\log p(2/P_{\mathrm{rot}})$ also increases in Hα, the signal remains insignificant. In the case of EV Lac, significant signals are seen at $2/P_{\mathrm{rot}}$ in RV VIS and at $1/P_{\mathrm{rot}}$ in TiO 7050 in the first data subsets. Over time, these signals become less significant to insignificant, whereas a significant signal in RV VIS appears at $1/P_{\mathrm{rot}}$. This signal disappears again in the last data subsets, which include data points from observations with a higher cadence than once per night. However, the signal at $2/P_{\mathrm{rot}}$ in RV VIS is significant again in these subsets, and in some of these subsets significant signals appear at $1/P_{\mathrm{rot}}$ in TiO 7050 and Hα.

5.3. Discussion

Using GLS periodograms to iteratively determine three best-fit frequencies in each indicator for each star, I found in Sect. 5.1 that TiO 7050, Hα, Ca IRT-b, and CaH 3* show the rotation frequency $1/P_{\mathrm{rot}}$ as one of the three best-fit frequencies for more than 10% of the stars with a known rotation period $P_{\mathrm{rot}} > 1$ d. In Schöfer et al. (2019), CaH 3* was not used, and TiO 8430 also showed the rotation frequency as one of the best-fit frequencies for more than 10% of the stars with $P_{\mathrm{rot}} > 1$ d. Since July 2018, not only the number of sample stars and the total number of observations increased, but also more rotation periods were added to Carmencita. While the number of stars that show the rotation period in TiO 7050 remained constant at 19, the fraction therefore decreased, as there are now 148 stars with $P_{\mathrm{rot}} > 1$ d instead of 133. For most other indicators, the fraction also decreased. Fuhrmeister et al. (2019b) searched for rotation periods of 16 early-type stars of the sample in Hα, Na D, and Ca IRT using different kinds of periodograms, and also found that Hα and Ca IRT are more likely to show the rotation period than Na D.

For 69 of 148 stars (47%) with a known rotation period $P_{\mathrm{rot}} > 1$ d the rotation frequency $1/P_{\mathrm{rot}}$ appears as one of the three best-fit frequencies in at least one indicator. This is true in more than two indicators for 18 stars (12%). In Schöfer et al. (2019), 66 of 133 stars (50%) showed the rotation period among the three best-fit frequencies in at least one indicator, and 15 (11%) in more than two indicators. While more spectra, four more photospheric absorption band indices, and more rotation periods were added, the fractions of stars showing a signal remained almost constant. Of the 15 stars that showed rotational variation in more than two indicators in July 2018, the signal was lost for 4 stars. Of the seven stars that now show the rotation period in more than two indicators, but did not fulfil this criterion in July 2018, three stars did not have a known rotation period, one star was not in Carmencita, and one star shows the rotation period in the CaH 3* index that was not considered previously. For the remaining two stars, only more spectra were added to the analysis. Three more stars would now fulfil the criteria to be included in

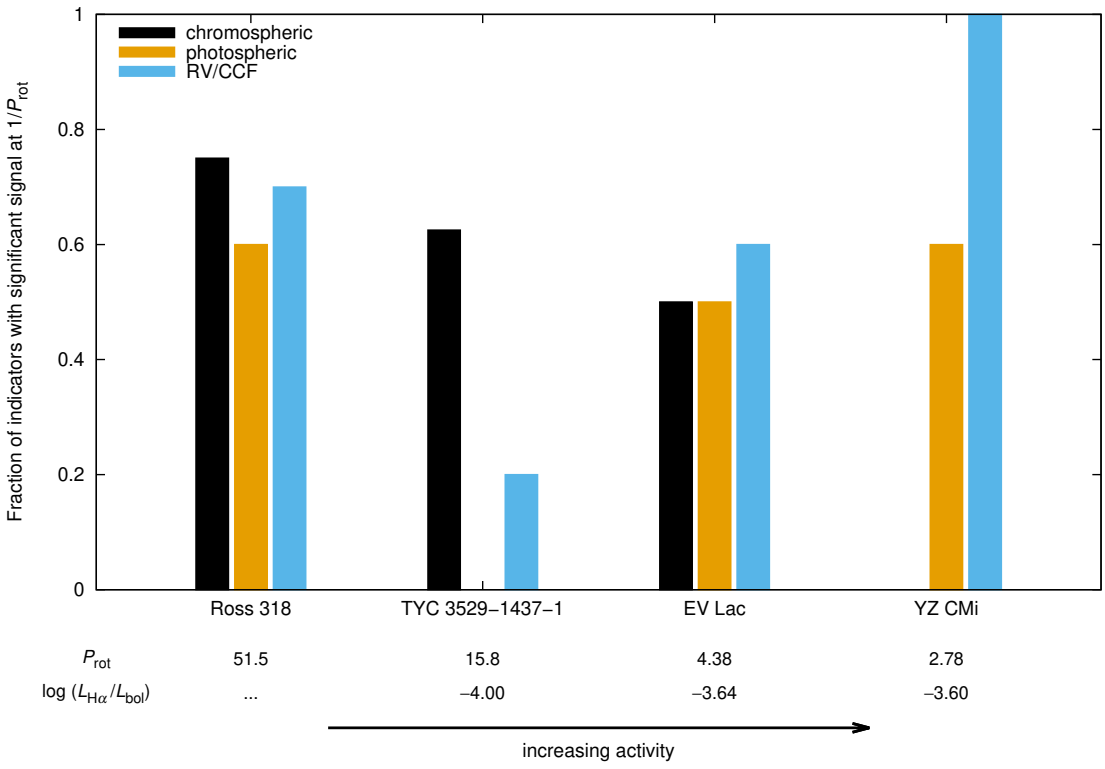

Figure 5.6.: Fractions of the eight chromospheric, the ten photospheric, and the ten RV or CCF indicators that show a significant signal at $1/P_{\rm rot}$ per star.

the more detailed analysis in Sect. 5.2: The low-active M1.0 star J07361–031 was now observed 41 times, the Hα inactive M4.0 star J10508+068 was now observed 47 times and has a known $P_{\rm rot} = (64 \pm 19)$ d from Díez Alonso et al. (2019), and the Hα active M6.5 star J10482–113 was now observed 79 times and has a known $P_{\rm rot} = (1.5 \pm 0.2)$ d from Morin et al. (2010). As the rotation periods of the latter two stars have relatively large error bars, a large part of the frequency space is covered by the 3σ-confidence interval, and the best-fit frequencies of the different indicators do not agree with each other. In the case of J07361–031, however, the best-fit frequencies for Hα (0.0822 $\rm d^{-1}$), Ca IRT-a (0.0821 $\rm d^{-1}$), and Ca IRT-c (0.0822 $\rm d^{-1}$) are all in good agreement with the rotation frequency $1/P_{\rm rot} = (0.0820 \pm 0.0007)$ $\rm d^{-1}$. No other indicator shows this frequency as one of the three best-fit frequencies.

The four stars analysed in detail in Sect. 5.2 do not have much in common. They cover diverse ranges of spectral subtypes, rotation periods, and normalised Hα luminosities. While they all show a significant signal at the rotation frequency in several indicators, the analysis revealed that there are also peculiarities in the rotation signals of each star. As a summary of the signals, I show a histogram of the fraction of the chromospheric (pEW's), photospheric (indices and dLW), and RV or CCF indicators (CRX, RV, and all CCF parameters) per star in Fig. 5.6.

RV VIS is the only indicator that shows a significant signal at $1/P_{\mathrm{rot}}$ for all four stars, whereas He D_3, CaH 2^*, and VO 7942 do not show a significant signal at $1/P_{\mathrm{rot}}$ for any of the four stars. Although Hα inactive stars show only small variations in the chromospheric indicators and long rotation periods are hard to find (Fuhrmeister et al. 2019b), Ross 318 shows the rotation period in more indicators than the other three stars. Ross 318 is also the only of the four stars that shows a stronger signal in the dLW, CRX, CCF FWHM, and CCF BIS measured in the NIR channel, although there are fewer spectroscopic features in the NIR wavelength range (Reiners et al. 2018b) and therefore larger statistical fluctuations in the NIR parameters. As Zeeman broadening is wavelength-dependent, this could hint at an asymmetric magnetic field causing the variations. TYC 3529-1437-1 shows the fewest and weakest signals of the four stars. However, this is caused by a signal at $2/P_{\mathrm{rot}}$ that is introduced by the latest data. This is similar to photometric light curves, where the limited lifetime of active regions and differential rotations lead to one dip per rotation period, and at other times two dips per rotation period, as described in Sect. 1.4.1. In the TiO 7050 index, there is a clear trend towards lower values in the part of the data set that shows the signal at $2/P_{\mathrm{rot}}$. A lower TiO 7050 could be caused by more or larger starspots. Similarly, $\mathrm{pEW}'_{\mathrm{H}\alpha}$ trends towards stronger excess emission. This also hints at a higher activity level of the star.

EV Lac has a higher normalised Hα luminosity and shows an even more complicated behaviour. In general, indicators that measure the strength of spectral lines (pEW′s, photospheric band indices, dLW, CCF contrast) show a stronger signal at $1/P_{\mathrm{rot}}$, while indicators that measure the position of spectral lines (CRX, RV) or a higher-order moment (CCF FWHM, CCF BIS) show a stronger signal at $2/P_{\mathrm{rot}}$. In RV VIS, EV Lac also shows the stronger signal at $1/P_{\mathrm{rot}}$ at some times and $2/P_{\mathrm{rot}}$ at other times. Photometric data published by Alekseev & Kozhevnikova (2017) also show single-dip episodes and double-dip episodes for EV Lac. In contrast, YZ CMi does not show double-dip episodes in these data and also shows more stable signals at $1/P_{\mathrm{rot}}$ in most of the photospheric and RV or CCF parameters. EV Lac and YZ CMi have similar normalised Hα luminosities and magnetic field strengths (Shulyak et al. 2019), but EV Lac has a more complex magnetic topology according to Morin et al. (2008). YZ CMi is the only of the four stars that does not show a significant signal in any chromospheric indicator. While strong flaring events were discarded with a 2σ clipping, there may still be non-periodic variations in the chromospheric indicators from observations during microflares or the decay of a strong flare, whereas the other indicators are less sensitive to these events (e.g. Zechmeister et al. 2009). Alternatively, the structures in the chromosphere might be distributed more homogeneously than the structures in the photosphere, leading to less rotational variation.

6. Summary and conclusion

In this thesis, I presented pEW′ measurements of eight spectral lines with a chromospheric component using a spectral subtraction technique and indices of eight photospheric absorption bands to study the activity of 337 M dwarfs in the CARMENES sample. To conclude the thesis, I now briefly summarise the results from Chapters 3, 4 and 5. For each of the topics covered by these three chapters, I also present an idea for future work.

Chromospheric activity indicators were measured after subtracting the spectrum of a reference star of the same spectral subtype. While this technique successfully removed photospheric lines from the line windows for He D_3 and Hα, the line shapes of the photospheric components of the Na D and Ca IRT lines were too different for stars of the same spectral type to be removed by the spectral subtraction. By defining stars with $\mathrm{pEW}'_{\mathrm{H}\alpha} < -0.3$ Å as Hα active and the remaining stars as Hα inactive, I obtained fractions of Hα active stars per spectral subtype that agree with the results for similar samples of nearby M dwarfs (e.g. Reiners et al. 2012; West et al. 2015; Jeffers et al. 2018). The fraction increases drastically between spectral subtypes M3.5 and M4.0, where stars become fully convective (Stassun et al. 2011). I found a very strong correlation between Hα and He D_3, whereas correlations between Hα and Na D or Hα and Ca IRT lines are disturbed by the remaining photospheric components of the latter lines and by different absolute levels of the pseudo-continuum flux. For He 10833 and Paβ, I found no correlation. I derived a relative variation of the pEW′ of each line for each star, and found that the relative He D_3 and Hα variations are anti-correlated with the normalised Hα luminosity, whereas the relative variations of Na D and the Ca IRT lines are again biased by the photospheric components, and the relative variations of He 10833 and Paβ are not useful because a division by a number close to zero is involved. Using a second set of reference stars for the spectral subtraction, I found that the results differ mostly be a constant offset that is larger for the lines with a strong photospheric component. Comparing the results with previous results for observations before July 2018 (Schöfer et al. 2019), I found that the method is stable. The results are also comparable with pEW values from Jeffers et al. (2018) that were derived with different spectrographs and methods. I also verified the relations between activity and rotation using the projected rotational velocities and the rotation periods listed in Table A.1, between activity and magnetic fields using the measurements by Shulyak et al. (2019), and between activity and age by calculating the fraction of Hα active stars per stellar population as given by Cortés-Contreras et al. (in prep.).

With the availability of spectra corrected for telluric absorption lines (Nagel et al. submitted), the previously discarded K I λ7700 Å and Na I λ8200 Å doublets (Robertson

et al. 2016) could now be reconsidered. While most telluric lines were already removed from the co-added template spectra, now also useful measurements from individual observations would be available. However, these doublets have a photospheric component similar to Na D and the Ca IRT, so the challenges in measuring those lines would also appear for these doublets.

For the photospheric absorption band indices, I found that they are all strongly correlated with each other. The scatter plots of different indices usually show different behaviours of Hα inactive and Hα active stars. While activity effects on photospheric bands were already described by Hawley et al. (1996) and Alonso-Floriano et al. (2015), their origin is not clear. To quantify these effects, I defined an inactivity line in the scatter plots and calculated the orthogonal distance of each star from this line. Colour-coding the scatter plots by metallicities from Schweitzer et al. (2019) revealed that the lowest metallicities are reported for very active stars. However, it is not plausible that the active stars are systematically metal-poor. The inactivity line and the orthogonal distances from it may help to better constrain the metallicity. Further, I found that the relative variations of the indices appear to be dominated by statistical fluctuations. Comparing again the results with previous results from Schöfer et al. (2019), I found no stability issue of the index measurement. The results are also comparable with similar indices from low-resolution spectroscopy.

The concept of the inactivity line can not only be improved with a better fit of this line. It would also be possible to calculate the indices for artificially broadened spectra of inactive stars. This way, isovelocity lines for a given rotational velocities could be derived. It might then be possible to disentangle the potential effects on the indices from rotational broadening and magnetic fields that were suggested by Schöfer et al. (2019).

Finally, the search for periodic variations of both the chromospheric and the photospheric indicators with the rotation period yielded a similar result as for the subset of observations before July 2018 that was analysed in Schöfer et al. (2019). While 18 of 148 stars with a known rotation period $P_{\rm rot} > 1$ d show this period among the three best-fit frequencies for each indicator in more than two indicators. A periodic modulation with the rotation period is most commonly seen in TiO 7050, Ca IRT-b, Hα, and CaH 3*. Although the four stars Ross 318, YZ CMi, TYC 3529-1437-1, and EV Lac all show significant signals in several indicators, a detailed analysis revealed that each star has its peculiarities, as their very different parameters suggest. Ross 318 shows stronger signals in some parameters derived from the NIR channel than in their VIS counterparts, although the information content in the VIS channel is higher. YZ CMi is a very active star and does not show any significant signal in the chromospheric indicators, but a very stable signal in photospheric indicators. TYC 3529-1437-1 transitioned from showing signals at $1/P_{\rm rot}$ to showing signals at $2/P_{\rm rot}$. EV Lac shows signals at $1/P_{\rm rot}$ in some indicators, but at $2/P_{\rm rot}$ in other indicators.

In the case of TYC 3529-1437-1, the new signals at $2/P_{\rm rot}$ led to a decreasing significance of the signals at $1/P_{\rm rot}$ in the periodograms of the full dataset. If other stars behave similarly, it is therefore possible that this remains unnoticed when only periodograms of

full datasets are considered. Another approach is to compute rolling periodograms for all stars. However, this produces an enormous amount of data and it is likely that many times a signal at the rotation frequency or its harmonics appears by chance. 61 stars show a significant signal at least once at either $1/P_{\mathrm{rot}}$ or $2/P_{\mathrm{rot}}$ in any of the three indicators Hα, TiO 7050, and RV VIS. With sophisticated criteria, it might be possible to automatically detect stars that show a behaviour similar to TYC 3529-1437-1.

A. Table of stars

In the following Table A.1, I list the 337 stars of the CARMENES sample analysed in this thesis, their basic parameters used to calculate the results, the $\mathrm{pEW}'_{\mathrm{H}\alpha}$ values derived from the co-added template spectra, and the normalised Hα luminosities. The following reference codes are used for the spectral types, projected rotational velocities, and rotation periods:

AF15: Alonso-Floriano et al. (2015); Benn17: Benneke et al. (2017); Bro10: Browning et al. (2010); DA19: Díez Alonso et al. (2019); Davi16: David et al. (2016); Del98: Delfosse et al. (1998); Fou18: Fouqué et al. (2018); Gig10: Gigoyan et al. (2010); Gra03: Gray et al. (2003); Gra06: Gray et al. (2006); HM15: Houdebine & Mullan (2015); HMR14: Martínez-Rodríguez (2014); Jeff18: Jeffers et al. (2018); Jen09: Jenkins et al. (2009); Kir91: Kirkpatrick et al. (1991); Kira12: Kiraga (2012); KS07: Kiraga & Stepien (2007); Lep03: Lépine et al. (2003); Lep13: Lépine et al. (2013); Mes11: Messina et al. (2011); Mor08: Morin et al. (2008); Mor10: Morin et al. (2010); New14: Newton et al. (2014); New16: Newton et al. (2016); PMSU: Palomar/Michigan State University Survey (Reid et al. 1995; Hawley et al. 1996); Rein18: Reiners et al. (2018b); Ria06: Riaz et al. (2006); Sch05: Scholz et al. (2005); Schm07: Schmidt et al. (2007); Shk09: Shkolnik et al. (2009); SM15: Suárez Mascareño et al. (2015); SM17: Suárez Mascareño et al. (2017); SM18: Suárez Mascareño et al. (2018); Tor06: Torres et al. (2006); Wat06: Watson et al. (2006); West15: West et al. (2015).

Table A.1.: Identifications, common names, Gliese numbers, spectral types, projected rotational velocities, rotation periods, $pEW'_{H\alpha}$ values, and normalised Hα luminosities of the analysed stars. Reference codes for SpT, $v \sin i$, and P_{rot} are defined in Appendix A.

No.	Karmn	Name	Gl/GJ	SpT	Ref.	$v \sin i$ [km s^{-1}]	Ref.	P_{rot} [d]	Ref.	$pEW'_{H\alpha}$ [Å]	$\log(L_{H\alpha}/L_{bol})$
1	J00051+457	GJ 2	2	M1.0 V	PMSU	< 2	Rein18	15.37 ± 0.09	DA19	−0.077 ± 0.007	…
2	J00067–075	GJ 1002	1002	M5.5 V	PMSU	< 2	Rein18	…	…	0	…
3	J00162+198E	LP 404-062	1006B	M4.0 V	AF15	< 2	Rein18	105 ± 44	DA19	0.053 ± 0.011	…
4	J00183+440	GX And	15A	M1.0 V	AF15	< 2	Rein18	45.0 ± 4.4	SM18	−0.074 ± 0.008	…
5	J00184+440	GQ And	15B	M3.5 V	PMSU	< 2	Rein18	…	…	−0.033 ± 0.012	…
6	J00286–066	GJ 1012	1012	M4.0 V	PMSU	< 2	Rein18	…	…	0.117 ± 0.012	…
7	J00389+306	Wolf 1056	26	M2.5 V	AF15	< 2	Rein18	50.2 ± 1.3	DA19	0.010 ± 0.006	…
8	J00570+450	G 172-030	…	M3.0 V	Lep13	< 2	Rein18	…	…	−0.057 ± 0.008	…
9	J01013+613	GJ 47	47	M2.0 V	PMSU	< 2	Rein18	34.7 ± 0.1	SM18	−0.079 ± 0.009	…
10	J01019+541	G 218-020	3069	M5.0 V	PMSU	30.6 ± 3.1	Rein18	0.2779 ± 0.0006	DA19	−5.13 ± 0.05	−3.81 ± 0.01
11	J01025+716	Ross 318	48	M3.0 V	PMSU	< 2	Rein18	51.5 ± 2.6	DA19	0.072 ± 0.015	…
12	J01026+623	BD+61 195	49	M1.5 V	AF15	< 2	Rein18	19.9 ± 0.4	DA19	−0.051 ± 0.013	…
13	J01033+623	V388 Cas	51	M5.0 V	AF15	10.5 ± 1.5	Rein18	1.02 ± 0.01	DA19	−9.77 ± 0.04	−3.53 ± 0.01
14	J01048–181	GJ 1028	1028	M5.0 V	PMSU	< 2	Rein18	…	…	0.048 ± 0.011	…
15	J01125–169	YZ Cet	54.1	M4.5 V	PMSU	3.4 ± 0.8	Fou18	69.2 ± 2.4	DA19	−1.35 ± 0.04	−4.34 ± 0.02
16	J01339–176	LP 768-113	…	M4.0 V	Sch05	< 2	Rein18	27.1 ± 0.4	DA19	−1.640 ± 0.028	−4.17 ± 0.01
17	J01352–072	Barta 161 12	…	M4.0 V	Ria06	59.8 ± 6.9	Rein18	0.7031	Kira12	−7.81 ± 0.06	−3.49 ± 0.01
18	J01433+043	GJ 70	70	M2.0 V	PMSU	< 2	Rein18	…	…	−0.088 ± 0.005	…
19	J01518+644	G 244-037	3117A	M2.5 V	PMSU	< 2	Rein18	…	…	0.002 ± 0.009	…
20	J02002+130	TZ Ari	83.1	M3.5 V:	AF15	< 2	Rein18	…	…	−2.048 ± 0.026	−4.04 ± 0.01
21	J02015+637	G 244-047	3126	M3.0 V	PMSU	< 2	Rein18	…	…	0.056 ± 0.009	…
22	J02070+496	G 173-037	…	M3.5 V	Lep13	< 2	Rein18	7.20 ± 0.13	DA19	−0.505 ± 0.023	−4.64 ± 0.02
23	J02088+494	G 173-039	3136	M3.5 V	PMSU	24.1 ± 2.4	Rein18	0.74759 ± 0.00019	DA19	−6.41 ± 0.05	−3.54 ± 0.01
24	J02123+035	BD+02 348	87	M1.5 V	PMSU	< 2	Rein18	…	…	0.062 ± 0.011	…
25	J02222+478	BD+47 612	96	M0.5 V	PMSU	< 2	Rein18	29.5 ± 0.4	DA19	0.050 ± 0.004	…
26	J02336+249	GJ 102	102	M4.0 V	PMSU	3.0 ± 1.5	Rein18	…	…	−2.557 ± 0.012	−3.98 ± 0.01
27	J02358+202	BD+19 381	104	M2.0 V	PMSU	< 2	Rein18	31.9 ± 0.6	DA19	0.061 ± 0.010	…
28	J02362+068	BX Cet	105B	M4.0 V	AF15	< 2	Rein18	…	…	0.073 ± 0.010	…
29	J02442+255	VX Ari	109	M3.0 V	PMSU	< 2	Rein18	38.7 ± 3.7	DA19	0.015 ± 0.005	…
30	J02519+224	RBS 365	…	M4.0 V	Ria06	27.2 ± 2.7	Rein18	0.85757 ± 0.00003	DA19	−5.943 ± 0.022	−3.61 ± 0.01
31	J02530+168	Teegarden's Star	…	M7.0 V	AF15	< 2	Rein18	…	…	−0.49 ± 0.04	−5.37 ± 0.03
32	J02565+554W	Ross 364	119A	M1.0 V	PMSU	< 2	Rein18	51.2 ± 4.4	SM18	0.110 ± 0.013	…
33	J03133+047	CD Cet	1057	M5.0 V	PMSU	< 2	Rein18	126.2	New16	0	…
34	J03181+382	HD 275122	134	M1.5 V	PMSU	< 2	Rein18	77.2 ± 3.0	DA19	0.169 ± 0.017	…
35	J03213+799	GJ 133	133	M2.0 V	PMSU	< 2	Rein18	32.4 ± 1.0	DA19	−0.040 ± 0.013	…
36	J03217–066	G 077-046	3218	M2.0 V	PMSU	< 2	Rein18	21.1 ± 0.1	DA19	−0.320 ± 0.015	−4.73 ± 0.02
37	J03463+262	HD 23453	154	M0.0 V	PMSU	3.3 ± 4.0	Rein18	…	…	−0.113 ± 0.010	…

Table A.1.: Identifications, basic parameters, $pEW'_{H\alpha}$ values, and normalised Hα luminosities of the analysed stars (cont.)

No.	Karmn	Name	Gl/GJ	SpT	Ref.	$v \sin i$ [km s^{-1}]	Ref.	P_{rot} [d]	Ref.	$pEW'_{H\alpha}$ [Å]	$\log(L_{H\alpha}/L_{bol})$
38	J03473–019	G 080-021	…	M3.0 V	AF15	5.2 ± 1.5	Rein18	3.87 ± 0.01	DA19	−3.950 ± 0.015	−3.67 ± 0.01
39	J03531+625	Ross 567	…	M3.0 V	Lep13	< 2	Rein18	…	…	0.062 ± 0.008	…
40	J04153–076	o^{02} Eri C	166C	M4.5 V	AF15	2.1 ± 1.5	Rein18	…	…	−3.429 ± 0.026	−3.94 ± 0.01
41	J04173+088	LTT 11392	3270	M4.5 V	PMSU	190.3	Jeff18	0.1849	West15	…	…
42	J04198+425	LSR J0419+4233	…	M8.5 V	Lep03	3.6 ± 2.3	Rein18	…	…	−12.94 ± 0.22	−4.16 ± 0.01
43	J04219+213	LP 415-17	…	M0.0 V	…	…	…	…	…	0.10 ± 0.05	…
44	J04225+105	LSPM J0422+1031	…	M3.5 V	Lep13	< 2	Rein18	5.48 ± 0.01	DA19	0.069 ± 0.016	…
45	J04290+219	BD+21 652	169	M0.5 V	Gra06	3.9 ± 1.5	Rein18	25.4 ± 0.3	DA19	0.190 ± 0.023	…
46	J04311+589	STN 2051A	169.1A	M4.0 V+	PMSU	< 1.9	Del98	…	…	−0.014 ± 0.012	…
47	J04376–110	BD-11 916	173	M1.5 V	PMSU	< 2	Rein18	…	…	0.064 ± 0.013	…
48	J04376+528	BD+52 857	172	M0.0 V	Gra03	3.4 ± 1.5	Rein18	…	…	−0.020 ± 0.013	…
49	J04429+189	HD 285968	176	M2.0 V	PMSU	< 2	Rein18	40.7 ± 0.4	DA19	0.001 ± 0.009	…
50	J04429+214	2M J04425586+2128230	…	M3.5 V	Lep13	< 2	Rein18	47.8 ± 1.1	DA19	−0.043 ± 0.015	…
51	J04472+206	RX J0447.2+2038	…	M5.0 V	AF15	47.6 ± 26.8	Rein18	0.3426 ± 0.0003	DA19	−9.84 ± 0.05	−3.53 ± 0.01
52	J04520+064	Wolf 1539	179	M3.5 V	PMSU	< 2	Rein18	…	…	−0.049 ± 0.014	…
53	J04538–177	GJ 180	180	M2.0 V	PMSU	< 2	Rein18	…	…	0.027 ± 0.010	…
54	J04588+498	BD+49 1280	181	M0.0 V	PMSU	< 2	Rein18	…	…	−0.074 ± 0.007	…
55	J05019–069	LP 656-038	3323	M4.0 V	PMSU	3.8 ± 1.3	Fou18	88.5	Kira12	−0.67 ± 0.04	−4.56 ± 0.03
56	J05019+011	1RXS J050156.7+010845	…	M4.0 V	AF15	6.5 ± 1.5	Rein18	2.12 ± 0.02	DA19	−6.379 ± 0.019	−3.58 ± 0.01
57	J05033–173	LP 776-046	3325	M3.0 V	PMSU	< 2	Rein18	…	…	0.019 ± 0.006	…
58	J05062+046	RX J0506.2+0439	…	M4.0 V	AF15	24.9 ± 2.5	Rein18	0.8650 ± 0.0006	DA19	−7.22 ± 0.04	−3.53 ± 0.01
59	J05084–210	2M J05082729-2101444	…	M5.0 V	Ria06	25.2 ± 2.5	Rein18	…	…	−15.77 ± 0.08	−3.33 ± 0.01
60	J05127+196	GJ 192	192	M2.0 V	PMSU	< 2	Rein18	…	…	0.038 ± 0.012	…
61	J05280+096	Ross 41	203	M3.5 V	PMSU	< 2	Rein18	17.2 ± 0.1	DA19	−0.038 ± 0.009	…
62	J05314–036	HD 36395	205	M1.5 V	AF15	< 2	Rein18	33.8 ± 0.6	DA19	0.101 ± 0.019	…
63	J05337+019	V371 Ori	207.1	M2.5 V	PMSU	9.8 ± 1.5	Rein18	2.81 ± 0.25	HM15	−5.03 ± 0.04	−3.55 ± 0.01
64	J05348+138	Ross 46	3356	M3.5 V	PMSU	< 2	Rein18	…	…	0.016 ± 0.014	…
65	J05360–076	Wolf 1457	3357	M4.0 V	PMSU	< 2	Rein18	…	…	0.061 ± 0.013	…
66	J05365+113	V2689 Ori	208	M0.0 V	Lep13	3.8 ± 1.5	Rein18	12.3 ± 0.1	DA19	−0.447 ± 0.012	−4.53 ± 0.02
67	J05366+112	2M J05363846+1117487	…	M4.0 V	Lep13	2.4 ± 1.5	Rein18	…	…	−2.878 ± 0.021	−3.92 ± 0.01
68	J05394+406	LSR J0539+4038	…	M8.0 V	Lep03	4.1 ± 1.5	Rein18	…	…	−4.81 ± 0.12	−4.50 ± 0.02
69	J05415+534	HD 233153	212	M1.0 V	AF15	< 2	Rein18	…	…	−0.056 ± 0.010	…
70	J05421+124	V1352 Ori	213	M4.0 V	AF15	< 2	Rein18	…	…	0.069 ± 0.010	…
71	J06000+027	G 099-049	3379	M4.0 V	PMSU	4.9 ± 1.5	Rein18	1.81 ± 0.01	DA19	−2.710 ± 0.018	−3.95 ± 0.01
72	J06011+595	G 192-013	3378	M3.5 V	PMSU	< 2	Rein18	…	…	−0.033 ± 0.009	…
73	J06024+498	G 192-015	3380	M5.0 V	AF15	< 2	Rein18	105 ± 6	DA19	0.025 ± 0.014	…
74	J06103+821	GJ 226	226	M2.0 V	PMSU	< 2	Rein18	44.6 ± 1.0	DA19	0	…
75	J06105–218	HD 42581 A	229A	M0.5 V	PMSU	< 2	Rein18	27.3 ± 0.2	DA19	0.000 ± 0.009	…
76	J06246+234	Ross 64	232	M4.0 V	AF15	< 2	Rein18	…	…	0.041 ± 0.014	…
77	J06318+414	LP 205-044	3396	M5.0 V	PMSU	58.4 ± 26.1	Rein18	0.29952 ± 0.00007	DA19	…	…

Table A.1.: Identifications, basic parameters, $pEW'_{H\alpha}$ values, and normalised Hα luminosities of the analysed stars (cont.)

No.	Karmn	Name	Gl/GJ	SpT	Ref.	$v \sin i$ [km s^{-1}]	Ref.	P_{rot} [d]	Ref.	$pEW'_{H\alpha}$ [Å]	$\log(L_{H\alpha}/L_{bol})$
78	J06371+175	HD 260655	239	M0.0 V	Lep13	< 2	Rein18	…	…	−0.061 ± 0.021	…
79	J06396–210	LP 780-032	…	M4.0 V	Sch05	< 2	Rein18	…	…	−0.134 ± 0.020	…
80	J06421+035	G 108-021	3404A	M3.5 V	PMSU	< 2	Rein18	83.4 ± 7	DA19	0.039 ± 0.013	…
81	J06548+332	Wolf 294	251	M3.0 V	AF15	< 2	Rein18	18.1 ± 0.3	DA19	0.018 ± 0.009	…
82	J06574+740	2M J06572616+7405265	…	M4.0 V	Lep13	27.1 ± 2.7	Rein18	…	…	−5.49 ± 0.05	−3.64 ± 0.01
83	J06594+193	GJ 1093	1093	M5.0 V	PMSU	< 2	Rein18	…	…	−0.279 ± 0.024	…
84	J07001–190	2M J07000682-1901235	…	M5.0 V	AF15	3.8 ± 1.5	Rein18	…	…	−7.05 ± 0.03	−3.68 ± 0.01
85	J07033+346	LP 255-011	3423	M4.0 V	PMSU	< 2	Rein18	8.04 ± 0.03	DA19	−3.005 ± 0.028	−3.91 ± 0.01
86	J07044+682	GJ 258	258	M3.0 V	PMSU	< 2	Rein18	…	…	0.084 ± 0.009	…
87	J07274+052	Luyten's Star	273	M3.5 V	AF15	< 2	Rein18	93.5 ± 16	SM17	−0.042 ± 0.015	…
88	J07287–032	GJ 1097	1097	M3.0 V	PMSU	< 2	Rein18	…	…	0.040 ± 0.008	…
89	J07319+362N	BL Lyn	277C	M3.5 V	AF15	< 2	Rein18	16.4 ± 0.3	DA19	−2.727 ± 0.018	−3.91 ± 0.01
90	J07353+548	GJ 3452	3452	M2.0 V	PMSU	< 2	Rein18	21.8 ± 1.0	DA19	−0.034 ± 0.009	…
91	J07361–031	BD-02 2198	282C	M1.0 V	AF15	3.1 ± 1.5	Rein18	12.2 ± 0.1	DA19	−0.867 ± 0.014	−4.28 ± 0.01
92	J07386–212	LP 763-001	3459	M3.0 V	PMSU	< 2	Rein18	…	…	0.033 ± 0.009	…
93	J07393+021	BD+02 1729	281	M0.0 V	PMSU	< 2	Rein18	…	…	0.005 ± 0.007	…
94	J07403–174	LP 783-002	283B	M6.0 V	PMSU	< 2	Rein18	…	…	0	…
95	J07446+035	YZ CMi	285	M4.5 V	PMSU	4.0 ± 1.5	Rein18	2.78 ± 0.01	DA19	−7.386 ± 0.023	−3.60 ± 0.01
96	J07472+503	2M J07471385+5020386	…	M4.0 V	Lep13	10.1 ± 1.5	Rein18	1.32 ± 0.01	DA19	−3.812 ± 0.024	−3.80 ± 0.01
97	J07558+833	GJ 1101	1101	M4.5 V:	AF15	12.1 ± 1.5	Rein18	1.11 ± 0.01	DA19	−5.257 ± 0.029	−3.75 ± 0.01
98	J07582+413	GJ 1105	1105	M3.5 V	PMSU	< 2	Rein18	…	…	−0.029 ± 0.011	…
99	J08023+033	G 050-016 A	3473	M4.0 V	PMSU	…	…	…	…	0.137 ± 0.014	…
100	J08119+087	Ross 619	299	M4.5 V	PMSU	3.0 ± 1.7	Del98	5.42 ± 0.15	DA19	−0.02 ± 0.04	…
101	J08126–215	GJ 300	300	M4.0 V	PMSU	< 2	Rein18	…	…	0.021 ± 0.016	…
102	J08161+013	GJ 2066	2066	M2.0 V	AF15	< 2	Rein18	40.7 ± 0.4	DA19	0.010 ± 0.007	…
103	J08293+039	2M J08292191+0355092	…	M2.5 V	Lep13	< 2	Rein18	…	…	0.040 ± 0.011	…
104	J08298+267	DX Cnc	1111	M6.5 V	AF15	10.5 ± 1.5	Rein18	0.45900 ± 0.00001	DA19	−5.15 ± 0.07	−4.27 ± 0.01
105	J08315+730	LP 035-219	…	M4.0 V	Lep13	< 2	Rein18	105 ± 11	DA19	0.074 ± 0.011	…
106	J08358+680	G 234-037	3506	M2.5 V	PMSU	< 2	Rein18	…	…	−0.207 ± 0.009	…
107	J08402+314	LSPM J0840+3127	…	M3.5 V	Lep13	< 2	Rein18	118 ± 14	DA19	0.021 ± 0.010	…
108	J08409–234	LP 844-008	317	M3.5 V	Lep13	< 2.5	Bro10	…	…	0.012 ± 0.013	…
109	J08413+594	LP 090-018	3512	M5.5 V	PMSU	< 2	Rein18	…	…	−1.370 ± 0.012	−4.44 ± 0.01
110	J08526+283	rho Cnc B	324B	M4.5 V	AF15	< 2	Rein18	…	…	0.047 ± 0.011	…
111	J08536–034	LP 666-009	3517	M9.0 V	Jen09	9.3 ± 2.8	Rein18	…	…	…	…
112	J09003+218	LP 368-128	…	M6.5 V	AF15	14.3 ± 1.5	Rein18	0.439	New16	−6.88 ± 0.06	−4.15 ± 0.01
113	J09005+465	GJ 1119	1119	M4.5 V	PMSU	< 2	Rein18	8	West15	−0.970 ± 0.013	−4.49 ± 0.01
114	J09028+680	LP 060-179	3526	M4.0 V	PMSU	< 2	Rein18	…	…	0.079 ± 0.011	…
115	J09033+056	NLTT 20861	…	M7.0 V	New14	9.7 ± 1.5	Rein18	…	…	−3.70 ± 0.09	−4.49 ± 0.01
116	J09133+688	G 234-057	…	M2.5 V	Lep13	< 2	Rein18	10.4 ± 0.1	SM18	−0.565 ± 0.017	−4.50 ± 0.02
117	J09140+196	LP 427-016	…	M3.0 V	Lep13	< 2	Rein18	89.9 ± 2	DA19	−0.148 ± 0.010	…

Table A.1.: Identifications, basic parameters, $pEW'_{H\alpha}$ values, and normalised Hα luminosities of the analysed stars (cont.)

No.	Karmn	Name	Gl/GJ	SpT	Ref.	$v \sin i$ [km s^{-1}]	Ref.	P_{rot} [d]	Ref.	$pEW'_{H\alpha}$ [Å]	$\log(L_{H\alpha}/L_{bol})$
118	J09143+526	HD 79210	338A	M0.0 V	AF15	2.9 ± 1.2	Del98	…	…	−0.027 ± 0.012	…
119	J09144+526	HD 79211	338B	M0.0 V	AF15	2.3 ± 1.5	Rein18	…	…	−0.027 ± 0.01	…
120	J09161+018	RX J0916.1+0153	…	M4.0 V	Lep13	10.4 ± 1.5	Rein18	…	…	−5.066 ± 0.029	−3.68 ± 0.01
121	J09163–186	LP 787-052	3543	M1.5 V	PMSU	< 2	Rein18	…	…	−0.378 ± 0.012	−4.65 ± 0.02
122	J09307+003	GJ 1125	1125	M3.5 V	PMSU	< 2	Rein18	…	…	−0.004 ± 0.012	…
123	J09360–216	GJ 357	357	M2.5 V	PMSU	2.5 ± 1.1	Fou18	74.3 ± 1.7	SM15	−0.027 ± 0.012	…
124	J09411+132	Ross 85	361	M1.5 V	PMSU	< 2	Rein18	…	…	0.005 ± 0.011	…
125	J09423+559	GJ 363	363	M3.5 V	PMSU	< 2	Rein18	74.3 ± 2.8	DA19	−0.029 ± 0.015	…
126	J09425+700	GJ 360	360	M2.0 V	PMSU	< 2	Rein18	21 ± 0.4	DA19	−0.598 ± 0.009	−4.45 ± 0.01
127	J09428+700	GJ 362	362	M3.0 V	PMSU	< 2	Rein18	23.9 ± 0.6	DA19	−0.775 ± 0.013	−4.38 ± 0.01
128	J09439+269	Ross 93	3564	M3.5 V	PMSU	< 2	Rein18	13.7 ± 0.9	DA19	0.069 ± 0.016	…
129	J09447–182	GJ 1129	1129	M4.0 V	PMSU	< 2	Rein18	…	…	0.088 ± 0.012	…
130	J09449–123	G 161-071	…	M5.0 V	AF15	31.2 ± 3.1	Rein18	…	…	−14.08 ± 0.08	−3.38 ± 0.01
131	J09468+760	BD+76 3952	366	M1.5 V	PMSU	< 2	Rein18	…	…	0.116 ± 0.014	…
132	J09511–123	BD-11 2741	369	M0.5 V	PMSU	< 2	Rein18	…	…	−0.022 ± 0.013	…
133	J09561+627	BD+63 869	373	M0.0 V	PMSU	< 2	Rein18	…	…	−0.078 ± 0.006	…
134	J10023+480	BD+48 1829	378	M1.0 V	PMSU	< 2	Rein18	…	…	0.081 ± 0.013	…
135	J10122–037	AN Sex	382	M1.5 V	PMSU	< 2	Rein18	21.6 ± 0.2	DA19	−0.030 ± 0.012	…
136	J10125+570	LP 092-048	…	M3.5 V	Lep13	< 2	Rein18	…	…	−0.004 ± 0.015	…
137	J10167–119	GJ 386	386	M3.0 V	PMSU	< 2	Rein18	…	…	0.086 ± 0.011	…
138	J10196+198	AD Leo	388	M3.0 V+	AF15	4.35 ± 0.03	HMR14	2.2399 ± 0.0006	Mor08	−4.53 ± 0.04	−3.61 ± 0.01
139	J10251–102	BD-09 3070	390	M1.0 V	PMSU	< 2	Rein18	…	…	−0.102 ± 0.011	…
140	J10289+008	BD+01 2447	393	M2.0 V	PMSU	< 2	Rein18	…	…	−0.008 ± 0.008	…
141	J10350–094	LP 670-017	…	M3.0 V	Sch05	< 2	Rein18	…	…	0.037 ± 0.008	…
142	J10360+051	RY Sex	398	M3.5 V	PMSU	2.9 ± 1.6	Rein18	…	…	−5.081 ± 0.029	−3.64 ± 0.01
143	J10396–069	GJ 399	399	M2.5 V	PMSU	< 2	Rein18	…	…	0.002 ± 0.010	…
144	J10416+376	GJ 1134	1134	M4.5 V	PMSU	< 2	Rein18	54.3 ± 4.4	DA19	0.074 ± 0.015	…
145	J10482–113	LP 731-058	3622	M6.5 V	AF15	2.1 ± 1.5	Rein18	1.5 ± 0.2	Mor10	−2.45 ± 0.05	−4.60 ± 0.01
146	J10504+331	G 119-037	3626	M4.0 V	PMSU	< 2	Rein18	…	…	0.112 ± 0.014	…
147	J10508+068	EE Leo	402	M4.0 V	AF15	< 2	Rein18	64 ± 19	DA19	0.065 ± 0.011	…
148	J10564+070	CN Leo	406	M6.0 V	AF15	2.9 ± 0.8	Fou18	2.704 ± 0.003	DA19	−7.62 ± 0.07	−3.96 ± 0.01
149	J10584–107	LP 731-076	…	M5.0 V	AF15	3.2 ± 1.5	Rein18	…	…	−4.69 ± 0.04	−3.85 ± 0.01
150	J11000+228	Ross 104	408	M2.5 V	PMSU	< 2	Rein18	…	…	−0.032 ± 0.006	…
151	J11026+219	DS Leo	410	M1.0 V	Lep13	2.6 ± 1.5	Rein18	14.6 ± 0.2	DA19	−0.489 ± 0.014	−4.53 ± 0.02
152	J11033+359	Lalande 21185	411	M1.5 V	AF15	< 2	Rein18	48	KS07	−0.035 ± 0.011	…
153	J11054+435	BD+44 2051A	412A	M1.0 V	AF15	< 2	Rein18	100.9 ± 0.3	SM18	−0.094 ± 0.009	…
154	J11055+435	WX UMa	412B	M5.5 V	AF15	8.2 ± 2.7	Rein18	0.78 ± 0.02	Mor10	−10.51 ± 0.16	−3.56 ± 0.01
155	J11110+304W	HD 97101 B	414B	M2.0 V	Lep13	< 2	Rein18	…	…	0.056 ± 0.015	…
156	J11126+189	StKM 1-928	3649	M1.5 V	PMSU	< 2	Rein18	…	…	0.088 ± 0.012	…
157	J11201–104	LP 733-099	…	M2.0 V	Ria06	3.6 ± 1.5	Rein18	…	…	−1.937 ± 0.016	−3.94 ± 0.01

Table A.1.: Identifications, basic parameters, $pEW'_{H\alpha}$ values, and normalised Hα luminosities of the analysed stars (cont.)

No.	Karmn	Name	Gl/GJ	SpT	Ref.	$v \sin i$ [km s^{-1}]	Ref.	P_{rot} [d]	Ref.	$pEW'_{H\alpha}$ [Å]	$\log(L_{H\alpha}/L_{bol})$
158	J11289+101	Wolf 398	3666	M3.5 V	PMSU	< 2	Rein18	…	…	0.016 ± 0.013	…
159	J11302+076	K2-18	…	M2.5 V	Benn17	< 2	Rein18	36.4 ± 0.3	DA19	0.026 ± 0.011	…
160	J11306–080	LP 672-042	…	M3.5 V	AF15	< 2	Rein18	…	…	0.011 ± 0.014	…
161	J11417+427	Ross 1003	1148	M4.0 V	PMSU	< 2	Rein18	71.5 ± 5.1	DA19	0.11 ± 0.01	…
162	J11421+267	Ross 905	436	M2.5 V	AF15	< 2	Rein18	44.6 ± 2	DA19	−0.018 ± 0.011	…
163	J11467–140	GJ 443	443	M3.0 V	PMSU	< 2	Rein18	…	…	0.086 ± 0.010	…
164	J11474+667	1RXS J114728.8+664405	…	M5.0 V	AF15	2.7 ± 1.5	Rein18	…	…	−6.86 ± 0.05	−3.69 ± 0.01
165	J11476+002	LP 613-049 A	3685A	M4.0 V	PMSU	2.4 ± 1.5	Rein18	11.6 ± 0.04	DA19	−5.072 ± 0.029	−3.68 ± 0.01
166	J11476+786	GJ 445	445	M3.5 V	PMSU	< 2	Rein18	…	…	0.003 ± 0.009	…
167	J11477+008	FI Vir	447	M4.0 V	PMSU	2.1 ± 1.0	Fou18	163 ± 3	DA19	0	…
168	J11509+483	GJ 1151	1151	M4.5 V	PMSU	2.5 ± 1.0	Fou18	125 ± 23	DA19	−0.102 ± 0.024	…
169	J11511+352	BD+36 2219	450	M1.5 V	AF15	< 2	Rein18	22.8 ± 1	DA19	−0.074 ± 0.010	…
170	J12054+695	Ross 689	3704	M4.0 V	PMSU	< 2	Rein18	100 ± 10	DA19	0.018 ± 0.011	…
171	J12100–150	LP 734-032	3707	M3.5 V	PMSU	< 2	Rein18	…	…	−0.026 ± 0.019	…
172	J12111–199	LTT 4562	3708A	M3.0 V	PMSU	< 2	Rein18	…	…	0.024 ± 0.006	…
173	J12123+544S	HD 238090	458A	M0.0 V	PMSU	< 2	Rein18	…	…	0.03 ± 0.01	…
174	J12156+526	StKM 2-809	…	M4.0 V	Lep13	35.3 ± 3.5	Rein18	…	…	−5.56 ± 0.07	−3.64 ± 0.01
175	J12189+111	GL Vir	1156	M5.0 V	PMSU	15.5 ± 1.6	Rein18	0.49102 ± 0.00003	DA19	−5.82 ± 0.05	−3.76 ± 0.01
176	J12230+640	Ross 690	463	M3.0 V	PMSU	< 2	Rein18	32.9 ± 1.1	DA19	0.133 ± 0.026	…
177	J12248–182	Ross 695	465	M2.0 V	PMSU	< 2	Rein18	…	…	−0.010 ± 0.013	…
178	J12312+086	BD+09 2636	471	M0.5 V	Lep13	< 2	Rein18	…	…	0.014 ± 0.008	…
179	J12350+098	GJ 476	476	M2.5 V	PMSU	< 2	Rein18	36.6 ± 1.3	DA19	0.099 ± 0.012	…
180	J12373–208	LP 795-038	…	M4.0 V	Sch05	< 2	Rein18	…	…	0.089 ± 0.013	…
181	J12388+116	Wolf 433	480	M3.0 V	PMSU	< 2	Rein18	…	…	0.006 ± 0.020	…
182	J12428+418	G 123-055	…	M4.0 V	Lep13	< 2	Rein18	16.2 ± 0.1	DA19	−2.416 ± 0.023	−4.00 ± 0.01
183	J12479+097	Wolf 437	486	M3.5 V	PMSU	< 2	Rein18	…	…	−0.006 ± 0.014	…
184	J13005+056	FN Vir	493.1	M4.5 V	PMSU	16.4 ± 1.6	Rein18	0.60022 ± 0.00004	DA19	−5.13 ± 0.03	−3.76 ± 0.01
185	J13102+477	G 177-025	…	M5.0 V	AF15	4.5 ± 0.9	Fou18	28.8 ± 0.8	DA19	−3.17 ± 0.06	−4.02 ± 0.01
186	J13196+333	Ross 1007	507.1	M1.5 V	PMSU	< 2	Rein18	48 ± 4.8	SM18	0.141 ± 0.016	…
187	J13209+342	BD+35 2439	508.2	M1.0 V	PMSU	< 2	Rein18	…	…	−0.006 ± 0.011	…
188	J13229+244	Ross 1020	3779	M4.0 V	PMSU	< 2	Rein18	…	…	0.061 ± 0.012	…
189	J13283–023W	Ross 486A	512A	M3.0 V	PMSU	< 2	Rein18	…	…	0.059 ± 0.012	…
190	J13293+114	GJ 513	513	M3.5 V	PMSU	< 2	Rein18	…	…	0.052 ± 0.016	…
191	J13299+102	BD+11 2576	514	M0.5 V	PMSU	2.0 ± 0.8	Fou18	30 ± 0.9	SM17	−0.010 ± 0.014	…
192	J13427+332	Ross1015	3801	M3.5 V	Lep13	< 2	Rein18	…	…	−0.022 ± 0.01	…
193	J13450+176	BD+18 2776	525	M0.0 V	Lep13	2.3 ± 1.5	Rein18	…	…	−0.044 ± 0.024	…
194	J13457+148	HD 119850	526	M1.5 V	PMSU	< 2	Rein18	52.3 ± 1.7	SM15	0.135 ± 0.009	…
195	J13458–179	LP 798-034	3804	M3.5 V	PMSU	< 2	Rein18	…	…	0.010 ± 0.013	…
196	J13536+776	RX J1353.6+7737	…	M4.0 V	Lep13	8.9 ± 1.5	Rein18	1.23 ± 0.01	DA19	−4.012 ± 0.027	−3.78 ± 0.01
197	J13582+125	Ross 837	3817	M3.0 V	PMSU	< 2	Rein18	…	…	−0.036 ± 0.010	…

Table A.1.: Identifications, basic parameters, $pEW'_{H\alpha}$ values, and normalised Hα luminosities of the analysed stars (cont.)

No.	Karmn	Name	Gl/GJ	SpT	Ref.	$v \sin i$ [km s^{-1}]	Ref.	P_{rot} [d]	Ref.	$pEW'_{H\alpha}$ [Å]	$\log(L_{H\alpha}/L_{bol})$
198	J13591–198	LP 799-007	3820	M4.0 V	PMSU	3.2 ± 1.5	Rein18	…	…	−2.981 ± 0.013	−3.91 ± 0.01
199	J14010–026	HD 122303	536	M1.0 V	PMSU	< 2	Rein18	43.9 ± 0.8	SM17	0.006 ± 0.01	…
200	J14082+805	BD+81 465	540	M1.0 V	PMSU	< 2	Rein18	…	…	0.040 ± 0.013	…
201	J14152+450	Ross 992	3836	M3.0 V	PMSU	< 2	Rein18	52.8 ± 1.4	DA19	0.056 ± 0.016	…
202	J14173+454	RX J1417.3+4525	…	M5.0 V	Gig10	15.9 ± 1.6	Rein18	…	…	−3.86 ± 0.05	−3.94 ± 0.01
203	J14251+518	tet Boo B	549B	M2.5 V	AF15	< 2	Rein18	…	…	−0.011 ± 0.008	…
204	J14257+236E	BD+24 2733B	548B	M0.5 V	PMSU	< 2	Rein18	17.6 ± 0.5	DA19	0.017 ± 0.008	…
205	J14257+236W	BD+24 2733A	548A	M0.0 V	PMSU	< 2	Rein18	111 ± 12	DA19	0	…
206	J14294+155	Ross 130	552	M2.0 V	PMSU	< 2	Rein18	43.5 ± 1.5	SM18	0.044 ± 0.010	…
207	J14307–086	BD-07 3856	553	M0.5 V	Gra03	2.4 ± 1.5	Rein18	…	…	0.176 ± 0.014	…
208	J14310–122	Wolf 1478	553.1	M3.5 V	PMSU	< 2	Rein18	…	…	−0.008 ± 0.014	…
209	J14321+081	LP 560-035	…	M6.0 V	New14	6.3 ± 1.5	Rein18	…	…	−4.76 ± 0.06	−4.16 ± 0.01
210	J14342–125	HN Lib	555	M4.0 V	PMSU	< 2	Rein18	…	…	0.031 ± 0.011	…
211	J14524+123	G 066-037	3871	M2.0 V	PMSU	< 2	Rein18	…	…	−0.051 ± 0.009	…
212	J14544+355	Ross 1041	3873	M3.5 V	PMSU	< 2	Rein18	…	…	−0.013 ± 0.016	…
213	J15013+055	G 015-002	3885	M3.0 V	PMSU	< 2	Rein18	…	…	−0.055 ± 0.009	…
214	J15095+031	Ross 1047	3892	M3.0 V	PMSU	< 2	Rein18	…	…	0.051 ± 0.010	…
215	J15194–077	HO Lib	581	M3.0 V	PMSU	< 2	Rein18	132.5 ± 6.3	SM15	0	…
216	J15218+209	OT Ser	9520	M1.5 V	PMSU	4.3 ± 1.5	Rein18	3.37 ± 0.01	DA19	−2.905 ± 0.018	−3.76 ± 0.01
217	J15305+094	NLTT 40406	…	M5.5 V	AF15	16.3 ± 1.6	Rein18	0.3048 ± 0.0006	DA19	−4.14 ± 0.05	−3.96 ± 0.01
218	J15369–141	Ross 802	592	M4.0 V	PMSU	< 2	Rein18	…	…	0.086 ± 0.013	…
219	J15474–108	LP 743-031	3916	M2.0 V	PMSU	< 3	Jeff18	…	…	−0.038 ± 0.019	…
220	J15499+796	LP 022-420	…	M5.0 V	AF15	26.9 ± 2.7	Rein18	…	…	−5.16 ± 0.05	−3.81 ± 0.01
221	J15598–082	BD-07 4156	606	M1.0 V	PMSU	< 2	Rein18	20 ± 2	SM18	−0.125 ± 0.009	…
222	J16028+205	GJ 609	609	M4.0 V	PMSU	< 2	Rein18	…	…	0.041 ± 0.010	…
223	J16092+093	G 137-084	…	M3.0 V	Lep13	< 2	Rein18	…	…	−0.051 ± 0.009	…
224	J16102–193	K2-33	…	M3.0 V	Davi16	7.3 ± 1.5	Rein18	6.263 ± 0.150	DA19	−1.48 ± 0.04	−4.10 ± 0.02
225	J16167+672N	EW Dra	617B	M3.0 V	PMSU	< 2	Rein18	…	…	0.062 ± 0.010	…
226	J16167+672S	HD 147379	617A	M0.0 V	AF15	2.7 ± 1.5	Rein18	…	…	0.052 ± 0.012	…
227	J16254+543	GJ 625	625	M1.5 V	AF15	2.2 ± 0.7	Fou18	76.79 ± 0.13	DA19	0	…
228	J16303–126	V2306 Oph	628	M3.5 V	PMSU	< 2	Rein18	119 ± 1	DA19	0.011 ± 0.012	…
229	J16313+408	G 180-060	3959	M5.0 V	PMSU	7.1 ± 1.5	Rein18	0.512 ± 0.001	DA19	−7.44 ± 0.04	−3.65 ± 0.01
230	J16327+126	GJ 1203	1203	M3.0 V	PMSU	< 2	Rein18	…	…	0.117 ± 0.014	…
231	J16462+164	LP 446-006	3972	M2.5 V	PMSU	< 2	Rein18	…	…	−0.001 ± 0.008	…
232	J16554–083N	GJ 643	643	M3.5 V	PMSU	< 2	Rein18	6.52 ± 0.01	DA19	−0.001 ± 0.010	…
233	J16555–083	vB 8	644C	M7.0 V	AF15	10.1 ± 0.8	Fou18	…	…	−4.87 ± 0.11	−4.37 ± 0.01
234	J16570–043	LP 686-027	1207	M3.5 V	PMSU	10.1 ± 1.5	Rein18	0.547 ± 0.001	DA19	−4.563 ± 0.015	−3.69 ± 0.01
235	J16581+257	BD+25 3173	649	M1.0 V	PMSU	< 2	Rein18	23.8 ± 0.1	DA19	−0.049 ± 0.006	…
236	J17033+514	G 203-042	3988	M4.5 V	PMSU	< 2	Rein18	…	…	−0.003 ± 0.013	…
237	J17052–050	Wolf 636	654	M1.5 V	AF15	< 2	Rein18	50.2 ± 1.3	DA19	0.103 ± 0.016	…

Table A.1.: Identifications, basic parameters, $pEW'_{H\alpha}$ values, and normalised Hα luminosities of the analysed stars (cont.)

No.	Karmn	Name	Gl/GJ	SpT	Ref.	$v \sin i$ [km s^{-1}]	Ref.	P_{rot} [d]	Ref.	$pEW'_{H\alpha}$ [Å]	$\log(L_{H\alpha}/L_{bol})$
238	J17071+215	Ross 863	655	M3.0 V	PMSU	< 2	Rein18	…	…	0.064 ± 0.008	…
239	J17115+384	Wolf 654	3992	M3.5 V	PMSU	< 2	Rein18	62.6 ± 2	DA19	0.082 ± 0.014	…
240	J17166+080	GJ 2128	2128	M2.0 V	PMSU	< 2	Rein18	…	…	−0.004 ± 0.007	…
241	J17198+417	GJ 671	671	M2.5 V	PMSU	< 2	Rein18	71.5 ± 2.6	DA19	0	…
242	J17303+055	BD+05 3409	678.1 A	M0.0 V	PMSU	< 2	Rein18	…	…	−0.038 ± 0.013	…
243	J17338+169	1RXS J173353.5+165515	…	M5.5 V	Lep13	41.5 ± 7.7	Rein18	0.26593 ± 0.0003	DA19	−12.17 ± 0.07	−3.49 ± 0.01
244	J17355+616	BD+61 1678C	685	M0.5 V	PMSU	< 2	Rein18	19.3 ± 0.3	DA19	−0.088 ± 0.013	…
245	J17364+683	BD+68 946 AB	687AB	M3.0 V+	AF15	< 2.5	Bro10	…	…	0.023 ± 0.026	…
246	J17378+185	BD+18 3421	686	M1.0 V	PMSU	< 2	Rein18	…	…	−0.058 ± 0.006	…
247	J17542+073	GJ 1222	1222	M4.0 V	PMSU	< 2	Rein18	…	…	0.09 ± 0.04	…
248	J17578+046	Barnard's Star	699	M3.5 V	AF15	3.1 ± 1.2	Fou18	148.6 ± 0.1	SM15	0	…
249	J17578+465	G 204-039	4040	M2.5 V	AF15	2 ± 1.1	Fou18	30.3 ± 0.9	DA19	−0.187 ± 0.024	…
250	J18022+642	LP 071-082	…	M5.0 V	AF15	11.3 ± 1.5	Rein18	0.28027 ± 0.00002	DA19	−5.17 ± 0.06	−3.81 ± 0.01
251	J18027+375	GJ 1223	1223	M5.0 V	PMSU	< 2	Rein18	123.8	New16	0.050 ± 0.014	…
252	J18051–030	HD 165222	701	M1.0 V	PMSU	< 2	Rein18	127.8 ± 3.2	SM15	0	…
253	J18075–159	GJ 1224	1224	M4.5 V	PMSU	2.2 ± 1.5	Rein18	3.866 ± 0.008	DA19	−4.65 ± 0.04	−3.81 ± 0.01
254	J18131+260	LP 390-016	4044	M4.0 V	AF15	7.5 ± 0.7	Fou18	2.28 ± 0.01	DA19	−6.021 ± 0.027	−3.60 ± 0.01
255	J18165+048	G 140-051	…	M5.0 V	New14	< 2	Rein18	…	…	0.103 ± 0.013	…
256	J18174+483	TYC 3529-1437-1	…	M2.0 V	Ria06	3.1 ± 1	Fou18	15.8 ± 0.1	DA19	−1.697 ± 0.015	−4.00 ± 0.01
257	J18180+387E	G 204-058	4048A	M3.0 V	PMSU	< 2	Rein18	…	…	0.034 ± 0.007	…
258	J18189+661	LP 071-165	4053	M4.5 V	PMSU	15.3 ± 1.5	Rein18	…	…	−2.58 ± 0.05	−4.06 ± 0.01
259	J18221+063	Ross 136	712	M4.0 V	PMSU	< 2	Rein18	…	…	0.148 ± 0.019	…
260	J18224+620	GJ 1227	1227	M4.0 V	AF15	< 2	Rein18	…	…	−0.088 ± 0.022	…
261	J18319+406	G 205-028	4062	M3.5 V	PMSU	< 2	Rein18	50.2 ± 1.3	DA19	−0.032 ± 0.017	…
262	J18346+401	LP 229-017	4063	M3.5 V	PMSU	< 2	Rein18	40.2 ± 0.8	DA19	−0.039 ± 0.016	…
263	J18353+457	BD+45 2743	720A	M0.5 V	AF15	< 2	Rein18	34 ± 2.9	DA19	0.109 ± 0.006	…
264	J18356+329	LSR J1835+3259	…	M8.5 V	Schm07	49.2 ± 4.9	Rein18	0.118 ± 0.001	DA19	−1.92 ± 0.16	−4.99 ± 0.04
265	J18363+136	Ross 149	4065	M4.0 V	PMSU	< 2	Rein18	50.2 ± 1.6	DA19	−0.735 ± 0.015	−4.52 ± 0.01
266	J18409–133	BD-13 5069	724	M1.0 V	PMSU	< 2	Rein18	…	…	0.03 ± 0.01	…
267	J18419+318	Ross 145	4070	M3.0 V	PMSU	< 2	Rein18	…	…	0.042 ± 0.007	…
268	J18427+596N	HD 173739	725A	M3.0 V	AF15	< 2.5	Bro10	…	…	0.004 ± 0.019	…
269	J18427+596S	HD 173740	725B	M3.5 V	AF15	< 2.5	Bro10	…	…	0.014 ± 0.021	…
270	J18480–145	G 155-042	4077	M2.5 V	PMSU	< 2	Rein18	…	…	−0.007 ± 0.007	…
271	J18482+076	G 141-036	…	M5.0 V	AF15	2.4 ± 1.5	Rein18	2.76 ± 0.01	DA19	−3.217 ± 0.019	−4.02 ± 0.01
272	J18498–238	V1216 Sgr	729	M3.5 V	Ria06	3 ± 1.5	Rein18	2.87 ± 0.01	DA19	−2.258 ± 0.019	−3.99 ± 0.01
273	J18580+059	BD+05 3993	740	M0.5 V	PMSU	< 2	Rein18	35.2 ± 0.3	DA19	0	…
274	J19070+208	Ross 730	745A	M2.0 V	AF15	< 2	Rein18	…	…	−0.116 ± 0.017	…
275	J19072+208	HD 349726	745B	M2.0 V	PMSU	< 2	Rein18	3.8 ± 0.01	DA19	−0.104 ± 0.016	…
276	J19084+322	G 207-019	4098	M3.0 V	PMSU	< 2	Rein18	74.1 ± 2.8	DA19	0.030 ± 0.008	…
277	J19098+176	GJ 1232	1232	M4.5 V	PMSU	< 2	Rein18	80.1 ± 3.2	DA19	0.003 ± 0.013	…

Table A.1.: Identifications, basic parameters, $pEW'_{H\alpha}$ values, and normalised Hα luminosities of the analysed stars (cont.)

No.	Karmn	Name	Gl/GJ	SpT	Ref.	$v \sin i$ [km s^{-1}]	Ref.	P_{rot} [d]	Ref.	$pEW'_{H\alpha}$ [Å]	$\log(L_{H\alpha}/L_{bol})$
278	J19169+051N	V1428 Aql	752A	M2.5 V	AF15	< 2	Rein18	46 ± 0.2	DA19	0.028 ± 0.009	…
279	J19169+051S	V1298 Aql (vB 10)	752B	M8.0 V	AF15	5.3 ± 0.9	Fou18	23.6 ± 0.3	DA19	−5.33 ± 0.09	−4.45 ± 0.01
280	J19216+208	GJ 1235	1235	M4.5 V	PMSU	< 2	Rein18	133 ± 9	DA19	0	…
281	J19251+283	Ross 164	4109	M3.0 V	PMSU	< 2	Rein18	…	…	−0.070 ± 0.019	…
282	J19255+096	LSPM J1925+0938	…	M8.0 V	New14	34.7 ± 3.5	Rein18	…	…	2.07 ± 0.08	…
283	J19346+045	BD+04 4157	763	M0.0 V	Kir91	3.9 ± 1.5	Rein18	12.9 ± 0.8	DA19	0.087 ± 0.018	…
284	J19422–207	2M J19421282-2045477	…	M5.1 V	Shk09	6.2 ± 1.5	Rein18	…	…	−5.73 ± 0.04	−3.77 ± 0.01
285	J19511+464	G 208-042	1243	M4.0 V	PMSU	22.1 ± 0.9	Fou18	0.59278 ± 0.00012	DA19	−4.49 ± 0.03	−3.73 ± 0.01
286	J20093–012	2M J20091824-0113377	…	M5.0 V	AF15	4.3 ± 1.5	Rein18	…	…	−5.108 ± 0.026	−3.82 ± 0.01
287	J20260+585	Wolf 1069	1253	M5.0 V	PMSU	< 2	Rein18	57.7 ± 0.4	DA19	0.001 ± 0.009	…
288	J20305+654	GJ 793	793	M2.5 V	PMSU	< 2	Rein18	32.8 ± 0.5	DA19	−0.241 ± 0.010	…
289	J20336+617	GJ 1254	1254	M4.0 V	PMSU	< 2	Rein18	12.6 ± 0.7	DA19	0.065 ± 0.012	…
290	J20405+154	GJ 1256	1256	M4.5 V	AF15	< 2	Rein18	106 ± 6	DA19	−0.195 ± 0.012	…
291	J20450+444	BD+44 3567	806	M1.5 V	PMSU	< 2	Rein18	19.9 ± 0.6	DA19	0.061 ± 0.010	…
292	J20451–313	AU Mic	803	M0.5 V	Ria06	9.3 ± 1.2	Tor06	4.84 ± 0.04	Mes11	−3.028 ± 0.018	−3.71 ± 0.01
293	J20525–169	LP 816-060	…	M4.0 V	Gra06	< 2	Rein18	67.6 ± 0.6	DA19	−0.012 ± 0.010	…
294	J20533+621	HD 199305	809A	M1.0 V	Lep13	< 2	Rein18	…	…	−0.010 ± 0.009	…
295	J20556–140S	GJ 810 B	810B	M5.0 V	PMSU	…	…	…	…	0.148 ± 0.017	…
296	J20567–104	Wolf 896	811.1	M2.5 V	PMSU	< 2	Rein18	9.63 ± 0.01	DA19	0.005 ± 0.011	…
297	J21019–063	Wolf 906	816	M2.5 V	AF15	< 2	Rein18	…	…	0.012 ± 0.008	…
298	J21152+257	LP 397-041	4184	M3.0 V	PMSU	< 2	Rein18	34.8 ± 0.2	DA19	0.100 ± 0.013	…
299	J21164+025	LSPM J2116+0234	…	M3.0 V	Lep13	< 2	Rein18	…	…	0.102 ± 0.005	…
300	J21221+229	TYC 2187-512-1	…	M1.0 V	Lep13	< 2	Rein18	41 ± 1.7	DA19	−0.027 ± 0.006	…
301	J21348+515	Wolf 926	4205	M3.0 V	PMSU	< 2	Rein18	54.3 ± 1.5	DA19	0.075 ± 0.013	…
302	J21463+382	LSPM J2146+3813	…	M4.0 V	Lep13	< 2	Rein18	…	…	0.095 ± 0.013	…
303	J21466–001	Wolf 940	1263A	M4.0 V	PMSU	< 2	Rein18	…	…	0.089 ± 0.010	…
304	J21466+668	G 264-012	…	M4.0 V	AF15	< 2	Rein18	…	…	0.076 ± 0.010	…
305	J22012+283	V374 Peg	4247	M4.0 V	PMSU	36.9 ± 0.7	Fou18	0.44571 ± 0.00002	DA19	−4.49 ± 0.04	−3.73 ± 0.01
306	J22020–194	LP 819-017	843	M3.5 V	PMSU	< 2	Rein18	…	…	0.064 ± 0.019	…
307	J22021+014	BD+00 4810	846	M0.5 V	AF15	< 2	Rein18	29.5 ± 0.1	DA19	0.019 ± 0.005	…
308	J22057+656	G 264-018 A	4258	M1.5 V	PMSU	< 2	Rein18	…	…	0.111 ± 0.011	…
309	J22096–046	BD-05 5715	849	M3.5 V	PMSU	< 2	Rein18	39.2 ± 6.3	SM15	0.143 ± 0.019	…
310	J22114+409	1RXS J221124.3+410000	…	M5.5 V	AF15	< 2	Rein18	30 ± 1.3	DA19	−4.94 ± 0.04	−3.89 ± 0.01
311	J22115+184	Ross 271	851	M2.0 V	PMSU	< 2	Rein18	36.3 ± 0.2	DA19	0.056 ± 0.010	…
312	J22125+085	Wolf 1014	9773	M3.0 V	PMSU	< 2	Rein18	…	…	0.034 ± 0.006	…
313	J22137–176	LP 819-052	1265	M4.5 V	PMSU	< 2	Rein18	…	…	0.042 ± 0.017	…
314	J22231–176	LP 820-012	4274	M4.5 V	PMSU	< 2	Rein18	…	…	−3.977 ± 0.022	−3.87 ± 0.01
315	J22252+594	G 232-070	4276	M4.0 V	PMSU	< 2	Rein18	64.6 ± 2.1	DA19	0.077 ± 0.010	…
316	J22298+414	G 215-050	1270	M4.0 V	PMSU	< 2	Rein18	99.8 ± 1.2	DA19	0.076 ± 0.010	…
317	J22330+093	BD+08 4887	863	M1.0 V	PMSU	< 2	Rein18	…	…	−0.014 ± 0.005	…

Table A.1.: Identifications, basic parameters, $pEW'_{H\alpha}$ values, and normalised Hα luminosities of the analysed stars (cont.)

No.	Karmn	Name	Gl/GJ	SpT	Ref.	$v \sin i$ [km s^{-1}]	Ref.	P_{rot} [d]	Ref.	$pEW'_{H\alpha}$ [Å]	$\log(L_{H\alpha}/L_{bol})$
318	J22468+443	EV Lac	873	M3.5 V	PMSU	5.9 ± 0.1	Fou18	4.38 ± 0.03	DA19	−5.098 ± 0.029	−3.64 ± 0.01
319	J22503–070	BD-07 5871	875	M0.5 V	Gra03	< 2	Rein18	…	…	0.003 ± 0.010	…
320	J22518+317	GT Peg	875.1	M3.0 V	PMSU	13.2 ± 0.9	Fou18	1.63 ± 0.01	DA19	−5.186 ± 0.021	−3.55 ± 0.01
321	J22532–142	IL Aqr	876	M4.0 V	PMSU	< 2	Rein18	81 ± 0.8	DA19	0.054 ± 0.011	…
322	J22559+178	StKM 1-2065	4306	M1.0 V	PMSU	< 2	Rein18	27 ± 2.5	SM18	−0.032 ± 0.009	…
323	J22565+165	HD 216899	880	M1.5 V	PMSU	< 2	Rein18	39.5 ± 0.2	DA19	0.065 ± 0.014	…
324	J23064–050	2MUCD 12171 (Trappist-1)	…	M8.0 V	Schm07	< 2	Rein18	3.304 ± 0.011	DA19	−2.49 ± 0.14	−4.79 ± 0.03
325	J23113+085	NLTT 56083	…	M3.5 V	Lep13	< 2	Rein18	…	…	0.013 ± 0.013	…
326	J23216+172	LP 462-027	4333	M4.0 V	PMSU	< 2	Rein18	74.7 ± 0.7	DA19	0.026 ± 0.011	…
327	J23245+578	BD+57 2735	895	M1.0 V	PMSU	< 2	Rein18	…	…	−0.022 ± 0.011	…
328	J23340+001	GJ 899	899	M2.5 V	PMSU	< 2	Rein18	…	…	0.068 ± 0.009	…
329	J23351–023	GJ 1286	1286	M5.5 V	PMSU	< 2	Rein18	…	…	−0.472 ± 0.009	−4.91 ± 0.01
330	J23381–162	G 273-093	4352	M2.0 V	PMSU	2.1 ± 1.2	Fou18	61.66	Wat06	0.017 ± 0.011	…
331	J23419+441	HH And	905	M5.0 V	AF15	< 2	Rein18	106 ± 6	DA19	−0.313 ± 0.014	−5.03 ± 0.02
332	J23431+365	GJ 1289	1289	M4.0 V	PMSU	< 2	Rein18	83.6 ± 7	DA19	−0.943 ± 0.009	−4.41 ± 0.01
333	J23492+024	BR Psc	908	M1.0 V	PMSU	< 2	Rein18	49.9 ± 3.5	SM18	−0.031 ± 0.014	…
334	J23505–095	LP 763-012	4367	M4.0 V	PMSU	< 2	Rein18	…	…	−0.040 ± 0.009	…
335	J23548+385	RX J2354.8+3831	…	M4.0 V	Lep13	3.6 ± 1.5	Rein18	4.70 ± 0.04	DA19	−3.35 ± 0.05	−3.86 ± 0.01
336	J23556–061	GJ 912	912	M2.5 V	PMSU	< 2	Rein18	…	…	0.025 ± 0.010	…
337	J23585+076	Wolf 1051	4383	M3.0 V	PMSU	< 2	Rein18	…	…	0.048 ± 0.009	…

B. Periodograms

The periodograms of the four stars analysed in Sect. 5.2 are collected in this appendix.

In Fig. B.5 for Ross 318, Fig. B.6 for YZ CMi, Fig. B.7 for TYC 3529-1437-1, and Fig. B.8 for EV Lac, rolling GLS periodograms of $pEW'_{H\alpha}$ (left), TiO 7050 index (centre), and RV VIS (right) are shown. Each colour-coded stripe is a GLS periodogram of a subset of 21 consecutive data points. Its position on the y-axis corresponds to the median barycentric Julian date (BJD) of the subset. Subsets that span more than 180 d are shown in lighter colour shades.

On top of each rolling periodogram, the GLS periodogram calculated from the full data set is shown for comparison. On the right side of each rolling periodogram, the individual data points are shown. The dashed line marks the average value, while the dotted lines enclose the 2σ interval around the average. Data points outside of the 2σ interval are not used for calculating the periodograms and are shown in grey. Data points outside the date range are shown at the beginning of the date range and marked with an arrow.

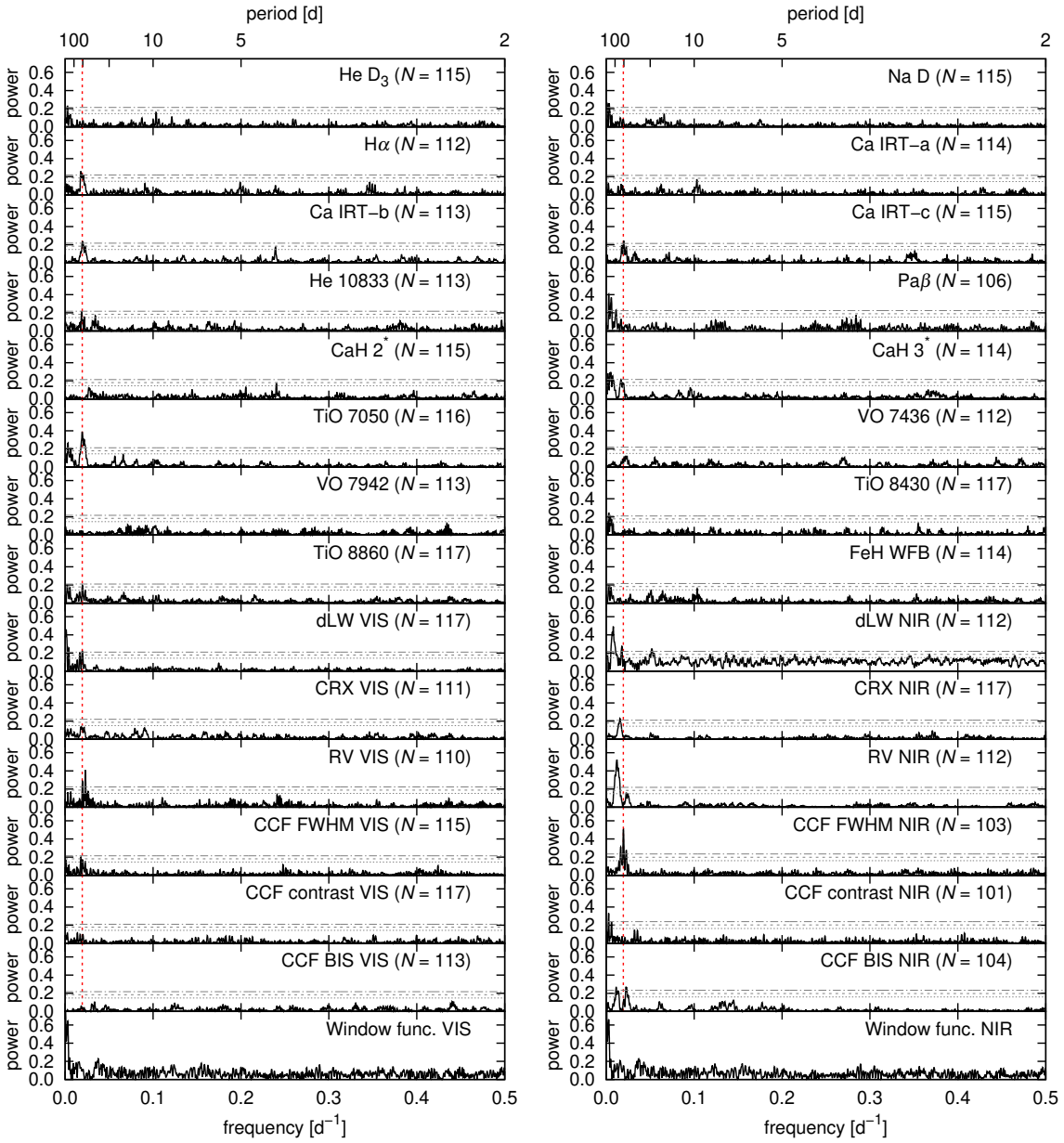

Figure B.1.: GLS periodograms of indicators and window functions for Ross 318. Horizontal lines indicate the analytical 10% (dotted), 1% (dashed), and 0.1% (dash-dotted) false alarm probability levels. N is the number of used data points after a 2σ clipping for each indicator. The red dotted line marks the rotation frequency $f_{\rm rot} = 0.0194\,{\rm d}^{-1}$ ($P_{\rm rot} = 51.5\,{\rm d}$).

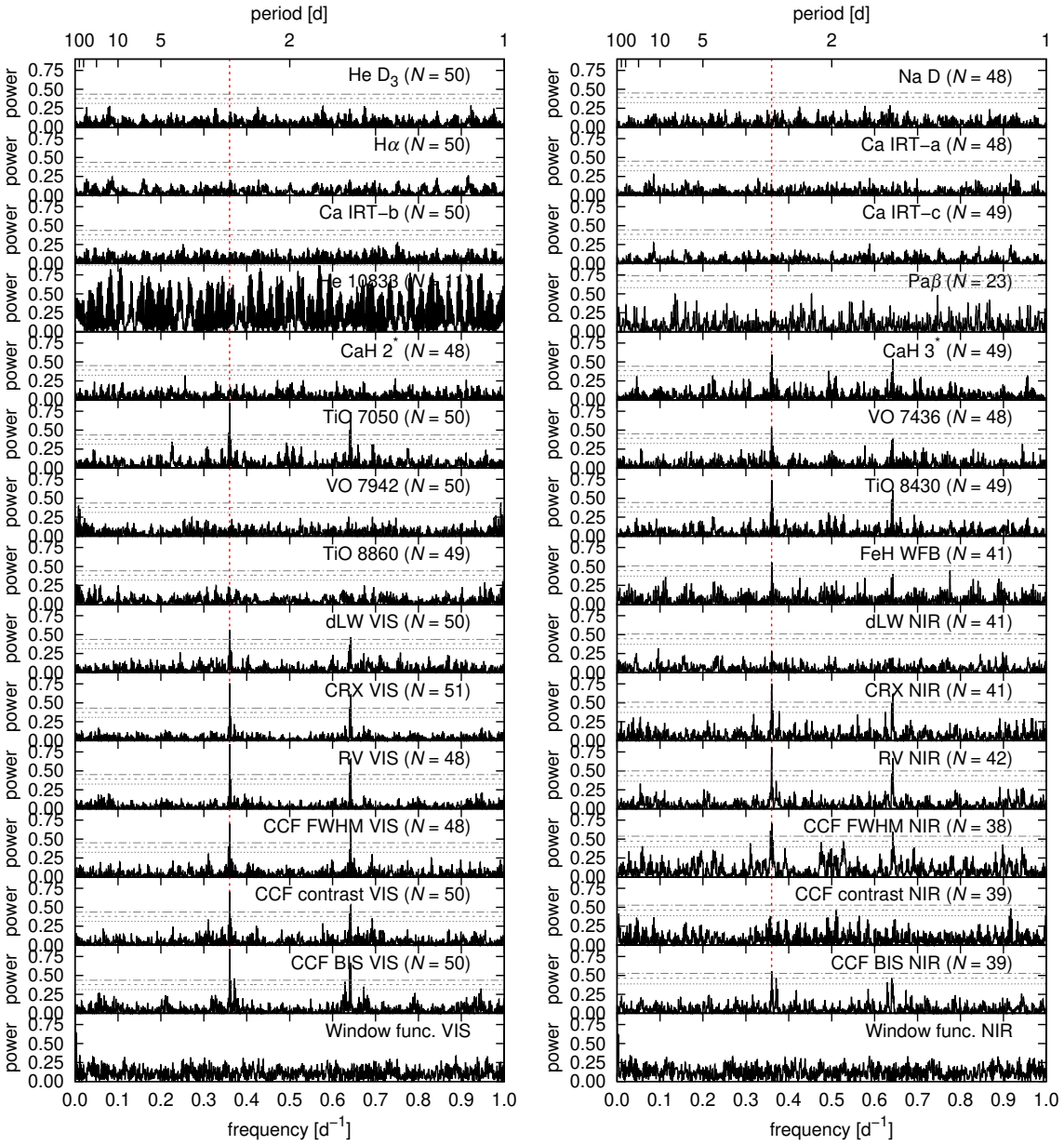

Figure B.2.: Same as Fig. B.1, but for YZ CMi. The red dotted line marks the rotation frequency $f_{\rm rot} = 0.36\,{\rm d}^{-1}$ ($P_{\rm rot} = 2.78\,{\rm d}$).

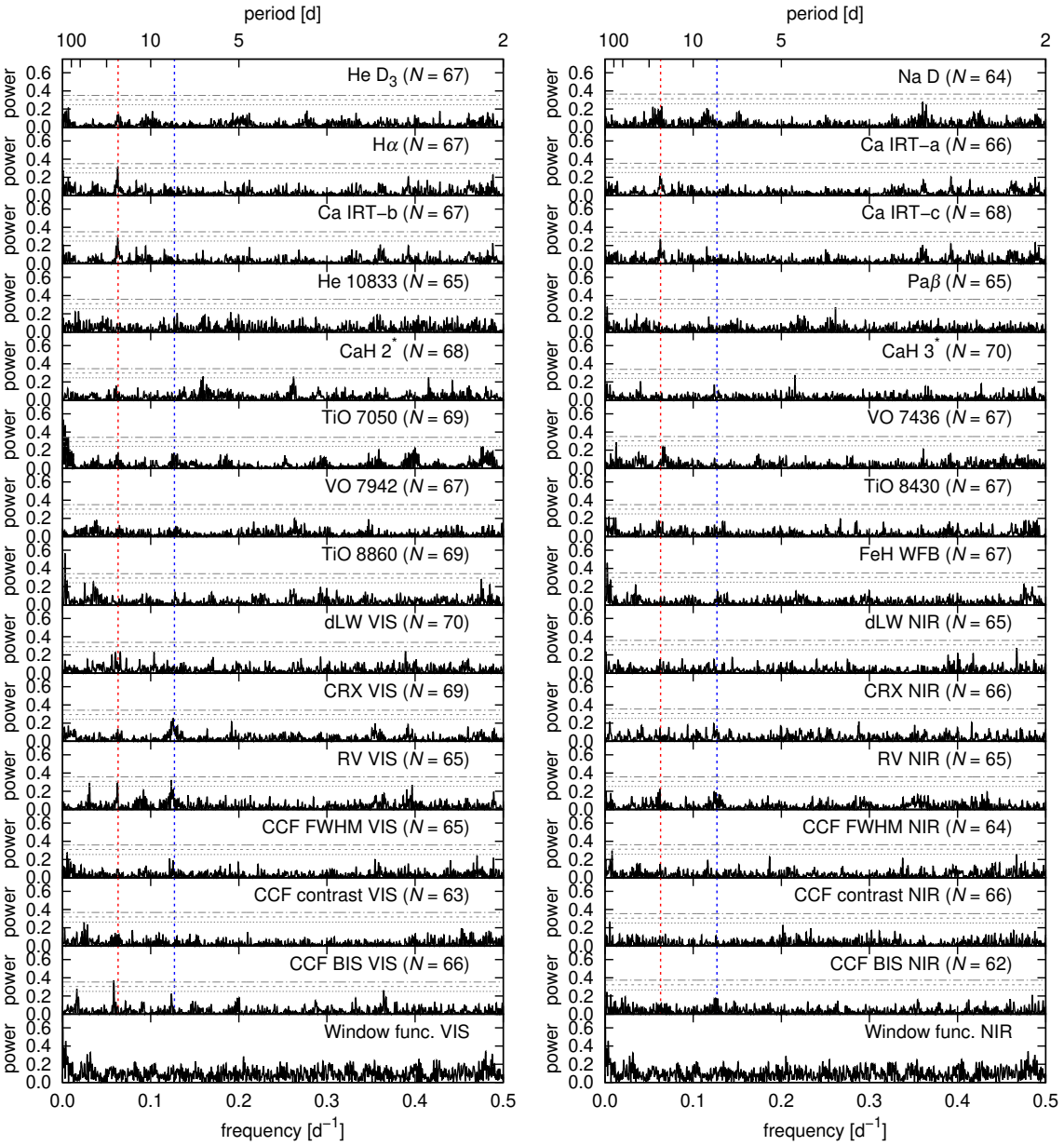

Figure B.3.: Same as Fig. B.1, but for TYC 3529-1437-1. The red dotted line marks the rotation frequency $f_{\rm rot} = 0.063\,{\rm d}^{-1}$ ($P_{\rm rot} = 15.8\,{\rm d}$), the blue dotted line marks its first harmonic $2\,f_{\rm rot}$.

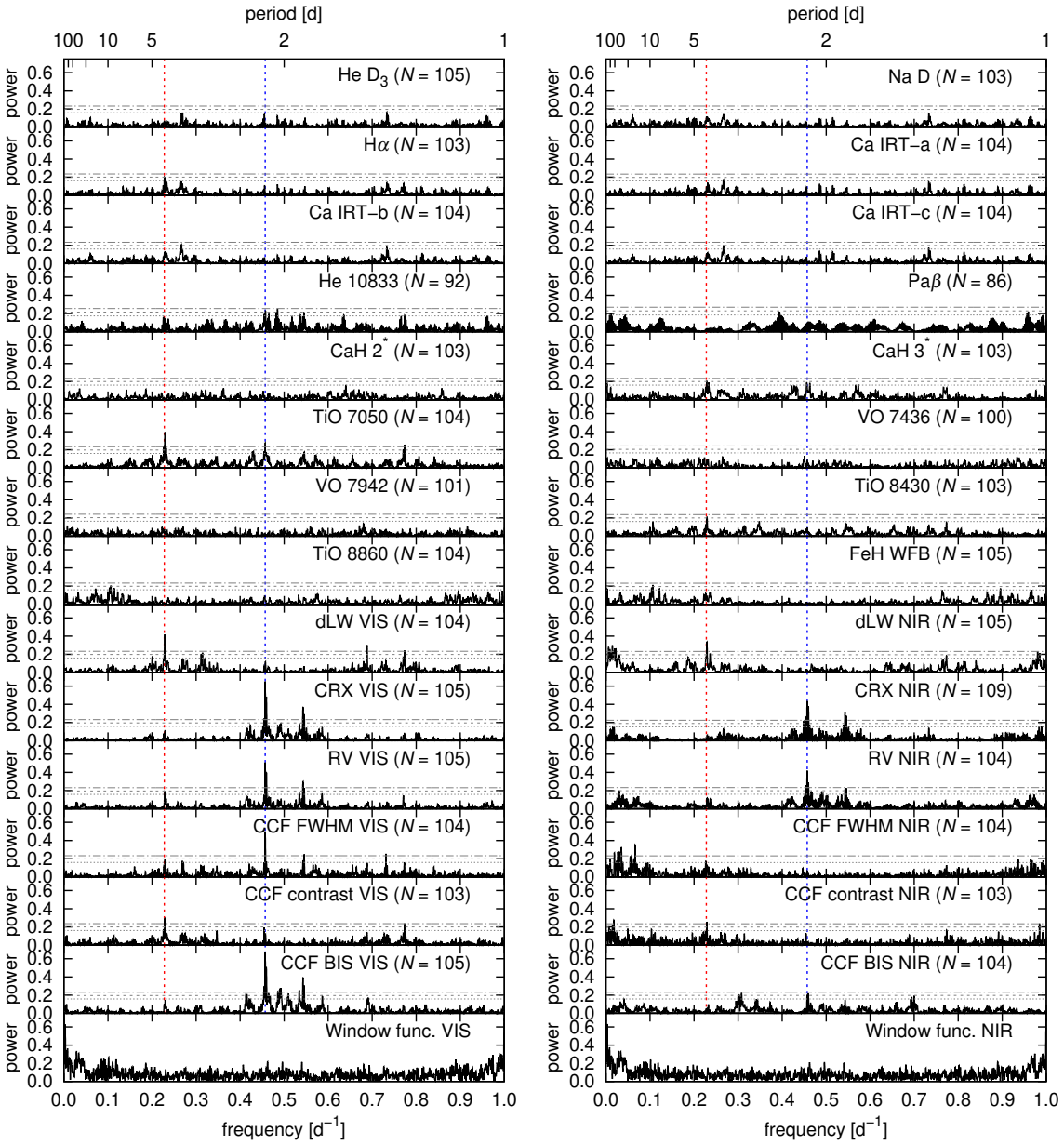

Figure B.4.: Same as Fig. B.1, but for EV Lac. The red dotted line marks the rotation frequency $f_{\rm rot} = 0.228\,{\rm d}^{-1}$ ($P_{\rm rot} = 4.38\,{\rm d}$), the blue dotted line marks its first harmonic $2\,f_{\rm rot}$.

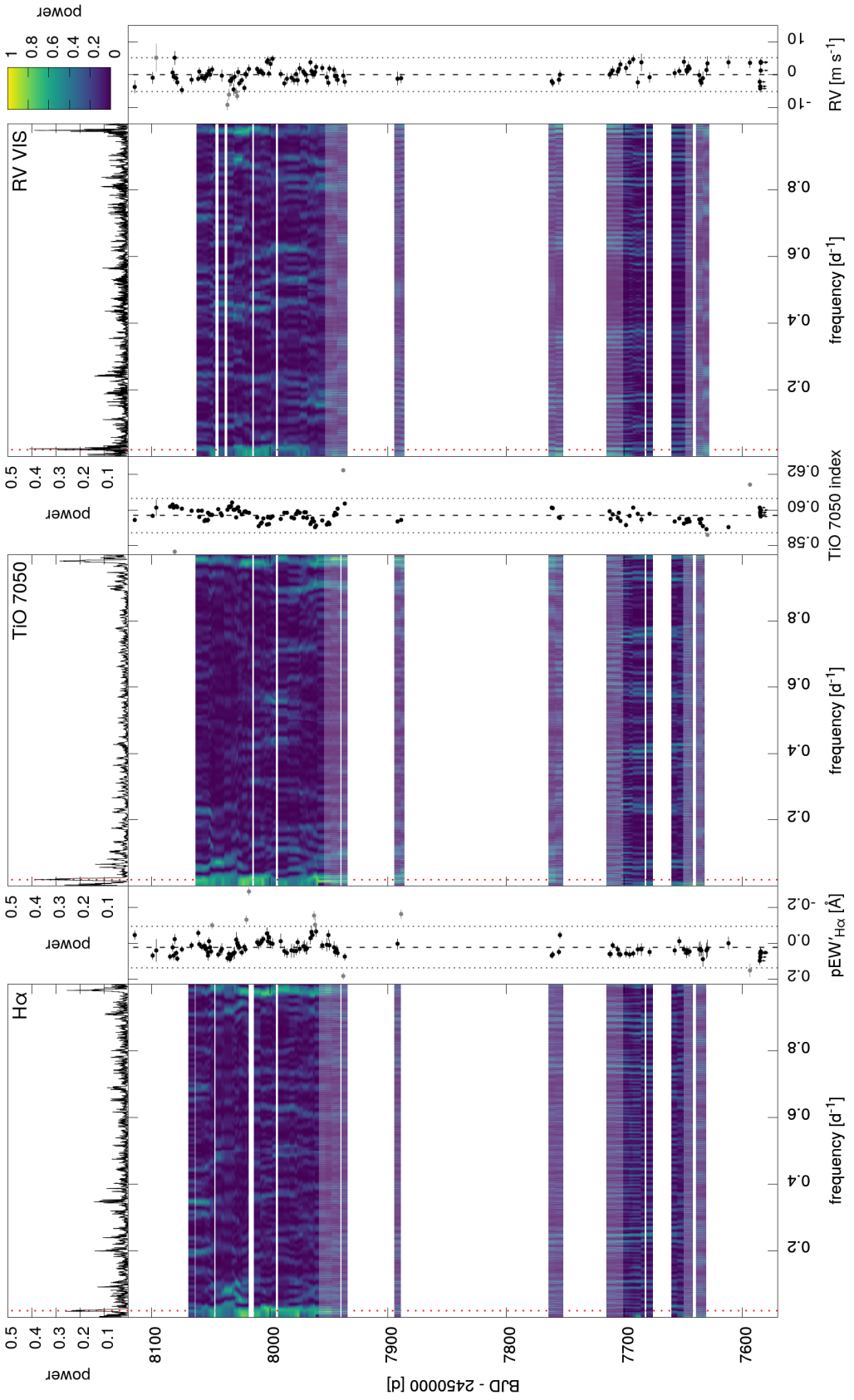

Figure B.5.: Rolling GLS periodograms for Ross 318 as described in Appendix B. The red dotted line marks f_{rot}.

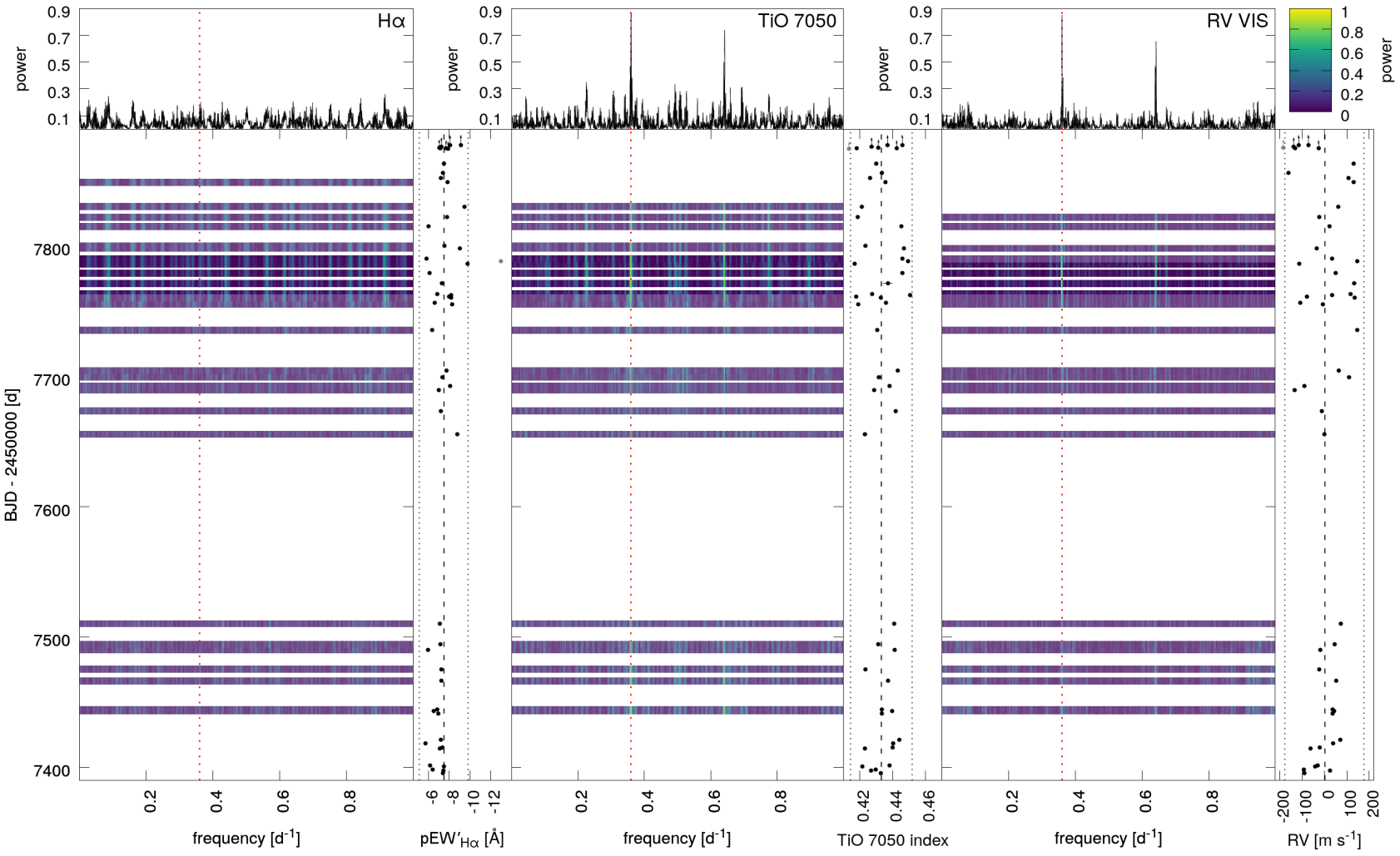

Figure B.6.: Rolling GLS periodograms for YZ CMi as described in Appendix B. The red dotted line marks $f_{\rm rot}$.

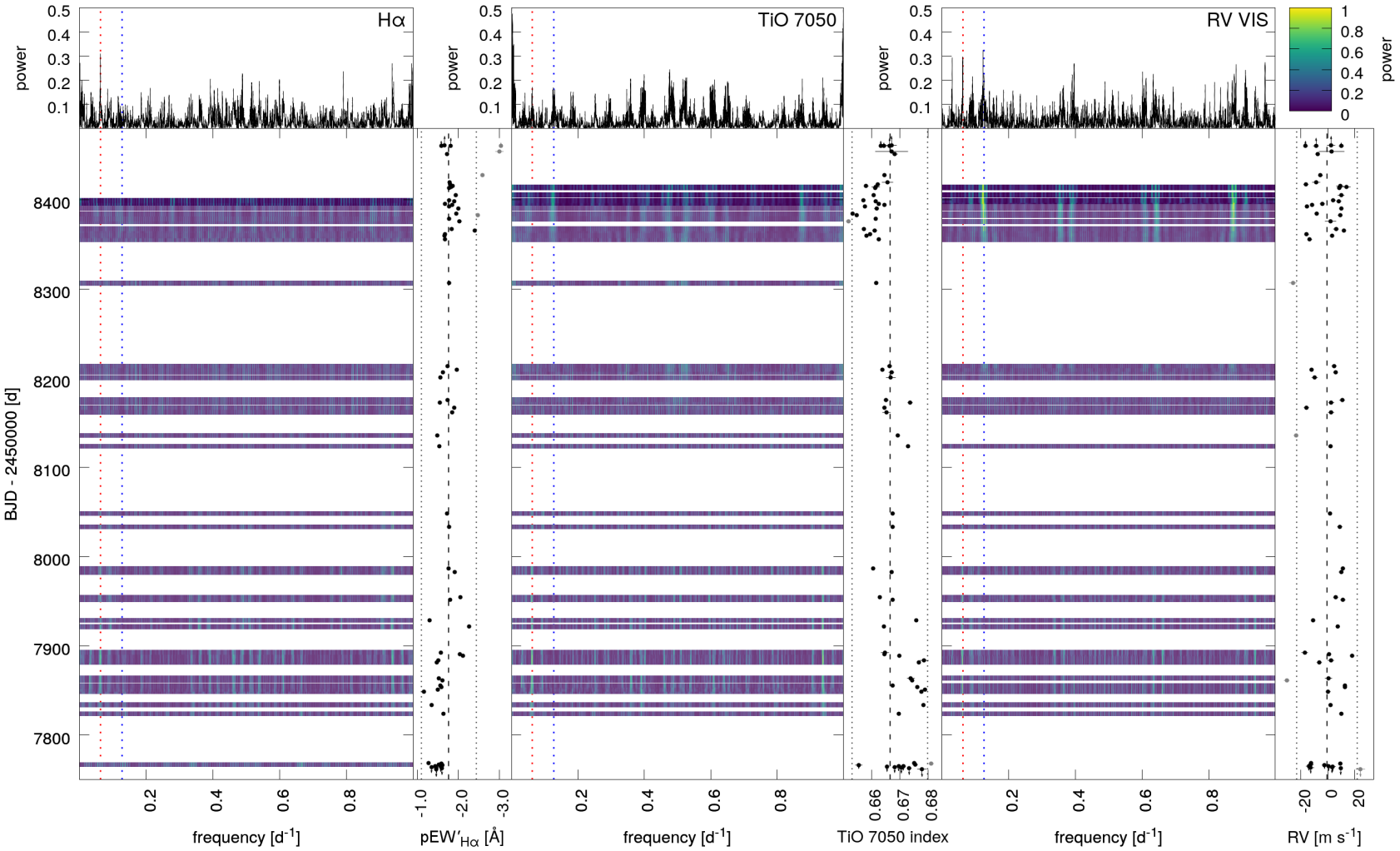

Figure B.7.: Rolling GLS periodograms for TYC 3529-1437-1 as described in Appendix B. The dotted lines mark f_{rot} (red) and 2 f_{rot} (blue).

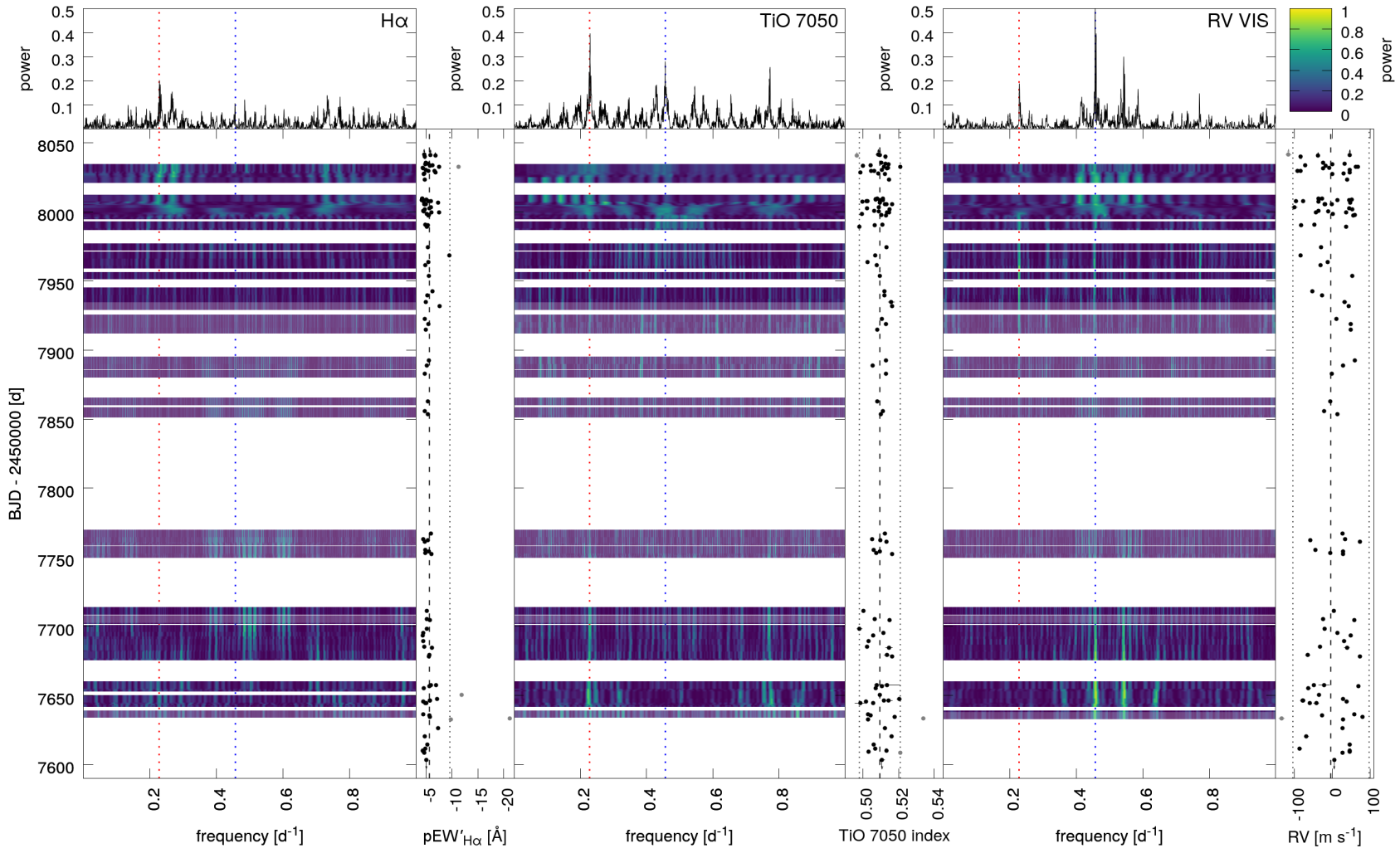

Figure B.8.: Rolling GLS periodograms for EV Lac as described in Appendix B. The dotted lines mark $f_{\rm rot}$ (red) and 2 $f_{\rm rot}$ (blue).

Bibliography

Adelberger, E. G., García, A., Robertson, R. G. H. et al. (2011) Solar fusion cross sections. II. The pp chain and CNO cycles. *Reviews of Modern Physics*, **83**(1), 195–246.

Alekseev, I. Y. & Kozhevnikova, A. V. (2017) Long-term variations in the spottedness of BY Dra M dwarfs. *Astronomy Reports*, **61**(3), 221–232.

Alfvén, H. (1947) Magneto hydrodynamic waves, and the heating of the solar corona. *MNRAS*, **107**, 211.

Allard, F., Hauschildt, P. H., Alexander, D. R., Tamanai, A. & Schweitzer, A. (2001) The Limiting Effects of Dust in Brown Dwarf Model Atmospheres. *ApJ*, **556**(1), 357–372.

Allart, R., Bourrier, V., Lovis, C. et al. (2018) Spectrally resolved helium absorption from the extended atmosphere of a warm Neptune-mass exoplanet. *Science*, **362**(6421), 1384–1387.

Alonso-Floriano, F. J., Morales, J. C., Caballero, J. A. et al. (2015) CARMENES input catalogue of M dwarfs. I. Low-resolution spectroscopy with CAFOS. *A&A*, **577**, A128.

Alonso-Floriano, F. J., Sánchez-López, A., Snellen, I. A. G. et al. (2019) Multiple water band detections in the CARMENES near-infrared transmission spectrum of HD 189733 b. *A&A*, **621**, A74.

Alvarado-Gómez, J. D., Drake, J. J., Fraschetti, F. et al. (2020) Tuning the Exospace Weather Radio for Stellar Coronal Mass Ejections. *ApJ*, **895**(1), 47.

Andretta, V., Doyle, J. G. & Byrne, P. B. (1997) The NaI $\lambda\lambda$5890,5896 resonance doublet as chromospheric diagnostics in M dwarfs. *A&A*, **322**, 266–279.

Anglada-Escudé, G., Arriagada, P., Tuomi, M. et al. (2014) Two planets around Kapteyn's star: a cold and a temperate super-Earth orbiting the nearest halo red dwarf. *MNRAS*, **443**, L89–L93.

Anglada-Escudé, G., Tuomi, M., Arriagada, P. et al. (2016) No Evidence for Activity Correlations in the Radial Velocities of Kapteyn's Star. *ApJ*, **830**(2), 74.

Artigau, É., Malo, L., Doyon, R. et al. (2018) Optical and Near-infrared Radial Velocity Content of M Dwarfs: Testing Models with Barnard's Star. *AJ*, **155**(5), 198.

Astudillo-Defru, N., Delfosse, X., Bonfils, X. et al. (2017) Magnetic activity in the HARPS M dwarf sample. The rotation-activity relationship for very low-mass stars through R'$_{HK}$. *A&A*, **600**, A13.

Ayres, T. R., Marstad, N. C. & Linsky, J. L. (1981) Outer atmospheres of cool stars. IX. A survey of ultraviolet emission from F-K dwarfs and giants with the IUE. *ApJ*, **247**, 545–559.

Babcock, H. W. (1961) The Topology of the Sun's Magnetic Field and the 22-YEAR Cycle. *ApJ*, **133**, 572.

Baliunas, S. L., Donahue, R. A., Soon, W. H. et al. (1995) Chromospheric Variations in Main-Sequence Stars. II. *ApJ*, **438**, 269.

Baranne, A., Queloz, D., Mayor, M. et al. (1996) ELODIE: A spectrograph for accurate radial velocity measurements. *A&AS*, **119**, 373–390.

Barnes, J. R., Collier Cameron, A., Donati, J. F. et al. (2005) The dependence of differential rotation on temperature and rotation. *MNRAS*, **357**(1), L1–L5.

Barnes, J. R., James, D. J. & Collier Cameron, A. (2002) The boundaries of Doppler imaging: Starspot patterns on M dwarfs. *Astronomische Nachrichten*, **323**, 333–335.

Barnes, J. R., Jeffers, S. V., Haswell, C. A. et al. (2017) Surprisingly different star-spot distributions on the near equal-mass equal-rotation-rate stars in the M dwarf binary GJ 65 AB. *MNRAS*, **471**(1), 811–823.

Barnes, J. R., Jeffers, S. V., Jones, H. R. A. et al. (2015) Starspot Distributions on Fully Convective M Dwarfs: Implications for Radial Velocity Planet Searches. *ApJ*, **812**(1), 42.

Barnes, R. & Heller, R. (2013) Habitable Planets Around White and Brown Dwarfs: The Perils of a Cooling Primary. *Astrobiology*, **13**(3), 279–291.

Baroch, D., Morales, J. C., Ribas, I. et al. (2018) The CARMENES search for exoplanets around M dwarfs. Nine new double-line spectroscopic binary stars. *A&A*, **619**, A32.

Basri, G. & Nguyen, H. T. (2018) Double Dipping: A New Relation between Stellar Rotation and Starspot Activity. *ApJ*, **863**(2), 190.

Basri, G. & Shah, R. (2020) The Information Content in Analytic Spot Models of Broadband Precision Light Curves. II. Spot Distributions and Lifetimes and Global and Differential Rotation. *ApJ*, **901**(1), 14.

Bauer, F. F., Reiners, A., Beeck, B. & Jeffers, S. V. (2018) The influence of convective blueshift on radial velocities of F, G, and K stars. *A&A*, **610**, A52.

Bauer, F. F., Zechmeister, M., Kaminski, A. et al. (2020) The CARMENES search for exoplanets around M dwarfs. Measuring precise radial velocities in the near infrared: The example of the super-Earth CD Cet b. *A&A*, **640**, A50.

Bauer, F. F., Zechmeister, M. & Reiners, A. (2015) Calibrating echelle spectrographs with Fabry-Pérot etalons. *A&A*, **581**, A117.

Beckers, J. M. & Nelson, G. D. (1978) Some comments on the limb shift of solar lines. II: The effect of granular motions. *Sol. Phys.*, **58**(2), 243–261.

Bell, K. J., Hilton, E. J., Davenport, J. R. A. et al. (2012) Hα Emission Variability in Active M Dwarfs. *PASP*, **124**, 14.

Benneke, B., Werner, M., Petigura, E. et al. (2017) Spitzer Observations Confirm and Rescue the Habitable-zone Super-Earth K2-18b for Future Characterization. *ApJ*, **834**(2), 187.

Benz, A. O. (2017) Flare Observations. *Living Reviews in Solar Physics*, **14**(1), 2.

Benz, A. O., Conway, J. & Güdel, M. (1998) First VLBI images of a main-sequence star. *A&A*, **331**, 596–600.

Benz, A. O. & Güdel, M. (1994) X-ray/microwave ratio of flares and coronae. *A&A*, **285**, 621–630.

Benz, A. O. & Güdel, M. (2010) Physical Processes in Magnetically Driven Flares on the Sun, Stars, and Young Stellar Objects. *ARA&A*, **48**, 241–287.

Berdyugina, S. V. (2005) Starspots: A Key to the Stellar Dynamo. *Living Reviews in Solar Physics*, **2**(1), 8.

Berdyugina, S. V. & Solanki, S. K. (2002) The molecular Zeeman effect and diagnostics of solar and stellar magnetic fields. I. Theoretical spectral patterns in the Zeeman regime. *A&A*, **385**, 701–715.

Biermann, L. (1946) Zur Deutung der chromosphärischen Turbulenz und des Exzesses der UV-Strahlung der Sonne. *Naturwissenschaften*, **33**(4), 118–119.

Biermann, L. (1951) Kometenschweife und solare Korpuskularstrahlung. *ZAp*, **29**, 274.

Bond, H. E., Mullan, D. J., O'Brien, M. S. & Sion, E. M. (2001) Detection of Coronal Mass Ejections in V471 Tauri with the Hubble Space Telescope. *ApJ*, **560**(2), 919–927.

Bopp, B. W. & Evans, D. S. (1973) The spotted flare stars BY Dra and CC Eri: a model for the spots and some astrophysical implications. *MNRAS*, **164**, 343–356.

Boro Saikia, S., Jeffers, S. V., Morin, J. et al. (2016) A solar-like magnetic cycle on the mature K-dwarf 61 Cygni A (HD 201091). *A&A*, **594**, A29.

Boro Saikia, S., Marvin, C. J., Jeffers, S. V. et al. (2018) Chromospheric activity catalogue of 4454 cool stars. Questioning the active branch of stellar activity cycles. *A&A*, **616**, A108.

Bowen, I. S. & Vaughan, A. H., J. (1973) "Nonobjective" Gratings. *PASP*, **85**(504), 174.

Boyajian, T. S., von Braun, K., van Belle, G. et al. (2012) Stellar Diameters and Temperatures. II. Main-sequence K- and M-stars. *ApJ*, **757**(2), 112.

Browning, M. K. (2008) Simulations of Dynamo Action in Fully Convective Stars. *ApJ*, **676**(2), 1262–1280.

Browning, M. K., Basri, G., Marcy, G. W., West, A. A. & Zhang, J. (2010) Rotation and Magnetic Activity in a Sample of M-Dwarfs. *AJ*, **139**(2), 504–518.

Burgasser, A. J., Geballe, T. R., Leggett, S. K., Kirkpatrick, J. D. & Golimowski, D. A. (2006) A Unified Near-Infrared Spectral Classification Scheme for T Dwarfs. *ApJ*, **637**(2), 1067–1093.

Burnight, T. R. (1949) Soft X-radiation in the upper atmosphere. *Phys. Rev.*, **76**, 165.

Busà, I., Aznar Cuadrado, R., Terranegra, L., Andretta, V. & Gomez, M. T. (2007) The Ca II infrared triplet as a stellar activity diagnostic. II. Test and calibration with high resolution observations. *A&A*, **466**(3), 1089–1098.

Caballero, J. A., Cortés-Contreras, M., Alonso-Floriano, F. J. et al. (2016) Carmencita, The CARMENES Input Catalogue of Bright, Nearby M Dwarfs. In *19th Cambridge Workshop on Cool Stars, Stellar Systems, and the Sun (CS19)*, edited by G. A. Feiden, Zenodo.

Campbell, B. & Walker, G. A. H. (1979) Precision radial velocities with an absorption cell. *PASP*, **91**, 540–545.

Cannon, A. J. & Pickering, E. C. (1901) Spectra of bright southern stars photographed with the 13-inch Boyden telescope as part of the Henry Draper Memorial. *Annals of Harvard College Observatory*, **28**, 129–P.6.

Carrington, R. C. (1858) On the Distribution of the Solar Spots in Latitudes since the Beginning of the Year 1854, with a Map. *MNRAS*, **19**, 1–3.

Carrington, R. C. (1859) Description of a Singular Appearance seen in the Sun on September 1, 1859. *MNRAS*, **20**, 13–15.

Catalano, S., Biazzo, K., Frasca, A. & Marilli, E. (2002) Measuring starspot temperature from line depth ratios. I. The method. *A&A*, **394**, 1009–1021.

Catalano, S. & Marilli, E. (1983) CA II chromospheric emission and rotation of main sequence stars. *A&A*, **121**, 190–197.

Catura, R. C., Acton, L. W. & Johnson, H. M. (1975) Evidence for X-ray emission from Capella. *ApJL*, **196**, L47–L49.

Chabrier, G. & Baraffe, I. (1997) Structure and evolution of low-mass stars. *A&A*, **327**, 1039–1053.

Chabrier, G. & Baraffe, I. (2000) Theory of Low-Mass Stars and Substellar Objects. *ARA&A*, **38**, 337–377.

Chabrier, G. & Küker, M. (2006) Large-scale $\alpha\hat{2}$-dynamo in low-mass stars and brown dwarfs. *A&A*, **446**(3), 1027–1037.

Chapman, G. A. & Sheeley, N. R., J. (1968) The Photospheric Network. *Sol. Phys.*, **5**(4), 442–461.

Charbonneau, P. (2020) Dynamo models of the solar cycle. *Living Reviews in Solar Physics*, **17**(1), 4.

Chen, J. (2017) Physics of erupting solar flux ropes: Coronal mass ejections (CMEs) — Recent advances in theory and observation. *Physics of Plasmas*, **24**(9), 090501.

Cho, K., Lee, J., Chae, J. et al. (2016) Strong Blue Asymmetry in Hα Line as a Preflare Activity. *Sol. Phys.*, **291**(8), 2391–2406.

Chugainov, P. F. (1966) On the Variability of HD 234677. *Information Bulletin on Variable Stars*, **122**, 1.

Cohen, O., Drake, J. J., Glocer, A. et al. (2014) Magnetospheric Structure and Atmospheric Joule Heating of Habitable Planets Orbiting M-dwarf Stars. *ApJ*, **790**(1), 57.

Cortés-Contreras, M., Domínguez-Fernández, A. J., Caballero, J. A. et al. (in prep.) CARMENES input catalogue of M dwarfs. VI. Kinematics in the solar neighbourhood. *A&A*, in prep.

Cram, L. E. & Giampapa, M. S. (1987) Formation of Chromospheric Lines in Cool Dwarf Stars. *ApJ*, **323**, 316.

Cram, L. E. & Mullan, D. J. (1979) Model chromospheres of flare stars.I. Balmer-line profiles. *ApJ*, **234**, 579–587.

Crosley, M. K. & Osten, R. A. (2018) Low-frequency Radio Transients on the Active M-dwarf EQ Peg and the Search for Coronal Mass Ejections. *ApJ*, **862**(2), 113.

Cuntz, M., Saar, S. H. & Musielak, Z. E. (2000) On Stellar Activity Enhancement Due to Interactions with Extrasolar Giant Planets. *ApJL*, **533**(2), L151–L154.

Davenport, J. R. A. (2016) The Kepler Catalog of Stellar Flares. *ApJ*, **829**(1), 23.

David, T. J., Hillenbrand, L. A., Petigura, E. A. et al. (2016) A Neptune-sized transiting planet closely orbiting a 5-10-million-year-old star. *Nature*, **534**(7609), 658–661.

Dekker, H., D'Odorico, S., Kaufer, A., Delabre, B. & Kotzlowski, H. (2000) Design, construction, and performance of UVES, the echelle spectrograph for the UT2 Kueyen Telescope at the ESO Paranal Observatory. In *Proc. SPIE*, edited by M. Iye & A. F. Moorwood, vol. 4008 of *Society of Photo-Optical Instrumentation Engineers (SPIE) Conference Series*, pp. 534–545.

Delfosse, X., Forveille, T., Perrier, C. & Mayor, M. (1998) Rotation and chromospheric activity in field M dwarfs. *A&A*, **331**, 581–595.

Delisle, J. B., Ségransan, D., Dumusque, X. et al. (2018) The HARPS search for southern extra-solar planets. XLIII. A compact system of four super-Earth planets orbiting HD 215152. *A&A*, **614**, A133.

Desort, M., Lagrange, A. M., Galland, F., Udry, S. & Mayor, M. (2007) Search for exoplanets with the radial-velocity technique: quantitative diagnostics of stellar activity. *A&A*, **473**(3), 983–993.

Díaz, R. F., Cincunegui, C. & Mauas, P. J. D. (2007) The NaI D resonance lines in main-sequence late-type stars. *MNRAS*, **378**(3), 1007–1018.

Díez Alonso, E., Caballero, J. A., Montes, D. et al. (2019) CARMENES input catalogue of M dwarfs. IV. New rotation periods from photometric time series. *A&A*, **621**, A126.

Dobler, W., Stix, M. & Brandenburg, A. (2006) Magnetic Field Generation in Fully Convective Rotating Spheres. *ApJ*, **638**(1), 336–347.

Donahue, R. A., Saar, S. H. & Baliunas, S. L. (1996) A Relationship between Mean Rotation Period in Lower Main-Sequence Stars and Its Observed Range. *ApJ*, **466**, 384.

Donati, J. F. & Collier Cameron, A. (1997) Differential rotation and magnetic polarity patterns on AB Doradus. *MNRAS*, **291**(1), 1–19.

Donati, J.-F., Kouach, D., Lacombe, M. et al. (2018) SPIRou: A NIR Spectro-polarimeter/High-Precision Velocimeter for the CFHT. In *Handbook of Exoplanets*, Springer International Publishing, pp. 903–929.

Donati, J. F., Morin, J., Petit, P. et al. (2008) Large-scale magnetic topologies of early M dwarfs. *MNRAS*, **390**(2), 545–560.

Donati, J. F., Semel, M. & Praderie, F. (1989) Zeeman-Doppler imaging of active stars. II. Numerical simulation and first observational results. *A&A*, **225**, 467–478.

Dorn, R. J., Anglada-Escude, G., Baade, D. et al. (2014) CRIRES+: Exploring the Cold Universe at High Spectral Resolution. *The Messenger*, **156**, 7–11.

Dravins, D. (1982) Photospheric spectrum line asymmetries and wavelength shifts. *ARA&A*, **20**, 61–89.

Dumusque, X. (2018) Measuring precise radial velocities on individual spectral lines. I. Validation of the method and application to mitigate stellar activity. *A&A*, **620**, A47.

Dumusque, X., Pepe, F., Lovis, C. et al. (2012) An Earth-mass planet orbiting α Centauri B. *Nature*, **491**(7423), 207–211.

Dumusque, X., Udry, S., Lovis, C., Santos, N. C. & Monteiro, M. J. P. F. G. (2011) Planetary detection limits taking into account stellar noise. I. Observational strategies to reduce stellar oscillation and granulation effects. *A&A*, **525**, A140.

Duncan, D. K., Vaughan, A. H., Wilson, O. C. et al. (1991) CA II H and K Measurements Made at Mount Wilson Observatory, 1966–1983. *ApJS*, **76**, 383.

Durney, B. R., De Young, D. S. & Roxburgh, I. W. (1993) On the Generation of the Largescale and Turbulent Magnetic Fields in the Solar Type Stars. *Sol. Phys.*, **145**(2), 207–225.

Eberhard, G. & Schwarzschild, K. (1913) On the reversal of the calcium lines H and K in stellar spectra. *ApJ*, **38**, 292–295.

Edlén, B. (1943) Die Deutung der Emissionslinien im Spektrum der Sonnenkorona. *ZAp*, **22**, 30.

Endl, M., Kürster, M., Rouesnel, F. et al. (2003) Extrasolar Terrestrial Planets: Can We Detect Them Already? In *Scientific Frontiers in Research on Extrasolar Planets*, edited by D. Deming & S. Seager, vol. 294 of *Astronomical Society of the Pacific Conference Series*, pp. 75–78.

Favata, F. & Schmitt, J. H. M. M. (1999) Spectroscopic analysis of a super-hot giant flare observed on Algol by BeppoSAX on 30 August 1997. *A&A*, **350**, 900–916.

Fontenla, J. M., Linsky, J. L., Witbrod, J. et al. (2016) Semi-empirical Modeling of the Photosphere, Chromosphere, Transition Region, and Corona of the M-dwarf Host Star GJ 832. *ApJ*, **830**(2), 154.

Fouqué, P., Moutou, C., Malo, L. et al. (2018) SPIRou Input Catalogue: global properties of 440 M dwarfs observed with ESPaDOnS at CFHT. *MNRAS*, **475**(2), 1960–1986.

Fröhlich, C. (2002) Total solar irradiance variations since 1978. *Advances in Space Research*, **29**(10), 1409–1416.

Fuhrmeister, B., Czesla, S., Hildebrandt, L. et al. (2019a) The CARMENES search for exoplanets around M dwarfs. The He I triplet at 10830 Å across the M dwarf sequence. *A&A*, **632**, A24.

Fuhrmeister, B., Czesla, S., Schmitt, J. H. M. M. et al. (2018) The CARMENES search for exoplanets around M dwarfs. Wing asymmetries of Hα, Na I D, and He I lines. *A&A*, **615**, A14.

Fuhrmeister, B., Czesla, S., Schmitt, J. H. M. M. et al. (2019b) The CARMENES search for exoplanets around M dwarfs. Period search in Hα, Na I D, and Ca II IRT lines. *A&A*, **623**, A24.

Fuhrmeister, B., Liefke, C., Schmitt, J. H. M. M. & Reiners, A. (2008) Multiwavelength observations of a giant flare on CN Leonis. I. The chromosphere as seen in the optical spectra. *A&A*, **487**(1), 293–306.

Gaia Collaboration, Brown, A. G. A., Vallenari, A. et al. (2018) Gaia Data Release 2. Summary of the contents and survey properties. *A&A*, **616**, A1.

Gaidos, E., Mann, A. W., Kraus, A. L. & Ireland, M. (2016) They are small worlds after all: revised properties of Kepler M dwarf stars and their planets. *MNRAS*, **457**(3), 2877–2899.

Gershberg, R. E. (1972) Some results of the cooperative photometric observations of the UV Cet-type flare stars in the years 1967 71. *Ap&SS*, **19**(1), 75–92.

Gigoyan, K. S., Sinamyan, P. K., Engels, D. & Mickaelian, A. M. (2010) Late-type stars found in the DFBS. *Astrophysics*, **53**(1), 123–132.

Giridhar, S. (2010) Spectral Classification: Old and Contemporary. *Astrophysics and Space Science Proceedings*, **16**, 165.

Gizis, J. E., Reid, I. N. & Hawley, S. L. (2002) The Palomar/MSU Nearby Star Spectroscopic Survey. III. Chromospheric Activity, M Dwarf Ages, and the Local Star Formation History. *AJ*, **123**(6), 3356–3369.

Gomes da Silva, J., Santos, N. C., Bonfils, X. et al. (2011) Long-term magnetic activity of a sample of M-dwarf stars from the HARPS program. I. Comparison of activity indices. *A&A*, **534**, A30.

Gopalswamy, N., Thompson, W. T., Davila, J. M. et al. (2009) Relation Between Type II Bursts and CMEs Inferred from STEREO Observations. *Sol. Phys.*, **259**(1-2), 227–254.

Gray, R. O., Corbally, C. J., Garrison, R. F., McFadden, M. T. & Robinson, P. E. (2003) Contributions to the Nearby Stars (NStars) Project: Spectroscopy of Stars Earlier than M0 within 40 Parsecs: The Northern Sample. I. *AJ*, **126**(4), 2048–2059.

Gray, R. O., Corbally, C. J., Garrison, R. F. et al. (2006) Contributions to the Nearby Stars (NStars) Project: Spectroscopy of Stars Earlier than M0 within 40 pc-The Southern Sample. *AJ*, **132**(1), 161–170.

Griffin, R. & Griffin, R. (1973) On the possibility of determining stellar radial velocities to 0.01 km s^{-1}. *MNRAS*, **162**, 243–253.

Gringauz, K. I., Bezrukikh, V. V., Ozerov, V. D. & Rybchinskii, R. E. (1962) The study of interplanetary ionized gas, high-energy electrons and corpuscular radiation of the sun, employing three-electrode charged particle traps on the second Soviet space rocket. *Planet. Space Sci.*, **9**(3), 103–107.

Güdel, M. (2002) Stellar Radio Astronomy: Probing Stellar Atmospheres from Protostars to Giants. *ARA&A*, **40**, 217–261.

Güdel, M. (2004) X-ray astronomy of stellar coronae. *A&A Rev.*, **12**(2-3), 71–237.

Güdel, M. & Benz, A. O. (1993) X-Ray/Microwave Relation of Different Types of Active Stars. *ApJL*, **405**, L63.

Güdel, M. & Nazé, Y. (2009) X-ray spectroscopy of stars. *A&A Rev.*, **17**(3), 309–408.

Guenther, E. W. & Emerson, J. P. (1997) Spectrophotometry of flares and short time scale variations in weak line, and classical T Tauri stars in Chamaeleon. *A&A*, **321**, 803–810.

Haisch, B., Strong, K. T. & Rodono, M. (1991) Flares on the Sun and other stars. *ARA&A*, **29**, 275–324.

Haisch, B. M., Slee, O. B., Siegman, B. C. et al. (1981) Simultaneous X-ray, ultraviolet, optical, and radio observations of the flare star Proxima Centauri. *ApJ*, **245**, 1009–1017.

Hale, G. E. (1908) On the Probable Existence of a Magnetic Field in Sun-Spots. *ApJ*, **28**, 315.

Hall, D. S. & Henry, G. W. (1994) The Law of Starspot Lifetimes. *International Amateur-Professional Photoelectric Photometry Communications*, **55**, 51.

Hall, J. C. (2008) Stellar Chromospheric Activity. *Living Reviews in Solar Physics*, **5**(1), 2.

Hardegree-Ullman, K. K., Cushing, M. C., Muirhead, P. S. & Christiansen, J. L. (2019) Kepler Planet Occurrence Rates for Mid-type M Dwarfs as a Function of Spectral Type. *AJ*, **158**(2), 75.

Harrell, F. E. & Davis, C. E. (1982) A new distribution-free quantile estimator. *Biometrika*, **69**(3), 635–640.

Harrison, G. R. (1949) The production of Diffraction Gratings: II. Design of Echelle Gratings and Spectrographs. *Journal of the Optical Society of America (1917-1983)*, **39**(7), 522.

Hathaway, D. H. (2015) The Solar Cycle. *Living Reviews in Solar Physics*, **12**(1), 4.

Hatzes, A. P. (2013) The Radial Velocity Detection of Earth-mass Planets in the Presence of Activity Noise: The Case of α Centauri Bb. *ApJ*, **770**(2), 133.

Hawley, S. L., Gizis, J. E. & Reid, I. N. (1996) The Palomar/MSU Nearby Star Spectroscopic Survey. II. The Southern M Dwarfs and Investigation of Magnetic Activity. *AJ*, **112**, 2799.

Hawley, S. L. & Pettersen, B. R. (1991) The Great Flare of 1985 April 12 on AD Leonis. *ApJ*, **378**, 725.

Haywood, R. D., Collier Cameron, A., Queloz, D. et al. (2014) Planets and stellar activity: hide and seek in the CoRoT-7 system. *MNRAS*, **443**(3), 2517–2531.

Hearnshaw, J. B. (2009) *Astronomical Spectrographs and their History*. Cambridge University Press.

Hearnshaw, J. B. (2014) *The Analysis of Starlight: Two Centuries of Astronomical Spectroscopy*. 2nd edn., Cambridge University Press.

Henry, T. J., Jao, W.-C., Winters, J. G. et al. (2018) The Solar Neighborhood XLIV: RECONS Discoveries within 10 parsecs. *AJ*, **155**(6), 265.

Henwood, R., Chapman, S. C. & Willis, D. M. (2010) Increasing Lifetime of Recurrent Sunspot Groups Within the Greenwich Photoheliographic Results. *Sol. Phys.*, **262**(2), 299–313.

Hertzsprung, E. (1911) Über die Verwendung photographischer effektiver Wellenlängen zur Bestimmung von Farbenäquivalenten. *Publikationen des Astrophysikalischen Ob-servatoriums zu Potsdam*, **22**(63), 1–40.

Heyvaerts, J. (1990) Coronal Heating by DC Currents. In *Basic Plasma Processes on the Sun*, edited by E. R. Priest & V. Krishan, vol. 142, p. 207.

Hidalgo, D., Pallé, E., Alonso, R. et al. (2020) Three planets transiting the evolved star EPIC 249893012: a hot 8.8-$M_\oplus$ super-Earth and two warm 14.7 and 10.2-$M_\oplus$ sub-Neptunes. *A&A*, **636**, A89.

Hintz, D., Fuhrmeister, B., Czesla, S. et al. (2019) The CARMENES search for exoplanets around M dwarfs. Chromospheric modeling of M 2-3 V stars with PHOENIX. *A&A*, **623**, A136.

Hodgson, R. (1859) On a curious Appearance seen in the Sun. *MNRAS*, **20**, 15–16.

Houdebine, E. R. (2012) Observation and modelling of main-sequence star chromospheres - XVIII. Observations of the Ca II resonance lines and Hα line for dM4 stars and dK5 stars. *MNRAS*, **421**(4), 3189–3205.

Houdebine, E. R., Foing, B. H. & Rodono, M. (1990) Dynamics of flares on late-type dMe stars. I. Flare mass ejections and stellar evolution. *A&A*, **238**, 249.

Houdebine, E. R., Junghans, K., Heanue, M. C. & Andrews, A. D. (2009) Observation and modelling of main sequence star chromospheres. VIII. High resolution observations of M and K dwarf chromospheric lines. *A&A*, **503**(3), 929–944.

Houdebine, E. R. & Mullan, D. J. (2015) Dynamics of Rotation in M Dwarfs: Indications for a Change in the Dynamo Regime in Stars at the Onset of Complete Convection. *ApJ*, **801**(2), 106.

Huenemoerder, D. P., Ramsey, L. W. & Buzasi, D. L. (1989) Titanium Oxide Variations in II Pegasi. *AJ*, **98**, 2264.

Husser, T. O., Wende-von Berg, S., Dreizler, S. et al. (2013) A new extensive library of PHOENIX stellar atmospheres and synthetic spectra. *A&A*, **553**, A6.

Ichimoto, K. & Kurokawa, H. (1984) Hα Red Asymmetry of Solar Flares. *Sol. Phys.*, **93**(1), 105–121.

Jacquinot, P. (1954) The luminosity of spectrometers with prisms, gratings, or Fabry Perot etalons. *Journal of the Optical Society of America (1917-1983)*, **44**(10), 761.

Jefferies, S. M., McIntosh, S. W., Armstrong, J. D. et al. (2006) Magnetoacoustic Portals and the Basal Heating of the Solar Chromosphere. *ApJL*, **648**(2), L151–L155.

Jeffers, S. V., Barnes, J. R. & Collier Cameron, A. (2002) The latitude distribution of star-spots on He 699. *MNRAS*, **331**(3), 666–672.

Jeffers, S. V., Barnes, J. R., Jones, H. R. A. et al. (2014) Is it possible to detect planets around young active G and K dwarfs? *MNRAS*, **438**(4), 2717–2731.

Jeffers, S. V., Schöfer, P., Lamert, A. et al. (2018) CARMENES input catalogue of M dwarfs. III. Rotation and activity from high-resolution spectroscopic observations. *A&A*, **614**, A76.

Jenkins, J. S., Ramsey, L. W., Jones, H. R. A. et al. (2009) Rotational Velocities for M Dwarfs. *ApJ*, **704**(2), 975–988.

Johnson, E. N., Czesla, S., Fuhrmeister, B. et al. (2021) Simultaneous photometric and CARMENES spectroscopic monitoring of fast-rotating M dwarf GJ 3270. Discovery of a post-flare corotating feature. *A&A*, **651**, A105.

Johnson, H. L. & Morgan, W. W. (1953) Fundamental stellar photometry for standards of spectral type on the Revised System of the Yerkes Spectral Atlas. *ApJ*, **117**, 313.

Joy, A. H. (1947) Radial Velocities and Spectral Types of 181 Dwarf Stars. *ApJ*, **105**, 96.

Joy, A. H. & Abt, H. A. (1974) Spectral Types of M Dwarf Stars. *ApJS*, **28**, 1.

Joy, A. H. & Humason, M. L. (1949) Observations of the Faint Dwarf Star L 726-8. *PASP*, **61**(360), 133–134.

Judge, P. G., Carlsson, M. & Stein, R. F. (2003) On the Origin of the Basal Emission from Stellar Atmospheres: Analysis of Solar C II Lines. *ApJ*, **597**(2), 1158–1177.

Kafka, S. & Honeycutt, R. K. (2006) Spectroscopy of Active and Inactive M Dwarfs in Praesepe. *AJ*, **132**(4), 1517–1526.

Kahler, S. W. (1992) Solar flares and coronal mass ejections. *ARA&A*, **30**, 113–141.

Kasting, J. F., Whitmire, D. P. & Reynolds, R. T. (1993) Habitable Zones around Main Sequence Stars. *Icarus*, **101**(1), 108–128.

Kay, C., Opher, M. & Kornbleuth, M. (2016) Probability of CME Impact on Exoplanets Orbiting M Dwarfs and Solar-like Stars. *ApJ*, **826**(2), 195.

Kerber, F., Nave, G., Sansonetti, C. J., Bristow, P. & Rosa, M. R. (2007) The Spectrum of Th-Ar Hollow Cathode Lamps in the 900-4500 nm Region: Establishing Wavelength Standards for the Calibration of VLT Spectrographs. In *The Future of Photometric, Spectrophotometric and Polarimetric Standardization*, edited by C. Sterken, vol. 364 of *Astronomical Society of the Pacific Conference Series*, pp. 461–478.

Khodachenko, M. L., Lammer, H., Lichtenegger, H. I. M. et al. (2007) Mass loss of "Hot Jupiters"—Implications for CoRoT discoveries. Part I: The importance of magnetospheric protection of a planet against ion loss caused by coronal mass ejections. *Planet. Space Sci.*, **55**(5), 631–642.

Kiraga, M. (2012) ASAS Photometry of ROSAT Sources. I. Periodic Variable Stars Coincident with Bright Sources from the ROSAT All Sky Survey. *Acta Astron.*, **62**(1), 67–95.

Kiraga, M. & Stepien, K. (2007) Age-Rotation-Activity Relations for M Dwarf Stars. *Acta Astron.*, **57**, 149–172.

Kirkpatrick, J. D., Henry, T. J. & McCarthy, Donald W., J. (1991) A Standard Stellar Spectral Sequence in the Red/Near-Infrared: Classes K5 to M9. *ApJS*, **77**, 417.

Kirkpatrick, J. D., Reid, I. N., Liebert, J. et al. (1999) Dwarfs Cooler than "M": The Definition of Spectral Type "L" Using Discoveries from the 2 Micron All-Sky Survey (2MASS). *ApJ*, **519**(2), 802–833.

Kopparapu, R. K., Ramirez, R., Kasting, J. F. et al. (2013) Habitable Zones around Main-sequence Stars: New Estimates. *ApJ*, **765**(2), 131.

Kotani, T., Tamura, M., Suto, H. et al. (2014) Infrared Doppler instrument (IRD) for the Subaru telescope to search for Earth-like planets around nearby M-dwarfs. In *Proc. SPIE*, vol. 9147 of *Society of Photo-Optical Instrumentation Engineers (SPIE) Conference Series*, pp. 411–422.

Kowalski, A. F., Hawley, S. L., Hilton, E. J. et al. (2009) M Dwarfs in Sloan Digital Sky Survey Stripe 82: Photometric Light Curves and Flare Rate Analysis. *AJ*, **138**(2), 633–648.

Kowalski, A. F., Hawley, S. L., Holtzman, J. A., Wisniewski, J. P. & Hilton, E. J. (2010) A White Light Megaflare on the dM4.5e Star YZ CMi. *ApJL*, **714**(1), L98–L102.

Kron, G. E. (1947) The Probable Detecting of Surface Spots on AR Lacertae B. *PASP*, **59**(350), 261.

Kuerster, M., Schmitt, J. H. M. M. & Cutispoto, G. (1994) Doppler imaging with a CLEAN-like approach II. A photospheric image of AB Doradus (=HD 36705). *A&A*, **289**, 899–921.

Kunkel, W. E. (1970) On the Spectra of Stellar Flares. *ApJ*, **161**, 503.

Lacy, C. H., Moffett, T. J. & Evans, D. S. (1976) UV Ceti stars: statistical analysis of observational data. *ApJS*, **30**, 85–96.

Lafarga, M., Ribas, I., Lovis, C. et al. (2020) The CARMENES search for exoplanets around M dwarfs. Radial velocities and activity indicators from cross-correlation functions with weighted binary masks. *A&A*, **636**, A36.

Lagrange, A. M., Desort, M. & Meunier, N. (2010) Using the Sun to estimate Earth-like planets detection capabilities . I. Impact of cold spots. *A&A*, **512**, A38.

Lammer, H., Selsis, F., Ribas, I. et al. (2003) Atmospheric Loss of Exoplanets Resulting from Stellar X-Ray and Extreme-Ultraviolet Heating. *ApJL*, **598**(2), L121–L124.

Lamy, P. L., Floyd, O., Boclet, B. et al. (2019) Coronal Mass Ejections over Solar Cycles 23 and 24. *Space Sci. Rev.*, **215**(5), 39.

Laughlin, G., Bodenheimer, P. & Adams, F. C. (1997) The End of the Main Sequence. *ApJ*, **482**(1), 420–432.

Leighton, R. B. (1964) Transport of Magnetic Fields on the Sun. *ApJ*, **140**, 1547.

Leighton, R. B. (1969) A Magneto-Kinematic Model of the Solar Cycle. *ApJ*, **156**, 1.

Leitzinger, M., Odert, P., Ribas, I. et al. (2011) Search for indications of stellar mass ejections using FUV spectra. *A&A*, **536**, A62.

Lépine, S., Hilton, E. J., Mann, A. W. et al. (2013) A Spectroscopic Catalog of the Brightest (J < 9) M Dwarfs in the Northern Sky. *AJ*, **145**(4), 102.

Lépine, S., Rich, R. M. & Shara, M. M. (2003) Spectroscopy of New High Proper Motion Stars in the Northern Sky. I. New Nearby Stars, New High-Velocity Stars, and an Enhanced Classification Scheme for M Dwarfs. *AJ*, **125**(3), 1598–1622.

Lépine, S., Rich, R. M. & Shara, M. M. (2007) Revised Metallicity Classes for Low-Mass Stars: Dwarfs (dM), Subdwarfs (sdM), Extreme Subdwarfs (esdM), and Ultrasubdwarfs (usdM). *ApJ*, **669**(2), 1235–1247.

Liebert, J., Kirkpatrick, J. D., Reid, I. N. & Fisher, M. D. (1999) A 2MASS Ultracool M Dwarf Observed in a Spectacular Flare. *ApJ*, **519**(1), 345–353.

Lindegren, L. & Dravins, D. (2003) The fundamental definition of "radial velocity". *A&A*, **401**, 1185–1201.

Lingam, M. & Loeb, A. (2017a) Reduced Diversity of Life around Proxima Centauri and TRAPPIST-1. *ApJL*, **846**(2), L21.

Lingam, M. & Loeb, A. (2017b) Risks for Life on Habitable Planets from Superflares of Their Host Stars. *ApJ*, **848**(1), 41.

Linsky, J. L. (2000) Stellar flares: How common? How Important? In *Cosmic Explosions: Tenth AstroPhysics Conference*, edited by S. S. Holt & W. W. Zhang, vol. 522 of *American Institute of Physics Conference Series*, pp. 389–399.

Linsky, J. L. (2017) Stellar Model Chromospheres and Spectroscopic Diagnostics. *ARA&A*, **55**(1), 159–211.

Linsky, J. L. & Avrett, E. H. (1970) The Solar H and K Lines. *PASP*, **82**(485), 169.

Linsky, J. L., Hunten, D. M., Sowell, R., Glackin, D. L. & Kelch, W. L. (1979) Stellar model chromospheres. XI. A survey of CA II λ8542 line profiles in late-type stars of differing chromospheric activity. *ApJS*, **41**, 481–500.

Linsky, J. L. & Schöller, M. (2015) Observations of Strong Magnetic Fields in Nondegenerate Stars. *Space Sci. Rev.*, **191**(1-4), 27–76.

Littmann, M., Espenak, F. & Willcox, K. (2008) *Totality: Eclipses of the Sun*. 3rd edn., Oxford University Press.

Livingston, W., Wallace, L., White, O. R. & Giampapa, M. S. (2007) Sun-as-a-Star Spectrum Variations 1974-2006. *ApJ*, **657**(2), 1137–1149.

Lockyer, J. N. (1868) Spectroscopic Observation of the Sun, No. II. *Proceedings of the Royal Society of London Series I*, **17**, 131–132.

Loewenstein, E. V. (1966) The history and current status of Fourier transform spectroscopy. *Appl. Opt.*, **5**(5), 845.

Lovis, C., Dumusque, X., Santos, N. C. et al. (2011) The HARPS search for southern extra-solar planets. XXXI. Magnetic activity cycles in solar-type stars: statistics and impact on precise radial velocities. *arXiv e-prints*, arXiv:1107.5325.

Luger, R. & Barnes, R. (2015) Extreme Water Loss and Abiotic O2Buildup on Planets Throughout the Habitable Zones of M Dwarfs. *Astrobiology*, **15**(2), 119–143.

Luger, R., Barnes, R., Lopez, E. et al. (2015) Habitable Evaporated Cores: Transforming Mini-Neptunes into Super-Earths in the Habitable Zones of M Dwarfs. *Astrobiology*, **15**(1), 57–88.

Luque, R., Nowak, G., Pallé, E. et al. (2019a) Detection and characterization of an ultra-dense sub-Neptunian planet orbiting the Sun-like star K2-292. *A&A*, **623**, A114.

Luque, R., Pallé, E., Kossakowski, D. et al. (2019b) Planetary system around the nearby M dwarf GJ 357 including a transiting, hot, Earth-sized planet optimal for atmospheric characterization. *A&A*, **628**, A39.

Mahadevan, S., Ramsey, L. W., Terrien, R. et al. (2014) The Habitable-zone Planet Finder: A status update on the development of a stabilized fiber-fed near-infrared spectrograph for the for the Hobby-Eberly telescope. In *Proc. SPIE*, vol. 9147 of *Society of Photo-Optical Instrumentation Engineers (SPIE) Conference Series*, pp. 543–552.

Mallik, S. V. (1997) The CA II triplet lines as diagnostics of luminosity, metallicity and chromospheric activity in cool stars. *A&AS*, **124**, 359–384.

Marcy, G. W. & Butler, R. P. (1992) Precision Radial Velocities with an Iodine Absorption cell. *PASP*, **104**, 270.

Mariska, J. T. (1986) The quiet solar transition region. *ARA&A*, **24**, 23–48.

Marsden, S. C., Petit, P., Jeffers, S. V. et al. (2014) A BCool magnetic snapshot survey of solar-type stars. *MNRAS*, **444**(4), 3517–3536.

Martín, E. L., Delfosse, X., Basri, G. et al. (1999) Spectroscopic Classification of Late-M and L Field Dwarfs. *AJ*, **118**(5), 2466–2482.

Martin, J., Fuhrmeister, B., Mittag, M. et al. (2017) The Ca II infrared triplet's performance as an activity indicator compared to Ca II H and K. Empirical relations to convert Ca II infrared triplet measurements to common activity indices. *A&A*, **605**, A113.

Martínez-Arnáiz, R., López-Santiago, J., Crespo-Chacón, I. & Montes, D. (2011) Effect of magnetic activity saturation in chromospheric flux-flux relationships. *MNRAS*, **414**(3), 2629–2641.

Martínez-Rodríguez, H. (2014) *CARMENES target characterisation: mining public archives for high-resolution spectra of M dwarfs with exoplanets*. Master's thesis, Universidad Complutense de Madrid, Spain.

Mauas, P. J. D. (2000) Building Reliable Models of M Dwarf Chromospheres: The Spectral Diagnostics. *ApJ*, **539**(2), 858–864.

Maunder, E. W. (1922) The Prolonged Sunspot Minimum, 1645-1715. *Journal of the British Astronomical Association*, **32**, 140–145.

Mayor, M., Pepe, F., Queloz, D. et al. (2003) Setting New Standards with HARPS. *The Messenger*, **114**, 20–24.

Mayor, M. & Queloz, D. (1995) A Jupiter-mass companion to a solar-type star. *Nature*, **378**(6555), 355–359.

McLean, M., Berger, E. & Reiners, A. (2012) The Radio Activity-Rotation Relation of Ultracool Dwarfs. *ApJ*, **746**(1), 23.

Messina, S., Desidera, S., Lanzafame, A. C., Turatto, M. & Guinan, E. F. (2011) RACE-OC project: rotation and variability in the ϵ Chamaeleontis, Octans, and Argus stellar associations. *A&A*, **532**, A10.

Metcalf, A. J., Anderson, T., Bender, C. F. et al. (2019) Stellar spectroscopy in the near-infrared with a laser frequency comb. *Optica*, **6**(2), 233.

Meunier, N., Lagrange, A. M. & Desort, M. (2010) Reconstructing the solar integrated radial velocity using MDI/SOHO. *A&A*, **519**, A66.

Montes, D., Fernandez-Figueroa, M. J., de Castro, E. & Cornide, M. (1995) Excess Hα emission in chromospherically active binaries. *A&A*, **294**, 165–176.

Morales, J. C., Mustill, A. J., Ribas, I. et al. (2019) A giant exoplanet orbiting a very-low-mass star challenges planet formation models. *Science*, **365**(6460), 1441–1445.

Morgan, W. W., Keenan, P. C. & Kellman, E. (1943) *An atlas of stellar spectra, with an outline of spectral classification*. University of Chicago Press.

Morin, J., Donati, J. F., Petit, P. et al. (2008) Large-scale magnetic topologies of mid M dwarfs. *MNRAS*, **390**(2), 567–581.

Morin, J., Donati, J. F., Petit, P. et al. (2010) Large-scale magnetic topologies of late M dwarfs. *MNRAS*, **407**(4), 2269–2286.

Morris, B. M., Agol, E., Davenport, J. R. A. & Hawley, S. L. (2018) Possible Bright Starspots on TRAPPIST-1. *ApJ*, **857**(1), 39.

Moschou, S.-P., Drake, J. J., Cohen, O., Alvarado-Gomez, J. D. & Garraffo, C. (2017) A Monster CME Obscuring a Demon Star Flare. *ApJ*, **850**(2), 191.

Moschou, S.-P., Drake, J. J., Cohen, O. et al. (2019) The Stellar CME-Flare Relation: What Do Historic Observations Reveal? *ApJ*, **877**(2), 105.

Muheki, P., Guenther, E. W., Mutabazi, T. & Jurua, E. (2020) High-resolution spectroscopy of flares and CMEs on AD Leonis. *A&A*, **637**, A13.

Mulders, G. D., Pascucci, I. & Apai, D. (2015) A Stellar-mass-dependent Drop in Planet Occurrence Rates. *ApJ*, **798**(2), 112.

Mullan, D. J. & Paudel, R. R. (2019) Origin of Radio-quiet Coronal Mass Ejections in Flare Stars. *ApJ*, **873**(1), 1.

Murphy, M. T., Udem, T., Holzwarth, R. et al. (2007) High-precision wavelength calibration of astronomical spectrographs with laser frequency combs. *MNRAS*, **380**(2), 839–847.

Nagel, E., Czesla, S., Kaminski, A. et al. (submitted) The CARMENES search for exoplanets around M dwarfs. The template division telluric modeling technique and its application to optical and near-infrared radial velocities. *A&A*, submitted.

Namekata, K., Maehara, H., Notsu, Y. et al. (2019) Lifetimes and Emergence/Decay Rates of Star Spots on Solar-type Stars Estimated by Kepler Data in Comparison with Those of Sunspots. *ApJ*, **871**(2), 187.

Narain, U. & Ulmschneider, P. (1990) Chromospheric and Coronal Heating Mechanisms. *Space Sci. Rev.*, **54**(3-4), 377–445.

Narain, U. & Ulmschneider, P. (1996) Chromospheric and Coronal Heating Mechanisms II. *Space Sci. Rev.*, **75**(3-4), 453–509.

Neff, J. E., O'Neal, D. & Saar, S. H. (1995) Absolute Measurements of Starspot Area and Temperature: II Pegasi in 1989 October. *ApJ*, **452**, 879.

Newton, E. R., Charbonneau, D., Irwin, J. et al. (2014) Near-infrared Metallicities, Radial Velocities, and Spectral Types for 447 Nearby M Dwarfs. *AJ*, **147**(1), 20.

Newton, E. R., Irwin, J., Charbonneau, D. et al. (2016) The Rotation and Galactic Kinematics of Mid M Dwarfs in the Solar Neighborhood. *ApJ*, **821**(2), 93.

Newton, E. R., Irwin, J., Charbonneau, D. et al. (2017) The Hα Emission of Nearby M Dwarfs and its Relation to Stellar Rotation. *ApJ*, **834**(1), 85.

Niven, C. (1874) On a method of finding the parallax of double stars and on the displacement of the lines in the spectrum of a planet. *MNRAS*, **34**, 339–347.

Nortmann, L., Pallé, E., Salz, M. et al. (2018) Ground-based detection of an extended helium atmosphere in the Saturn-mass exoplanet WASP-69b. *Science*, **362**(6421), 1388–1391.

Noyes, R. W., Hartmann, L. W., Baliunas, S. L., Duncan, D. K. & Vaughan, A. H. (1984) Rotation, convection, and magnetic activity in lower main-sequence stars. *ApJ*, **279**, 763–777.

O'Neal, D., Neff, J. E. & Saar, S. H. (1998) Measurements of Starspot Parameters on Active Stars using Molecular Bands in Echelle Spectra. *ApJ*, **507**(2), 919–937.

Ossendrijver, M. (2003) The solar dynamo. *A&A Rev.*, **11**(4), 287–367.

Osten, R. A., Hawley, S. L., Allred, J. C., Johns-Krull, C. M. & Roark, C. (2005) From Radio to X-Ray: Flares on the dMe Flare Star EV Lacertae. *ApJ*, **621**(1), 398–416.

Owen, J. E. & Mohanty, S. (2016) Habitability of terrestrial-mass planets in the HZ of M Dwarfs - I. H/He-dominated atmospheres. *MNRAS*, **459**(4), 4088–4108.

Pallavicini, R., Golub, L., Rosner, R. et al. (1981) Relations among stellar X-ray emission observed from Einstein, stellar rotation and bolometric luminosity. *ApJ*, **248**, 279–290.

Palle, E., Nowak, G., Luque, R. et al. (2019) Detection and Doppler monitoring of K2-285 (EPIC 246471491), a system of four transiting planets smaller than Neptune. *A&A*, **623**, A41.

Parker, E. N. (1955) Hydromagnetic Dynamo Models. *ApJ*, **122**, 293.

Parker, E. N. (1958) Dynamics of the Interplanetary Gas and Magnetic Fields. *ApJ*, **128**, 664.

Parker, E. N. (1988) Nanoflares and the Solar X-Ray Corona. *ApJ*, **330**, 474.

Parks, J. R., White, R. J., Baron, F. et al. (2015) First Images of Cool Starspots on a Star Other than the Sun: Interferometric Imaging of λ Andromedae. *arXiv e-prints*, arXiv:1508.04755.

Passegger, V. M., Reiners, A., Jeffers, S. V. et al. (2018) The CARMENES search for exoplanets around M dwarfs. Photospheric parameters of target stars from high-resolution spectroscopy. *A&A*, **615**, A6.

Pecaut, M. J. & Mamajek, E. E. (2013) Intrinsic Colors, Temperatures, and Bolometric Corrections of Pre-main-sequence Stars. *ApJS*, **208**(1), 9.

Pepe, F., Cristiani, S., Rebolo, R. et al. (2021) ESPRESSO at VLT. On-sky performance and first results. *A&A*, **645**, A96.

Perryman, M. (2018) *The Exoplanet Handbook*. 2nd edn., Cambridge University Press.

Pestalozzi, M. R., Benz, A. O., Conway, J. E. & Güdel, M. (2000) VLBI observations of two single dMe stars: spatial resolution and astrometry. *A&A*, **353**, 569–574.

Petrovay, K. & van Driel-Gesztelyi, L. (1997) Making Sense of Sunspot Decay. I. Parabolic Decay Law and Gnevyshev-Waldmeier Relation. *Sol. Phys.*, **176**(2), 249–266.

Pettersen, B. R. (1989) A Review of Stellar Flares and Their Characteristics. *Sol. Phys.*, **121**(1-2), 299–312.

Pevtsov, A. A., Fisher, G. H., Acton, L. W. et al. (2003) The Relationship Between X-Ray Radiance and Magnetic Flux. *ApJ*, **598**(2), 1387–1391.

Piskunov, N. E. & Valenti, J. A. (2002) New algorithms for reducing cross-dispersed echelle spectra. *A&A*, **385**, 1095–1106.

Pizzolato, N., Maggio, A., Micela, G., Sciortino, S. & Ventura, P. (2003) The stellar activity-rotation relationship revisited: Dependence of saturated and non-saturated X-ray emission regimes on stellar mass for late-type dwarfs. *A&A*, **397**, 147–157.

Poppenhaeger, K. (2019) How stars and planets interact: A look through the high-energy window. *Astronomische Nachrichten*, **340**(4), 329–333.

Preston, G. W. (1971) The Mean Surface Fields of Magnetic Stars. *ApJ*, **164**, 309.

Queloz, D., Henry, G. W., Sivan, J. P. et al. (2001) No planet for HD 166435. *A&A*, **379**, 279–287.

Quirrenbach, A., Amado, P. J., Ribas, I. et al. (2018) CARMENES: high-resolution spectra and precise radial velocities in the red and infrared. In *Proc. SPIE*, vol. 10702 of *Society of Photo-Optical Instrumentation Engineers (SPIE) Conference Series*, pp. 246–263.

Radick, R. R., Lockwood, G. W., Skiff, B. A. & Baliunas, S. L. (1998) Patterns of Variation among Sun-like Stars. *ApJS*, **118**(1), 239–258.

Reid, I. N. & Hawley, S. L. (2005) *New light on dark stars : red dwarfs, low-mass stars, brown dwarfs*. 2nd edn., Praxis Publishing Ltd.

Reid, I. N., Hawley, S. L. & Gizis, J. E. (1995) The Palomar/MSU Nearby-Star Spectroscopic Survey. I. The Northern M Dwarfs -Bandstrengths and Kinematics. *AJ*, **110**, 1838.

Reiners, A. (2012) Observations of Cool-Star Magnetic Fields. *Living Reviews in Solar Physics*, **9**(1), 1.

Reiners, A. & Basri, G. (2008) Chromospheric Activity, Rotation, and Rotational Braking in M and L Dwarfs. *ApJ*, **684**(2), 1390–1403.

Reiners, A. & Basri, G. (2010) A Volume-Limited Sample of 63 M7-M9.5 Dwarfs. II. Activity, Magnetism, and the Fade of the Rotation-Dominated Dynamo. *ApJ*, **710**(2), 924–935.

Reiners, A., Basri, G. & Browning, M. (2009) Evidence for Magnetic Flux Saturation in Rapidly Rotating M Stars. *ApJ*, **692**(1), 538–545.

Reiners, A., Joshi, N. & Goldman, B. (2012) A Catalog of Rotation and Activity in Early-M Stars. *AJ*, **143**(4), 93.

Reiners, A., Ribas, I., Zechmeister, M. et al. (2018a) The CARMENES search for exoplanets around M dwarfs. HD147379 b: A nearby Neptune in the temperate zone of an early-M dwarf. *A&A*, **609**, L5.

Reiners, A. & Schmitt, J. H. M. M. (2003) Rotation and differential rotation in field F- and G-type stars. *A&A*, **398**, 647–661.

Reiners, A., Schüssler, M. & Passegger, V. M. (2014) Generalized Investigation of the Rotation-Activity Relation: Favoring Rotation Period instead of Rossby Number. *ApJ*, **794**(2), 144.

Reiners, A. & Zechmeister, M. (2020) Radial Velocity Photon Limits for the Dwarf Stars of Spectral Classes FM. *ApJS*, **247**(1), 11.

Reiners, A., Zechmeister, M., Caballero, J. A. et al. (2018b) The CARMENES search for exoplanets around M dwarfs. High-resolution optical and near-infrared spectroscopy of 324 survey stars. *A&A*, **612**, A49.

Reinhold, T., Reiners, A. & Basri, G. (2013) Rotation and differential rotation of active Kepler stars. *A&A*, **560**, A4.

Riaz, B., Gizis, J. E. & Harvin, J. (2006) Identification of New M Dwarfs in the Solar Neighborhood. *AJ*, **132**(2), 866–872.

Ribas, I., Guinan, E. F., Güdel, M. & Audard, M. (2005) Evolution of the Solar Activity over Time and Effects on Planetary Atmospheres. I. High-Energy Irradiances (1-1700 Å). *ApJ*, **622**(1), 680–694.

Ribas, I., Tuomi, M., Reiners, A. et al. (2018) A candidate super-Earth planet orbiting near the snow line of Barnard's star. *Nature*, **563**(7731), 365–368.

Robertson, P., Bender, C., Mahadevan, S., Roy, A. & Ramsey, L. W. (2016) Proxima Centauri as a Benchmark for Stellar Activity Indicators in the Near-infrared. *ApJ*, **832**(2), 112.

Robertson, P., Roy, A. & Mahadevan, S. (2015) Stellar Activity Mimics a Habitable-zone Planet around Kapteyn's Star. *ApJL*, **805**(2), L22.

Robinson, Jr., R. D. (1980) Magnetic field measurements on stellar sources - A new method. *ApJ*, **239**, 961–967.

Roettenbacher, R. M., Monnier, J. D., Korhonen, H. et al. (2016) No Sun-like dynamo on the active star ζ Andromedae from starspot asymmetry. *Nature*, **533**(7602), 217–220.

Russell, H. N. (1913) "Giant" and "dwarf" stars. *The Observatory*, **36**, 324–329.

Saar, S. H. (1988) Measurements of Magnetic Fields on Cool Stars. In *The Impact of Very High S/N Spectroscopy on Stellar Physics*, edited by G. Cayrel de Strobel & M. Spite, vol. 132 of *IAU Symposium*, pp. 295–300.

Saar, S. H. & Donahue, R. A. (1997) Activity-Related Radial Velocity Variation in Cool Stars. *ApJ*, **485**(1), 319–327.

Sanz-Forcada, J. & Dupree, A. K. (2008) Active cool stars and He I 10 830 Å: the coronal connection. *A&A*, **488**(2), 715–721.

Sanz-Forcada, J., Micela, G., Ribas, I. et al. (2011) Estimation of the XUV radiation onto close planets and their evaporation. *A&A*, **532**, A6.

Sarmiento, L. F., Reiners, A., Huke, P. et al. (2018) Comparing the emission spectra of U and Th hollow cathode lamps and a new U line list. *A&A*, **618**, A118.

Schäfer, S., Guenther, E. W., Reiners, A. et al. (2018) Two Fabry-Pérots and two calibration units for CARMENES. In *Proc. SPIE*, vol. 10702 of *Society of Photo-Optical Instrumentation Engineers (SPIE) Conference Series*, pp. 2141–2150.

Schatzman, E. (1949) The heating of the solar corona and chromosphere. *Annales d'Astrophysique*, **12**, 203.

Schlieder, J. E., Lépine, S., Rice, E. et al. (2012) The Na 8200 Å Doublet as an Age Indicator in Low-mass Stars. *AJ*, **143**(5), 114.

Schmidt, S. J., Cruz, K. L., Bongiorno, B. J., Liebert, J. & Reid, I. N. (2007) Activity and Kinematics of Ultracool Dwarfs, Including an Amazing Flare Observation. *AJ*, **133**(5), 2258–2273.

Schmidt, S. J., Kowalski, A. F., Hawley, S. L. et al. (2012) Probing the Flare Atmospheres of M Dwarfs Using Infrared Emission Lines. *ApJ*, **745**(1), 14.

Schmidt, S. J., Shappee, B. J., van Saders, J. L. et al. (2019) The Largest M Dwarf Flares from ASAS-SN. *ApJ*, **876**(2), 115.

Schöfer, P., Jeffers, S. V., Reiners, A. et al. (2019) The CARMENES search for exoplanets around M dwarfs. Activity indicators at visible and near-infrared wavelengths. *A&A*, **623**, A44.

Schöfer, P., Jeffers, S. V., Reiners, A. et al. (submitted) The CARMENES search for exoplanets around M dwarfs. Rotational variation in activity indicators of EV Lac, YZ CMi, and two northern slow rotators. *A&A*, submitted.

Scholz, R. D., Meusinger, H. & Jahreiss, H. (2005) Search for nearby stars among proper motion stars selected by optical-to-infrared photometry. III. Spectroscopic distances of 322 NLTT stars. *A&A*, **442**(1), 211–227.

Schrijver, C. J. (1987) Magnetic structure in cool stars. XI. Relations between radiative fluxes mesuring stellar activity, and evidence for two components in stellar chromospheres. *A&A*, **172**, 111–123.

Schrijver, C. J., Beer, J., Baltensperger, U. et al. (2012) Estimating the frequency of extremely energetic solar events, based on solar, stellar, lunar, and terrestrial records. *Journal of Geophysical Research (Space Physics)*, **117**(A8), A08103.

Schrijver, C. J. & Zwaan, C. (1991) Activity in tidally interacting binaries. *A&A*, **251**, 183.

Schwabe, H. (1844) Sonnenbeobachtungen im Jahre 1843. *Astronomische Nachrichten*, **21**(15), 233.

Schwarzschild, M. (1948) On Noise Arising from the Solar Granulation. *ApJ*, **107**, 1.

Schweitzer, A., Passegger, V. M., Cifuentes, C. et al. (2019) The CARMENES search for exoplanets around M dwarfs. Different roads to radii and masses of the target stars. *A&A*, **625**, A68.

Segura, A., Walkowicz, L. M., Meadows, V., Kasting, J. & Hawley, S. (2010) The Effect of a Strong Stellar Flare on the Atmospheric Chemistry of an Earth-like Planet Orbiting an M Dwarf. *Astrobiology*, **10**(7), 751–771.

Seifahrt, A., Käufl, H. U., Zängl, G. et al. (2010) Synthesising, using, and correcting for telluric features in high-resolution astronomical spectra . A near-infrared case study using CRIRES. *A&A*, **524**, A11.

Semel, M. (1989) Zeeman-Doppler imaging of active stars. I - Basic principles. *A&A*, **225**, 456–466.

Shapiro, A. I., Solanki, S. K., Krivova, N. A., Yeo, K. L. & Schmutz, W. K. (2016) Are solar brightness variations faculae- or spot-dominated? *A&A*, **589**, A46.

Shine, R. A. & Linsky, J. L. (1972) Physical Properties of Solar Chromospheric Plages. I. Line Profiles of the Ca II H, K, and Infrared Triplet Lines. *Sol. Phys.*, **25**(2), 357–379.

Shkolnik, E., Bohlender, D. A., Walker, G. A. H. & Collier Cameron, A. (2008) The On/Off Nature of Star-Planet Interactions. *ApJ*, **676**(1), 628–638.

Shkolnik, E., Liu, M. C. & Reid, I. N. (2009) Identifying the Young Low-mass Stars within 25 pc. I. Spectroscopic Observations. *ApJ*, **699**(1), 649–666.

Shkolnik, E., Walker, G. A. H., Bohlender, D. A., Gu, P. G. & Kürster, M. (2005) Hot Jupiters and Hot Spots: The Short- and Long-Term Chromospheric Activity on Stars with Giant Planets. *ApJ*, **622**(2), 1075–1090.

Shopov, Y. Y., Stoykova, D. A., Stoitchkova, K. et al. (2008) Structure of the solar dust corona and its interaction with the other coronal components. *Journal of Atmospheric and Solar-Terrestrial Physics*, **70**(2-4), 356–364.

Short, C. I. & Doyle, J. G. (1997) Chromospheric line blanketing and the hydrogen spectrum in M dwarfs. *A&A*, **326**, 287–299.

Short, C. I. & Doyle, J. G. (1998) Pa-beta as a chromospheric diagnostic in M dwarfs. *A&A*, **331**, L5–L8.

Shulyak, D., Reiners, A., Engeln, A. et al. (2017) Strong dipole magnetic fields in fast rotating fully convective stars. *Nature Astronomy*, **1**, 0184.

Shulyak, D., Reiners, A., Nagel, E. et al. (2019) Magnetic fields in M dwarfs from the CARMENES survey. *A&A*, **626**, A86.

Siarkowski, M., Pres, P., Drake, S. A., White, N. E. & Singh, K. P. (1996) Corona(e) of AR Lacertae. II. The Spatial Structure. *ApJ*, **473**, 470.

Silva, A. V. R. (2003) Method for Spot Detection on Solar-like Stars. *ApJL*, **585**(2), L147–L150.

Silva-Valio, A., Lanza, A. F., Alonso, R. & Barge, P. (2010) Properties of starspots on CoRoT-2. *A&A*, **510**, A25.

Simon, T., Ayres, T. R., Redfield, S. & Linsky, J. L. (2002) Limits on Chromospheres and Convection among the Main-Sequence A Stars. *ApJ*, **579**(2), 800–809.

Skumanich, A. (1972) Time Scales for Ca II Emission Decay, Rotational Braking, and Lithium Depletion. *ApJ*, **171**, 565.

Smith, K., Güdel, M. & Audard, M. (2005) Flares observed with XMM-Newton and the VLA. *A&A*, **436**(1), 241–251.

Soderblom, D. R., Stauffer, J. R., Hudon, J. D. & Jones, B. F. (1993) Rotation and Chromospheric Emission among F, G, and K Dwarfs of the Pleiades. *ApJS*, **85**, 315.

Spörer, F. G. W. (1887) Über die Periodizität der Sonnenflecken seit dem Jahre 1618, vornehmlich in Bezug auf die heliographische Breite derselben, und Hinweis auf eine erhebliche Streuung dieser Periodizität während eines langen Zeitraumes. *Vierteljahrsschrift der Astronomischen Gesellschaft*, **22**, 323–329.

Spruit, H. C. (2011) Theories of the Solar Cycle: A Critical View. In *The Sun, the Solar Wind, and the Heliosphere*, edited by M. P. Miralles & J. Sánchez Almeida, vol. 4, p. 39.

Stassun, K. G., Hebb, L., Covey, K. et al. (2011) The M4 Transition: Toward a Comprehensive Understanding of the Transition into the Fully Convective Regime. In *16th Cambridge Workshop on Cool Stars, Stellar Systems, and the Sun*, edited by C. Johns-Krull, M. K. Browning & A. A. West, vol. 448 of *Astronomical Society of the Pacific Conference Series*, pp. 505–516.

Stauffer, J. R. & Hartmann, L. W. (1986) Chromospheric Activity, Kinematics, and Metallicities of Nearby M Dwarfs. *ApJS*, **61**, 531.

Stelzer, B., Marino, A., Micela, G., López-Santiago, J. & Liefke, C. (2013) The UV and X-ray activity of the M dwarfs within 10 pc of the Sun. *MNRAS*, **431**(3), 2063–2079.

Stewart, R. T., Innis, J. L., Slee, O. B., Nelson, G. J. & Wright, A. E. (1988) A Relation Between Radio Luminosity and Rotation for Late-Type Stars. *AJ*, **96**, 371.

Stix, M. (1989) The Sun's Differential Rotation. *Reviews in Modern Astronomy*, **2**, 248–266.

Strassmeier, K. G. (2009) Starspots. *A&A Rev.*, **17**(3), 251–308.

Strassmeier, K. G., Bartus, J., Cutispoto, G. & Rodono, M. (1997) Starspot photometry with robotic telescopes: Continuous UBV and V(RI)$_C$ photometry of 23 stars in 1991-1996. *A&AS*, **125**, 11–63.

Strassmeier, K. G., Rice, J. B., Wehlau, W. H. et al. (1991) Doppler imaging of hig-latitude SPOT activity on HD 26337. *A&A*, **247**, 130.

Suárez Mascareño, A., Rebolo, R. & González Hernández, J. I. (2016) Magnetic cycles and rotation periods of late-type stars from photometric time series. *A&A*, **595**, A12.

Suárez Mascareño, A., Rebolo, R., González Hernández, J. I. & Esposito, M. (2015) Rotation periods of late-type dwarf stars from time series high-resolution spectroscopy of chromospheric indicators. *MNRAS*, **452**(3), 2745–2756.

Suárez Mascareño, A., Rebolo, R., González Hernández, J. I. & Esposito, M. (2017) Characterization of the radial velocity signal induced by rotation in late-type dwarfs. *MNRAS*, **468**(4), 4772–4781.

Suárez Mascareño, A., Rebolo, R., González Hernández, J. I. et al. (2018) HADES RV programme with HARPS-N at TNG. VII. Rotation and activity of M-dwarfs from time-series high-resolution spectroscopy of chromospheric indicators. *A&A*, **612**, A89.

Tal-Or, L., Trifonov, T., Zucker, S., Mazeh, T. & Zechmeister, M. (2019) Correcting HIRES/Keck radial velocities for small systematic errors. *MNRAS*, **484**(1), L8–L13.

Tal-Or, L., Zechmeister, M., Reiners, A. et al. (2018) The CARMENES search for exoplanets around M dwarfs. Radial-velocity variations of active stars in visual-channel spectra. *A&A*, **614**, A122.

Tian, F., France, K., Linsky, J. L., Mauas, P. J. D. & Vieytes, M. C. (2014) High stellar FUV/NUV ratio and oxygen contents in the atmospheres of potentially habitable planets. *Earth and Planetary Science Letters*, **385**, 22–27.

Tinney, C. G. & Reid, I. N. (1998) High-resolution spectra of very low-mass stars. *MNRAS*, **301**(4), 1031–1048.

Torres, C. A. O., Quast, G. R., da Silva, L. et al. (2006) Search for associations containing young stars (SACY). I. Sample and searching method. *A&A*, **460**(3), 695–708.

Toupance, G., Bossard, A. & Raulin, F. (1977) Far UV irradiation of model prebiotic atmospheres. *Origins of Life*, **8**(3), 259–266.

Tousey, R. (1973) The solar corona. In *Proceedings of Open Meetings of Working Groups on Physical Sciences of the 15th Plenary Meeting of COSPAR, Madrid, Spain, 10–24 May, 1972*, edited by M. J. Rycroft & S. K. Runcorn, vol. 2 of *Space Research XIII*, pp. 713–730.

Tregloan-Reed, J. & Unda-Sanzana, E. (2019) Simulations of starspot anomalies within TESS exoplanetary transit light curves. I. Detection limits of starspot anomalies in TESS light curves. *A&A*, **630**, A114.

Trifonov, T., Kürster, M., Zechmeister, M. et al. (2018) The CARMENES search for exoplanets around M dwarfs . First visual-channel radial-velocity measurements and orbital parameter updates of seven M-dwarf planetary systems. *A&A*, **609**, A117.

Tsuji, T., Ohnaka, K. & Aoki, W. (1996) Dust formation in stellar photospheres: a case of very low mass stars and a possible resolution on the effective temperature scale of M dwarfs. *A&A*, **305**, L1.

Tuomi, M., Anglada-Escudé, G., Gerlach, E. et al. (2013) Habitable-zone super-Earth candidate in a six-planet system around the K2.5V star HD 40307. *A&A*, **549**, A48.

Valenti, J. A. & Johns-Krull, C. (2001) Magnetic Field Measurements for Cool Stars. In *Magnetic Fields Across the Hertzsprung-Russell Diagram*, edited by G. Mathys, S. K. Solanki & D. T. Wickramasinghe, vol. 248 of *Astronomical Society of the Pacific Conference Series*, pp. 179–188.

Valenti, J. A., Piskunov, N. & Johns-Krull, C. M. (1998) Spectral Synthesis of TiO Lines. *ApJ*, **498**(2), 851–862.

Vaquero, J. M. (2007) Letter to the Editor: Sunspot observations by Theophrastus revisited. *Journal of the British Astronomical Association*, **117**, 346.

Vaughan, A. H., Baliunas, S. L., Middelkoop, F. et al. (1981) Stellar rotation in lower main-sequence stars measured from time variations in H and K emission-line fluxes. I. Initial results. *ApJ*, **250**, 276–283.

Vaughan, A. H., Preston, G. W. & Wilson, O. C. (1978) Flux measurements of Ca II and K emission. *PASP*, **90**, 267–274.

Vaughan, Arthur H., J. & Zirin, H. (1968) The Helium Line λ 10830 Å in Late-Type Stars. *ApJ*, **152**, 123.

Vernazza, J. E., Avrett, E. H. & Loeser, R. (1981) Structure of the solar chromosphere. III. Models of the EUV brightness components of the quiet sun. *ApJS*, **45**, 635–725.

Vida, K., Kriskovics, L., Oláh, K. et al. (2016) Investigating magnetic activity in very stable stellar magnetic fields. Long-term photometric and spectroscopic study of the fully convective M4 dwarf V374 Pegasi. *A&A*, **590**, A11.

Vida, K., Leitzinger, M., Kriskovics, L. et al. (2019) The quest for stellar coronal mass ejections in late-type stars. I. Investigating Balmer-line asymmetries of single stars in Virtual Observatory data. *A&A*, **623**, A49.

Vidal-Madjar, A., Lecavelier des Etangs, A., Désert, J. M. et al. (2003) An extended upper atmosphere around the extrasolar planet HD209458b. *Nature*, **422**(6928), 143–146.

Vidotto, A. A., Gregory, S. G., Jardine, M. et al. (2014) Stellar magnetism: empirical trends with age and rotation. *MNRAS*, **441**(3), 2361–2374.

Villadsen, J. & Hallinan, G. (2019) Ultra-wideband Detection of 22 Coherent Radio Bursts on M Dwarfs. *ApJ*, **871**(2), 214.

Vogt, S. S. (1979) A spectroscopic and photometric study of the star spot on HD 224085. *PASP*, **91**, 616.

Vogt, S. S., Allen, S. L., Bigelow, B. C. et al. (1994) HIRES: the high-resolution echelle spectrometer on the Keck 10-m Telescope. In *Proc. SPIE*, edited by D. L. Crawford & E. R. Craine, vol. 2198 of *Society of Photo-Optical Instrumentation Engineers (SPIE) Conference Series*, pp. 362–375.

Vogt, S. S. & Penrod, G. D. (1983) Doppler imaging of spotted stars : application to the RS Canum Venaticorum star HR 1099. *PASP*, **95**, 565–576.

Vollmann, K. & Eversberg, T. (2006) Remarks on statistical errors in equivalent widths. *Astronomische Nachrichten*, **327**(9), 862.

Walkowicz, L. M., Hawley, S. L. & West, A. A. (2004) The χ Factor: Determining the Strength of Activity in Low-Mass Dwarfs. *PASP*, **116**(826), 1105–1110.

Walton, S. R., Preminger, D. G. & Chapman, G. A. (2003) The Contribution of Faculae and Network to Long-Term Changes in the Total Solar Irradiance. *ApJ*, **590**(2), 1088–1094.

Watson, C. L., Henden, A. A. & Price, A. (2006) The International Variable Star Index (VSX). *Society for Astronomical Sciences Annual Symposium*, **25**, 47.

Webb, D. F. & Howard, R. A. (1994) The solar cycle variation of coronal mass ejections and the solar wind mass flux. *J. Geophys. Res.*, **99**(A3), 4201–4220.

Webb, D. F. & Howard, T. A. (2012) Coronal Mass Ejections: Observations. *Living Reviews in Solar Physics*, **9**(1), 3.

Weber, E. J. & Davis, Leverett, J. (1967) The Angular Momentum of the Solar Wind. *ApJ*, **148**, 217–227.

Weiss, N. O. (1990) Periodicity and Aperiodicity in Solar Magnetic Activity. *Philosophi-cal Transactions of the Royal Society of London Series A*, **330**(1615), 617–625.

West, A. A., Hawley, S. L., Walkowicz, L. M. et al. (2004) Spectroscopic Properties of Cool Stars in the Sloan Digital Sky Survey: An Analysis of Magnetic Activity and a Search for Subdwarfs. *AJ*, **128**(1), 426–436.

West, A. A., Weisenburger, K. L., Irwin, J. et al. (2015) An Activity-Rotation Relationship and Kinematic Analysis of Nearby Mid-to-Late-Type M Dwarfs. *ApJ*, **812**(1), 3.

Wildi, F., Blind, N., Reshetov, V. et al. (2017) NIRPS: an adaptive-optics assisted radial velocity spectrograph to chase exoplanets around M-stars. In *Proc. SPIE*, vol. 10400 of *Society of Photo-Optical Instrumentation Engineers (SPIE) Conference Series*, pp. 321–335.

Wildi, F., Pepe, F., Chazelas, B., Lo Curto, G. & Lovis, C. (2010) A Fabry-Perot calibrator of the HARPS radial velocity spectrograph: performance report. In *Proc. SPIE*, vol. 7735 of *Society of Photo-Optical Instrumentation Engineers (SPIE) Conference Series*, pp. 1853–1863.

Willson, R. C. & Hudson, H. S. (1991) The Sun's luminosity over a complete solar cycle. *Nature*, **351**(6321), 42–44.

Wilson, O. C. (1963) A Probable Correlation Between Chromospheric Activity and Age in Main-Sequence Stars. *ApJ*, **138**, 832.

Wilson, O. C. (1968) Flux Measurements at the Centers of Stellar H- and K-Lines. *ApJ*, **153**, 221.

Wilson, O. C. (1978) Chromospheric variations in main-sequence stars. *ApJ*, **226**, 379–396.

Wing, R. F. & Ford, Jr., W. K. (1969) The Infrared Spectrum of the Cool Dwarf Wolf 359. *PASP*, **81**(482), 527–529.

Wolf, R. (1852) Bericht über neue Untersuchungen über die Periode der Sonnenflecken und ihrer Bedeutung. *Astronomische Nachrichten*, **35**(25), 369.

Wolszczan, A. & Frail, D. A. (1992) A planetary system around the millisecond pulsar PSR1257 + 12. *Nature*, **355**(6356), 145–147.

Wood, B. E. (2004) Astrospheres and Solar-like Stellar Winds. *Living Reviews in Solar Physics*, **1**(1), 2.

Wood, B. E. (2006) The Solar Wind and the Sun in the Past. *Space Sci. Rev.*, **126**(1-4), 3–14.

Wood, B. E., Müller, H. R., Zank, G. P., Linsky, J. L. & Redfield, S. (2005) New Mass-Loss Measurements from Astrospheric Lyα Absorption. *ApJL*, **628**(2), L143–L146.

Woolf, V. M. & Wallerstein, G. (2006) Calibrating M Dwarf Metallicities Using Molecular Indices. *PASP*, **118**(840), 218–226.

Wright, N. J. & Drake, J. J. (2016) Solar-type dynamo behaviour in fully convective stars without a tachocline. *Nature*, **535**(7613), 526–528.

Wright, N. J., Drake, J. J., Mamajek, E. E. & Henry, G. W. (2011) The Stellar-activity-Rotation Relationship and the Evolution of Stellar Dynamos. *ApJ*, **743**(1), 48.

Wright, N. J., Newton, E. R., Williams, P. K. G., Drake, J. J. & Yadav, R. K. (2018) The stellar rotation-activity relationship in fully convective M dwarfs. *MNRAS*, **479**(2), 2351–2360.

Yan, F., Casasayas-Barris, N., Molaverdikhani, K. et al. (2019) Ionized calcium in the atmospheres of two ultra-hot exoplanets WASP-33b and KELT-9b. *A&A*, **632**, A69.

Yang, H., Liu, J., Gao, Q. et al. (2017) The Flaring Activity of M Dwarfs in the Kepler Field. *ApJ*, **849**(1), 36.

Yashiro, S., Akiyama, S., Gopalswamy, N. & Howard, R. A. (2006) Different Power-Law Indices in the Frequency Distributions of Flares with and without Coronal Mass Ejections. *ApJL*, **650**(2), L143–L146.

Yashiro, S., Gopalswamy, N., Akiyama, S., Michalek, G. & Howard, R. A. (2005) Visibility of coronal mass ejections as a function of flare location and intensity. *Journal of Geophysical Research (Space Physics)*, **110**(A12), A12S05.

Yau, K. K. C. & Stephenson, F. R. (1988) A revised catalogue of Far Eastern observations of sunspots (165 BC to AD 1918). *QJRAS*, **29**, 175–197.

Young, A., Skumanich, A., Stauffer, J. R., Bopp, B. W. & Harlan, E. (1989) A Study of Excess H alpha Emission in Chromospherically Active M Dwarf Stars. *ApJ*, **344**, 427.

Young, C. A. (1872) Letter to the superintendent of the U. S. Coast Survey, containing a catalogue of bright lines in the spectrum of the solar atmosphere, observed at Sherman, Wyoming territory, USA, during July and August, 1872. *American Journal of Science*, **4**(23), 356–361.

Zechmeister, M., Anglada-Escudé, G. & Reiners, A. (2014) Flat-relative optimal extraction. A quick and efficient algorithm for stabilised spectrographs. *A&A*, **561**, A59.

Zechmeister, M., Dreizler, S., Ribas, I. et al. (2019) The CARMENES search for exoplanets around M dwarfs. Two temperate Earth-mass planet candidates around Teegarden's Star. *A&A*, **627**, A49.

Zechmeister, M. & Kürster, M. (2009) The generalised Lomb-Scargle periodogram. A new formalism for the floating-mean and Keplerian periodograms. *A&A*, **496**(2), 577–584.

Zechmeister, M., Kürster, M. & Endl, M. (2009) The M dwarf planet search programme at the ESO VLT + UVES. A search for terrestrial planets in the habitable zone of M dwarfs. *A&A*, **505**(2), 859–871.

Zechmeister, M., Reiners, A., Amado, P. J. et al. (2018) Spectrum radial velocity analyser (SERVAL). High-precision radial velocities and two alternative spectral indicators. *A&A*, **609**, A12.

Zendejas, J., Segura, A. & Raga, A. C. (2010) Atmospheric mass loss by stellar wind from planets around main sequence M stars. *Icarus*, **210**(2), 539–544.

Zirin, H. (1982) λ10830 He I observations of 455 stars. *ApJ*, **260**, 655–669.

Acknowledgements

The asses of experience go slowly, but even a slow ass reaches its goal eventually. Finishing this thesis would not have been possible without the help and support from many people.

First of all, I would like to thank Ansgar for his support in supervising my PhD work and many useful discussions. I would also like to thank the other members of my thesis advisory committee, Sandra and Stefan, for the helpful discussions in my TAC meetings. Sandra also helped me a lot with writing papers and this thesis.

I am grateful to everyone in the working group, in particular to Erik, Lev, Mathias, and Oliver, for their ideas and comments, and fruitful discussions on the interpretation of the results. I enjoyed working with the CARMENES consortium and would like to extend thanks in particular to José for many useful comments and discussions.

Finally, thanks to my parents for their enduring support throughout the years, and a happy hee-haw to my friends at SETI.Germany.